Towards a Better Understanding of the Flight Mechanics of Compound Helicopter Configurations

Kevin M. Ferguson, B.Eng

Submitted in partial fulfilment of the requirements for the degree of

Doctor of Philosophy

November 6, 2015

School of Engineering
College of Science and Engineering
University of Glasgow

Abstract

The compound helicopter is a high speed design concept that is once again being explored due to the emerging requirements for rotorcraft to obtain speeds that significantly surpass the conventional helicopter. The speed of the conventional helicopter is limited by retreating blade stall, however the introduction of compounding delays the onset of this aerodynamic limitation until greater flight speeds. There are two common types of compounding known as lift and thrust compounding. Lift compounding, provided by the addition of a wing offloads the main rotor of its lifting responsibilities in high speed flight. Thrust compounding, provided by the addition of a propulsive source such as a propeller, provides additional axial force divorcing the main rotor of its propulsive duties at high speeds. The addition of compounding to the helicopter design can therefore increase the maximum speed of the aircraft. This increase in speed, provided that efficient hover capability is maintained, would make the compound helicopter suitable for various roles and missions in both military and civil markets.

The compound helicopter is not a novel idea with many compound helicopter configurations flight tested in the 1960's. Due to these test programmes, as well as other studies, there is some material relating to the compound helicopter in the literature. However, the majority of the compound helicopter work describes flight tests of experimental aircraft or focuses on the design of the aircraft configuration. There are no systematic studies of the flight dynamics of compound helicopters which have been published. This Thesis targets this gap in the literature. Consequently, the aim of this Thesis is to investigate the effects of compounding on the conventional helicopter and how this addition to the helicopter design influences the flight mechanics of this aircraft class. With the renewed interest in the compound helicopter design this work is both original and timely. To investigate the flight dynamics of this aircraft class, two mathematical models of compound helicopter configurations are developed and compared with a conventional helicopter. The first compound helicopter configuration features a coaxial rotor with a pusher propeller providing additional axial thrust, and is referred to as the coaxial compound helicopter. The second configuration, known as the hybrid compound helicopter, features two wings each with a tip mounted propeller providing thrust compounding. The conventional helicopter features a standard helicopter design with a main rotor providing the propulsive and lifting forces, whereas a tail rotor, mounted at the rear of the aircraft, provides the yaw control.

Other authors have focused on design considerations and have quantified all of the benefits of compounding but to date, a comprehensive study of the effect of compounding on the flight dynamics of a helicopter has not been published. The strategy of the work is to take the three aircraft configurations, the two compound helicopter configurations and the conventional helicopter, and determine their flight mechanics characteristics. Subsequently, the compound helicopter results can be compared with the baseline configuration, thereby isolating the effects of compounding. The flight mechanics characteristics that are determined in this Thesis include: trim, performance, stability and manoeuvrability attributes of the three helicopter configurations. These attributes are assessed by calculating the control angles which result in a steady flight condition and by the use of numerical linearisation and inverse simulation algorithms. All of these flight mechanics characteristics were assessed with the results, in some aspects, reinforcing the potential of the compound helicopter as well as highlighting some possible difficulties that will have to be addressed in the design of a compound helicopter.

Nomenclature

$\mathbf{a}$	Acceleration vector (m/s^2)
a_0	Lift curve slope of a rotor blade element (1/rad)
$a_{\mathrm{x}}^{\mathrm{blade}}$, $a_{\mathrm{y}}^{\mathrm{blade}}$, $a_{\mathrm{z}}^{\mathrm{blade}}$	Translational acceleration components of a rotor blade element in blade axes (m/s^2)
$a_{\mathrm{x}}^{\mathrm{disc}}$, $a_{\mathrm{y}}^{\mathrm{disc}}$, $a_{\mathrm{z}}^{\mathrm{disc}}$	Acceleration components of the rotor hub in disc axes (m/s^2)
c	Chord length (m)
$\bar{d}$	Drag per unit span (N/m)
e	Main rotor root cut out as a fraction of the rotor span
$\mathbf{f}_{\mathrm{aero}}^{\mathrm{blade}}$	Local aerodynamic force vector of a rotor blade element in blade axes (N/m)
$\mathbf{f}_{\mathrm{el}}^{\mathrm{blade}}$	Force per unit span of a rotor blade element in blade axes (N/m)
$\mathbf{f}_{\mathrm{in}}^{\mathrm{blade}}$	Local inertial force of a rotor blade element in blade axes (N/m)
$\mathbf{f}_{\mathrm{p}}^{\mathrm{p.bl.}}$	Force of a propeller blade element in propeller blade axes, per unit span (N/m)
$\mathbf{f}_{\mathrm{w}}^{\mathrm{anh}}$	Force of a wing strip in anhedral axes, per unit span (N/m)
x^{anh}, y^{anh}, z^{anh}	Force components of the vector $\mathbf{f}_{\mathrm{w}}^{\mathrm{anh}}$ (N/m)
$f_{\mathrm{x}}^{\mathrm{p.bl.}}$, $f_{\mathrm{y}}^{\mathrm{p.bl.}}$, $f_{\mathrm{z}}^{\mathrm{p.bl.}}$	Force components of $\mathbf{f}_{\mathrm{p}}^{\mathrm{p.bl.}}$ (N/m)
g	Acceleration due to gravity (m/s^2)
h	Altitude above mean sea level (m)
h_{prop}	Height of the propeller hub from the reference point in body axes (m)
h_w	Distance of the wing root above the centre of gravity (m)
$\mathbf{i}, \mathbf{j}, \mathbf{k}$	Unit vectors
k	Empirical factor representing the main rotor's contribution to the wing

l_{prop}	Length of the propeller hub from the reference point in body axes (m)
$\bar{l}$	Lift per unit span (N/m)
l_w	Length from the vehicle reference point to the quarter chord position of a wing strip (m)
m_0	Mass per unit span of a rotor blade element in blade axes (kg/m)
$\mathbf{m}_{\mathrm{p}}^{\mathrm{p.bl.}}$	Moment vector of a propeller blade element in propeller blade axes, per unit span
$\mathbf{m}_{\mathrm{w}}^{\mathrm{anh}}$	Moment vector of the wing in anhedral axes, per unit span
$\mathbf{m}_{\mathrm{w}}^{\mathrm{body}}$	Moment vector of the wing in body axes, per unit span
n	Propeller revolutions per second (rev/s) or load factor
n_{clock}	Direction of rotational of the propeller
p, q, r	Small perturbations of angular velocities in body axes (rad/s)
$\mathbf{r}$	Position vector (m)
$\bar{r}$	Normalised rotor blade position (m)
$\mathbf{r}_{\mathrm{c.g.}\to\mathrm{w}}^{\mathrm{body}}$	Position vector from the centre of gravity to the quarter chord point of a wing strip in body axes (m)
$r_{\mathrm{x}}^{\mathrm{body}}$, $r_{\mathrm{y}}^{\mathrm{body}}$, $r_{\mathrm{z}}^{\mathrm{body}}$	Components of the vector of $\mathbf{r}_{\mathrm{c.g.}\to\mathrm{w}}^{\mathrm{body}}$
$\mathbf{u}$	Control vector (rad)
u, v, w	Small perturbations of translational velocities in body axes (m/s)
$u^{\mathrm{p.d.}}$, $v^{\mathrm{p.d.}}$, $w^{\mathrm{p.d.}}$	Translational components of $\mathbf{v}_{\mathrm{p.h.}}^{\mathrm{p.d.}}$ (m/s)
$\mathbf{v}$	Velocity vector (m/s)
v_0, v_{1s}, v_{1c}	Uniform and first harmonic rotor inflow terms (m/s)
v_i	Induced velocity (m/s)
$\bar{v}_n$	Normalised normal velocity
v_n	Normal velocity (m/s)
$\mathbf{v}_{\mathrm{p.h.}}^{\mathrm{p.d.}}$	Velocity vector of the propeller hub in propeller disc axes (m/s)
$\mathbf{v}_{\mathrm{p}}^{\mathrm{p.bl.}}$	Velocity vector at the quarter chord point of a propeller section in propeller disc axes (m/s)
v_{res}	Resultant velocity across an aerofoil section (m/s)
$\bar{v}_{tan}$	Normalised tangential velocity
v_{tan}	Tangential velocity (m/s)

$\mathbf{v}_{\mathrm{w}}^{\mathrm{anh}}$	Velocity vector at the quarter chord point of a wing strip in anhedral axes (m/s)
u^{anh}, v^{anh}, w^{anh}	Velocity components of the vector $\mathbf{v}_{\mathrm{w}}^{\mathrm{anh}}$
$v_{\mathrm{x}}^{\mathrm{p.bl.}}$, $v_{\mathrm{y}}^{\mathrm{p.bl.}}$, $v_{\mathrm{z}}^{\mathrm{p.bl.}}$	Components of the velocity vector $\mathbf{v}_{\mathrm{p}}^{\mathrm{p.bl.}}$
w_{prop}	Lateral distance of the propeller hub from the reference point in body axes (m)
$\mathbf{x}$	The state vector (varying units)
$\dot{x}_e$, $\dot{y}_e$, $\dot{z}_e$	Translational velocities in the Earth axes (m/s)
$x_{c.g.}$	Centre of gravity position from the reference point (m)
$\dot{\mathbf{x}}$	Time derivative of the state vector
y_i	Distance of the quarter chord point of a wing strip in the $\mathbf{j}_{\mathrm{b}}$ direction (m)
A	Rotor or propeller disc area, πR^2 (m^2)
$\mathbf{A}$, $\mathbf{B}$	The system and control matrices
AR	Wing aspect ratio
C	Coefficient
$\mathbf{C}_{\mathrm{rot}}^{\mathrm{blade}}$	Normalised force vector of the main rotor in blade axes
C_d	Drag coefficient
C_{D_i}	Drag coefficient representing the induced drag of the wing
$\mathbf{C}_{\mathrm{I}}$	Time-dependent damping matrix in individual blade flapping equations
C_l	Lift coefficient
$\bar{C}L$	Mean lift coefficient across the wing
$\mathbf{C}_{\mathrm{M}}$	Time-dependent damping matrix in multi-blade flapping equations
C_P	Power Coefficient, $P/\rho A(\Omega R)^3$
C_Q	Torque Coefficient, $Q/\rho AR(\Omega R)^2$
C_T	Thrust Coefficient, $T/\rho A(\Omega R)^2$
C_{T_L}	Lower rotor thrust coefficient
C_{T_U}	Upper rotor thrust coefficient
C_W	Weight Coefficient, $W/\rho A(\Omega R)^2$
D	Propeller diameter (m)
$\mathbf{D}_{\mathrm{I}}$	Time-dependent stiffness matrix in individual blade flapping equations

$\mathbf{D}_{\mathrm{M}}$	Time-dependent stiffness matrix in multi-blade flapping equations
$\mathbf{D}^{-1}_{\mathrm{M}\ 0}$	Constant stiffness matrix in multi-blade flapping equations
$\mathbf{F}^{\mathrm{body}}_{\mathrm{prop}}$	Force vector of the propeller in body axes (N)
$\mathbf{F}^{\mathrm{p.bl.}}_{\mathrm{prop}}$	Force vector of the propeller in propeller blade axes (N)
$\mathbf{F}^{\mathrm{body}}_{\mathrm{rot}}$	Force vector of the main rotor in body axes (N)
$\mathbf{F}^{\mathrm{body}}_{\mathrm{wing}}$	Force vector of the wing in body axes (N)
$\mathbf{H}_{\mathrm{I}}$	Time-dependent forcing function matrix in individual blade flapping equations
$\mathbf{H}_{\mathrm{M}}$	Time-dependent forcing function matrix in multi-blade flapping equations
$\mathbf{H}^{-1}_{\mathrm{M}\ 0}$	Forcing function matrix in multi-blade flapping equations
I_{xx}, I_{yy}, I_{zz}	Moments of inertia of the helicopter about the x_b, y_b and z_b body axes (kgm^2)
I_{xy}, I_{xz}, I_{yz}	Products of inertia of the helicopter about the body axes (kgm^2)
I_β	Flap moment of inertia (kg m^2)
J	Propeller advance ratio, V/nD
$\mathbf{J}$	Jacobian matrix
K_β	Centre-spring rotor stiffness (N.m/rad)
L, M, N	The external moments about the x_b, y_b and z_b body axes (N m)
$\mathbf{L}_\beta$	Transformation matrix from multi-blade to individual co-ordinates
$L^{\mathrm{blade}}_{\mathrm{rot}}$	Rolling moment of the main rotor in blade axes (Nm)
L_u, L_p, etc.	L force derivatives in semi-normalised form (rad/m.s, 1/s, etc.)
M_{a}	Aircraft mass (kg)
M	Mach number
$\mathbf{M}^{\mathrm{p.bl.}}_{\mathrm{p.h.}}$	Moment vector of the propeller hub in propeller blade axes (Nm)
$\mathbf{M}^{\mathrm{body}}_{\mathrm{p.h.}}$	Moment vector of the propeller hub in body axes (Nm)
$\mathbf{M}^{\mathrm{body}}_{\mathrm{prop}}$	Moment vector of the propeller in body axes (Nm)
$\mathbf{M}^{\mathrm{blade}}_{\mathrm{rot}}$	Moment vector of the main rotor in blade axes (Nm)
$M^{\mathrm{blade}}_{\mathrm{rot}}$	Pitching moment of the main rotor in blade axes (Nm)
M_u, M_p, etc.	M force derivatives in semi-normalised form (rad/m.s, 1/s, etc.)
$\mathbf{M}^{\mathrm{body}}_{\mathrm{wing}}$	Moment vector of the wing in body axes (Nm)
M_x	Upper rotor rolling moment (Nm)

N_b	Number of rotor blades
$N_{\text{rot}}^{\text{blade}}$	Yawing moment of the main rotor in blade axes (Nm)
N_u, N_p, etc.	N force derivatives in semi-normalised form (rad/m.s, 1/s, etc.)
P, Q, R	Angular velocity components about the x_b, y_b and z_b body axes (rad/s)
$\dot{P}$, $\dot{Q}$, $\dot{R}$	Angular accelerations in body axes (rad/s^2)
R	Rotor radius (m)
R_{prop}	Propeller radius (m)
$\mathbf{T}^{\text{body}\rightarrow\text{anh}}$	Transformation matrix from body to anhedral axes
$\mathbf{T}^{\text{body}\rightarrow\text{disc}}$	Transformation matrix between the body and disc axes sets
$\mathbf{T}^{\text{body}\rightarrow\text{p.d.}}$	Transformation matrix from body to propeller disc axes
$\mathbf{T}^{\text{disc}\rightarrow\text{shaft}}$	Transformation matrix between the disc and shaft axes sets
$\mathbf{T}^{\text{p.d.}\rightarrow\text{p.bl.}}$	Transformation from propeller disc to propeller blade axes
$\mathbf{T}^{\text{shaft}\rightarrow\text{blade}}$	Transformation matrix between shaft and blade axes
U, V, W	Translational velocity components of the x_b, y_b and z_b body axes (m/s)
$\dot{U}$, $\dot{V}$, $\dot{W}$	Translational accelerations in body axes (m/s^2)
V or V_f	Flight speed (m/s) or (kt)
W	Aircraft weight (N)
X, Y, Z	The external forces about the x_b, y_b and z_b body axes (N)
X_{e}, Y_{e}, Z_{e},	X, Y, Z body forces at a trimmed flight state (N)
X_{rot}, Y_{rot}, Z_{rot}	Components of the vector $\mathbf{F}_{\text{rot}}^{\text{body}}$
X_u, X_p, etc.	X force derivatives in semi-normalised form (1/s, m/s.rad, etc.)
Y_u, Y_p, etc.	Y force derivatives in semi-normalised form (1/s, m/s.rad, etc.)
Z_u, Z_p, etc.	Z force derivatives in semi-normalised form (1/s, m/s.rad, etc.)
$\mathbf{m}_{\text{el}}^{\text{blade}}$	Moment of a rotor blade element in blade axes per unit span
α	Angle of attack (rad)
$\boldsymbol{\alpha}$	Angular acceleration (rad/s^2)
α_{bl}	Angle of attack of a rotor blade element (rad)
α_{fus}	Angle of attack of the helicopter's fuselage, $\tan^{-1}(W/U)$, (rad)
β	Flapping angle (rad)
β_0	Main rotor coning angle (rad)
β_{0d}	Main rotor differential coning angle (rad)
β_{1c}	Main rotor longitudinal flapping angle (rad)

β_{1s}	Main rotor lateral flapping angle (rad)
β_i	Flapping angle of the ith blade (rad)
$\boldsymbol{\beta}_I$	Vector of individual blade co-ordinates (rad)
$\boldsymbol{\beta}_{\mathrm{I}}^{'}$	Derivative of $\boldsymbol{\beta}_{\mathrm{I}}$ with respect to the azimuth position
$\boldsymbol{\beta}_{\mathrm{I}}^{''}$	Derivative of $\boldsymbol{\beta}_{\mathrm{I}}^{'}$ with respect to the azimuth position
$\boldsymbol{\beta}_M$	Vector of multi-blade co-ordinates (rad)
$\boldsymbol{\beta}_{\mathrm{M}}^{'}$	Derivative of $\boldsymbol{\beta}_{\mathrm{M}}$ with respect to the azimuth position
$\boldsymbol{\beta}_{\mathrm{M}}^{''}$	Derivative of $\boldsymbol{\beta}_{\mathrm{M}}^{'}$ with respect to the azimuth position
δ	Main rotor profile drag coefficient or pressure ratio
ϵ'	Oswald efficiency factor
η	Anhedral angle of the wing (rad)
γ	Lock number $\rho a_0 c R^4/I_\beta$
γ_{sh}	Rotor shaft tilt, positive forward (rad)
$\lambda_0, \lambda_{1s}, \lambda_{1c}$	Normalised uniform and first harmonic rotor inflow terms
λ_l	Non-dimensional lower rotor inflow
λ_{sp}	Eigenvalue of the short period mode
λ_u	Non-dimensional upper rotor inflow
μ	Advance ratio $V/\Omega R$
μ_z	Non-dimensional normal velocity of the rotor hub
$\boldsymbol{\omega}$	Angular velocity (rad/s)
Ω	Main rotor or propeller rotational speed (rad/s)
ω_{dr}	Frequency of the Dutch-roll mode (rad/s)
$\boldsymbol{\omega}^{\mathrm{p.d}}$	Angular velocity vector in propeller disc axes (rad/s)
$\omega_{\mathrm{x}}^{\mathrm{p.d.}}$, $\omega_{\mathrm{y}}^{\mathrm{p.d.}}$, $\omega_{\mathrm{z}}^{\mathrm{p.d.}}$	Angular velocity components of $\boldsymbol{\omega}^{\mathrm{p.d}}$ (rad/s)
Φ, Θ, Ψ	Euler angles (rad)
ϕ	Inflow angle (rad)
ψ	Azimuth angle (rad)
ρ	Air density (kg/m^3)
σ	Main rotor solidity
τ	Tilt of the propeller disc axes relative to the body axes (rad)
θ	Temperature ratio
θ_0	Main rotor collective angle (rad)
$\bar{\theta}_0$	Mean coaxial rotor collective (rad)
θ_{1c}	Main rotor lateral cyclic angle (rad)

$\theta_{1c_{diff}}$	Coaxial rotor differential lateral cyclic control (rad)
θ_{1s}	Main rotor longitudinal cyclic angle (rad)
θ_{fix}	Wing pitch incidence relative to the y_b axis
θ_{diff}	Coaxial rotor differential control or propeller differential control (rad)
θ_l, θ_u	Rotor collective angles of the lower and upper rotors (rad)
θ_{pitch}	Main rotor pitch angle of a rotor blade element (rad)
θ_{port}	Propeller pitch of the port propeller (rad)
θ_{prop}	Propeller pitch angle (rad)
θ_{star}	Propeller pitch of the starboard propeller (rad)
θ_{twist}	Twist gradient(rad)

Acronyms

ABC	Advancing Blade Concept
ADS	Aeronautical Design Standard
AFCS	Automatic Flight Control System
CCH	Coaxial Compound Helicopter
DVE	Degraded Visual Environment
FVL	Future Vertical Lift
GVE	Good Visual Environment
HCH	Hybrid Compound Helicopter
HGS	Helicopter Generic Simulation
HQR	Handling Qualities Rating
IMC	Instrument Meteorological Conditions
MAM	Manoeuvrability Assessment Method
MSL	Mean Sea Level
MTE	Mission-task-element
NoE	Nap-of-the-earth
OFE	Operational Flight Envelope
RHILP	Rotorcraft Handling Interactions and Load Prediction
SAR	Specific Air Range
SCAS	Stability and Control Augmentation System
SE	Specific Endurance
SFC	Specific Fuel Consumption

UCE	Usable Cue Environment
VTM	Vorticity Transport Model

Superscripts

anh	Wing anhedral axes
blade	Main rotor blade axes
body	Body axes
body $\rightarrow$ anh	Body to the wing's anhedral axes
body $\rightarrow$ disc	Body to the main rotor's disc axes
body $\rightarrow$ p.d.	Body to the propeller's disc axes
disc	Main rotor disc axes
disc $\rightarrow$ shaft	Main rotor's disc to shaft axes
hub	Main rotor hub axes
p.bl.	Propeller blade axes
p.d.	Propeller disc axes
p.d. $\rightarrow$ p.bl.	Propeller's disc to blade axes
shaft	Main rotor shaft axes
shaft $\rightarrow$ disc	Main rotor's shaft to blade axes
wind	Main rotor wind axes

Subscripts

1c	First harmonic cosine component
1s	First harmonic sine component
aero	Aerodynamic force
b	Body axes
c.g.	Centre of gravity
cut	Cut out
e	Earth axes or trimmed state
el	Main rotor blade element
hub	Main rotor hub
in	Inertial force
p	Quarter chord point of a propeller blade element
p.h.	Propeller hub
port	Port propeller

prop	Propeller
Q	Main rotor torque
star	Starboard propeller
trot	Tail-rotor
w	Quarter chord point of a wing strip
X,Y,Z	Forces in the x, y and z directions

Contents

List of Figures

List of Tables

Acknowledgements

I would like to express my sincere thanks and gratitude to Dr Douglas Thomson for his supervision and support throughout this period of research. I firmly believe that the technical advice and support I received was of the finest standard.

I am grateful to the Scottish Funding Council for providing me with this GRPE Scholarship to conduct the research presented within.

I also want to this opportunity to thank my colleagues for their help throughout this period of research. In particular, I would like to thank Dr Murray Ireland, Dr Kevin Rafferty, Mr John Walker, Mr Aldo Vargas, Mr. Craig Murray, Mr Jonathan McColgan and Mr Shaun Skinner for their technical support. Additional thanks are due to Mr John Walker and Dr Murray Ireland who proof read this manuscript.

Finally, I would like to take this opportunity to thank my family and friends. They are a plethora of people who I should be thanking. Due to amount of people I am reluctant to name each person individually, as I will inevitably forget to mention someone! However, I would like to single one person out for special recognition - namely my mother Maria Berry. I am incapable of truly articulating my thanks to her. I hope this Thesis, in some small way, repays her for the encouragement and support she has given me over the years.

Author's Declaration

I, Kevin Michael Ferguson, declare that this thesis titled, 'Towards a Better Understanding of the Flight Mechanics of Compound Helicopter Configurations' and the work presented in it are my own. I confirm that:

- This work was done wholly or mainly while in candidature for a research degree at this University.
- Where any part of this thesis has previously been submitted for a degree or any other qualification at this University or any other institution, this has been clearly stated.
- Where I have consulted the published work of others, this is always clearly attributed.
- Where I have quoted from the work of others, the source is always given. With the exception of such quotations, this thesis is entirely my own work.
- I have acknowledged all main sources of help.
- Where the thesis is based on work done by myself jointly with others, I have made clear exactly what was done by others and what I have contributed myself.

Signed:

Date:

Kevin Ferguson
Glasgow, Scotland

"With a good conscience our only sure reward, with history the final judge of our deeds, let us go forth to lead the land we love, asking His blessing and His help, but knowing that here on earth God's work must truly be our own."

President John F. Kennedy (1961)

Publication List

Journal Articles

Ferguson, K., and Thomson, D., "Flight dynamics investigation of compound helicopter configurations," *Journal of Aircraft*, 52(1), 2015, pp. 156-167.
(doi:10.2514/1.C032657)

Ferguson, K., and Thomson, D., "Performance comparison between a conventional helicopter and compound helicopter configurations," *Proceedings of the Institution of Mechanical Engineers, Part G: Journal of Aerospace Engineering*, 2015
(doi: 10.1177/0954410015577997)

Ferguson, K., and Thomson, D., "Maneuverability assessment of a compound helicopter configuration," *Journal of the American Helicopter Society*, 2015, (Accepted for Publication)

Conference Proceedings

Ferguson, K., and Thomson, D. (2014) Manoeuvrability assessment of a hybrid compound helicopter configuration. In: 40th European Rotorcraft Forum, Southampton, UK, 2-5 Sep 2014.

Ferguson, K., and Thomson, D. (2014) A performance analysis of compound helicopter configurations. In: AHS 70th Annual Forum, Montreal, Canada, 20-22 May 2014.

Ferguson, K., and Thomson, D. (2013) A flight dynamics investigation of compound helicopter configurations. In: AHS 69th Annual Forum and Technology Display, Phoenix, AZ, USA, 21-23 May 2013, pp. 1-15.

Chapter 1

Introduction

1.1 The Compound Helicopter

The main rotor of a conventional helicopter is responsible for providing the lifting and propulsive forces of the vehicle. The maximum speed of a conventional helicopter is limited by the main rotor's aerodynamic characteristics, installed engine power and airframe drag [1–3]. The problems associated with installed engine power and airframe drag can be minimised through careful design, but the main factor limiting the maximum speed of the helicopter is retreating blade stall [2]. The lifting capability of the retreating side of the disc deteriorates with forward speed as the local dynamic pressure is lower than that of the advancing side [4]. Therefore, to satisfy the condition of zero hub roll moment, which is required in steady level flight, the local blade incidence of the retreating side of the disc must be greater than the advancing side. High blade incidence on the retreating side, coupled with the low local dynamic pressure results in blade stalling. This restricts the maximum speed of the conventional helicopter to approximately 150kt [5], which is a modest flight speed when compared to a fixed wing aircraft [1].

There are a number of civil and military applications where vertical take-off and landing capability combined with high speed cruise speed would be advantageous. For example, rapid insertion of troops or ship replenishment missions. Compounding has often been proposed as a solution to increase the maximum speed of the helicopter. There are two common types of compounding known as lift and thrust compounding. The concept of lift compounding is that a wing offloads the main rotor at high speeds thereby delaying the onset of retreating blade stall. Whereas thrust compounding, which is supplied by a propulsive device such as a propeller, provides additional axial thrust in high speed therefore divorcing the main rotor of its propulsive duties. In order to appreciably expand the flight envelope of a winged helicopter, the wing must be supplemented with an additional source of axial thrust [2, 6–9]. The reason for this is that a wing-only compound helicopter tends to have a more pitch-down attitude relative to a conventional helicopter [6]. In forward flight, the wing offloads the main rotor thereby reducing rotor loading. The rotor thrust vector is still required to overcome the fuselage drag as well as the additional drag of the wing; hence to trim the helicopter, the smaller rotor thrust vector must be tilted more forward to provide the propulsive force. As a consequence, the pitch of the helicopter tends to be more nose down than that of the conventional configuration, which reduces the angle of attack of the wing, and therefore its lifting capability. The solution to this issue is to introduce thrust compounding to offload the main rotor of its propulsive duties in high speed flight so that the pitch attitude can be controlled to fully exploit the lifting capability of the wing.

The compound helicopter is again being explored as it can potentially satisfy the emerging requirements for the next generation of rotorcraft. The compound helicopter is a high speed design concept which aims to expand the flight envelope of the helicopter, therefore making it suitable for various roles such as ship replenishment and scouting missions. Although this is not a new concept, the development of a compound helicopter has proven elusive due to a combination of technical problems and economical issues [10]. Recently, various compound helicopter demonstrators have been built, all of which are capable of reaching speeds that significantly surpass its conventional counterpart. It is clear that the design of the compound helicopter is being taken seriously by the leading helicopter manufacturers in their pursuit to deliver a helicopter which can fulfil the new requirements for greater speed and range.

History of High Speed Helicopters

It has long been recognised that a rotorcraft that can obtain high speeds whilst maintaining efficient hover capability would be an effective aircraft, able to complete various missions and roles. As a result, there have been various high speed design concepts which have attempted to realise this goal. These designs include: the tilt-rotor, the X-wing concept and variable diameter rotor concepts [1]. With the exception of the tilt-rotor aircraft, none of these designs have been utilised in a production vehicle. Nevertheless, it is clear that the rotorcraft community has realised the potential benefits of a high speed helicopter. This interest continues today with the resurgence of the compound helicopter.

The compounding of a helicopter is not a new idea with most of the major helicopter manufacturers testing compound helicopter designs at one time. The testing of the compound helicopter was particularly popular in the decade of the 1960s, with Figure 1.1 presenting some of the aircraft that were flight tested. With reference to Figure 1.1, it is clear that a wide variety of helicopters which feature compounding aircraft have been flown. These vehicles include: the UH-2 [11], the XH-51A [12], the S-67 [13], the NH-3A [14], the 16H-1A [15], the Lockheed Cheyenne [16], the RSRA research aircraft [17] and the XH-59A aircraft [18]. Although these programmes never led to an operational vehicle, they did provide some insight into the problems that designers may face with the development of a compound helicopter. One issue is the inherent control redundancy that results from compounding the conventional configuration. The compounding results in an additional control(s) relative to a conventional helicopter and therefore there is an issue on how to integrate this control into the vehicle. The Rotor Systems Research Aircraft (RSRA), Figure 1.1(g), conducted a series of flight tests which featured a fixed setting of collective pitch [17]. This set-up offers a reduction in terms of pilot workload but does not fully exploit the additional control offered by compounding. A successful compound helicopter would require a control system that exploits the additional control to enhance the performance benefits that compounding offers without significantly increasing pilot workload. Another issue that arose from the flight test programme of the XH-51A helicopter [19], Figure 1.1(b), was the tendency of the rotor to overspeed. During high speed manoeuvres the load factor of the main rotor increased quicker than that of the wing thus resulting in rotor overspeed. The automatic flight control system (AFCS) would have to reduce the collective pitch setting of the main rotor in high speed manoeuvres, thereby avoiding rotor overspeed. The Lockheed Cheyenne, Figure 1.1(f), another notable compound helicopter, encountered problems with its gyro design which led to a fatal crash [16]. The combination of this crash, as well as other problems with the design and political issues ended the Cheyenne programme despite promising flight test results. It is clear that the compounding of a helicopter presents some problems, all of which will have to be overcome, or at least ameliorated, but the advantages in terms of increasing the maximum speed of the helicopter are clear.

As well as flight test programmes, there have been collaborative studies which have explored the potential of the compound helicopter. The United Kingdom's Ministry

(a) UH-2 Compound Helicopter

(b) XH-51A Compound Helicopter

(c) S-67 Compound Helicopter

(d) NH-3A Compound Helicopter

(e) 16H-1A Compound Helicopter

(f) Lockheed Cheyenne

(g) RSRA Helicopter

(h) Sikorsky XH-59A

Figure 1.1: Pictures of various Compound Helicopter Configurations. (Figures has been removed due to Copyright restrictions.)

of Defence sponsored a programme to investigate the application of an advanced compound helicopter and the powerplant required for this purpose [20]. Balmford and Benger concluded that a compound helicopter would have numerous benefits such as quicker reaction due to its high speed capability and enhanced survivability due to the increased agility of the aircraft configuration. Furthermore, the proposed configuration would be capable of accelerating and decelerating at near level fuselage attitude which would enhance passenger comfort. All of these performance benefits as well as believing the compound helicopter was a low-risk evolution of the conventional helicopter prompted further work studying the powerplant that would be required for this Lynx Compound demonstrator [21].

Although the design of the compound helicopter has considerable merit, an alternative approach to achieve high speed flight is the tilt-rotor concept. The concept of the tilt-rotor is that two rotors are oriented in the same way as a conventional helicopter to provide the lifting force in the hover. As the vehicle moves into forward flight, the two rotors are progressively tilted forward so that the thrust from the two rotors provide a propulsive force. Eventually the aircraft reaches its "aeroplane" mode where it resembles a fixed wing aircraft with the two rotors effectively becoming two prop-rotors with the wing providing the lifting force. The testing of the NASA-US Army Bell XV-15 aircraft, which began in the 1970s, proved the viability of this design concept [22]. An extensive period of research followed to develop the tilt-rotor technology which culminated in the production of the Bell-Boeing V-22 Osprey. Although this aircraft is currently in production there were numerous difficulties encountered in the development of this aircraft. The predecessor of the XV-15, the XV-3, encountered significant aeroelastic issues [23]. Another problem was the design of the control system due to the mixing of the controls as the aircraft transitions from low speed flight to high speed flight. In addition, the design of the prop-rotors requires a compromise as the design of a rotor which offers good hover performance conflicts with the design of a propeller to provide high propulsive efficiency. For example, the tilt-rotor features a small rotor diameter which significantly increases the rotor disc loading when compared to a helicopter operating at a similar weight [1]. Moreover, in the hover and low speed flight the rotor wakes impinge over the aircraft wing providing an aerodynamic download. This wing download can be attenuated by the use of flaps which effectively reduce the wetted area of the wing in hover and low speed flight [24]. All of these challenges have been overcome and the tilt-rotor can fulfil roles that a conventional helicopter cannot. However, in effect the tilt-rotor design does forfeit the aerodynamic efficiency of a fixed wing aircraft to retain vertical lift capability. The compound helicopter is an alternative to tilt-rotor although it is appreciated that a compound helicopter would not be able to reach the high speeds of the tilt-rotor. However, the compound helicopter is perceived to be a low cost high speed design, that expands the helicopter's flight envelope, without the complexity and reliability issues of the tilt-rotor design.

The Design of the Compound Helicopter

It is evident that the addition of compounding to a helicopter design allows the aircraft to obtain greater flight speeds. However, the introduction of compounding to the vehicle presents some design issues, such as the location of the propulsive and lifting devices. The approach of Lockheed, with the Cheyenne as shown in Figure 1.1(f), was to mount a pusher propeller at the rear of the aircraft in close proximity to the tail-rotor. Lift compounding was provided by a stub wing. Conversely, the modern Eurocopter X^3 uses two propellers which are mounted either side of the fuselage, Figure 1.2. This design also features a wing to provide additional lift at high speeds. An interesting approach to increasing the maximum speed of the helicopter is the 1950's Gyrodyne concept that was recently revisited by Houston [25]. The Gyrodyne concept employs a propulsor mounted onto a side of the fuselage to replace the tail rotor and therefore fulfil the dual role of providing axial thrust and the anti-torque moment. Houston used the Puma SA330 helicopter in his study and showed that this Gyrodyne set-up could increase the maximum speed of the helicopter by 50 kt [25]. Clearly, there is no standard compound helicopter design and each design could feature very different layouts. The layout of the vehicle would depend on multiple factors such as targeted customer, the environment the aircraft is expected to operate within and aerodynamic interactions between the different components of the helicopter design.

Orchard and Newman provide some insight into the fundamental design of the compound helicopter [26]. Their study investigated the various design aspects of a compound helicopter such as the wing, rotor and propulsor design. The study suggests

Figure 1.2: The Eurocopter X^3 (Figure has been removed due to Copyright restrictions.)

that a medium size wing should be used to provide a compromise between the beneficial effect of offloading the rotor at high speeds and the adverse effect of creating aerodynamic download at low speeds [26]. Their study also highlights the importance of the wing design to the vehicle, suggesting that an aspect ratio of 6 would be appropriate so that the wing does not extend into a region where the the main rotor's tip vortex would adversely affect the wing's performance [26]. In terms of thrust compounding, Orchard and Newman propose that a ducted fan or a propeller(s) would be the most suitable, in the context of a compound helicopter design, due to their high propulsive efficiencies in the flight regimes where the compound helicopter is expected to operate [26].

More recently, Moodie and Yeo [27] conducted a design study of a compound helicopter similar in layout to the Lockheed Cheyenne. Their study focused on the design of a compound helicopter at its cruise condition of 240kt. The aircraft was sized to fulfil a mission consisting of carrying 11 troops, a payload of 4015lb, to a distance of 424 km from the departure point. Their results reinforce the potential of the compound helicopter and highlight the power benefit from slowing the main rotor at cruise [27]. Another potential benefit of the compound helicopter is its ability to carry significant payloads with various studies investigating compound helicopter designs which could carry more than 90 passengers [28, 29]. For example, Yeo and Johnson performed a parametric design study of a 100,000lb compound helicopter which was designed to be capable of transporting 120 passengers over a 1200nm radius. Their study focused on a compound helicopter configuration which featured a single main rotor, a wing and two propellers mounted on either side of the fuselage. One of the primary aims of the study was to investigate the effects of blade, disc and wing loading on aircraft performance [28]. The study also examined the influence of the rotor blade design, i.e. rotor blade twist, taper ratio of the blades and tip speed, on the cruise performance of the vehicle [28]. Again, the results indicate the possible benefits of the compound helicopter.

Renewed Interest in the Compound Helicopter

The resurgence of interest in the compound helicopter is partly due to the US Army's Future Vertical Lift (FVL) acquisition programme, which aims to replace their existing fleet of helicopters. The US Army are reviewing the potential of the compound helicopter as it may be capable of satisfying their requirements for the next generation of helicopter. The unique capabilities of the compound helicopter would allow the vehicle to fulfil various roles in both civil and military markets. One perceived role of the

Figure 1.3: Piasecki X-49A Speedhawk. (Figure has been removed due to Copyright restrictions)

compound helicopter is in emergency aid missions. The compound helicopter could replace the conventional helicopter in this role with the additional benefit of reducing transit time, due to its greater speed, which is critical in emergency aid situations. A study by Tannabe et.al. recognised the compound helicopter's ability to fulfil this mission requirement as well as additional roles such as disaster relief and maritime patrol [30]. Due to the potential benefits of the compound helicopter, various helicopter manufacturers have begun or completed testing of their prototype vehicles. For example, Piasecki have recently flight tested the X-49A Speedhawk, Figure 1.3, which is a variant of the original Piasecki 16H Pathfinder which flew in the 1960s [31]. This design features a wing and a vectored fan at the rear of the aircraft which fulfils the dual purpose of providing additional axial thrust as well as the anti-torque moment. In addition, both Sikorsky and Eurocopter have been testing their demonstrators, the Sikorsky X2 and the Eurocopter X^3.

Due to the need for rotorcraft to travel faster, Sikorsky have revisited the Advancing Blade Concept (ABC) with the Sikorsky X2 demonstrator aircraft, Figure 1.4. The Sikorsky X2 with its coaxial rotor, uses the ABC (Advancing Blade Concept) rotor system to offload the retreating sides of the discs at high speeds and therefore avoid blade stalling. In high speed flight the lifting duties are shifted towards the advancing sides of the rotor discs where the local dynamic pressure is high [18]. In this flight regime, the two rotors provide significant rolling moments around the rotor hub as the advancing sides of the disc produce much greater lift than the opposing retreating sides. However, overall hub rolling moment trim is achieved as the upper and lower rotors provide rolling moments equal in magnitude but in opposing directions. This was achieved on the XH-59A aircraft by two methods. Firstly, by variable phase angle

Figure 1.4: Sikorsky X2 (Figure has been removed due to Copyright restrictions.)

control which alters the azimuth position where the cyclic controls change the rotor blade pitch [18]. Secondly, by the introduction of a differential lateral cyclic control to promote greater loading across the advancing sides of the discs in high speed flight [18]. This concept was originally developed in the 1960s, named the XH-59A aircraft, but the aircraft never entered production [32]. Recently, the ABC rotor system has been revisited and the design improved upon with the use of advanced aerofoil sections and active vibration control [33, 34]. Due to these improvements as well as the pusher propeller providing an extra component of axial thrust, the Sikorsky X2 is able to reach speeds of 250kt [35].

In contrast, the wings of the Eurocopter (now Airbus Helicopters) X^3 offload the rotor at high speeds and the propellers provide the propulsive force to overcome the airframe drag. The two propellers, which are mounted on either side of the aircraft's fuselage, provide the yaw control of the vehicle so that a tail rotor is not required. In high speed flight, the anti-torque responsibilities are shifted to the fin at the rear of the aircraft which is capable of producing a significant sideforce due to the velocity of the local airflow. This aircraft design has been flight tested and recent publications have reported that the Eurocopter X^3 is able of reaching a maximum speed of 232kt. It is therefore clear that these helicopters are capable of greater speeds than their conventional counterparts. Whilst this is true, there are some other factors with the compound helicopter design that should be considered. For example, the introduction of compounding device(s) to the helicopter is likely to increase the total mass of the vehicle, hence reducing the amount of payload the aircraft can carry. In addition, this increase in mass would also degrade the hover performance of the vehicle. The additional complexity of the compound helicopter design could increase the operating costs of the vehicle due to the need for greater man-hours to maintain the aircraft. These issues will need to be addressed in the successful design of a compound helicopter.

1.2 Aims of Research and Structure of this Thesis

It is obvious that the compound helicopter is being taken seriously by the major helicopter manufacturers in their pursuit to deliver a rotorcraft with greater speed and range, whilst maintaining efficient hover capability. It is also clear that due to previous flight test programmes, and more modern research, there is some literature concerning the compound configuration. However, the majority of these programmes and studies are specific to a particular experimental aircraft project. In addition, most of the open literature focuses of the design and the performance of the compound helicopter. With the interest of the compound helicopter design increasing, there is a need to investigate and understand the flight mechanics of the configuration. To this end, the main aim of this Thesis is to undertake a comprehensive study of the effects of compounding and how this influences, in a broad sense, the flight mechanics of this class of vehicle. It is hoped that the conclusions and results from this work will improve the helicopter community's understanding of the flight mechanics of the compound helicopter. To achieve this aim, mathematical models of compound helicopter configurations are developed and their results are compared with a conventional helicopter configuration. This comparative element allows the changes of the flight mechanics characteristics, which arise exclusively from the introduction of compounding to the design, to be identified. The various flight mechanics attributes which are studied within this Thesis are the trim, performance, stability and manoeuvrability of these vehicles. The handling qualities issues of a compound helicopter are also discussed. The structure of the Thesis follows the research objectives. The following provides a detailed account of the main objectives of this Thesis.

(i) **Generic Compound Helicopter Mathematical Model**

The Helicopter Generic Simulation (HGS) package is a well established conventional helicopter package featuring main rotor, tail rotor, fuselage, tailplane and fin models to successfully simulate a conventional helicopter. Generally, compound helicopters feature wings and a form of thrust compounding commonly supplied by a propeller. Therefore, it is evident that in order to simulate a generic compound helicopter that wing and propeller models must be developed. Furthermore, the ABC coaxial rotor features heavily in the compound helicopter literature with its ability to relieve the main rotor of retreating blade stall until high flight speeds. The ABC rotor has been taken seriously with the flight tests of the Sikorsky X2 and therefore it is only logical that any treatment of compound helicopters would assess this type of helicopter. Hence, developing a model of a coaxial rotor system is required. Therefore, the first aim of this research work is to extend the existing HGS software package to permit the modelling of a compound helicopter.

(ii) **Development of Compound Helicopter Configurations**

As a generic mathematical model of the compound helicopter is used, the next aim is to develop data sets which represent compound helicopter configurations which are of interest to the rotorcraft community. The strategy used to develop compound configuration data-sets is to take an established mathematical model of a conventional helicopter, and to introduce compounding to the design by adding propeller(s) and/or wing(s). It is assumed that the introduction of validated propeller and wing models to a conventional helicopter model, of known validity, will produce results of sufficient fidelity that meaningful conclusions can be drawn. Recall that the main aim of the Thesis is to examine the effects of compounding, therefore all of the helicopter configurations feature the same vehicle shape, size and mass, so that the effects of compounding are isolated from other factors. As a consequence, the design differences between the aircraft configurations are exclusively due to the introduction of thrust and wing compounding to the designs.

To develop compound helicopter configurations requires a selection of the helicopter layout as well as a preliminary design process. Although this is not a formal design process, where the shape, weight and installed power are selected to fulfil a particular mission, it is necessary to perform some preliminary design study to size the compounding device (either propeller(s) or wing(s)) appropriately. Some design effort is required but it is important to highlight that the design issues with the compound helicopter are not the focus of the Thesis. Once the compound helicopters are developed, the next aim is to calculate the control angles required to trim the aircraft configuration at a given flight condition. As the compound helicopter configurations feature some level of control redundancy, the standard trim algorithm will have to be amended to accommodate this issue. Hence, the amended trim algorithm and trim results will be discussed in this Chapter.

(iii) **Performance**

Having developed compound helicopter configurations and trimmed the configurations the next logical step is to assess the performance of each configuration. In the context of this Thesis, helicopter performance is focused on the power required at a certain flight condition. Performance can be quantified by the calculation of standard parameters such as estimation of the power required, lift-to-drag ratios, hover ceilings, maximum speeds, range and endurance, which all define the capability of the helicopter. The aim of this performance work is to investigate the compounding of the conventional helicopter and how the addition of thrust and wing compounding influences the performance of this aircraft class. It is worth stressing that this work is not a design exercise, where the weights and power of each aircraft are sized to fulfil a required mission, but a study to determine the effects of compounding. Therefore, the performance results should be viewed in this context.

(iv) **Stability**

The next research aim of this study is to investigate the stability of these compound helicopter configurations and how their stability differs from that of the conventional helicopter. The stability of the conventional helicopter is well understood, and is discussed in various standard helicopter textbooks [7, 36–38], but to the author's knowledge how the addition of the wings and propellers alter that stability has never been reported. Therefore, the aim of this Chapter is to assess the stability of the compound helicopter configurations through a numerical linearisation algorithm and compare the results with the baseline helicopter. Subsequently, the influence of compounding to the stability of the vehicles can be determined. Chapter 5 begins with an overview of the linearisation algorithm before presenting the salient stability and control derivatives. The Chapter ends with a discussion of the predicted eigenvalues of the natural modes of motion of the compound helicopter configurations and compares these results with the conventional helicopter.

(v) **Manoeuvrability**

Another logical question that relates to compound helicopters is how their manoeuvrability differs from that of a conventional helicopter. The aim of the current work is to determine the maximum manoeuvring capability of the aircraft configurations, then to subsequently investigate if the compounding of the conventional helicopter offers an advantage in this regard. In this Chapter the integration method of inverse simulation is used to capture the maximum manoeuvrability of the three aircraft configurations flying standard helicopter manoeuvres.

(vi) **Handling Qualities**

One critical component of the compound helicopter configuration are its so-called handling qualities, as it directly influences mission effectiveness. The addition of compounding to the aircraft design introduces control redundancy and changes the response characteristics of the vehicle. It also expands the flight envelope of the aircraft exposing it to unfamiliar flight regimes. All three of these elements are important and will strongly influence the handling qualities of this aircraft class. In the context of simulation, this work takes a broad view of handling qualities and the issues that need to be addressed to quantify the handling qualities of a compound helicopter configuration. The main aim of this Chapter is to examine the existing conventional helicopter handling qualities specification and determine whether it is applicable to compound helicopters. In the areas where the current handling qualities standards are deemed to be insufficient, incomplete or inappropriate, then some suggestions are offered.

Research Questions

Fundamentally this Thesis aims to investigate the effects of compounding to the flight mechanics of this aircraft class. Conveniently, the objectives of this work may be stated in the form of research questions. The first research question is how does the additional of compounding influence the flight mechanics of this aircraft type? And in terms of handling qualities, are the existing helicopter handling qualities specifications applicable to a compound helicopter?. If not, what are the challenges to make the current specifications suitable for a high speed compound helicopter?. The work presented in this Thesis aims to answer these broad research questions.

Research Conclusions

The Thesis is completed with Chapter 8 discussing the conclusions of the work. The Chapter summarises the main findings of the Thesis and how the main research questions were answered.

1.3 Originality and Contribution

A significant body of work relating to the compound helicopter is available in the open literature. However, the majority of the literature describes experimental test programmes and focuses on the design of the compound helicopter. There seems to be a gap in the literature which reports the effects of compounding on the trim, stability, manoeuvrability and handling qualities of this aircraft class. The major contribution of this Thesis is to address this gap in the literature highlighting the novelty of this research. This gap has been partly filled by the results from this work which have been published in the literature. The following is a brief summary of the published work

Journal Articles

Ferguson, K., and Thomson, D., "Flight dynamics investigation of compound helicopter configurations," *Journal of Aircraft*, 52(1), 2015, pp. 156-167.
(doi:10.2514/1.C032657)

Ferguson, K., and Thomson, D., "Performance comparison between a conventional helicopter and compound helicopter configurations," *Proceedings of the Institution of Mechanical Engineers, Part G: Journal of Aerospace Engineering*, 2015
(doi: 10.1177/0954410015577997)

Ferguson, K., and Thomson, D., "Maneuverability assessment of a compound helicopter configuration," *Journal of the American Helicopter Society*, 2015 (Accepted for Publication)

Conference Proceedings

Ferguson, K., and Thomson, D. (2014) Manoeuvrability assessment of a hybrid compound helicopter configuration. In: 40th European Rotorcraft Forum, Southampton, UK, 2-5 Sep 2014.

Ferguson, K., and Thomson, D. (2014) A performance analysis of compound helicopter configurations. In: AHS 70th Annual Forum, Montreal, Canada, 20-22 May 2014.

Ferguson, K., and Thomson, D. (2013) A flight dynamics investigation of compound helicopter configurations. In: AHS 69th Annual Forum and Technology Display, Phoenix, AZ, USA, 21-23 May 2013, pp. 1-15.

In this publication list, the application of inverse simulation to a compound helicopter, which has not been reported in the literature, has been recently published by the author highlighting the novelty of this research. This is only one example as there are other elements of this Thesis which may be viewed as original. For example, the stability of the compound helicopter is also reported in this list. This publication list reinforces that the work presented within this Thesis is both timely and original. In addition, it is not only the results that can be viewed as novel but also the tools and techniques which are required to assess the compound helicopter. For example, the Thesis presents an inverse simulation algorithm that has been altered to accommodate the inherent control redundancy of the compound helicopter. Hence, both the results and the extension of the inverse simulation algorithm can be viewed as original pieces of work.

At the time of writing, there is a veritable interest in the compound helicopter by the major helicopter manufacturers as they attempt to develop a helicopter to satisfy the demands placed on the next generation of rotorcraft. To date, there is no single source which covers all of the flight dynamics aspects of the compound configuration. This alone is a major contribution to the industry. More importantly, the outcomes of this Thesis will highlight the salient flight mechanics issues of the compound helicopter. This would improve the industry's understanding of the compound helicopter and the results from this Thesis may be used in the design process. Consequently, the results from this work are important, timely and relevant. It is also possible that the tools developed in Thesis will be used by the industry to further investigate the merits of the compound helicopter. Overall this Thesis will significantly contribute to the rotorcraft community's understanding of the compound helicopter.

Chapter 2

Mathematical Modelling of Compound Helicopters

2.1 Introduction

The main aim of this Thesis is to undertake a comprehensive study of the effects of compounding and how it influences the flight mechanics of this aircraft class. The starting point is to develop mathematical models which represent compound helicopter configurations. The modelling approach is to take the HGS package which is an existing, and well established, helicopter simulation package and extend this to be capable of simulating a compound vehicle. To achieve this aim, it is necessary to develop mathematical models which represent a propeller and a wing. In addition, the Sikorsky advancing blade concept features significantly in the compound helicopter literature, therefore a coaxial rotor model is also required. To this end, the main objective of this Chapter is to describe the modelling approach. The Chapter begins by giving an overview of the modelling approach and then describes the development of the main rotor model. It is important to highlight that the modelling of the single main rotor is not a novel piece of work. However, the main rotor is a significant component to the helicopter and therefore it is worthwhile presenting the model to understand the model's distinguishing features. The Chapter then proceeds to discuss the enhancement of the HGS package, which includes the creation of a coaxial rotor, propeller and wing models. Each of these new models is validated with wind-tunnel experiments to ensure that the models are of sufficient fidelity to capture the fundamental behaviour of the appropriate device. The achievements of this Chapter are then listed in a summary at the end of this Chapter.

2.2 An Overview of the Modelling

In order to analyse the dynamic characteristics of any vehicle is it necessary to develop the equations of motion of the vehicle. For most engineering applications the rigid body Euler equations are used to calculate the vehicle's dynamic states relative to its centre of gravity position. The familiar Euler rigid body equations are:

$$\dot{U} = -(WQ - VR) + \frac{X}{M_a} - g\sin\Theta \tag{2.1a}$$
$$\dot{V} = -(UR - WP) + \frac{Y}{M_a} + g\cos\Theta\sin\Phi \tag{2.1b}$$
$$\dot{W} = -(WQ - VR) + \frac{Z}{M_a} - g\sin\Theta \tag{2.1c}$$
$$I_{xx}\dot{P} = (I_{yy} - I_{zz})QR + I_{xz}(\dot{R} + PQ) + L \tag{2.1d}$$
$$I_{yy}\dot{Q} = (I_{zz} - I_{zz})RP + I_{xz}(R^2 - P^2) + M \tag{2.1e}$$
$$I_{zz}\dot{R} = (I_{xx} - I_{yy})PQ + I_{xz}(\dot{P} - QR) + N \tag{2.1f}$$

Referring to Figure 2.1, the U, V, W terms are the translational velocities relative to the body axes set in the directions of the unit vectors $\mathbf{i}_\mathrm{b}, \mathbf{j}_\mathrm{b}, \mathbf{k}_\mathrm{b}$. The angular rates relative to the aircraft centre of gravity are P, Q, R were positive rotation is defined by the right hand screw rule. The mass of the helicopter is represented by M_a and is assumed to be constant. The terms I_{xx}, I_{yy}, I_{zz} are the moments of inertia of the helicopter around the x_b, y_b, z_b axes and I_{xz} is the product of inertia of the helicopter. It is assumed that these equations of motion, Equations (2.1), are for a vehicle with a plane of symmetry in the x_b-z_b plane. This is usually the case for most helicopter configurations, therefore I_{xy} and I_{yz} are assumed to be zero throughout this Thesis. However, it is recognised that if the vehicle did not have an inertial plane of symmetry then the terms I_{xy} and I_{yz} would need to be computed, leading to additional terms in Equations (2.1d) - (2.1f). The fuselage pitch and roll attitudes are given by Θ, Φ and the X, Y, Z terms are the external forces acting in the unit directions $\mathbf{i}_\mathrm{b}, \mathbf{j}_\mathrm{b}, \mathbf{k}_\mathrm{b}$, respectively. Similarly, the L, M, N terms are the external moments about the body axes. Figure 2.1 shows the states and external moments and how they are defined relative to the body axes set.

The kinematic expressions relating the Euler rates to the body states are

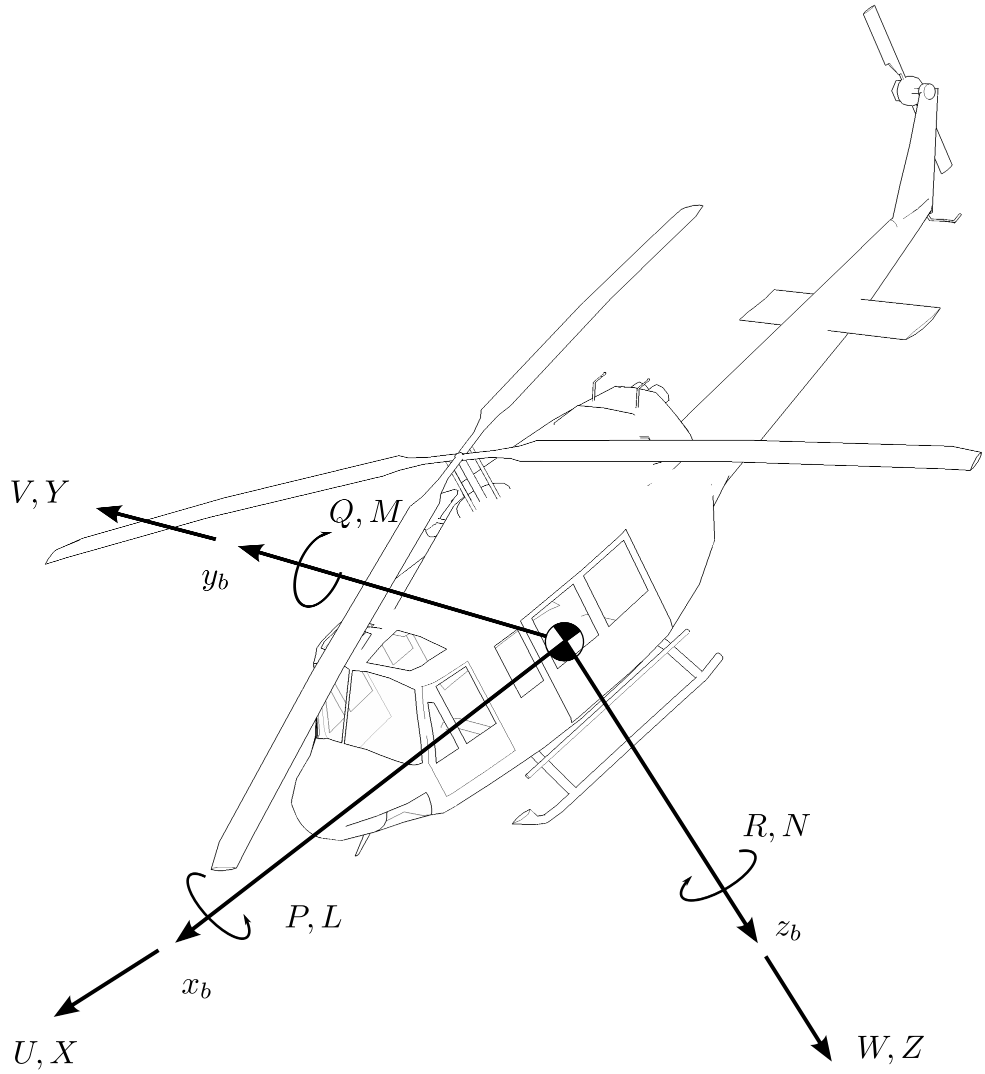

Figure 2.1: States Variables as Referred to the Body Axes Set

$$\dot{\Phi} = P + Q\sin\Phi\tan\Theta + R\cos\Phi\tan\Theta \tag{2.2a}$$

$$\dot{\Theta} = Q\cos\Theta - R\sin\Theta \tag{2.2b}$$

$$\dot{\Psi} = Q\sin\Phi\sec\Theta + R\cos\Phi\sec\Theta \tag{2.2c}$$

where Ψ is the heading angle of the helicopter. The fuselage angles are relative to an axes set which is inertially fixed at a point on the Earth, known as the Earth axes (x_e, y_e, z_e). The relationship between the body axes and the Earth axes set is seen in Figure 2.2. The helicopter velocities relative to the Earth can be found by using the fuselage attitudes as well as applying a transformation matrix

$$\begin{bmatrix} \dot{x}_e \\ \dot{y}_e \\ \dot{z}_e \end{bmatrix} = \begin{bmatrix} l_1 & m_1 & n_1 \\ l_2 & m_2 & n_2 \\ l_3 & m_3 & n_3 \end{bmatrix} \begin{bmatrix} U \\ V \\ W \end{bmatrix} \tag{2.3}$$

where,

$$\begin{aligned}
l_1 &= \cos\Theta\cos\Psi \\
l_2 &= \cos\Theta\sin\Psi \\
l_3 &= -\sin\Theta \\
m_1 &= \sin\Phi\sin\Theta\cos\Psi - \cos\Phi\sin\Psi \\
m_2 &= \sin\Phi\sin\Theta\sin\Psi + \cos\Phi\cos\Psi \\
m_3 &= \sin\Phi\cos\Theta \\
n_1 &= \cos\Phi\sin\Theta\cos\Psi + \cos\Phi\sin\Psi \\
n_2 &= \cos\Phi\sin\Theta\sin\Psi - \cos\Phi\cos\Psi \\
n_3 &= \cos\Phi\cos\Theta
\end{aligned}$$

These Equations, Equations (2.1) - (2.3), are given in generic form and can therefore simulate any vehicle assuming that the external forces and moments of the vehicle can be calculated. To successfully simulate a compound helicopter it is necessary to calculate the external forces and moments acting at and around the compound helicopter's centre of gravity. This is most conveniently achieved by considering the aircraft to be composed of a number of major components (rotor, fuselage, wing, etc.) and to sum together the contributions from each of these to obtain the total values of the forces and moments. For each component expressions are derived for the contribution to the total external forces and moments. By adding the various aircraft components together it is assumed that each system acts independently from one another. Therefore, aerodynamic interactions between components are not modelled. Aerodynamic interactions could be modelled by the use of semi-empirical models which are derived from extensive wind-tunnel testing. In the absence of the wind-tunnel results which represents the helicopter configurations presented in this Thesis, it is difficult to take into account aerodynamic interactions between different aircraft components. Due to the lack of experimental data, it is assumed that aerodynamic interactions are small and will not significantly influence the results. Considering a conventional helicopter, the forces and moments are composed as follows

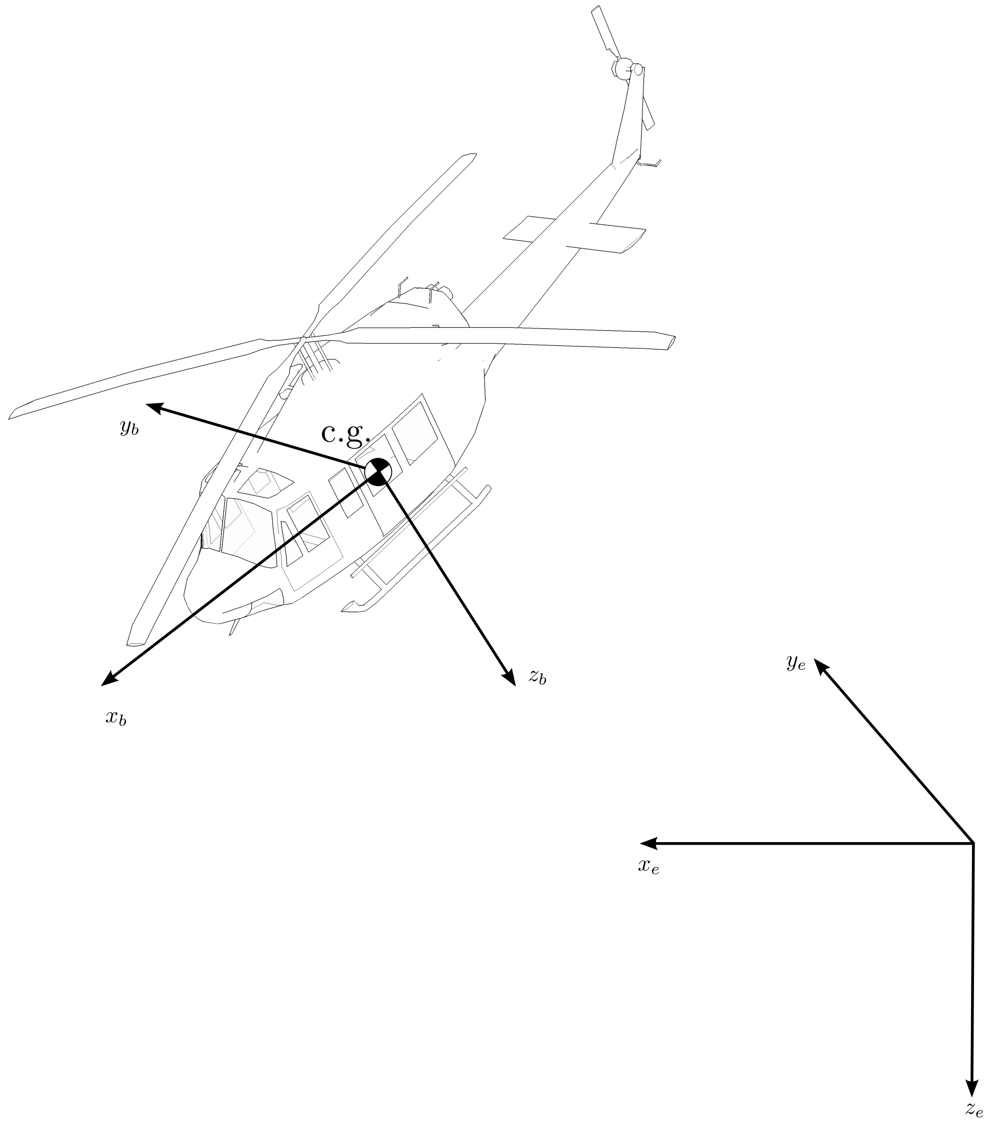

Figure 2.2: Earth and Body Frames of Reference

$$
\begin{aligned}
X &= X_{rot} + X_{t.r} + X_{fus} + X_{t.p} + X_{fin} \\
Y &= Y_{rot} + Y_{t.r} + Y_{fus} + Y_{t.p} + Y_{fin} \\
Z &= Z_{rot} + Z_{t.r} + Z_{fus} + Z_{t.p} + Z_{fin} \\
L &= L_{rot} + L_{t.r} + L_{fus} + L_{t.p} + L_{fin} \\
M &= M_{rot} + M_{t.r} + M_{fus} + M_{t.p} + M_{fin} \\
N &= N_{rot} + N_{t.r} + N_{fus} + N_{t.p} + N_{fin}
\end{aligned}
$$

However, with a compound helicopter the above Equations will have additional terms representing the forces and moments produced by the appropriate source of compounding. So for example, for a configuration with contra-rotating main rotor and a propeller providing thrust compounding, the external forces and moments would be

$$
\begin{aligned}
X &= X_{rot}^{upper} + X_{rot}^{lower} + X_{fus} + X_{t.p} + X_{fin} + X_{prop} \\
Y &= Y_{rot}^{upper} + Y_{rot}^{lower} + Y_{fus} + Y_{t.p} + Y_{fin} + Y_{prop} \\
Z &= Z_{rot}^{upper} + Z_{rot}^{lower} + Z_{fus} + Z_{t.p} + Z_{fin} + Z_{prop} \\
L &= L_{rot}^{upper} + L_{rot}^{lower} + L_{fus} + L_{t.p} + L_{fin} + L_{prop} \\
M &= M_{rot}^{upper} + M_{rot}^{lower} + M_{fus} + M_{t.p} + M_{fin} + M_{prop} \\
N &= N_{rot}^{upper} + N_{rot}^{lower} + N_{fus} + N_{t.p} + N_{fin} + N_{prop}
\end{aligned}
$$

Individual calculations are made for the upper and lower rotors, the tail-rotor is not present in this vehicle, and a component for the thrust of the propeller is added. The methods used to model each of the helicopter's components are important as they define the level of fidelity of the simulation. Consequently, the approaches to calculate each component's contribution to the overall external forces and moments are presented in the following sections.

2.3 The Helicopter Generic Simulation (HGS) Package

The compound helicopter models are developed using the Helicopter Generic Simulation (HGS) package [36, 39]. The HGS package is a conventional disc-type rotorcraft model, as described by Padfield [36], and has found extensive use in studies of helicopter flight dynamics. The HGS software has been validated by configuring the package to represent the AgustaWestland Lynx and subsequently comparing simulation results to flight test trials. The validation data was supplied by the Defence Research Agency [40] and the simulation results compared favourably with the flight tests [41, 42]. The HGS package is generic in structure, with only the helicopter's parameters required to model the vehicle. Therefore, the HGS package can be easily edited to represent different conventional helicopters. For example, the HGS software package has been used to represent the AgustaWestland Lynx and the Puma helicopter [41]. The HGS package is developed on the MATLAB® environment, which is a technical language used for many engineering applications. Perhaps the most distinguishing feature of the package is the main rotor model. The main rotor model ignores the lagging degree of freedom therefore assuming that the flapping dynamics have the most influence in terms of the helicopter's flight dynamic characteristics. The flapping dynamics are assumed to be quasi-steady, a common assumption in main rotor modelling, therefore permitting a multi-blade representation of the main rotor. The main rotor is assumed to be centrally hinged with stiffness in flap with the main rotor chord assumed to be constant. One important assumption, within the rotor model, is that the aerodynamics are linear, so that lift is a linear function of the local blade angle of attack whereas the drag is modelled by a simple polynomial. Due to this assumption, non-linear aerodynamics such as retreating blade stall and compressibility are not modelled. Regarding the modelling of the other subsystems of the rotorcraft, the forces and moments of the tailplane, fuselage and fin calculated using a series of look-up tables derived from experimental data. The subsequent section describes fully the rotor model used in the HGS software package.

2.4 Rotor Model

In helicopter simulation, the main rotor consumes the most modelling effort. The main rotor is the most significant component of the helicopter and it needs to be modelled accurately so that meaningful results can be obtained. It is also the most complex component of the helicopter due to rotor blades flapping and lagging motions which occur as the rotor blades travel around the rotor's shaft. This particular section gives an overview of the rotor model within the HGS Package which was developed by Thomson [39]. Most rotor models begin with calculating the velocities and accelerations at each blade element to derive the forces and moments around the main rotor's hub. The aerodynamic, inertial and flapping forces all combine to produce the total force produced by a rotor blade, which can be calculated by integrating the blade sectional forces. Generally, the loads can be determined through either numerical or analytical integration of the elemental forces, with the HGS rotor model integrating the loads analytically. Note that typically the HGS rotor model is referred to as a "disc" model. As the elemental velocities and accelerations vary with both radial and azimuth position then the forces and moments are inherently periodic. However, the HGS rotor model does not model the periodicity of the rotor blades: instead it applies the quasi-steady assumption that only the steady components of the periodic forces influence the vehicle's rigid body dynamics. In order to faithfully model the periodicity of the rotor blades would require an "individual blade" model, examples of which are given by Rutherford, Houston and Mansur [43–45], which consequently results in unsteady forcing of the main rotor, even in trimmed flight. The individual blade model does offer higher levels of fidelity and allows for the inclusion of complex rotor blade shapes.

However, integrating the inertial and aerodynamic loads numerically does increase run times and increase complexity. In contrast, a disc model is able to run quickly regardless of the processing power of the computer.

In the development of the rotor model, various assumptions are required to integrate the loads analytically and therefore derive closed loop expressions that determine the rotor forces and moments. In terms of the aerodynamics, the main assumptions are the following:

- The airflow is assumed steady and incompressible, therefore compressibility effects are ignored.
- The reverse flow region of the rotor disc is assumed to be small.
- The aerodynamics of each rotor blade element are assumed to be linear. Therefore, the lift coefficient is assumed to be of the form $C_l = a_0\alpha + a_1$ and the drag coefficient takes the form of $C_d = \delta_0 + \delta_1 C_T^2$.
- Blade stalling is not modelled.
- The induced velocity is comprised of a uniform component over the rotor disc with first harmonic variations, see Appendix A.
- Aeroelastic effects are not modelled.
- The local aerodynamic forces act at the quarter chord of the rotor blade, therefore it is assumed that the pitching moment of the blade is small and therefore ignored.

Furthermore, the geometric properties of each rotor blade, the subsequent assumptions are made:

- The rotor blades are centrally hinged and assumed to be rigid.
- The rotor blades feature constant chord and aerofoil profile.
- The lagging dynamics of the blade are not modelled.
- The twist across the blades is of linear form, given by $\theta_{twist}(\bar{r}/R)$.
- The root cut out region of the rotor blade is given by the distance eR from the centre of rotation.

Kinematics of a Rotor Blade Element

Velocity of a Rotor Blade Element

The starting point to calculate the rotor forces and moments begins with deriving expressions of the rotor blade's velocity and acceleration at a given point along the rotor blade. Due to the complex motion of the blade, various axes systems are required, namely the body, hub, shaft and blade axes sets, which all require transformation matrices to relate expressions from one axes set to another. Figure 2.3 shows the relationship between the body, hub and shaft axes. Beginning with the body axes set, the velocity of the rotor hub relative to the body axes is given by the expression

$$\mathbf{v}_{\text{hub}}^{\text{body}} = \mathbf{v}_{\text{c.g.}}^{\text{body}} + \boldsymbol{\omega}^{\text{body}} \times \mathbf{r}_{\text{c.g.}\to\text{hub}}^{\text{body}} \tag{2.4}$$

The body axes are rotated about $\mathbf{j}_{\text{b}}$ by the shaft angle, γ_{sh}, to form the disc axes set. Forward inclination of the disc axes is denoted by a positive angle with the following transformation matrix relating the body and disc axes sets

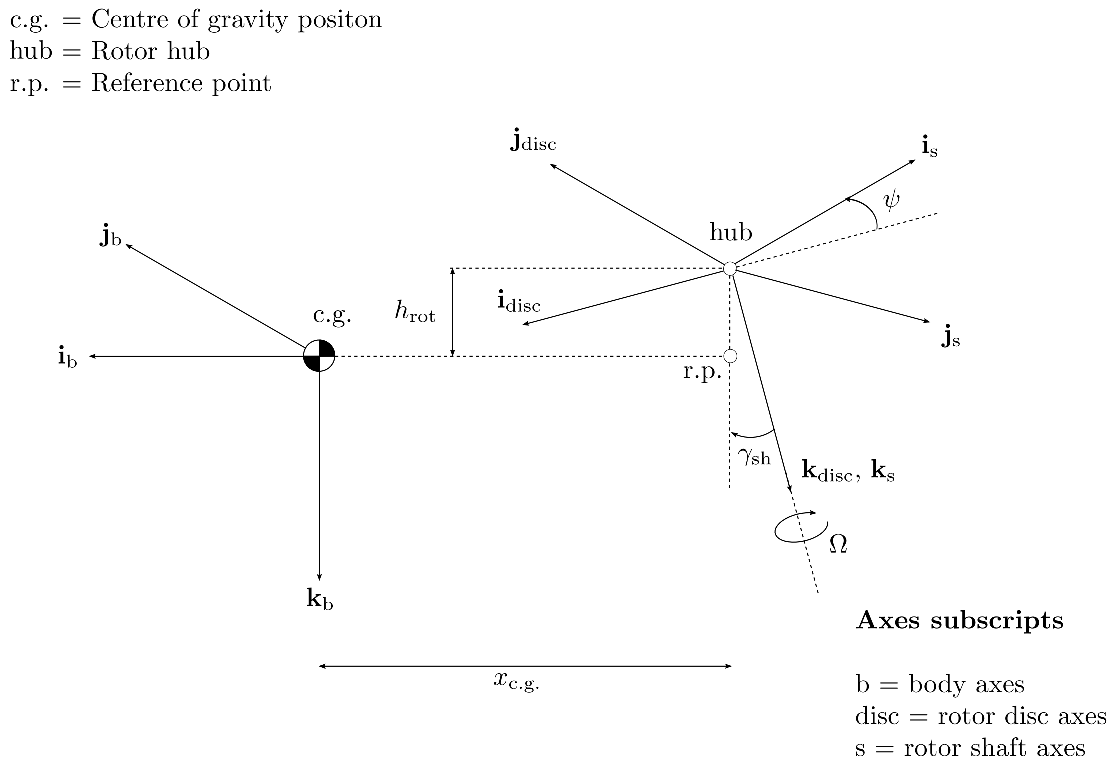

Figure 2.3: Relationship between the body, rotor disc and shaft axes

$$\mathbf{T}^{\text{body}\to\text{disc}} = \begin{bmatrix} \cos\gamma_{\text{sh}} & 0 & \sin\gamma_{\text{sh}} \\ 0 & 1 & 0 \\ -\sin\gamma_{\text{sh}} & 0 & \cos\gamma_{\text{sh}} \end{bmatrix} \tag{2.5}$$

The velocity of the rotor hub in the rotor disc axes can be determined with the product of the transformation matrix, given by Equation (2.5), and the rotor hub velocity in body axes

$$\mathbf{v}_{\text{hub}}^{\text{disc}} = \mathbf{T}^{\text{body}\to\text{disc}}\ \mathbf{v}_{\text{hub}}^{\text{body}} \tag{2.6}$$

Similarly, the rotational velocity of the disc axes set is the product of the transformation matrix, from body to disc axes, and the rotational velocity of the body axes set

$$\boldsymbol{\omega}^{\text{disc}} = \mathbf{T}^{\text{body}\to\text{disc}}\ \boldsymbol{\omega}^{\text{body}} \tag{2.7}$$

Following on from the disc axes set, another axes set is introduced which rotates with the rotor shaft and is known as the rotating shaft axes set. This axes set is seen in Figure 2.3. The transformation between the hub and shaft axes is related by the azimuth position of the rotor blades, which is given by

$$\mathbf{T}^{\text{disc}\to\text{shaft}} = \begin{bmatrix} -\cos\psi & \sin\psi & 0 \\ -\sin\psi & -\cos\psi & 0 \\ 0 & 0 & 1 \end{bmatrix} \tag{2.8}$$

Therefore, the velocity of the rotor hub in shaft axes is the following

$$\mathbf{v}_{\text{hub}}^{\text{shaft}} = \mathbf{T}^{\text{disc}\to\text{shaft}}\ \mathbf{v}_{\text{hub}}^{\text{disc}} \tag{2.9}$$

Meanwhile, the rotational velocity of the shaft axes set is determined by the addition of the rotational speed of the main rotor to the product of transformation matrix, Equation (2.8), and the rotational velocity of the disc axes set. This leads to the expression

$$\boldsymbol{\omega}^{\text{shaft}} = \mathbf{T}^{\text{disc}\to\text{shaft}}\ \boldsymbol{\omega}^{\text{disc}} + \begin{bmatrix} 0 \\ 0 \\ \Omega \end{bmatrix} \tag{2.10}$$

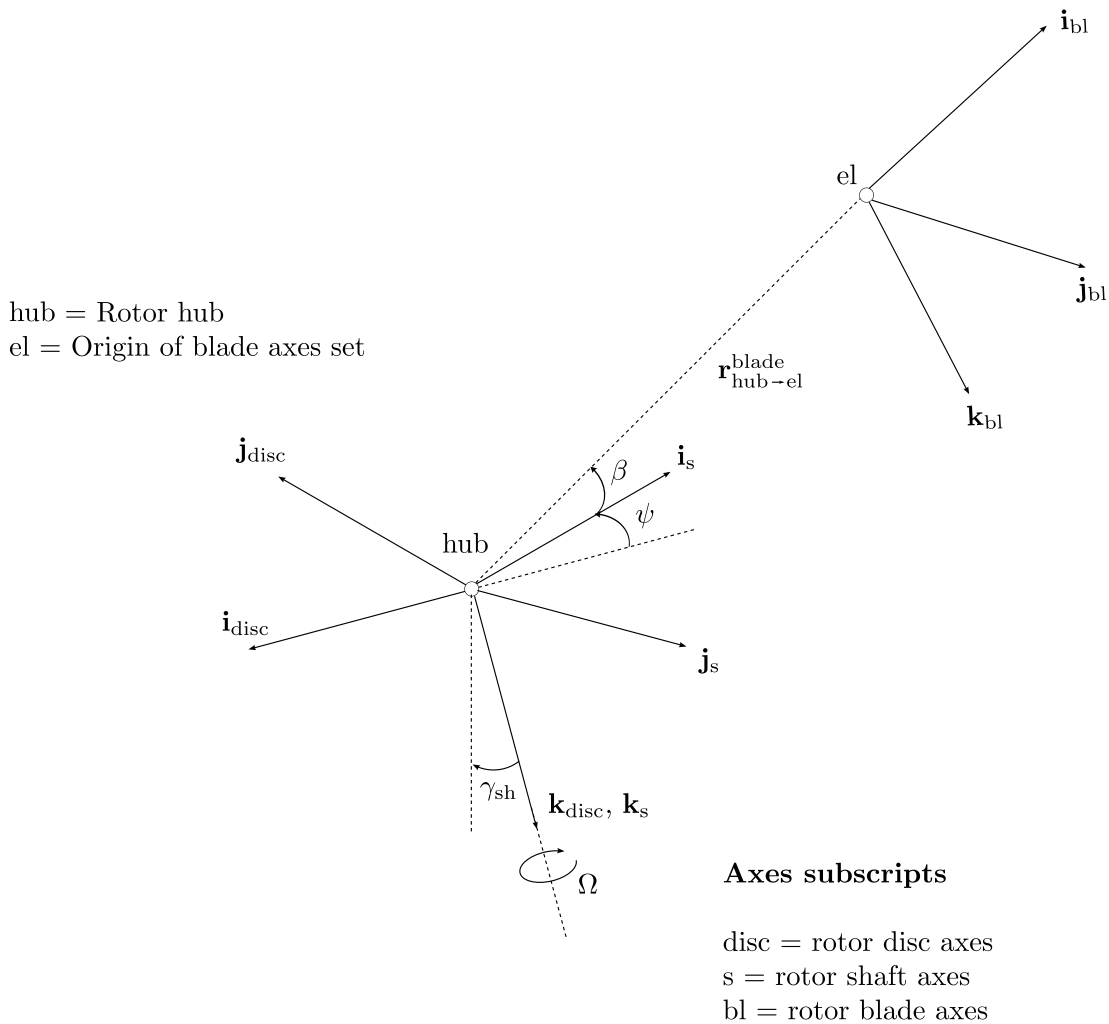

Figure 2.4: Relationship between the rotor shaft and blade axes

The translational and rotational velocities have been derived in the shaft axes set. The next step is to determine these kinematic expressions in the blade axes set, allowing for the calculation of the main rotor's aerodynamic and inertial forces. As seen in Figure 2.4, the shaft axes set is rotated by the flapping angle of the rotor blade to obtain the blade axes set. The blade axes set has its origin at the aerodynamic centre of the rotor blade element and the corresponding transformation matrix, assuming that the flapping angle is small, between shaft and blade axes is

$$\mathbf{T}^{\mathrm{shaft}\to\mathrm{blade}} = \begin{bmatrix} \cos\beta & 0 & -\sin\beta \\ 0 & 1 & 0 \\ \sin\beta & 0 & \cos\beta \end{bmatrix} \approx \begin{bmatrix} 1 & 0 & -\beta \\ 0 & 1 & 0 \\ \beta & 0 & 1 \end{bmatrix} \tag{2.11}$$

Therefore, the translational velocity of the rotor hub in the blade axes set is

$$\mathbf{v}_{\text{hub}}^{\text{blade}} = \mathbf{T}^{\text{shaft}\to\text{blade}}\ \mathbf{v}_{\text{hub}}^{\text{shaft}} \tag{2.12}$$

Moreover, the rotational velocity of the rotor hub in blade axes is

$$\boldsymbol{\omega}^{\text{blade}} = \mathbf{T}^{\text{shaft}\to\text{blade}}\ \boldsymbol{\omega}^{\text{shaft}} \tag{2.13}$$

With the translational and rotational velocities of the rotor hub in blades axes defined, Equations (2.12) and (2.13), the velocity of a given rotor blade element in blade axes can be determined by the following

$$\mathbf{v}_{\text{el}}^{\text{blade}} = \mathbf{v}_{\text{hub}}^{\text{shaft}} + (\boldsymbol{\omega}^{\text{blade}} \times \mathbf{r}_{\text{hub}\to\text{el}}^{\text{blade}}) \tag{2.14}$$

which may be written as

$$\mathbf{v}_{\text{el}}^{\text{blade}} = v_{\text{x}}^{\text{blade}}\mathbf{i}_{\text{bl}} + v_{\text{y}}^{\text{blade}}\mathbf{j}_{\text{bl}} + v_{\text{z}}^{\text{blade}}\mathbf{k}_{\text{bl}} \tag{2.15}$$

Acceleration of a Rotor Blade Element

The velocities of a rotor blade element have been developed but the accelerations are also required as they give rise to the main rotor's inertial forces. The derivation of the rotor blade accelerations are similar to that of the development of the velocity expressions. The acceleration of the main rotor hub relative to the body axes set is

$$\mathbf{a}_{\text{hub}}^{\text{body}} = \mathbf{a}_{\text{c.g.}}^{\text{body}} + \boldsymbol{\omega}^{\text{body}} \times (\boldsymbol{\omega}^{\text{body}} \times \mathbf{r}_{\text{c.g.}\to\text{hub}}^{\text{body}}) + (\boldsymbol{\alpha}^{\text{body}} \times \mathbf{r}_{\text{c.g.}\to\text{hub}}^{\text{body}}) \tag{2.16}$$

The transformation matrices, Equations (2.5), (2.8) and (2.11), allow the acceleration of the rotor hub to be expressed in blade axes

$$\mathbf{a}_{\text{hub}}^{\text{blade}} = \mathbf{T}^{\text{shaft}\to\text{blade}}\ \mathbf{T}^{\text{disc}\to\text{shaft}}\ \mathbf{T}^{\text{body}\to\text{disc}}\mathbf{a}_{\text{hub}}^{\text{body}} \tag{2.17}$$

where the acceleration of the centre of gravity, in body axes, is

$$\mathbf{a}_{\text{c.g.}}^{\text{body}} = \left(\dot{U} + WQ - VR\right)\mathbf{i}_{\text{b}} \tag{2.18}$$
$$+ \left(\dot{V} + UR - WP\right)\mathbf{j}_{\text{b}} \tag{2.19}$$
$$+ \left(\dot{W} + VP - UQ\right)\mathbf{k}_{\text{b}} \tag{2.20}$$
$$\tag{2.21}$$

and the rotational accelerations, in body axes, are

$$\boldsymbol{\alpha}^{\text{body}} = \begin{bmatrix}\dot{P} & \dot{Q} & \dot{R}\end{bmatrix}^T \tag{2.22}$$

The accelerations in the shaft axes can be derived by transforming between the relevant axes sets. The acceleration of the hub, in disc axes, is

$$\mathbf{a}_{\text{hub}}^{\text{disc}} = \mathbf{T}^{\text{body}\to\text{disc}}\mathbf{a}_{\text{hub}}^{\text{body}} \tag{2.23}$$

which can also be stated in the following manner

$$\mathbf{a}_{\text{hub}}^{\text{disc}} = a_{\text{x}}^{\text{disc}}\mathbf{i}_{\text{disc}} + a_{\text{y}}^{\text{disc}}\mathbf{j}_{\text{disc}} + a_{\text{z}}^{\text{disc}}\mathbf{k}_{\text{disc}} \tag{2.24}$$

and the rotational acceleration of the disc axes set is

$$\boldsymbol{\alpha}^{\text{disc}} = \mathbf{T}^{\text{body}\to\text{disc}}\boldsymbol{\alpha}^{\text{body}} \tag{2.25}$$

By applying the transformation between the disc and shaft axes sets, the acceleration of the rotor hub, in shaft axes, is

$$\mathbf{a}_{\text{hub}}^{\text{shaft}} = \mathbf{T}^{\text{disc}\to\text{shaft}}\mathbf{a}_{\text{hub}}^{\text{disc}} \tag{2.26}$$

Assuming that the rotorspeed can vary, then the rotational acceleration of the shaft axes is

$$\boldsymbol{\alpha}^{\text{shaft}} = \mathbf{T}^{\text{disc}\to\text{shaft}}\boldsymbol{\alpha}^{\text{disc}} + \begin{bmatrix} 0 & 0 & \dot{\Omega} \end{bmatrix}^T \tag{2.27}$$

The acceleration of the rotor hub, in blade axes, is

$$\mathbf{a}_{\text{hub}}^{\text{blade}} = \mathbf{T}^{\text{shaft}\to\text{blade}}\mathbf{a}_{\text{hub}}^{\text{shaft}} \tag{2.28}$$

The absolute acceleration of a point of a blade element, in blade axes, is given by

$$\mathbf{a}_{\text{el}}^{\text{blade}} = \mathbf{a}_{\text{hub}}^{\text{blade}} + \boldsymbol{\omega}^{\text{blade}} \times \left(\boldsymbol{\omega}^{\text{blade}} \times \mathbf{r}_{\text{hub}\to\text{el}}^{\text{blade}}\right) + \boldsymbol{\alpha}^{\text{blade}} \times \mathbf{r}_{\text{hub}\to\text{el}}^{\text{blade}} \tag{2.29}$$

which is conveniently expressed as

$$\mathbf{a}_{\text{el}}^{\text{blade}} = a_{\text{x}}^{\text{blade}}\mathbf{i}_{\text{bl}} + a_{\text{y}}^{\text{blade}}\mathbf{j}_{\text{bl}} + a_{\text{z}}^{\text{blade}}\mathbf{k}_{\text{bl}} \tag{2.30}$$

The rotational acceleration of the blade axes set is obtained by applying the standard transformation and including the second order flapping time derivative

$$\boldsymbol{\alpha}^{\text{blade}} = \mathbf{T}^{\text{shaft}\to\text{blade}}\boldsymbol{\alpha}^{\text{shaft}} + \begin{bmatrix} 0 & \ddot{\beta} & 0 \end{bmatrix}^T \tag{2.31}$$

Rotor Forces and Moments

There are two forces that act on a given rotor blade element; namely aerodynamic and inertial forces. Therefore, for a rotor blade element the local force may be expressed as

$$\mathbf{f}_{\text{el}}^{\text{blade}} = -m_0 a_{\text{x}}^{\text{blade}}\mathbf{i}_{\text{bl}} + \left(f_{\text{y}}^{\text{blade}} - m_0 a_{\text{y}}^{\text{blade}}\right)\mathbf{j}_{\text{bl}} + \left(f_{\text{z}}^{\text{blade}} - m_0 a_{\text{z}}^{\text{blade}}\right)\mathbf{k}_{\text{bl}} \tag{2.32}$$

where m_0 is the mass per unit span of the blade and the terms, $f_{\text{y}}^{\text{blade}}$ and $f_{\text{z}}^{\text{blade}}$, represent the aerodynamic forces in the $\mathbf{j}_{\text{bl}}$ and $\mathbf{k}_{\text{bl}}$ directions, respectively. To calculate the total force the main rotor produces requires integration across the blade and around the azimuth. Due to the complex nature of these forces it is convenient to discuss the aerodynamic and inertial forces separately.

Aerodynamic Forces

The aerodynamic forces at each element are a function of the local air velocity and local angle of attack. The local air velocity is given by the magnitude of $\mathbf{v}_{\mathrm{el}}^{\mathrm{blade}}$. The local angle of attack is best determined by splitting the local air velocity into tangential and normal components. The tangential velocity of a rotor blade element is

$$v_{\mathrm{tan}} = -v_{\mathrm{y}}^{\mathrm{blade}} \tag{2.33}$$

whereas the normal component of the velocity is

$$v_{\mathrm{n}} = v_{\mathrm{z}}^{\mathrm{blade}} - v_{\mathrm{i}} \tag{2.34}$$

where v_i is the induced velocity at the rotor disc. The induced velocity is composed of three elements - a steady inflow term and two first order harmonic terms. The inflow model allows for the induced velocity to vary with both radial and azimuth position, with a complete description of the model given in Appendix A. Ignoring spanwise flow, the local air velocity is therefore

$$v_{\mathrm{res}} = \sqrt{v_{\mathrm{n}}^2 + v_{\mathrm{tan}}^2} \tag{2.35}$$

The local blade angle of attack is a function of the inflow angle, blade pitch and the spanwise twist of the blade. The inflow angle, ϕ, is calculated by using the tangential and normal velocities of the blade element

$$\phi = \sin^{-1} \frac{v_{\mathrm{tan}}}{\sqrt{v_{\mathrm{tan}}^2 + v_{\mathrm{n}}^2}} \tag{2.36}$$

The pitch angle of the rotor blade element is a function of the collective and cyclic controls

$$\theta_{pitch} = \theta_0 + \theta_{1s} \sin\psi + \theta_{1c} \cos\psi \tag{2.37}$$

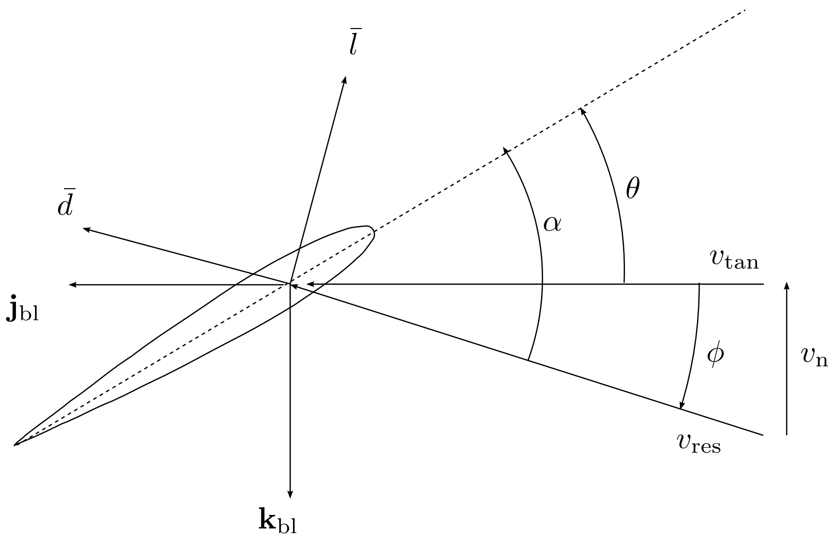

Figure 2.5: Lift and drag forces on a rotor blade element

Generally a rotor blade features twist in order to improve hover performance. Commonly the variation of twist along the rotor blade is linear, although in this model the twist can be nonlinear. In both cases the twist is a function of the blade element's radial position, $\theta_{\mathrm{twist}}(\bar{r})$. The local blade angle of attack is

$$\alpha_{bl} = \theta_{pitch} + \phi + \theta_{twist}(\bar{r}) \tag{2.38}$$

Since the local air velocity and angle of attack are known, then the local lift and drag forces of each blade element can be determined. The lift and drag forces, per unit span, are given by the following standard expressions

$$\bar{l} = \tfrac{1}{2}\rho v_{\mathrm{res}}^2 c a_0 \alpha \tag{2.39}$$

$$\bar{d} = \tfrac{1}{2}\rho v_{\mathrm{res}}^2 c \delta \tag{2.40}$$

The aerodynamic forces, lift and drag, act parallel and perpendicular to the local airflow direction as seen in Figure 2.5. It is also assumed that these aerodynamic forces act at the quarter chord point of the blade, which is a common modelling assumption. Due to this assumption the pitching moment of the rotor blade will be relatively small for most flight conditions and therefore has been neglected when the rotor moments are considered. Clearly, a transformation is required to determine the aerodynamic forces in the blade axes set. The aerodynamic forces, per blade element and in blade axes, are

$$\mathbf{f}_{\text{aero}}^{\text{blade}} = \begin{bmatrix} 0 \\ \bar{d}\cos\phi - \bar{l}\sin\phi \\ -\bar{l}\cos\phi - \bar{d}\sin\phi \end{bmatrix} \tag{2.41}$$

This type of rotor model, commonly referred to as a disc model, makes various assumptions to cast the forces and moments in closed loop form. The model assumes that the chord along the rotor blade is constant and that the local aerodynamics are two-dimensional. Further, one assumption is that Equation (2.41) can be simplified by assuming that the inflow angle, ϕ, is small thereby permitting the small angle assumption. In addition, the term $\bar{d}\phi$ is small compared to $\bar{l}$ so that the aerodynamic forces, per blade element and in blade axes, become

$$\mathbf{f}_{\text{aero}}^{\text{blade}} = \begin{bmatrix} 0 \\ \bar{d} - \bar{l}\phi \\ -\bar{l} - \bar{d}\phi \end{bmatrix} \tag{2.42}$$

In its fully expanded form, the aerodynamic forces are

$$\mathbf{f}_{\text{aero}}^{\text{blade}} = \frac{1}{2}\rho c a_0 \begin{bmatrix} 0 \\ \frac{\delta}{a_0} v_{\text{tan}}^2 - v_{\text{n}} v_{\text{tan}}\theta - v_{\text{n}}^2 \\ v_{\text{tan}}^2\theta + v_{\text{n}} v_{tan} \end{bmatrix} dr \tag{2.43}$$

where the term r represents the radial position of the blade element in dimensional form. The aerodynamic forces are expressed in non-dimensional form in the HGS package, with Equation (2.43) becoming

$$\begin{bmatrix} C_{\text{x aero}}^{\text{blade}} \\ C_{\text{y aero}}^{\text{blade}} \\ C_{\text{z aero}}^{\text{blade}} \end{bmatrix} = \frac{1}{2}\sigma a_0 \begin{bmatrix} 0 \\ \int_0^{1-e} \left(\frac{\delta}{a_0} \bar{v}_{\text{tan}}^2 - \bar{v}_{\text{n}} \bar{v}_{\text{tan}}\theta - \bar{v}_{\text{n}}^2 \right) \\ \int_0^{1-e} \left(\bar{v}_{\text{tan}}^2\theta + \bar{v}_{\text{n}} \bar{v}_{\text{tan}} \right) \end{bmatrix} d\bar{r} \tag{2.44}$$

$$\sigma = \frac{N_b c_{0.75}}{\pi R}$$

$$\bar{r} = \frac{r - eR}{R}$$

$$\bar{v}_{\text{tan}} = \frac{v_{\text{tan}}}{\Omega R}$$

$$\bar{v}_{\text{n}} = \frac{v_{\text{n}}}{\Omega R}$$

These forces can either be integrated analytically or numerically to determine the total force produced by the blade. This is one distinguishing feature between "individual blade" and "disc" models, with the "disc" model analytically integrating the equations. The analytical integration of Equation (2.44) is carried out with the aid of a symbolic mathematics package. The HGS package considers only the steady and one per rev forcing, which results in the aerodynamic coefficients

$$\begin{bmatrix} C_{\text{X aero}}^{\text{blade}} \\ C_{\text{Y aero}}^{\text{blade}} \\ C_{\text{Z aero}}^{\text{blade}} \end{bmatrix} = -\frac{1}{2N_b}\sigma a_0 \begin{bmatrix} 0 \\ C_{\text{Y 0 aero}}^{\text{blade}} + C_{\text{Y 1s aero}}^{\text{blade}} \sin\psi + C_{\text{Y 1c aero}}^{\text{blade}} \cos\psi \\ C_{\text{Z 0 aero}}^{\text{blade}} + C_{\text{Z 1s aero}}^{\text{blade}} \sin\psi + C_{\text{Z 1c aero}}^{\text{blade}} \cos\psi \end{bmatrix} \tag{2.45}$$

Inertial Forces

The local inertial force, which is given by Newton's 2nd law, is the product of the mass per unit span and the local acceleration of the quarter chord point, in blade axes. Hence, the inertial force of a blade element is

$$\mathbf{f}_{\text{in}}^{\text{blade}} = m_0 \begin{bmatrix} a_{\text{x}}^{\text{blade}} \\ a_{\text{y}}^{\text{blade}} \\ a_{\text{z}}^{\text{blade}} \end{bmatrix} \tag{2.46}$$

which can be integrated analytically to obtain the total inertial force of the blade. The inertial force is normalised and only the steady and one per rev forcing is considered, which results in the inertial force coefficients

$$\begin{bmatrix} C_{\text{X in}}^{\text{blade}} \\ C_{\text{Y in}}^{\text{blade}} \\ C_{\text{Z in}}^{\text{blade}} \end{bmatrix} = \begin{bmatrix} C_{\text{X 0 in}}^{\text{blade}} + C_{\text{X 1s in}}^{\text{blade}} \sin\psi + C_{\text{X 1c in}}^{\text{blade}} \cos\psi \\ C_{\text{Y 0 in}}^{\text{blade}} + C_{\text{Y 1s in}}^{\text{blade}} \sin\psi + C_{\text{Y 1c in}}^{\text{blade}} \cos\psi \\ C_{\text{Z 0 in}}^{\text{blade}} + C_{\text{Z 1s in}}^{\text{blade}} \sin\psi + C_{\text{Z 1c in}}^{\text{blade}} \cos\psi \end{bmatrix} \tag{2.47}$$

Total Rotor Forces

As stated previously, the total rotor forces comprise of aerodynamic and inertial terms as illustrated in Equation (2.32). The total rotor force is therefore the aerodynamic contribution minus the inertial force, leading to the following

$$\begin{bmatrix} C^{\text{blade}}_{\text{X rot}} \\ C^{\text{blade}}_{\text{Y rot}} \\ C^{\text{blade}}_{\text{Z rot}} \end{bmatrix} = \begin{bmatrix} C^{\text{blade}}_{\text{X 0}} + C^{\text{blade}}_{\text{X 1s}} \sin\psi + C^{\text{blade}}_{\text{X 1c}} \cos\psi \\ C^{\text{blade}}_{\text{Y 0}} + C^{\text{blade}}_{\text{Y 1s}} \sin\psi + C^{\text{blade}}_{\text{Y 1c}} \cos\psi \\ C^{\text{blade}}_{\text{Z 0}} + C^{\text{blade}}_{\text{Z 1s}} \sin\psi + C^{\text{blade}}_{\text{Z 1c}} \cos\psi \end{bmatrix} = \mathbf{C}^{\text{blade}}_{\text{rot}} \tag{2.48}$$

The final step involves converting the rotor force equations into body axes and multiplying them with $\rho(\Omega R)^2\pi R^2$ to determine their contribution to the total external forces. Hence, the forces the main rotor produces in body axes are predicted to be

$$\begin{bmatrix} X_{rot} \\ Y_{rot} \\ Z_{rot} \end{bmatrix} = \rho(\Omega R)^2\pi R^2 \left(\mathbf{T}^{\text{body}\to\text{disc}}\right)^T \left(\mathbf{T}^{\text{disc}\to\text{shaft}}\right)^T \left(\mathbf{T}^{\text{shaft}\to\text{blade}}\right)^T \mathbf{C}^{\text{blade}}_{\text{rot}} \tag{2.49}$$

External Moments

The contribution of the main rotor to the external moments arises from two sources. The first source is the rotor hub moment that is due to the blade lift shear force at the effective flap hinge [36]. Secondly, the rotor thrust vector is likely to be offset from the centre of gravity position, thereby producing an external moment. The hub moment per unit span is given by

$$\mathbf{m}^{\text{blade}}_{\text{el}} = \mathbf{r}^{\text{blade}}_{\text{hub}\to\text{el}} \times \mathbf{f}^{\text{blade}}_{\text{el}} \tag{2.50}$$

which in its expanded form becomes

$$\mathbf{m}^{\text{blade}}_{\text{el}} = -r\left(f^{\text{blade}}_{\text{z}} - m_0 a^{\text{blade}}_{\text{z}}\right)\mathbf{j}_{\text{bl}} + r\left(f^{\text{blade}}_{\text{y}} - m_0 a^{\text{blade}}_{\text{y}}\right)\mathbf{k}_{\text{bl}} \tag{2.51}$$

The $\mathbf{k}_{\text{bl}}$ moment term is the blade element contribution to the blade flapping moment, whereas the $\mathbf{j}_{\text{bl}}$ term describes the blade element contribution to the rotor torque. The total moments are conveniently split into aerodynamic and inertial contributions. The total external moment produced by one rotor blade is therefore

$$\int_{eR}^{R} \left(\mathbf{r}_{\text{hub}\to\text{el}}^{\text{blade}} \times \left(\mathbf{f}_{\text{aero}}^{\text{blade}} - \mathbf{f}_{\text{in}}^{\text{blade}} \right) \right) dr = \begin{bmatrix} 0 \\ K_\beta \beta \\ C_{\text{Q rot}}^{\text{blade}} \rho \left(\Omega R \right)^2 \pi R^3 \end{bmatrix} \tag{2.52}$$

The flapping equation is derived by assuming that the flapping motion is resisted by the stiffness of the rotor hub, K_β, with the flapping equations of motion discussed later. The value of K_β is chosen to match the flapping frequency ratio of the main rotor [36]. Typical values of this spring strength are 166 kN.m/rad, 113 kN.m/rad and 48 kN.m/rad which correspond to the Lynx, Bo-105 and Puma SA330 helicopters, respectively [36]. The torque equation, described by the $\mathbf{k}_{\text{bl}}$ term in Equation (2.51), is integrated analytically with the use of Mathematica. The aerodynamic contribution to the torque equation is

$$C_{\text{Q aero}}^{\text{blade}} = \frac{1}{2\sigma N_b} a_0 \int_0^{1-e} \left(\frac{\delta}{a_0} \bar{v}_{\text{tan}}^2 - \bar{v}_{\text{tan}} \bar{v}_{\text{n}} \theta - \bar{v}_{\text{n}}^2 \right) \left(\bar{r} + e \right) d\bar{r} \tag{2.53}$$

Considering only the steady and one-per-rev terms, the aerodynamic torque is given by

$$C_{\text{Q aero}}^{\text{blade}} = C_{\text{Q 0 aero}}^{\text{blade}} + C_{\text{Q 1s aero}}^{\text{blade}} \sin\psi + C_{\text{Q 1c aero}}^{\text{blade}} \cos\psi \tag{2.54}$$

where the coefficients $C_{\text{Q 0 aero}}^{\text{blade}}$, $C_{\text{Q 1s aero}}^{\text{blade}}$ and $C_{\text{Q 1c aero}}^{\text{blade}}$, are obtained by the analytical integration of Equation (2.53). The inertial contribution to the rotor torque, in dimensional form, is

$$Q_{\text{in}}^{\text{blade}} = -\int_{eR}^{R} \left(m_0 a_{\text{y}}^{\text{blade}} r \right) dr \tag{2.55}$$

The inertial contribution of one blade is in the form

$$C_{\text{Q in}}^{\text{blade}} = C_{\text{Q 0 in}}^{\text{blade}} + C_{\text{Q 1s in}}^{\text{blade}} \sin\psi + C_{\text{Q 1c in}}^{\text{blade}} \cos\psi \tag{2.56}$$

with the coefficients obtained by normalising Equation (2.55) and performing the analytical integration. Hence, the total rotor blade contribution can be expressed as

$$C_{\text{Q rot}}^{\text{blade}} = C_{\text{Q 0 rot}}^{\text{blade}} + C_{\text{Q 1s rot}}^{\text{blade}} \sin\psi + C_{\text{Q 1c rot}}^{\text{blade}} \cos\psi \tag{2.57}$$

where the coefficients are

$$C_{\text{Q 0 rot}}^{\text{blade}} = \frac{\sigma a_0}{2N_b} C_{\text{Q 0 aero}}^{\text{blade}} - C_{\text{Q 0 in}}^{\text{blade}}, \ldots etc \tag{2.58}$$

Therefore with the calculation of $C_{\text{Q rot}}^{\text{blade}}$, the external moments, in blade axes, can be determined with the use of Equation (2.52). The total moment vector, in blade axes, can be expressed as

$$\mathbf{M}_{\text{rot}}^{\text{blade}} = \begin{bmatrix} L_{\text{rot}}^{\text{blade}} & M_{\text{rot}}^{\text{blade}} & N_{\text{rot}}^{\text{blade}} \end{bmatrix}^T \tag{2.59}$$

so that the total external moment contribution of the main rotor, including the rotor thrust vector being offset from the centre of gravity, is

$$\begin{aligned} \mathbf{M}_{\text{rot}}^{\text{body}} = & \left(\mathbf{T}^{\text{body}\rightarrow\text{disc}}\right)^T \left(\mathbf{T}^{\text{disc}\rightarrow\text{shaft}}\right)^T \left(\mathbf{T}^{\text{shaft}\rightarrow\text{blade}}\right)^T \mathbf{M}_{\text{rot}}^{\text{blade}} \ldots \\ & + \left(\mathbf{r}_{\text{c.g.}\rightarrow\text{hub}}^{\text{body}} \times \mathbf{F}_{\text{rot}}^{\text{body}}\right) \end{aligned} \tag{2.60}$$

Flapping Equation

The flapping angles can be expressed in individual blade co-ordinates (IBC) or in multi-blade co-ordinates (MBC) [36]. With the IBC formulation, the flapping angles are dependent on the blade number and azimuth position. However, by transforming the IBC to the the MBC formulation, the flapping angles are described by the coning angle, β_0, the longitudinal flapping angle, β_{1c}, the lateral flapping angle, β_{1s}, and the differential coning angle, β_{0d}. The HGS rotor model, as outlined previously, describes the flapping angles in MBC, requiring a transformation from IBC to MBC. Assuming that the main rotor has four blades, the IBC are

$$\boldsymbol{\beta}_I = \begin{bmatrix} \beta_1 & \beta_2 & \beta_3 & \beta_4 \end{bmatrix}^T \tag{2.61}$$

which describes the flapping angles of the individual blades. This is the result that occurs when the evaluating the $\mathbf{j}_{\mathrm{bl}}$ component of Equation (2.52), which is

$$\int_{eR}^{R}\left(f_{\mathrm{z}}^{\mathrm{blade}}-m_0 a_{\mathrm{z}}^{\mathrm{blade}}\right)rdr=K_\beta \beta i \tag{2.62}$$

which can also be expressed in the form

$$\boldsymbol{\beta}_{\mathrm{I}}^{''}+\mathbf{C}_{\mathrm{I}}\left(\psi\right)\boldsymbol{\beta}_{\mathrm{I}}^{'}+\mathbf{D}_{\mathrm{I}}\left(\psi\right)\boldsymbol{\beta}_{\mathrm{I}}=\mathbf{H}_{\mathrm{I}}\left(\psi\right) \tag{2.63}$$

In contrast, the MBC are given by

$$\boldsymbol{\beta}_M=\begin{bmatrix}\beta_{\mathit{0}} & \beta_{\mathit{0d}} & \beta_{\mathit{1s}} & \beta_{\mathit{1c}}\end{bmatrix}^T \tag{2.64}$$

which effectively describes the tilt of the rotor disc relative to the hub axes. The transformation between IBC to MBC is discussed in detail by Padfield [36], and the transformation in vector form is

$$\boldsymbol{\beta}_I=\mathbf{L}_\beta\boldsymbol{\beta}_M \tag{2.65}$$

where

$$\mathbf{L}_\beta=\begin{bmatrix}1 & -1 & \cos\psi & \sin\psi\\ 1 & 1 & \sin\psi & -\cos\psi\\ 1 & -1 & -\cos\psi & -\sin\psi\\ 1 & 1 & -\sin\psi & \cos\psi\end{bmatrix} \tag{2.66}$$

Applying the transformation from IBC to MBC, Equation (2.63) becomes

$$\boldsymbol{\beta}_{\mathrm{M}}^{''}+\mathbf{C}_{\mathrm{M}}\left(\psi\right)\boldsymbol{\beta}_{\mathrm{M}}^{'}+\mathbf{D}_{\mathrm{M}}\left(\psi\right)\boldsymbol{\beta}_{\mathrm{M}}=\mathbf{H}_{\mathrm{M}}\left(\psi\right) \tag{2.67}$$

where

$$\mathbf{C}_{\mathrm{M}}=\mathbf{L}_\beta^{-1}\left(2\mathbf{L}_\beta^{\prime}+\mathbf{C}_{\mathrm{I}}\mathbf{L}_\beta\right)$$

$$\mathbf{D}_{\mathrm{M}} = \mathbf{L}_{\beta}^{-1}\left(\mathbf{L}_{\beta}'' + \mathbf{C}_{\mathrm{I}}\mathbf{L}_{\beta}' + \mathbf{D}_{\mathrm{I}}\mathbf{L}_{\beta}\right)$$

$$\mathbf{H}_{\mathrm{M}} = \mathbf{L}_{\beta}^{-1}\mathbf{H}_{\mathrm{I}}$$

Equation (2.67) describes the flapping angles in MBC, however the expression is commonly reduced further by exercising the quasi-steady assumption. This assumption implies that the rotor flapping motion is fully decoupled from the fuselage since the flapping modes are much faster than the body modes. Another assumption is to neglect the periodic terms in Equation (2.67) so that the MBC flapping angles can be calculated by

$$\boldsymbol{\beta}_{\mathrm{M}} = \mathbf{D}_{\mathrm{M}\ 0}^{-1}\mathbf{H}_{\mathrm{M}\ 0} \tag{2.68}$$

2.5 Coaxial Rotor Model

The coaxial rotor is modelled by using two multiblade rotor models spaced vertically apart. The upper rotor rotates in an anticlockwise direction (when viewed from above), whereas the lower rotor rotates in a clockwise direction. In terms of a conventional single rotor, the Pitt and Peters dynamic inflow model [46] is the most commonly used in helicopter flight dynamics. To date, an equivalent model representing the inflow through a coaxial rotor is not available within literature, although initial attempts have been made [47, 48]. The development of such a model would be a significant contribution to the rotorcraft community but unfortunately the development of such a model is beyond the scope of the current work. With the growth of interest in coaxial rotors, partly due to the development of the Sikorsky X2, clearly there is need for such a model and appropriate test data for validation. For the time being, a simple steady momentum theory approach, used in simple conventional rotor models, is adapted to represent the inflow of a coaxial configuration. This steady version assumes that the induced velocity changes instantaneously across the rotor disc, therefore not faithfully modelling the dynamic lag of the induced velocity [49]. In terms of steady coaxial inflow representations, various models have been created, with Leishman and Syal [50] and Leishman and Ananthan [51] developing a coaxial inflow model by slightly adapting the classical blade element momentum approach. The results show very good agreement with experiments in hover and in axial flight. Kim and Brown used another approach, using the vorticity transport model to estimate the performance of a coaxial rotor [52, 53]. The coaxial rotor inflow model used here is a similar inflow model to that of Leishman and Syal [50] and Leishman and Ananthan [51], with a few adaptations. The first assumption made in the development of the coaxial inflow model is that the inflow of the lower rotor does not affect the upper rotor's ability to generate thrust. The second assumption is that the rotors are sufficiently close together that the wake from the upper rotor does not contract radially inward and does not fully develop. This assumption can be justified as it is assumed that the rotor is similar to that of the ABC rotor, featuring very stiff blades with a small separation distance between the rotors. Hence, the relationship between the rotor thrust and the induced velocity of the upper rotor is

$$C_{T_U} = \lambda_u \sqrt{\mu^2 + (\mu_z - \lambda_u)^2} \tag{2.69}$$

where λ_u represents the normalised uniform inflow velocity across the upper rotor disc and μ_z is the normalised vertical velocity of the rotor hub. The lower rotor's inflow consists of a combination of its own induced velocity and the upper rotor's induced velocity. A similar approach was previously used by Sikorsky [54], and it showed good agreement with experimental results. The inflow equation for the lower rotor is

$$C_{T_L} = 2\lambda_l \sqrt{\mu^2 + (\mu_z - \lambda_l + \lambda_u)^2} \tag{2.70}$$

where λ_l is the normalised uniform inflow velocity across the lower rotor disc and μ_z

Validation

To gain confidence in the coaxial rotor model, the model is compared against "rotor 1" of Harrington's coaxial experimental results [55]. Harrington's rotor 1 is a two-bladed untwisted rotor with a solidity of 0.054, a rotor radius of 3.81 m, and a separation distance of 9.5% of the rotor diameter. The HGS rotor model was configured to match Harrington's coaxial arrangement and trimmed in the hover state for various thrust coefficients. Figure 2.6 compares the thrust and torque coefficients of the coaxial model to that of Harrington's experimental results at a blade tip speed of 392 ft/s. Also shown in the figure are the results produced by two rotors acting in isolation. These

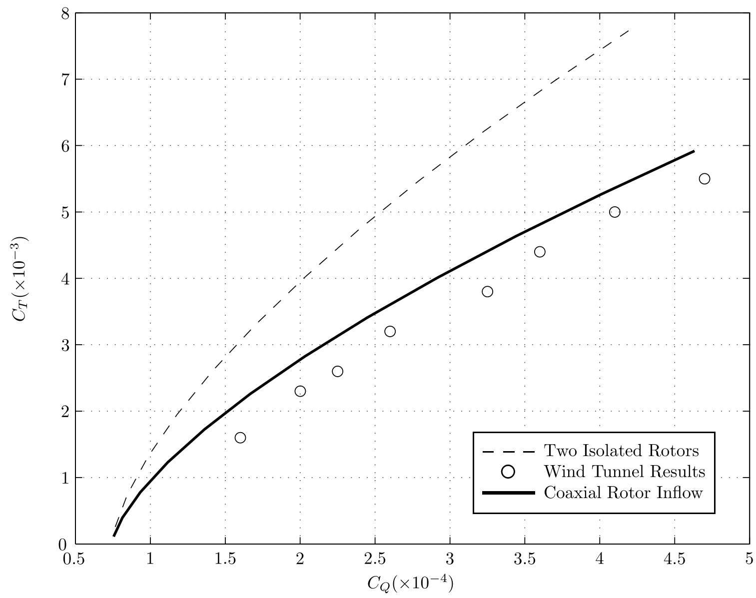

Figure 2.6: Comparison between the Coaxial Rotor Model and the ABC Hover Flight Test Results from Ref [55]

two isolated rotors significantly over-predict the thrust and torque produced by the rotor system. However, the results from the coaxial inflow model compare favourably with the experimental results.

The coaxial rotor model was compared to performance data of a coaxial rotor in forward flight that was obtained experimentally by Dingeldein [56]. The rotors used in the experiment were identical to that of Harrington's rotor 1 [55], and the power of the rotor system was measured for various advance ratios. The coaxial rotor system was trimmed for various flight speeds, with Figure 2.7 showing the comparison between Dingeldein's results [56] and the coaxial rotor model. Between advance ratios of 0.15 and 0.2, the coaxial rotor model under-predicts the power requirements of the coaxial rotor. As the forward speed increases, the wakes of the two rotors begin to skew back [57] and a portion of the upper rotor's wake is not ingested into the lower rotor. This effect is not modelled in the current coaxial rotor model and offers an explanation for the discrepancies with the experimental results. However, the results from the coaxial rotor model do follow the same form as Dingeldein's experimental results [56] and appear to come closer as forward speed increases. The coaxial rotor model appears to compare well with experimental results, particularly at hover and high speeds. This validation gives confidence to the worth of the coaxial rotor results, although a full validation is not possible due to the lack of experimental data.

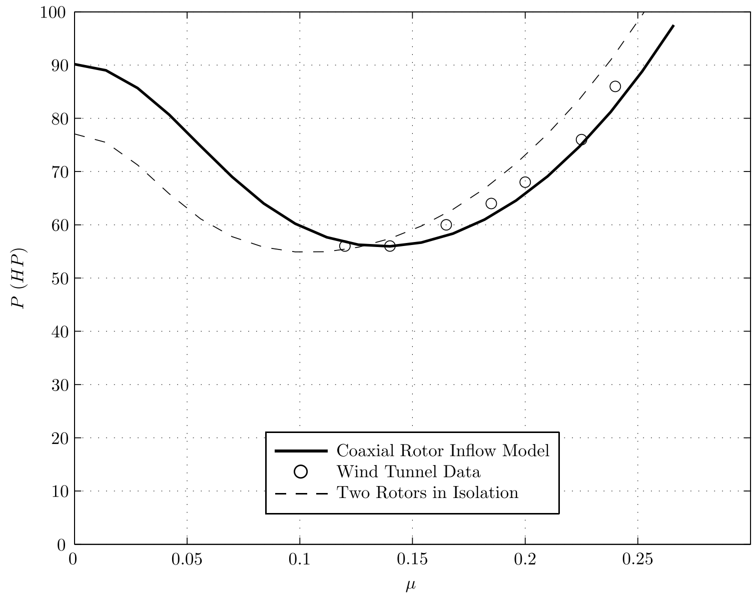

Figure 2.7: Comparison between the Coaxial Rotor Model and NACA Forward Flight Wind Tunnel Results from Ref [56]

The established coaxial rotor wind tunnel experiments by Harrington and Dingeldein [55, 56] have provided some valuable information regarding the coaxial rotor arrangement. The two experiments present the power of the coaxial rotor at various operating conditions which have are been conveniently used as a set of validation data, with the coaxial rotor model comparing favourably with the experiments, see Figures 2.6 and 2.7. The validation presented previously did not compare the control angles calculated from the simulation model with experiments. The reason for this is that Harrington and Dingeldein do not present the control angles in their respective experiments [55, 56]. In fact, there is a shortage of wind tunnel experiments or flight tests, which present the control angles of a coaxial rotor arrangement in a given flight regime. To remedy this issue, the simulated control angles are compared with results from Kim and Brown's study of a coaxial rotor [53]. Kim and Brown present the control angles to trim Dingeldein's coaxial rotor experiment [56] in forward flight by using the VTM model [53]. It is appreciated that this is not a classical validation process, where the simulated results are compared with results from wind tunnel experiments or flight tests, as Kim and Brown's results are derived from a simulation model. However, Kim and Brown's modelling approach is of a higher degree of fidelity than that of the coaxial rotor model used in this study as their simulation model takes into account complex aerodynamic interactions such as blade vortex interactions. Due to the sophistication of the VTM model coupled with the absence of suitable validation data, the coaxial

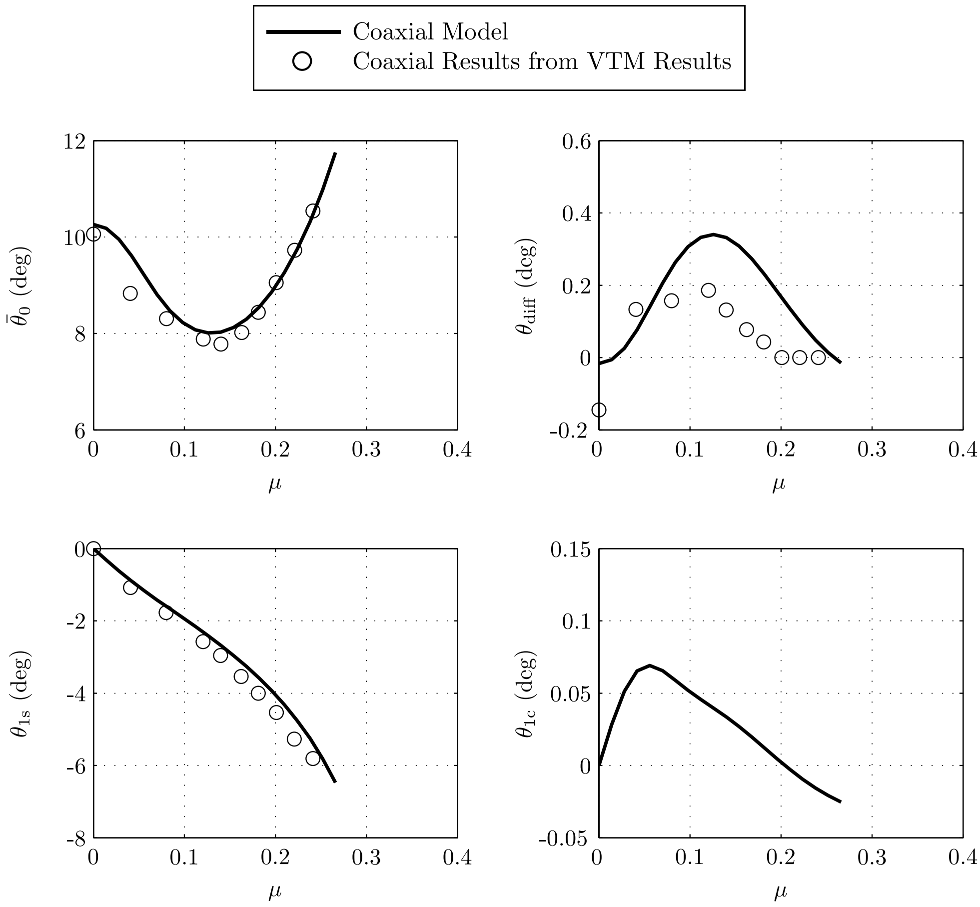

Figure 2.8: Comparison between the Coaxial Rotor Model and Forward Flight VTM Results from Ref [53]

rotor model used in this study is compared with the control angles calculated by Kim and Brown [53], with Figure 2.8 showing the comparison of results. The comparison between the two predicted mean values of coaxial rotor collective, $\bar{\theta}_0$ is good, particularly at higher advance ratios. The trend of the mean coaxial rotor collective is similar to that of a conventional helicopter collective as it reduces after the hover since the local dynamic pressure increases due to the increase of advance ratio. Recall, that the airframe drag is represented in Dingeldein's experiment by a flat plate with area 10 ft^2 [56]. Of course, at high advance ratios the plate produces more drag resulting in the increase of $\bar{\theta}_0$ required after an advance ratio of 0.15. The flat plate also requires negative longitudinal cyclic inputs, θ_{1s}, so that a component of the coaxial rotor thrust balances the drag from the flat plate. The comparison of the required longitudinal cyclic results at each advance ratio is fairly good. The only discrepancy appears to be the comparison of the yaw control, θ_{diff}. This is likely due to the rudimentary nature of the current coaxial rotor inflow model and its inability to accurately model aerodynamic environments across the upper and lower rotor discs.

2.6 Propeller Model

Overview of the Propeller Model

Blade element theory is used to model the propeller. Therefore in this sense, the helicopter rotor and propellers model are similar. Although, in the case of the propeller, the task is simplified as a propeller does not have flapping degrees of freedom. Ideally the propeller would be similar to that of the main rotor for the purposes of consistency. However, in the derivation of the main rotor expressions various assumptions are made in order to cast the equations in closed loop form. One of these assumptions is that the order of magnitude of the tangential velocity of a blade element is much greater than that of the in-plane velocity of a blade element. In the case of the propeller this assumption does not hold true as the normal velocity of a blade element will be composed of the forward speed of the aircraft. Hence, it is difficult to analytically integrate the loads across the propeller blade and maintain an appropriate level of validity. Consequently, the elemental forces and moments are integrated numerically. This is one of the distinguishing features between the propeller and main rotor model.

The development of this blade element propeller model requires certain assumptions. These assumptions are listed as follows:

- The blades are assumed rigid
- There are no flapping or lagging degrees of freedom
- There are no interference effects between blades
- The induced velocity is composed of a uniform component across the propeller disc
- Aerodynamic forces of each blade element are assumed to dominate the overall forces and therefore inertial forces have been excluded from the model
- Spanwise flow ignored

Propeller Kinematics

Velocity of the Propeller Hub

To determine the kinematics of a propeller blade element, it is necessary to find the velocity of the propeller hub. The propeller hub (p.h.), as seen in Figure 2.9, is positioned at a distance l_{prop} behind the fuselage reference point, a height h_{prop} above it and a distance of w_{prop} to the right of the reference point. Also shown in Figure 2.9 is a new axes set, denoted by the subscript p.h., which is named the propeller disc axes with its origin at the propeller hub. To make the propeller model as generic as possible, the propeller disc axes can be tilted in the aircraft longitudinal frame relative to the body axes by an appropriate selection of τ, Figure 2.9. A positive value of τ corresponds to a positive rotation around $\mathbf{j}_{\mathrm{b}}$, with $\tau = 270°$ in Figure 2.9. This allows the propeller hub to be placed at any position and orientation on the airframe. Therefore, the position vector, in body axes, of the propeller hub with respect to the centre of gravity is

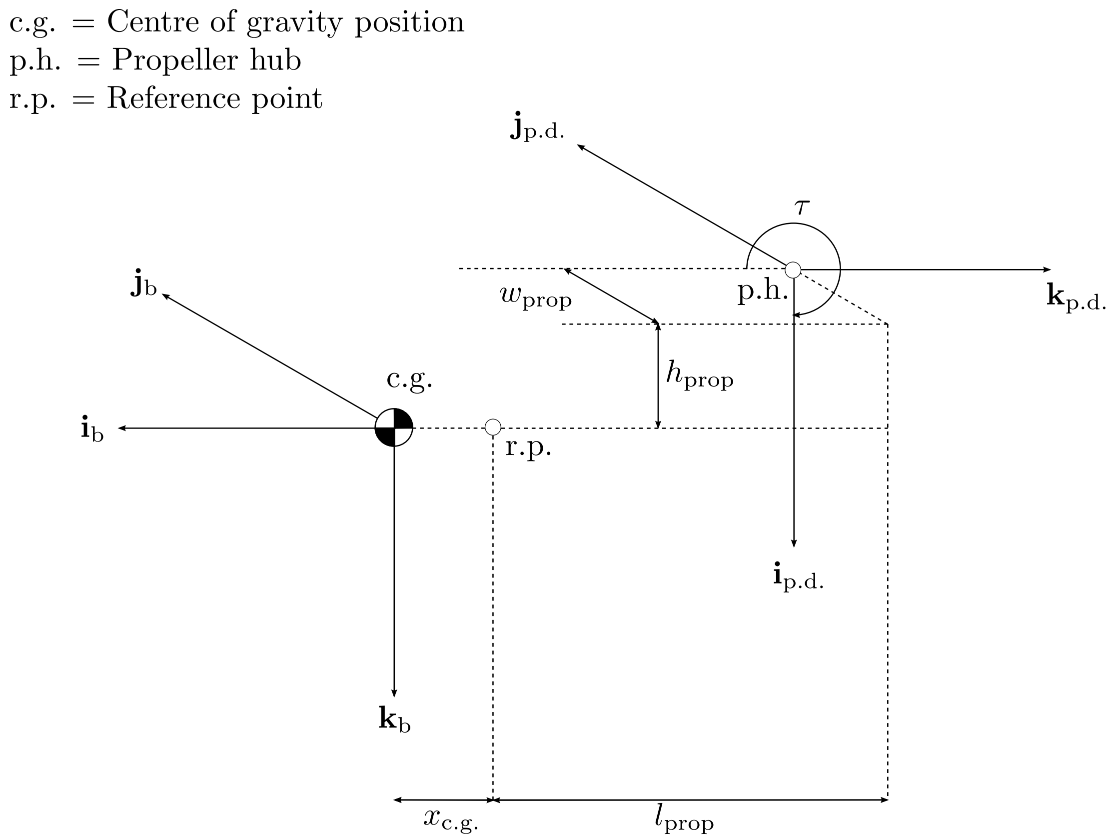

Figure 2.9: The Body Axes and the Propeller Hub Axes

$$\mathbf{r}_{\text{c.g.}\rightarrow\text{p.h.}} = -(l_{prop} + x_{c.g.})\mathbf{i_b} + w_{\text{prop}}\mathbf{j}_{\text{b}} - h_{\text{prop}}\mathbf{k_b} \tag{2.71}$$

Moreover, the velocity of the propeller hub, in body axes, is given by the following standard expression

$$\mathbf{v}^{\text{body}}_{\text{p.h.}} = \mathbf{v}^{\text{body}}_{\text{c.g.}} + (\boldsymbol{\omega}^{\text{body}} \times \mathbf{r}^{\text{body}}_{\text{c.g.}\rightarrow\text{p.h.}}) + \frac{d\mathbf{r}^{\text{body}}_{\text{c.g.}\rightarrow\text{p.h.}}}{dt} \tag{2.72}$$

The velocity can also be expressed in propeller disc axes. The transformation between the body and propeller disc axes sets, referring to Figure 2.9, is

$$\mathbf{T}^{\text{body}\rightarrow\text{p.d.}} = \begin{bmatrix} \cos\tau & 0 & -\sin\tau \\ 0 & 1 & 0 \\ \sin\tau & 0 & \cos\tau \end{bmatrix} \tag{2.73}$$

Applying the transformation matrix in Equation (2.73), the propeller hub velocity, in propeller disc axes, is

$$\mathbf{v}^{\text{p.d.}}_{\text{p.h}} = \mathbf{T}^{\text{body}\rightarrow\text{p.d.}}\mathbf{v}^{\text{body}}_{\text{p.h.}} \tag{2.74}$$

Or more conveniently written as

$$\mathbf{v}^{\text{p.d.}}_{\text{p.h.}} = u^{\text{p.d.}}\mathbf{i}_{\text{p.d.}} + v^{\text{p.d.}}\mathbf{j}_{\text{p.d.}} + w^{\text{p.d.}}\mathbf{k}_{\text{p.d.}} \tag{2.75}$$

Similarly, applying the transformation in Equation (2.73), the rotational velocity of the propeller disc axes set is

$$\boldsymbol{\omega}^{\text{p.d}} = \mathbf{T}^{\text{body}\rightarrow\text{p.d.}}\boldsymbol{\omega}^{\text{body}} \tag{2.76}$$

Which can be expressed as

$$\boldsymbol{\omega}^{\text{p.d}} = \omega^{\text{p.d.}}_{\text{x}}\mathbf{i}_{\text{p.d.}} + \omega^{\text{p.d.}}_{\text{y}}\mathbf{j}_{\text{p.d.}} + \omega^{\text{p.d.}}_{\text{z}}\mathbf{k}_{\text{p.d}} \tag{2.77}$$

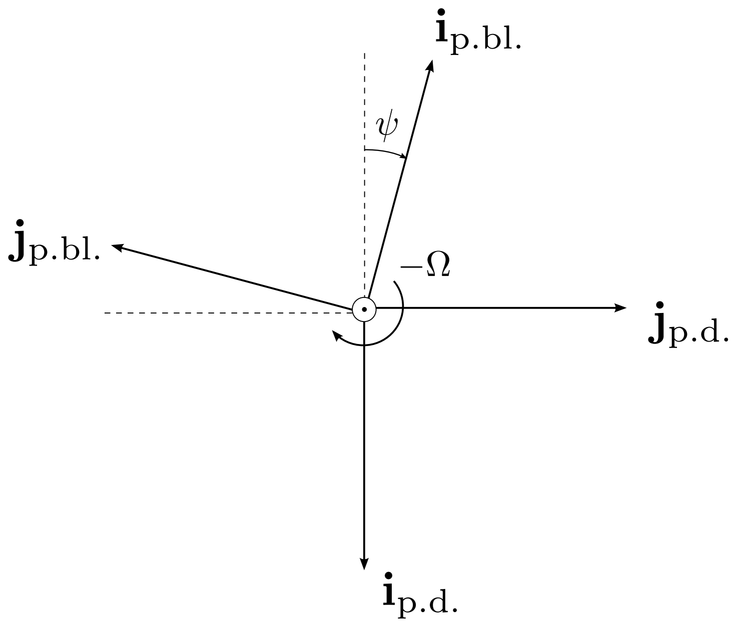

Figure 2.10: The Propeller Hub and Blade Element Axes Sets when the Propeller is Rotating Clockwise when viewed from behind

Velocity of a Blade Element

To determine the velocities of a given blade element, which is rotating with respect to the propeller hub, it is necessary to introduce another axes set. Therefore the propeller blade element axes are introduced, denoted by *p.bl.*, shown in Figure 2.10. Furthermore, Figure 2.11 shows the orientation of the blade axes set relative to the local aerofoil section. This axes set is positioned on the quarter chord position of the aerofoil, with the $\mathbf{i}_{\text{p.bl.}}$ position vector superimposed on the quarter chord position and in the direction of root to tip. The $\mathbf{j}_{\text{p.bl.}}$ position vector points from the leading edge to the trailing edge of each section whilst $\mathbf{k}_{\text{p.bl.}}$ points directly downwards. The transformation matrix from propeller disc to propeller blade axes is therefore

$$\mathbf{T}^{\text{p.d.}\rightarrow\text{p.bl.}} = \begin{bmatrix} -\cos\psi & \sin\psi & 0 \\ -\sin\psi & -\cos\psi & 0 \\ 0 & 0 & 1 \end{bmatrix} \tag{2.78}$$

The propeller hub velocity in propeller blade element axes is obtained by applying the transformation matrix in Equation (2.78) to Equation (2.75), leading to the following

$$\mathbf{v}_{\text{p.h.}}^{\text{p.bl.}} = \mathbf{T}^{\text{p.d.}\rightarrow\text{p.bl.}}\mathbf{v}_{\text{p.h.}}^{\text{p.d.}} \tag{2.79}$$

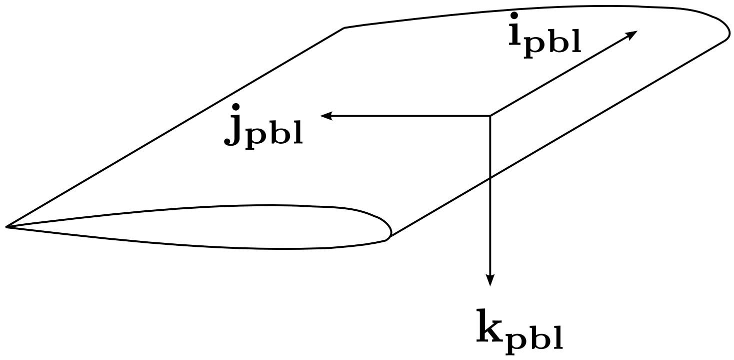

Figure 2.11: The Blade Axes Set

The angular velocity of the propeller blade element axes is determined in a similar manner but with the inclusion of the $n_{clock}\Omega\mathbf{k}_{\text{p.bl.}}$ term, which accounts for both the direction and rotational velocity of the shaft. The direction in which the propeller blades rotate is given by n_{clock}, with $n_{clock} = 1$ if the propeller rotates clockwise when viewed from behind the helicopter. Conversely $n_{clock} = -1$ if the propeller is chosen to rotate in the opposite direction. Therefore, the angular velocity of the propeller blade element axes set is

$$\boldsymbol{\omega}^{\text{p.bl.}} = \mathbf{T}^{\text{p.d.}\to\text{p.bl.}}\boldsymbol{\omega}^{\text{p.d.}} + \begin{bmatrix} 0 \\ 0 \\ n_{clock}\Omega \end{bmatrix} \tag{2.80}$$

The next task is to obtain an expression of the velocity of a propeller blade element so that the aerodynamics forces can be determined. The velocity of a quarter chord point of a propeller blade element, which is denoted by p, in propeller blade axes is given by the standard equation

$$\mathbf{v}_{\text{p}}^{\text{p.bl.}} = \mathbf{v}_{\text{p.h.}}^{\text{p.bl.}} + (\boldsymbol{\omega}^{\text{p.bl.}} \times \mathbf{r}_{\text{p.h.}\to\text{p}}^{\text{p.bl.}}) + \frac{d\mathbf{r}_{\text{p.h.}\to\text{p}}^{\text{p.bl.}}}{dt} \tag{2.81}$$

where, $\mathbf{r}_{\text{p.h.}\to\text{p}}^{\text{p.bl.}}$ is the position vector of the propeller hub to the quarter chord point of the given propeller blade element. This position vector is given by

$$\mathbf{r}_{\text{p.h.}\to\text{p}}^{\text{p.bl.}} = r_i\mathbf{i}_{\text{p.bl.}} \tag{2.82}$$

The distance r_i varies according to blade element's position relative to the propeller hub, where the subscript i denotes the section number with 1 being closest to the root.

Hence, the velocity of the point p in propeller blade element axes can be determined by using Equations (2.79), (2.80) and (2.82). The velocity term is split into its three components of

$$\mathbf{v}_{\mathrm{p}}^{\mathrm{p.bl.}} = v_{\mathrm{x}}^{\mathrm{p.bl.}}\mathbf{i}_{\mathrm{p.bl.}} + v_{\mathrm{y}}^{\mathrm{p.bl.}}\mathbf{j}_{\mathrm{p.bl.}} + v_{\mathrm{z}}^{\mathrm{p.bl.}}\mathbf{k}_{\mathrm{p.bl.}} \tag{2.83}$$

Propeller Forces and Moments

Propeller Forces

The aerodynamic forces of a propeller blade element are dependent on both the local velocity and angle of attack, which can be calculated using Equation (2.83). Figure 2.12 shows the aerodynamic forces and their relation to the propeller blade element axes for a clockwise rotating propeller when viewed from behind. The tangential and normal velocities of the propeller blade element are the components of Equation (2.83) with the inclusion of the induced velocity in the $\mathbf{k}_{\mathrm{p.bl.}}$ direction

$$v_{\mathrm{tan}} = n_{clock} v_{\mathrm{y}}^{\mathrm{p.bl.}} \tag{2.84}$$

$$v_{\mathrm{n}} = v_{\mathrm{z}}^{\mathrm{p.bl.}} - v_{\mathrm{i}} \tag{2.85}$$

Again, referring to Figure 2.12, the freestream velocity is given by

$${v_{res}}^2 = {v_n}^2 + {v_{tan}}^2 \tag{2.86}$$

and it also clear that the relationship between the local velocities and ϕ is

$$\phi = \tan^{-1}\left(\frac{v_n}{v_{tan}}\right) \tag{2.87}$$

The relationships between the inflow angle, propeller pitch and local angle attack are shown in Figure 2.12. Generally, propellers have significant spanwise twist so that each propeller blade element operates at an efficient angle of attack [58]. The propeller twist distribution can be nonlinear or linear depending on the design choice. For simplicity, the following analysis assumes that the twist distribution is linear, although this doesn't

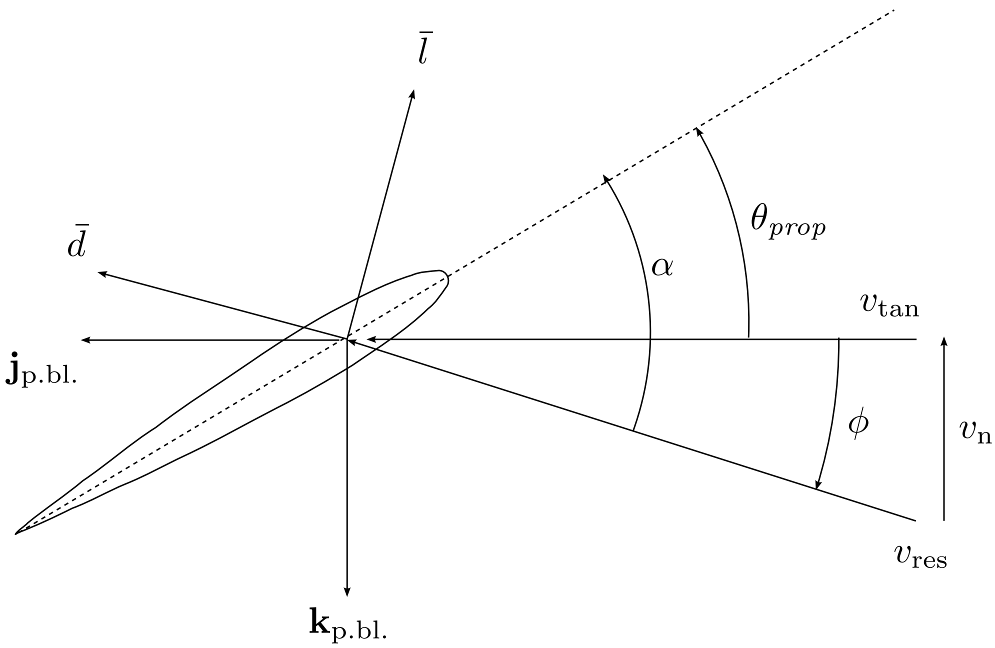

Figure 2.12: Angle of Attack of a Propeller Blade Element

necessarily have to be the case. The local propeller blade angle of attack is determined by propeller pitch angle, controlled by the pilot, the twist distribution and the local inflow angle

$$\alpha = \theta_{prop} + \tan^{-1}\left(\frac{v_{\mathrm{n}}}{v_{\mathrm{tan}}}\right) + \theta_{twist}\left(\frac{r_{\mathrm{i}}}{R_{prop}}\right) \tag{2.88}$$

where R_{prop} is the radius of the propeller blade. The transformation between the aerodynamic forces and propeller blade element axes is

$$\begin{bmatrix} \mathbf{j}_{\mathrm{p.bl.}} \\ \mathbf{k}_{\mathrm{p.bl.}} \end{bmatrix} = \begin{bmatrix} \cos\phi & -\sin\phi \\ -\sin\phi & -\cos\phi \end{bmatrix} \begin{bmatrix} \bar{d} \\ \bar{l} \end{bmatrix} \tag{2.89}$$

In terms of the aerodynamics forces, the lift and drag, per unit span, of each propeller blade element take the familiar form of

$$\bar{d} = \frac{1}{2}\rho v_{\mathrm{res}}^2 c_{\mathrm{i}} C_d(\alpha, M) \tag{2.90}$$

$$\bar{l} = \frac{1}{2}\rho v_{\mathrm{res}}^2 c_{\mathrm{i}} C_l(\alpha, M) \tag{2.91}$$

$$\tag{2.92}$$

Of course, the coefficients of lift and drag are still required to calculate the blade element forces. These coefficients are found with experimental aerofoil data which generally are calculated through a series of "look up tables" that are a function of the local angle of attack and Mach number. The local aerodynamic forces are then transformed into the propeller blade element axes, resulting in the following expression representing the force of each propeller blade element

$$\begin{aligned} \mathbf{f}_{\mathrm{p}}^{\mathrm{p.bl.}} &= n_{\mathrm{clock}}(\bar{d}\cos\phi - \bar{l}\sin\phi)\mathbf{j}_{\mathrm{p.bl.}} \\ &+ (-\bar{d}\sin\phi - \bar{l}\cos\phi)\mathbf{k}_{\mathrm{p.bl.}} \end{aligned} \tag{2.93}$$

Or more conveniently expressed as

$$\mathbf{f}_{\mathrm{p}}^{\mathrm{p.bl.}} = f_{\mathrm{x}}^{\mathrm{p.bl.}}\mathbf{i}_{\mathrm{p.bl.}} + f_{\mathrm{y}}^{\mathrm{p.bl.}}\mathbf{i}_{\mathrm{p.bl.}} + f_{\mathrm{z}}^{\mathrm{p.bl.}}\mathbf{k}_{\mathrm{p.bl.}} \tag{2.94}$$

In order to calculate the total force that a propeller blade requires the integration of Equation (2.93). The complex nature of the propeller forces is not amenable to analytical integration, therefore a numerical integration is used. Hence, the force across a propeller blade is described by

$$\mathbf{F}_{\mathrm{prop}}^{\mathrm{p.bl.}} = \int_{R_{\mathrm{cut}}}^{R_{\mathrm{prop}}} \mathbf{f}_{\mathrm{p}}^{\mathrm{p.bl.}} dr \tag{2.95}$$

where R_{cut} is the length of the propeller root cut out. The above equation, Equation (2.95), is limited as it expresses the force that a propeller blade produces at a discrete azimuth position. As the propeller rotates around the propeller hub, both the local velocities and aerodynamic forces vary azimuthally. In order to account for this, the aerodynamic forces that a propeller blade creates is calculated at various azimuth positions. Subsequently, the aerodynamic forces around the azimuth are averaged and then multiplied by the number of propeller blades to yield the total propeller force. Therefore the total force given by the propeller is stated as

$$\mathbf{F}_{\mathrm{prop}}^{\mathrm{p.bl.}} = \frac{N_{\mathrm{b}}}{2\pi} \int_{0}^{2\pi} \int_{R_{\mathrm{cut}}}^{R_{\mathrm{prop}}} \mathbf{f}_{\mathrm{p}}^{\mathrm{p.bl.}} dr d\psi \tag{2.96}$$

This Equation is readily solved with the use of a numerical integration technique. The propeller forces are required to be in body axes so the model can be applied to the Euler rigid body equations. Hence, the total force of the propeller in body axes is given by

$$\mathbf{F}^{\text{body}}_{\text{prop}} = \frac{N_{\text{b}}}{2\pi} \int_{0}^{2\pi} \int_{R_{\text{cut}}}^{R_{\text{prop}}} \left(\mathbf{T}^{\text{body}\to\text{p.d.}}\right)^{T} \left(\mathbf{T}^{\text{p.d.}\to\text{p.bl.}}\right)^{T} \mathbf{f}^{\text{p.bl.}}_{\text{p}} \delta r \delta \psi \tag{2.97}$$

Typically, 20 blade elements and 16 azimuth positions are used when numerically integrating the loads.

Propeller Moments

With the propeller forces derived, the next step is to calculate the external moments the propeller creates around the helicopter's centre of gravity. The total moment vector is a combination of the moments around the propeller hub and the propeller forces acting about the helicopter's centre of gravity. Therefore, the total external moment vector is given by the following

$$\mathbf{M}^{\text{body}}_{\text{prop}} = \mathbf{M}^{\text{body}}_{\text{p.h.}} + \left(\mathbf{r}^{\text{body}}_{\text{c.g.}\to\text{p.h.}} \times \mathbf{F}^{\text{body}}_{\text{prop}}\right) \tag{2.98}$$

The external moment around the propeller's hub, in body axes, can be derived by returning to Equation (2.94), which gives the blade element forces in propeller blade element axes. As the blade elements are not coincident with the propeller hub they produce moments around it, which transmit through to the helicopter's centre of gravity. The moment a blade element produces around the propeller hub in propeller blade element axes is simply

$$\mathbf{m}^{\text{p.bl.}}_{\text{p}} = \mathbf{r}^{\text{p.bl.}}_{\text{p.h.}\to\text{p}} \times \mathbf{f}^{\text{p.bl.}}_{\text{p}} \tag{2.99}$$

In the same manner as the forces, the total moment is obtained by integrating across the blade and around the azimuth. Therefore, the total moment is

$$\mathbf{M}^{\text{p.bl.}}_{\text{p.h.}} = \frac{N_b}{2\pi} \int_{0}^{2\pi} \int_{R_{\text{cut}}}^{R_{\text{prop}}} \left(\mathbf{r}^{\text{p.bl.}}_{\text{p.h.}\to\text{p}} \times \mathbf{f}^{\text{p.bl.}}_{\text{p}}\right) dr d\psi \tag{2.100}$$

Therefore, the total moments around the propeller hub can be expressed in body axes using Equations (2.5) and (2.73), yielding

$$\mathbf{M}_{\text{p.h.}}^{\text{body}} = \frac{N_{\text{b}}}{2\pi} \int_{0}^{2\pi} \int_{R_{\text{cut}}}^{R_{\text{prop}}} (\mathbf{T}^{\text{body}\to\text{p.d.}})^T \; (\mathbf{T}^{\text{p.d.}\to\text{p.bl.}})^T \; (\mathbf{r}_{\text{p.h.}\to\text{p}}^{\text{p.bl.}} \times \mathbf{f}_{\text{p}}^{\text{p.bl.}}) \delta r \delta \psi \tag{2.101}$$

Hence, the contribution of the propeller hub to the pitching, rolling and yawing moments are obtained by Equation (2.101). The propeller torque can be easily extracted from Equation (2.101).

Validation of the Propeller Model

To test the validity of the model, the propeller model is configured to represent "Propeller 5868-9" and compared to Hartman and Biermann's established wind tunnel results [59]. Hartman and Biermann provide the details of "Propeller 5868-9", however the salient information of this type of the propeller is given for the purposes of convenience. The diameter of this propeller is 10 ft, featuring a high level of blade twist. In addition, the propeller features Clark Y aerofoils with the chord distribution varying in a nonlinear manner. The wind tunnel results, presented in Figure 2.13, were obtained at different propeller rotational speeds ranging from 800 - 1200 rpm [59]. These different rotational speeds were modelled in the simulation results. Figure 2.13(a) compares the thrust coefficients with the propeller advance ratio J, for various operating conditions. These various conditions correspond to different advance ratios with different propeller twist settings which are denoted by β. The comparison between the thrust coefficients and advance ratios is very good, particularly at low advance ratios, highlighting the effectiveness of the propeller model. In addition, Figure 2.13(b) compares the power coefficients with the different advance ratios between the propeller model and the wind tunnel results. Again, the results are encouraging with the propeller model providing a good approximation to the amount of power required at the given operating condition. As a whole, the agreement between the propeller model and the wind tunnel results is very good for multiple operating conditions. Therefore it is reasonable to assume that the propeller model is capable of providing results of sufficient validity that meaningful conclusions can be drawn.

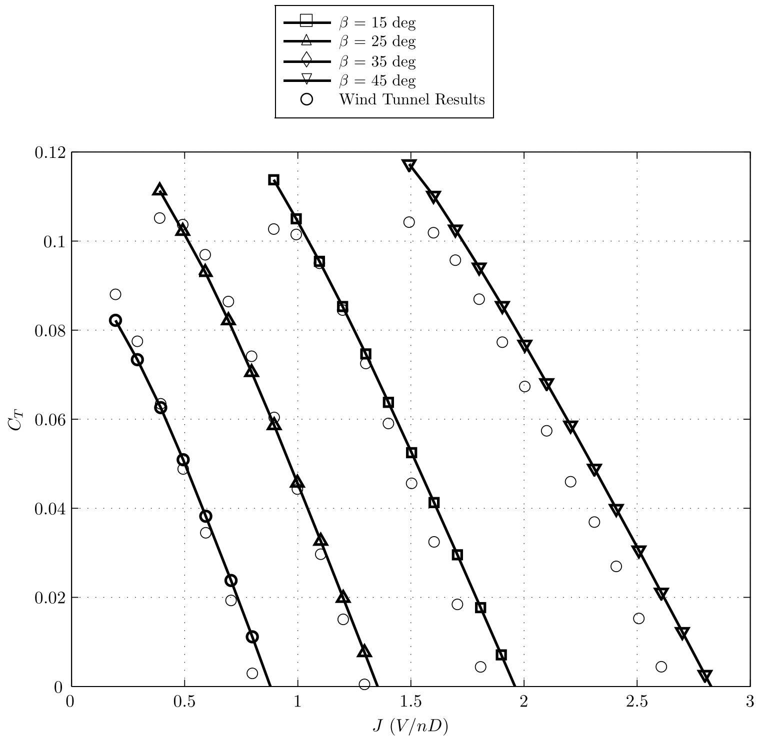

(a) C_T v J

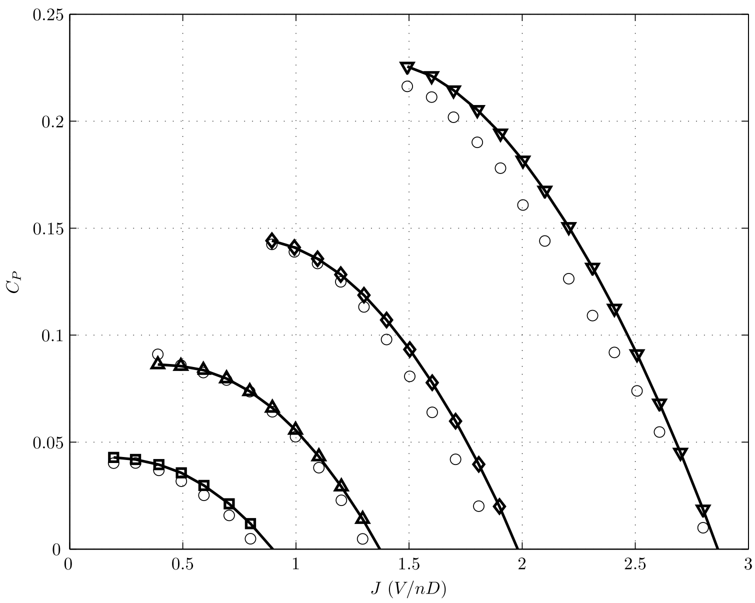

(b) C_P v J

Figure 2.13: Comparison of the Propeller Model and Wind Tunnel Results from Hartman and Biermann [59]

2.7 Wing Model

Overview of the Wing Model

Strip-theory, as described by Sequiera et.al [60] and Dreier [61], is an approach to model an aircraft's wing, whereby the wing planform is split into strips and the forces and moments of each strip are computed. The local forces and moments are then integrated in order to determine the total force and moment around the helicopter's centre of gravity position. Strip-theory is a well-established modelling method with some known features. Some of the assumptions made in the wing model are

- It is assumed that each strip does not influence another strip.
- Aerodynamic interactions between the fuselage and wing root are not considered.
- Spanwise flow is not modelled.
- The wing assumed to be rigid.

Fundamentally, strip-theory assumes that the aerodynamics forces acting at each strip of the wing are the same as if the portion of the wing were part of an infinite two-dimensional wing [62]. The basic strip-theory modelling approach does not faithfully model 3-D effects, such as the tip vortex which forms due to the pressure difference between the upper and lower surfaces at the wing tip. One consequence of this vortex, on a finite wing, is that the spanwise lift distribution tends to zero at the wing tip. Essentially, there is a reduction of circulation towards the wing tip due to the effect of the vortex. The other effect of the pressure difference at the wing tip is the formation of a trailing edge vortex system which creates additional drag. The standard form of strip-theory does not model this induced drag component, although the wing model presented in the following does include a term to predict the induced drag.

Before, proceeding to discuss the development of the wing model, it is worth noting that no validation results of the wing model are presented in this section. Since strip-theory is a well-established method, which is used by various researchers, then it is fair to postulate that the model will produce reasonable results. The wing model results were not validated as such but the results from the model where verified by testing the model experimentally. For example, at high speeds and at a moderate angle of attack the wing's lift to drag ratio seemed reasonable. From that condition the angle of attack was increased to an excessive amount, approximately 16°, to model wing stalling. As one would expect, the wing model predicted a reduction in wing lift and a significant increase of wing drag due to wing stalling. Therefore it was concluded that wing model was shown to model the fundamental behaviour of a wing. Further testing and validation of the wing model was not considered as it was decided that the model was of sufficient fidelity to capture the broad behaviour of a wing.

Kinematics of a Wing Strip

To derive the forces and moments of a given wing strip, it is necessary to calculate the local velocity at each strip. The model assumes a simple 2-D representation of the airflow and that the aerodynamic forces, lift and drag, act at the quarter chord of each strip. With reference to Figure 2.14, the position of the quarter chord position of a given wing strip relative to the centre of gravity is

$$\begin{aligned} \mathbf{r}^{\text{body}}_{\text{c.g.}\to\text{w}} &= (l_w + x_{c.g.} - (w_w + y_i)\tan\epsilon)\,\mathbf{i}_\text{b} && (2.102)\\ &+ (w_w + y_i)\,\mathbf{j}_\text{b} && (2.103)\\ &+ (-h_w + (w_w + y_i)\tan\eta)\,\mathbf{k}_\text{b} && (2.104) \end{aligned}$$

where, l_w is the length from the reference point to where the quarter chord position would meet the centreline of the fuselage. The width between the fuselage centreline and where the wing meets the fuselage is denoted by w_w. The term y_i is the distance, in the $\mathbf{j_b}$ direction, from the position of where the wing meets the fuselage to the mid-point of each wing blade element. The angle η is the anhedral angle of the wing. Equation (2.104) can be expressed in the more compact form of

$$\mathbf{r}^{\text{body}}_{\text{c.g.}\to\text{w}} = r^{\text{body}}_{\text{x}}\mathbf{i}_\text{b} + r^{\text{body}}_{\text{y}}\mathbf{j}_\text{b} + r^{\text{body}}_{\text{z}}\mathbf{k}_\text{b} \tag{2.105}$$

In terms of velocity, the general expression for the absolute velocity of a point relative to a rotating axes set, the velocity of a given wing strip, in body axes is

$$\mathbf{v}^{\text{body}}_{\text{w}} = \mathbf{v}^{\text{body}}_{\text{c.g.}} + (\boldsymbol{\omega}^{\text{body}} \times \mathbf{r}^{\text{body}}_{\text{c.g.}\to\text{w}}) + \frac{d\mathbf{r}^{\text{body}}_{\text{c.g.}\to\text{w}}}{dt} \tag{2.106}$$

In its complete form, the velocity of a given wing strip in body axes is

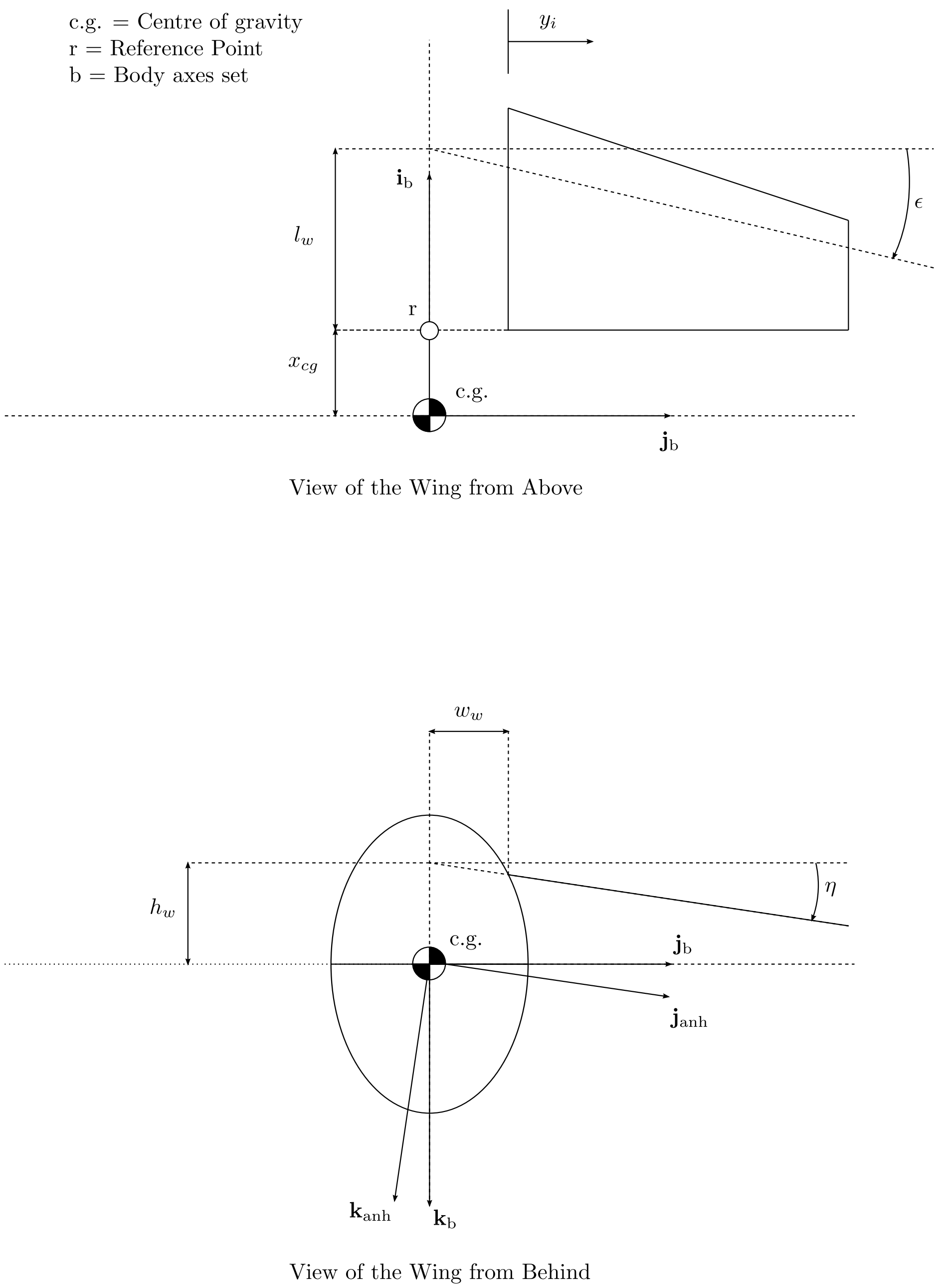

Figure 2.14: Two Views Showing the Position of the Wing with Respect to the Centre of Gravity Position

$$\mathbf{v}_\mathrm{w}^\mathrm{body} = \left(U + Qr_\mathrm{z}^\mathrm{body} - Rr_\mathrm{y}^\mathrm{body}\right)\mathbf{i}_\mathrm{b} \tag{2.107}$$

$$+ \left(V + Rr_\mathrm{y}^\mathrm{body} - Pr_\mathrm{z}^\mathrm{body}\right)\mathbf{j}_\mathrm{b} \tag{2.108}$$

$$+ \left(W + Pr_\mathrm{y}^\mathrm{body} - Qr_\mathrm{x}^\mathrm{body} - kv_0\right)\mathbf{k}_\mathrm{b} \tag{2.109}$$

In the hover, the rotor wake induces an aerodynamic download to the wing, thereby reducing low speed performance [63, 64]. This was observed in the development of the tilt-rotor aircraft with the aerodynamic download being as high as 15% of the total rotor thrust [24]. However, it was demonstrated that this value could be reduced with the addition of flaps to the wing, which when deployed reduce the wing's wetted area in low speed flight [65]. To model this download, Equation (2.109) includes the kv_0 term to represent the contribution of the main rotor's wake to the local velocity of each wing strip. The term, v_0 represents the mean induced velocity of the main rotor disc whereas k is an empirical factor. In this work, k is assumed to be a constant value of 1.5 to match the 10% hover download which was measured by Felker and Light in the experimental testing of the wing download of the V-22 [24]. Although k is assumed to be constant it is acknowledged that in reality it is likely to vary with flight speed as the rotor wake skews backwards with increasing forward speed. To date, there is a limited amount of data which documents the influence of the main rotor on a wing in forward flight. There is information in the literature regarding the interactions between the tilt-rotor and its wing [24, 63, 65, 66]. However, the local aerodynamic environment, in forward flight, across a tilt-rotor's wing will be different to that of a compound helicopter's wing. This is mainly due to the position of the rotor hub relative to the wing. With a tilt-rotor aircraft, the rotor hub is tilted forward in high speed flight, effectively converting the tilt-rotor to a fixed wing aircraft. In contrast, with perceived compound helicopter designs the rotor hub position will be fixed so that the oncoming flow to the rotor is in an edgewise direction. Therefore, due to the absence of any established wind tunnel or flight tests results, the current wing model assumes that the product of the empirical factor, k and the uniform induced component of the main rotor's wake affects the wing. Additionally, there is a lateral component of the rotor wake which consequently results in the port wing, for a main rotor rotating anti-clockwise when viewed from above, creating more lift than the starboard wing [9]. This was one conclusion drawn from the NH-3A flight test programme, however it was noted that the differential wing lift did not affect the control characteristics of the aircraft [67] and therefore has not been included within this wing model.

The velocity components of a point on the wing have been determined, however another axes system is introduced to take into account the anhedral angle's effect on the local velocities. The introduction of this axes set allows the wing model to be used as a tailplane or fin model, if required, which can be achieved by the appropriate selection of the anhedral angle η and determination of the position vector relative to the body axes set. The transformation between body and anhedral axes is

$$\mathbf{T}^{\text{body}\to\text{anh}} = \begin{bmatrix} 1 & 0 & 0 \\ 0 & \cos\eta & \sin\eta \\ 0 & -\sin\eta & \cos\eta \end{bmatrix} \tag{2.110}$$

Hence, the local velocities at point w on the wing, in anhedral axes, is

$$\mathbf{v}_{\text{w}}^{\text{anh}} = \mathbf{T}^{\text{body}\to\text{anh}}\mathbf{v}_{\text{w}}^{\text{body}} \tag{2.111}$$

or simply written as

$$\mathbf{v}_{\text{w}}^{\text{anh}} = u^{\text{anh}}\mathbf{i}_{\text{anh}} + v^{\text{anh}}\mathbf{j}_{\text{anh}} + w^{\text{anh}}\mathbf{k}_{\text{anh}} \tag{2.112}$$

Wing Forces and Moments

Figure 2.15 shows the aerodynamic forces, with the lift force acting perpendicular to the direction of the airflow whereas the drag force acts in the same direction as the airflow. The lift and drag forces, per unit span, as well as the pitching moment of the given strip are mathematically stated as

$$\bar{l} = \frac{1}{2}\rho {v_{res}}^2 c(y) C_l(\alpha, M) \tag{2.113}$$

$$\bar{d} = \frac{1}{2}\rho {v_{res}}^2 c(y) C_d(\alpha, M) \tag{2.114}$$

$$\bar{m} = \frac{1}{2}\rho {v_{res}}^2 c(y)^2 C_m(\alpha, M) \tag{2.115}$$

where the wing chord varies along the span and v_{res} is the magnitude of velocity vector shown in Equation (2.112). To model the induced drag of the wing an additional term, denoted by C_{D_i}, is added to Equation 2.114. This term is only added to the wing strip closest to the wing tip and approximates the drag of the wing due to the formation of the tip vortex. This induced drag component is given by

$$C_{D_i} = \frac{\bar{C}_L^2}{\pi\epsilon' AR} \tag{2.116}$$

where $\bar{C}_L$ is the mean lift coefficient of the entire wing, ϵ' is the Oswald efficiency factor and AR is the aspect ratio of the wing. In order to determine the lift and profile drag coefficients of each wing strip, the local angle of attack is required. From Figure 2.15, the local angle of attack is the addition of the fixed pitch incidence, θ_{fix}, and the angle, ϕ, as well as accounting for spanwise twist. The twist distribution across the wing span is a function of y_i and can vary in a linear or nonlinear manner. Hence, the local angle of attack is

$$\alpha = \theta_{fix} + \phi + \theta_{twist}(y) \tag{2.117}$$

where

$$\phi = \tan^{-1}\left(\frac{w^{\text{anh}}}{u^{\text{anh}}}\right) \tag{2.118}$$

Clearly, the aerodynamic forces of each wing strip are strongly influenced by the the aerodynamic coefficients. The aerodynamic coefficients of lift, drag and pitching moment are a function of the local angle of attack, given by Equation (2.117), as well as the physical properties of the aerofoil section. For the purposes of modelling, the aerodynamic coefficients can be obtained through a series of "look up tables" which are derived through the experimental testing of the particular aerofoil section. For a wing operating in the hover, the angle of attack of each wing strip will be close to

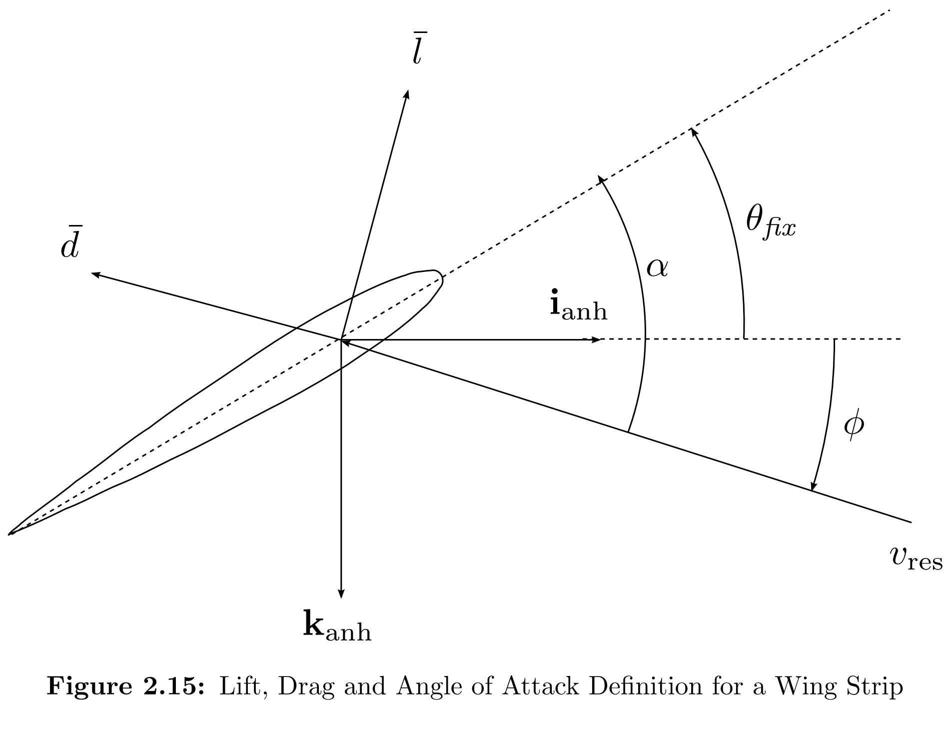

Figure 2.15: Lift, Drag and Angle of Attack Definition for a Wing Strip

-90^o (assuming there is no fixed pitch incidence relative to the fuselage). Hence, in the hover and at low speeds, the wing will create negative lift acting in the opposite direction of the rotor thrust and thus providing an aerodynamic download. As forward speed increases, the angle of attack will also increase and reach a flight regime whereby the wing is operating at more aerodynamically efficient angle of attack, consequently producing a lifting force. To model the download of the wing in the hover and at low speeds it would seem appropriate to use aerofoil sections which aerodynamic data exists at high angles of attack. For this reason the NACA 0012 aerofoil is used due the availability of aerodynamic coefficients at high angle of attack [68].

The previous discussion derived the aerodynamics forces at each wing strip. However, these expressions for the lift and drag forces are in wind axes and therefore are required to be transformed into body axes. The orientation of the wind and body axes are shown in Figure 2.15, with the transformation between the two axes set being

$$\begin{bmatrix} \mathbf{i}_{\text{anh}} \\ \mathbf{k}_{\text{anh}} \end{bmatrix} = \begin{bmatrix} \sin\phi & -\cos\phi \\ -\cos\phi & -\sin\phi \end{bmatrix} \begin{bmatrix} \bar{l} \\ \bar{d} \end{bmatrix} \tag{2.119}$$

Therefore, using Equations (2.113), (2.114), (2.119) the force, per unit span, acting at each wing strip is

$$\mathbf{f}_{\text{w}}^{\text{anh}} = \left(\frac{1}{2}\rho {v_{res}}^2 C_l c(y)\sin\phi - \frac{1}{2}\rho {v_{res}}^2 C_d c(y)\cos\phi\right)\mathbf{i}_{\text{anh}} \tag{2.120}$$

$$+\left(-\frac{1}{2}\rho {v_{res}}^2 C_l c(y)\cos\phi - \frac{1}{2}\rho {v_{res}}^2 C_d c(y)\sin\phi\right)\mathbf{k}_{\text{anh}} \tag{2.121}$$

which can be expressed in the more compact form of

$$\mathbf{f}_{\text{w}}^{\text{anh}} = x^{\text{anh}}\mathbf{i}_{\text{anh}} + y^{\text{anh}}\mathbf{j}_{\text{anh}} + z^{\text{anh}}\mathbf{k}_{\text{anh}} \tag{2.122}$$

Subsequently, the total force the starboard wing produces is obtained by integrating the local wing strip element forces across the wing span

$$\mathbf{F}_{\text{wing}}^{\text{body}} = \int_{w_{\text{w}}}^{\frac{b}{2}} \left(\mathbf{T}^{\text{body}\rightarrow\text{anh}}\right)^T \mathbf{f}_{\text{w}}^{\text{body}} dy \tag{2.123}$$

which is then numerically integrated to calculate the wing's contribution to the overall body forces.

Wing Moments

The wing moment of a given wing strip, in anhedral axes, is given by the following

$$\mathbf{m}_{\mathrm{w}}^{\mathrm{anh}} = \left(\mathbf{r}_{\mathrm{c.g.}\to\mathrm{w}}^{\mathrm{anh}} \times \mathbf{f}_{\mathrm{w}}^{\mathrm{anh}}\right) \tag{2.124}$$

plus the addition of the wing's own contribution to the overall aircraft pitching moment. Hence the wing strip moment in body axes is

$$\mathbf{m}_{\mathrm{w}}^{\mathrm{body}} = \left(\mathbf{T}^{\mathrm{body}\to\mathrm{anh}}\right)^{T} \mathbf{m}_{\mathrm{w}}^{\mathrm{anh}} \tag{2.125}$$

The entire wing's contribution to the rolling, pitching and yawing moments of the body axes are readily obtained by the integration of Equation (2.125), therefore the aerodynamic moments acting on one wing in body axes are

$$\mathbf{M}_{\mathrm{wing}}^{\mathrm{body}} = \int_{w_w}^{\frac{b}{2}} \mathbf{m}_{\mathrm{w}}^{\mathrm{body}} dy \tag{2.126}$$

2.8 Discussion of Model Validity

The preceding sections have described the development of various models which could potentially feature on a compound helicopter design. However, one question that naturally arises with the development of these mathematical models is their validity and if the results from these rotorcraft models would replicate the real aircraft. In terms of the conventional helicopter, inverse simulation results have shown good correlation for a range of manoeuvres [42] giving confidence in the value of the results produced by the HGS model. The limitations of this type of model are well understood [36] and include the inability to accurately capture off-axis effects and low fidelity at the edges of the flight envelope where, for example, aerodynamics are highly nonlinear. In relation to the compound helicopter models, it is appreciated that a strict validation based on the comparison of flight test with simulation results is not possible as these are hypothetical vehicles. Hence, due to the absence of available flight test data, the modelling approach in this study is to take an established conventional helicopter model and assume that the addition of validated propeller, wing and coaxial rotor models will produce realistic results.

One important limitation of the rotor model is its inability to model nonlinear aerodynamics. At very high speeds it is important to model nonlinear aerodynamics [28], such as reverse flow, as a large portion of the local airflow across the retreating side of the disc will travel from the trailing to the leading edge of the rotor blades. The current rotorcraft model does not model this nonlinear aerodynamic phenomenon and it is reasonable to expect that this limitation could produce unrealistic results at very high flight speeds. Hence, the flight mechanics analysis in this Thesis is restricted to speeds under 200kt, where the modelling assumptions within the main rotor are still considered valid. Although compressibility effects are not modelled, the issue is attenuated by reducing the rotorspeeds of the main rotor systems of the compound helicopter configurations, above 130kt. This reduction of rotorspeed is required as the local Mach number of the advancing blade tip would approach unity, if uncorrected, leading to the formation of shock waves, thereby resulting in a significant increase of drag [69]. Therefore the current work does not assess the flight mechanics of the compound helicopters at the edge of their perceived flight envelopes. Although the compound helicopter is capable of reaching speeds in the region of 250kt, it is still important to understand and quantify the flight dynamics of this aircraft class within the selected speed range where the aircraft will still spend a significant amount of time operating.

Although high speed helicopter designs are being taken seriously, Harris points out there still remains a challenge in successfully modelling the main rotor above an advance ratio of 0.62 [70]. Harris highlights that this is due to a lack of accuracy in the aerodynamic forces in the reverse flow region and the influence of blade torsional deflections [70]. In addition, Hodara and Smith illustrated that at high advance ratios spanwise flow (or "crossflow") across a rotor blade element becomes important [71]. Their study showed that this must be taken into account in the prediction of the local aerodynamic coefficients. This approach improved the aerodynamic predictions of the main rotor but it is clear that successfully modelling helicopters at high advance ratios still presents a formidable challenge. For these reasons and to expect reasonable results, the maximum speed of the compound helicopter configurations is restricted to 200kt, corresponding to an advance ratio of 0.6 for the CCH configuration.

The approach taken with this study is to use the HGS package, with the limitations discussed previously, to assess the flight mechanics of the compound helicopter configurations. In terms of the sophistication of the main rotor modelling, Padfield conveniently splits the level of fidelity into three categories: level 1, level 2 and level 3 [36]. Level 1 represents a low fidelity approach to the main rotor modelling whereas level 3 describes high level rotor modelling [36]. There are comprehensive rotorcraft codes which have been developed which fall into Padfield's level 3 category [36], examples of which are the CAMRAD II [72] and NASA/US Army GENHEL codes [73], that use high level simulation techniques. These high fidelity rotorcraft simulations are predominately used in studies which focus on rotor design, vibration and the main rotor's stability [36]. In contrast, lower fidelity modelling techniques have found use in flight mechanics and flying qualities research [36]. Commonly, in terms of rotorcraft performance simple methods have been used, with Stepniewski and Keys, Cooke, Fitzpatrick, Prouty and Leishman all providing analytical methods to quantify helicopter performance in their standard helicopter textbooks [1, 7, 74, 75]. These methods include momentum and blade element theories which can provide some good predictions of rotorcraft performance. The modelling in this study is not as basic as many of the methods described in these textbooks but neither is it as detailed as the modelling featured in some comprehensive rotorcraft codes. Hence, the modelling used in this work can perhaps be described as a reasonable compromise between these two extremes given the aims of the work. Comprehensive codes have been used in compound helicopter design studies [27, 28] where the aircraft was designed to operate at a speed in the region of 240kt. It is clear that high level modelling is required in this flight regime where accurate modelling of yawed flow, reverse flow and compressibility effects become critical [76]. However, with the assumption that 200kt is the compound helicopter's boundary, it is fair to expect realistic results from the level of modelling used within this study.

2.9 Chapter Summary

The primary aim of this Chapter was to enhance the HGS package so that compound helicopter configurations could be successfully modelled. Perceived compound helicopter designs are likely to feature wings, propellers and potentially a coaxial rotor. The established HGS package was capable of modelling conventional helicopters but it was evident that further models were required to simulate compound helicopters. Hence, the HGS package was enhanced by the addition of coaxial rotor, propeller and wing models. Each of these components can be placed on the airframe at a given position and orientation. Therefore the existing HGS package coupled with the newly developed coaxial rotor, propeller and wind model is capable of modelling a wide variety of rotorcraft configurations. The main conclusions from this Chapter are as follows:

- The single main rotor model has been amended to successfully simulate a coaxial rotor arrangement. Although there are some fundamental assumptions regarding the aerodynamic interactions between the upper and lower rotors, the coaxial rotor model has compared favourably with established wind tunnel results.
- Additionally, a blade element based propeller model has been developed to simulate the addition of thrust compounding to the helicopter design. The propeller model has been validated with established wind tunnel results giving confidence to the worth of the propeller model's results.
- As potential compound helicopter designs may feature a wing to reduce rotor loading at high speeds a strip-theory wing model has been developed.
- The Chapter finished by discussing the limitations of the modelling approach and the flight conditions where accurate results can be expected. It was highlighted due to the limitations of the modelling, particularly within the main rotor model, that unrealistic results could be expected at very high speeds. Therefore, the compound helicopter configurations are not assessed at the edge of their perceived flight envelopes but within the speed range of hover to 200kt, where the assumptions made in the rotor model are still considered valid. Although the compound helicopter is capable of reaching speeds in the region of 250kt, it is still important to understand and quantify the flight mechanics of this aircraft class within the selected speed range where the aircraft will still spend a significant amount of time operating.

Chapter 3

Compound Helicopter Configurations

3.1 Introduction

The previous chapter, Chapter 2, detailed the development of a simulation package to model advanced rotorcraft configurations. This package is capable of simulating a wide variety of vehicles which feature compounding. Naturally, the next step is to use this simulation package to model compound helicopter configurations. To this end, the aims of this Chapter are two-fold. The first aim is to select compound helicopter configurations and choose the design parameters of the vehicle. With the compound helicopter configurations developed, the next aim is to trim the flight model. The task of trimming the model is basically to calculate the control angles which hold the given aircraft configuration in steady level flight. As a result, it is generally the starting point of any meaningful analysis of an aircraft mathematical model. Once a flight model is trimmed then the vehicle's performance, stability and manoeuvrability can be assessed.

As discussed in Chapter 1, various compound helicopter prototypes have been flown. Each of these configurations have different layouts and there seems to be no general consensus on where the thrust and lift compounding device should be located on the compound helicopter's airframe. For example, the pusher propeller of the Lockheed Cheyenne was located at the rear of the aircraft next to the tail rotor, Figure 1.1(f). In contrast, the two propellers of the Eurocopter X^3, which is shown in Figure 1.2, are located on either side of the aircraft's fuselage. Another issue is the types of compounding that are used on the aircraft. The ABC helicopter, Figure 1.1(h), only featured thrust compounding whereas the Lockheed Cheyenne featured both thrust and lift compounding. Another example is the S-67 compound helicopter which only featured lift compounding [13]. Clearly, there are several potential configuration options, all of which have advantages and disadvantages, which could be used in the design of a compound helicopter [29].

As there are a number of the potential compound configurations, it is necessary to decide on which aircraft layouts to focus on, within this study. Recall that the primary aim of this Thesis is to determine how the addition of compounding influences the flight dynamics characteristics of the compound helicopter. Since the work is not a design exercise, it seems appropriate to focus on a small number of compound helicopter configurations, in this case two, so that their flight dynamics attributes can be comprehensively assessed. The only remaining question is the types of compound helicopter design which should be assessed. This decision is made by examining the compound helicopter designs which are being taken seriously by the major helicopter manufacturers at the time of writing this Thesis. With this qualifying criterion, the aircraft configurations which seem appropriate are the Sikorsky X2 and the Eurocopter X^3, as both prototype vehicles have been recently flying. The results from the flight tests of these two vehicles were promising. In particular, the results of the Sikorsky X2 programme were so successful that Sikorsky are taken this concept to the next level by developing the Sikorsky S-97 Raider. The Sikorsky S-97 Raider is envisioned to be a multi-role aircraft which can complete various military missions including close-air support and armed reconnaissance. Sikorsky plan to flight test the Sikorsky S-97 in 2015.

It is interesting to note the different approaches taken by Sikorsky and Eurocopter (now Airbus Helicopters) in their attempts to develop a successful compound helicopter. Sikorsky have flight tested the Sikorsky X2, which is largely based on the XH-59A aircraft, which was initially developed in the 1960's. Both of these aircraft use the ABC coaxial rotor design. The fundamental idea behind this concept is that the lift potential on the advancing sides of the rotor discs are realised in high speed flight [18]. In high speed flight, the two rotors provide significant rolling moments around the rotor hub as the advancing sides of the discs produce much greater lift than the opposing retreating sides. However, the overall hub rolling moment trim is achieved as the upper and lower rotors provide rolling moments equal in magnitude but in opposing directions. This was achieved on the XH-59A aircraft by two methods. Firstly, by variable phase angle control which alters the azimuth position where the cyclic controls change the rotor blade pitch [18]. Secondly, by the introduction of a differential lateral cyclic control to promote greater loading across the advancing sides of the discs in high speed flight [18].

Although the ABC rotor system used on the XH-59A allowed the aircraft to reach high speed flight, one of the drawbacks was the high vibration levels [77]. Additionally, there were also problems with reducing the coaxial rotor's rotational speed to the necessary levels in high speed flight as well as the disappointing aerodynamic efficiency of the coaxial rotor [78]. These problems ended the ABC test programme, however recently the ABC design has been resurrected. Sikorsky believe that the experience gained in the previous test programmes of the ABC rotor, added with modern rotor technology through the use of advanced aerofoil sections and active vibration control [33, 34], will result in a compound helicopter design that can potentially satisfy the emerging requirements placed on the next generation of rotorcraft.

In contrast, the wings of the Eurocopter (now Airbus Helicopters) X3 offload the rotor at high speeds and the propellers provide the propulsive force to overcome the airframe drag. The two propellers, which are mounted on either side of the aircraft's fuselage, provide the yaw control of the vehicle so that a tail rotor is not required. In high speed flight, the anti-torque responsibilities are shifted to the fin at the rear of the aircraft which is capable of producing a significant sideforce due to the velocity of the local airflow. This aircraft design has been flight tested with recent publications reporting that the Eurocopter X^3 is able to reach a maximum speed of 232kt. It is therefore evident that these helicopters are capable of greater speeds than their conventional counterparts.

With the decision made that the compound helicopter configurations will be similar to the Sikorsky X2 and Eurocopter X^3, the next challenge is to determine the configuration data of the two compound helicopter configurations. Unfortunately, the configurational data of the Sikorsky X2 and Eurocopter X^3 are not openly available. Therefore, the strategy for this work is to use an established mathematical model of a conventional helicopter (in this case the AgustaWestland Lynx), then convert this configuration to represent compound helicopter configurations, which are similar to the Sikorsky X2 and Eurocopter X^3. The Lynx was chosen as a well established data set [36] and model was available [39]. Another reason for the choice of the Lynx is that it features a semi-rigid rotor which is likely to be used in a compound helicopter design [26]. The primary advantage of the semi-rigid rotor is its ability to generate powerful moments independent of the amount of rotor thrust. This feature is particularly suited to a winged compound helicopter design as the wing offloads the main rotor in high speed flight. Therefore, the application of a rigid rotor would allow the aircraft to be controlled, by the main rotor, despite the low levels of rotor loading expected in high speed flight [19]. The first compound configuration is referred to as

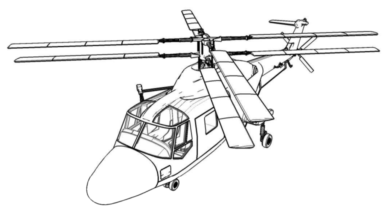

(a) Coaxial Compound Helicopter Sketch

(b) Hybrid Compound Helicopter Sketch

Figure 3.1: Sketches of the two Compound Helicopter Configurations

the Coaxial Compound Helicopter (CCH) configuration which features a coaxial rotor and a pusher propeller as seen in Figure 3.1(a). The second configuration is known as the Hybrid Compound Helicopter (HCH) configuration which features a wing and two propellers, as seen in Figure 3.1(b). These two compound configurations are changed as little as possible, relative to the baseline configuration, to allow for a fair and direct comparison between the results of the compound configurations and the baseline (BL) configuration. The end result is three aircraft configurations with identical fuselage aerodynamics, mass and moments of inertia values. Therefore, unless explicitly stated, the design features of the compound helicopter configurations are identical to that of the conventional Lynx helicopter. The result is two rather unusual looking vehicles, Figures 3.1(a) and 3.1(b). It is important to reinforce that this Thesis is not a design exercise where the weights, vehicle shape, moments of inertia, powerplant are all sized to fulfil a particular mission requirement. The main reason why this approach isn't adopted is to ensure that the effects of compounding are isolated from other design factors, so that the flight mechanics results between the three aircraft configurations are exclusively due to the introduction of thrust and lift compounding. Consequently, the work presented throughout this Thesis should not be classed as a design exercise but a flight mechanics investigation to determine the broad effects of compounding. Hence, all of the results presented in the Thesis should be viewed in this context. It is acknowledged that the results from this work could be supplemented in future studies with a parametric study of the compound helicopter design which would examine various design parameters and their effects on the helicopter's flight behaviour.

3.2 Preliminary Design of the Configurations

Coaxial Compound Helicopter (CCH) Configuration

Although this is not a design exercise, by altering the BL configuration to represent compound helicopter configurations it is necessary to size certain elements of the vehicle's design. Table 3.1 presents the important design parameters of the main rotors of the BL and CCH configurations. The main rotor of the AgustaWestland Lynx, the BL configuration, is obtained from a dataset which is in the open literature [36]. Concerning the CCH configuration, the coaxial rotor is sized similarly to that of the coaxial rotor used on the XH-59A helicopter with some available data [32, 79]. This approach is justified as the mass of the XH-59A helicopter is similar to that of the AgustaWestland Lynx. The design parameters of the coaxial rotor are shown in Table 3.1 and are chosen to match the XH-59A aircraft. Hence, the rotor solidity, rotorspeed and twist are identical to that featured on the XH-59A. The structural properties of the coaxial rotor blades, the spring stiffness and the flap moment of inertia are calculated to correspond with the data reported in the literature [32, 79]. For example, the spring stiffness of the coaxial rotor is 220500 N.m/rad which is selected to match the high flapping frequency of the XH-59A helicopter. One inherent feature of the ABC design is that the coaxial rotor features very stiff rotor blades [35] to carry the significant structural load due to the lifting duties of the two rotors shifting towards the advancing sides of the rotor discs, in high speed flight. One of the advantages of this design is that the vertical separation between the rotors is kept reasonably small to ensure a compact design. A large vertical separation creates some issues by exposing the shaft and control linkages resulting in an increase in parasitic drag at high speeds. Another concern is that a large separation distance would result in the upper rotor creating excessive moments due to the increased distance between its tip path plane and the centre of mass. Also note that the rotor blades are spaced 0.2R apart, which is typical of coaxial rotors, to account for the lateral flapping of the two rotor discs [38]. In terms of the empennage design, the fin's chord is orientated so it is parallel with the fuselage's centre-line. Generally, the fin is angled to offload the tail rotor at high speed but this is not required in the CCH configuration as the upper and lower rotors provide the torque balance.

The fundamental design of the CCH configuration is based on the ABC demonstrator aircraft. This aircraft configuration is unique as it uses the "lateral lift offset" concept to fully realise the lifting capability of the advancing side of the rotor discs [18]. Figure 3.2 compares a conventional single main rotor and the coaxial rotor ABC (or

Design Parameter	Symbol	BL Configuration	CCH Configuration
Rotor Radius	R	6.4m	5.49m
Rotorspeed	Ω	35.8 rad/s	35 rad/s
Spring Stiffness	K_β	166352 N.m/rad	220500 N.m/rad
Number of Blades	N_b	4	6
Rotor Solidity	σ	0.077	0.127
Lock Number	γ	7.12	5.41
Shaft Tilt	γ_{sh}	3 deg	3 deg
Flap Moment of Inertia	I_β	678 kg.m^2	450 kg.m^2
Twist Gradient	θ_{twist}	-8.02 deg	-10 deg

Table 3.1: Main Rotor Design of the BL and CCH Configurations.

lateral lift offset) concept. With a single main rotor, see Figure 3.2(a), the lift distribution across the advancing and retreating sides of the rotor disc must be equal to provide roll hub trim. As the flight speed increases, a single main rotor without any other source of lift compounding, is incapable of maintaining roll hub trim due to the onset of retreating blade stall. In contrast, the ABC concept uses a coaxial rotor to overcome this limitation of the single main rotor, see Figure 3.2(b). At high speeds, the lifting duties of the rotor system are transferred to the advancing sides of the rotor discs [18], thereby offloading the retreating sides of the rotor discs. In high speed flight the upper rotor produces a negative rolling moment whereas the lower provides a positive rolling moment, with the net effect of roll hub trim. This design therefore overcomes the aerodynamic limitations of a conventional single main rotor which allows a helicopter featuring the ABC rotor system to obtain speeds that surpass a typical helicopter. The lateral lift offset was achieved on the XH-59A aircraft by variable phase angle control or by the introduction of a differential lateral cyclic control to promote greater loading across the advancing sides of the discs in high speed flight [18]. This study uses a differential lateral cyclic control on the aircraft to fulfil the lift potential of the advancing sides of the discs at high speeds. Therefore, the differential lateral cyclic control, $\theta_{1c_{diff}}$ is used to match the lateral lift offset value, which is defined by Yeo and Johnson [80] as

$$LOS = \frac{\Delta M_x}{TR} \tag{3.1}$$

where ΔM_x is the upper rotor rolling moment, R is the rotor radius and T is the total rotor thrust. In high speed flight, LOS is selected to promote greater loading across the

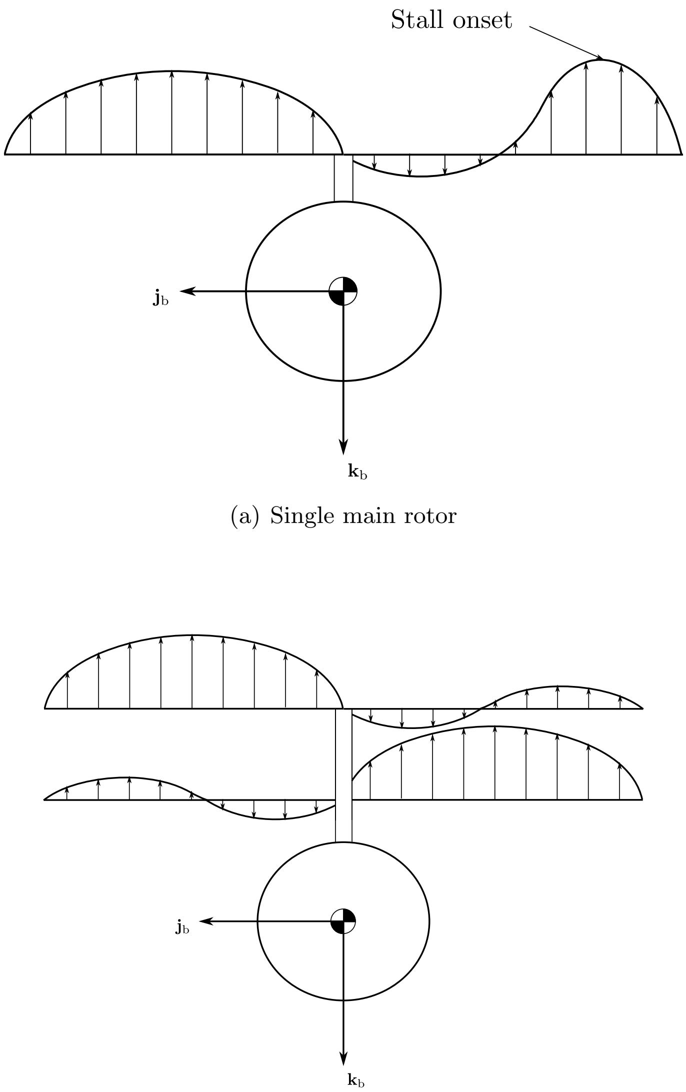

(a) Single main rotor

(b) ABC Concept

Figure 3.2: Typical lift distribution comparison between a single main rotor and the ABC concept, reproduced from [54]

advancing sides of the rotor discs thereby offloading the retreating sides of the discs.

In addition to the differential lateral cyclic control, a differential collective control is introduced that allows the pilot to yaw the helicopter. The upper and lower rotor collectives take the form

$$\theta_u = \bar{\theta}_0 + \theta_{diff} \tag{3.2}$$

$$\theta_l = \bar{\theta}_0 - \theta_{diff} \tag{3.3}$$

Hence, a positive differential collective input increases the blade incidence of the upper rotor whereas it has the opposite effect on the lower rotor, having the net effect of yawing the helicopter's nose to the right. The tail rotor control is replaced by a differential control, θ_{diff}, and a propeller collective control, θ_{prop}, is also introduced resulting in a total of six controls. As a result, control redundancy is present within this helicopter configuration. Another design issue is the sizing of the propeller with Table 3.2 showing the chosen design parameters of the propeller. The rotational speed is chosen to provide a high airflow velocity over the propeller blades without compressibility effects becoming an issue at high speeds. The propeller also features Clark Y aerofoils along the span with a high level of twist so that each propeller blade element operates at a favourable angle of attack [58].

Design Parameter	CCH Configuration
R_{prop}	1.3m
Ω_{prop}	162 rad/s
θ_{twist}	-30 deg
σ_{prop}	0.2
$\mathbf{x}_{\text{prop}}$	(-7.66, 0, 0)m

Table 3.2: Propeller Design of the CCH Configuration.

A design concern with compound helicopters is that compressibility effects at the advancing blade tip can be an issue in high speed flight. If the Mach number of the advancing blade tip approaches unity, then a portion of the local airflow becomes supersonic leading to the formation of shock waves, thereby resulting in a significant increase of drag [69]. The solution is to slow the main rotor at high speeds, for example the Sikorsky X2's coaxial rotor is slowed by 20% at high speeds [34]. In a design analysis of a compound helicopter, Yeo and Johnson slowed the main rotor considerably, from a blade tip speed of 750ft/s in hover to 502ft/s in the helicopter's cruise condition of 250kt, so that the advancing tip Mach number was 0.8 in cruise [28]. With the assumption that 200kt is the CCH configuration's forward speed boundary, it is necessary to reduce the rotational speed of the coaxial rotor to avoid the advancing tip Mach number approaching drag divergence. Figure 3.3(a) and 3.3(b) present the Mach number distribution across the upper and lower main rotor discs, when viewed from above, of the CCH configuration with and without rotorspeed reduction at V_f = 200kt. On the advancing sides of the rotor discs the Mach number approaches unity as the flight speed and rotorspeed combine, resulting in pockets of transonic flow. As the Mach number exceeds the critical Mach number, defined as the number where pockets of sonic flow

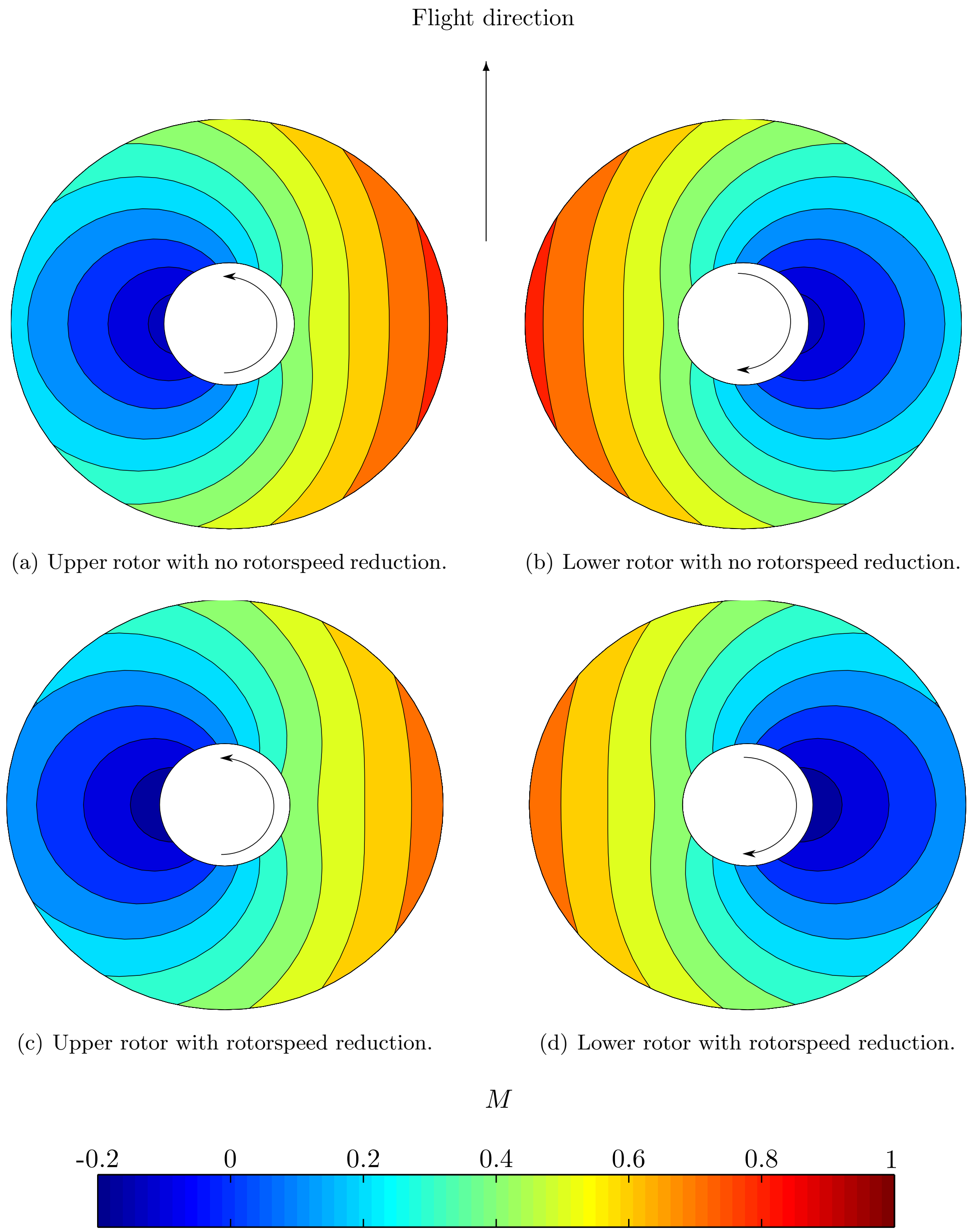

(a) Upper rotor with no rotorspeed reduction.

(b) Lower rotor with no rotorspeed reduction.

(c) Upper rotor with rotorspeed reduction.

(d) Lower rotor with rotorspeed reduction.

Figure 3.3: Mach number distribution across the upper and lower main rotor discs of the CCH configuration with and without rotorspeed reduction at $V_f = 200$kt.

form, there is a significant increase of drag due to the generation of shockwaves [1]. Another issue with transonic flow is the shifting of the aerodynamic centre of the aerofoil section creating adverse pitching moments. It is evident that the main rotor must be slowed to attenuate these issues. Figure 3.3(c) and 3.3(d) shows the Mach number

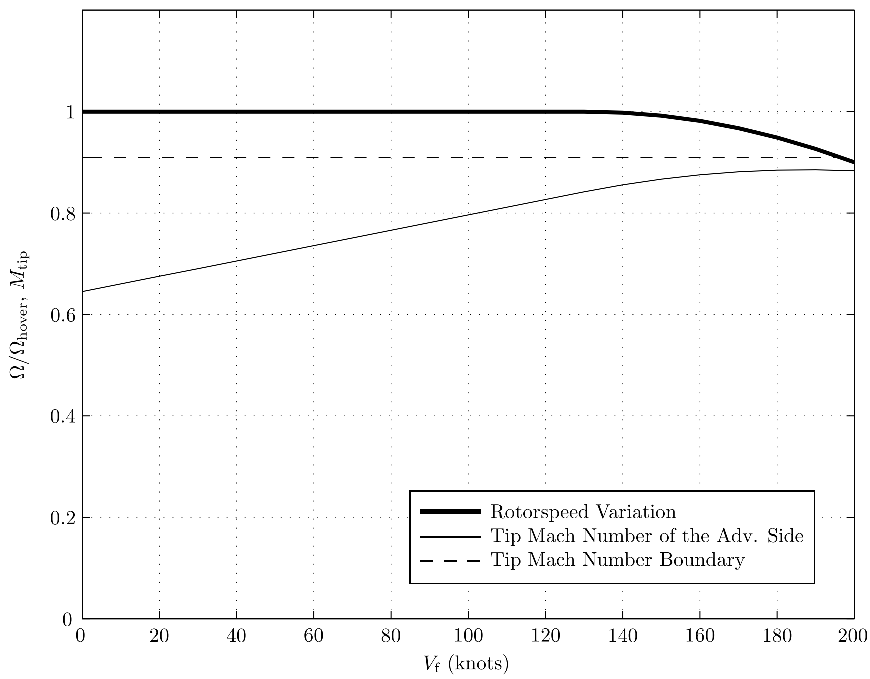

Figure 3.4: CCH Configuration's Variation of Rotorspeed.

distribution across the rotor discs with the rotorspeed slowed by 13% of its hover value. As expected, the Mach numbers of the advancing sides of the rotor discs have lowered consequently ameliorating the adverse compressibility effects. These compressibility issues arise above speeds of 140kt. Hence above this speed the rotational speed of the coaxial rotor is reduced, with Figure 3.4 showing both the variation of the rotorspeed and advancing tip Mach number.

Hybrid Compound Helicopter (HCH) Configuration

The HCH configuration features both lift and thrust compounding. The two propellers fulfil the dual purpose of providing the anti-torque moment and producing additional axial thrust in high speed flight. The lift compounding, supplied by a wing, offloads the main rotor of its lifting responsibilities at high speeds. Like the CCH configuration, it is necessary to take into account some design considerations. The main design task is the sizing of propellers and wing. The addition of a wing to any compound helicopter configuration degrades hover performance by creating an aerodynamic download as well as adding structural weight to the design. The download and extra weight must be compensated with an increase in rotor thrust and an increase in power consumption. To retain good VTOL capability the wing must be sized in a manner that does not adversely reduce hover performance whilst having the ability to offload the main rotor

Design Parameter	HCH Configuration
R_{prop}	1.3m
Ω_{prop}	162 rad/s
θ_{tw}	-30 deg
σ_{prop}	0.2
$\mathbf{x}_{\text{prop}}$	(0.05, ±3.87, 0.13)m

Table 3.3: Propeller Design of the HCH Configuration.

at high speeds. Another complication is that the sizing of the wing influences the design of the propellers. As mentioned previously, the propellers are required to provide the anti-torque moment in low speed flight. The propellers are mounted on the outer sections of the wing to provide adequate clearance between the propeller blades and the fuselage. It is clear that a greater wing span will result in lower propeller thrusts required to provide the anti-torque moment as the lever arm from the propeller to the centre of mass is increased. The selected wing area for the HCH configuration is 12m^2 with an aspect ratio of 6. This wing area can create a significant amount of lift at high speed without adversely degrading hover performance. Also this combination of the wing area and aspect ratio creates a sizable lever arm between the propellers and the centre of mass thus reducing the propeller thrusts at low speed flight. In terms of the aspect ratio, a value of 6 is chosen because a higher aspect ratio would lead to a wing span that would extend further into the higher velocities of the rotor wake whereas a lower aspect ratio would result in a greater induced drag penalty [74]. A choice of 6 is an appropriate compromise between these two effects and has been used on various winged helicopters [13, 81].

Concerning the control of the HCH configuration, a mean propeller collective setting controls the magnitude of the two propeller thrusts whereas a differential propeller collective controls the yawing motion of the helicopter. The starboard and port propeller collectives take the form

$$\theta_{star} = \bar{\theta}_{prop} + \theta_{diff} \tag{3.4}$$

$$\theta_{port} = \bar{\theta}_{prop} - \theta_{diff} \tag{3.5}$$

The differential propeller setting, θ_{diff}, mean propeller collective, $\bar{\theta}_{\text{prop}}$, as well as the standard main rotor collective and cyclic controls result in five controls. The end result is a level of control redundancy which requires an amendment to the trim algorithm,

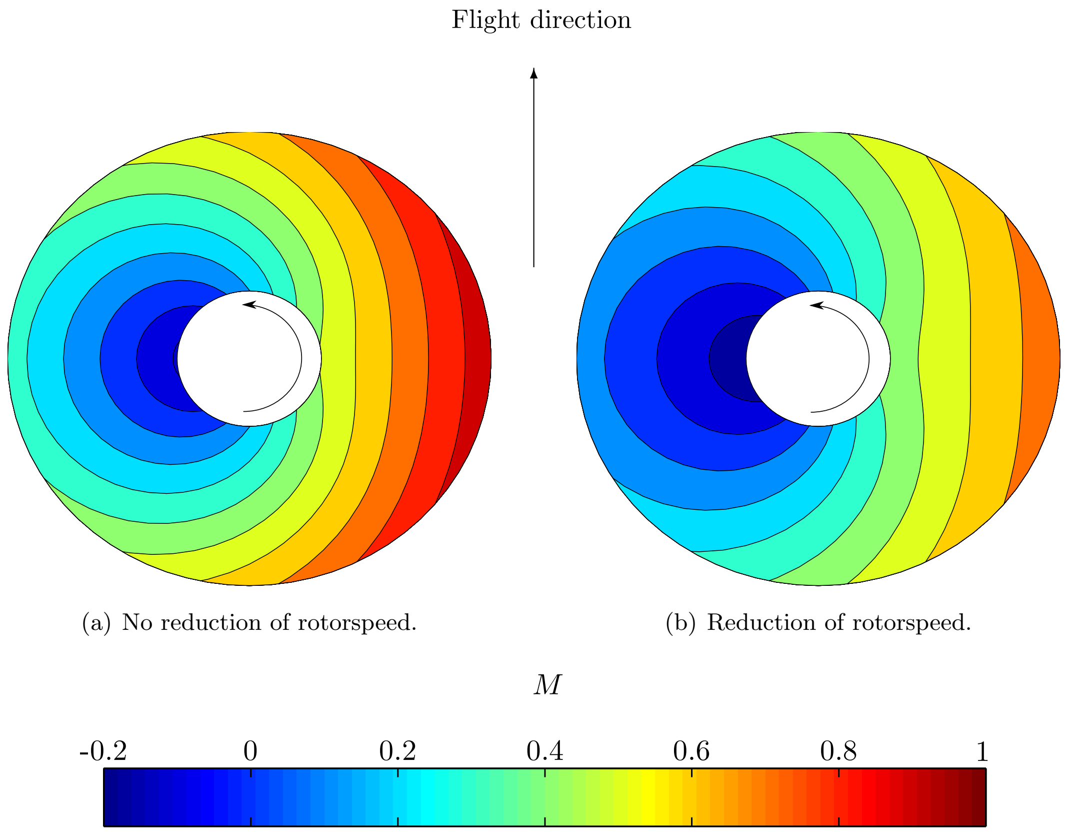

(a) No reduction of rotorspeed.

(b) Reduction of rotorspeed.

Figure 3.5: Local Mach number distribution across the main rotor disc of the HCH configuration with and without rotorspeed reduction at $V_f = 200$kt.

which is discussed in Section 3.3. The starboard and port propellers are identical with the exception of their positions on the airframe with Table 3.3 showing the important design properties of the propellers.

Figure 3.5(a) shows the distribution of local Mach numbers across the main rotor of the HCH configuration at a speed of 200kt without rotorspeed reduction. There is a region across the advancing side of the rotor disc with transonic flow, approaching local Mach numbers of unity. As discussed previously with the CCH configuration, it is necessary to slow the HCH configuration's main rotor to avoid adverse compressibility effects. Therefore, the main rotor is slowed by 17% relative to its hover rotorspeed, at 200kt with the local Mach number distribution presented in Figure 3.5(b). This rotor is slowed to a greater extent when compared to the CCH configuration as the vehicle's wing offloads the main rotor. As expected, the local Mach numbers of the advancing side of the disc have reduced. Another consequence of the reduction of rotorspeed is the increased region of reverse flow, as indicated by the negative Mach numbers in Figure 3.5(b). Compressibility effects become a concern after 140kt. Hence, the main

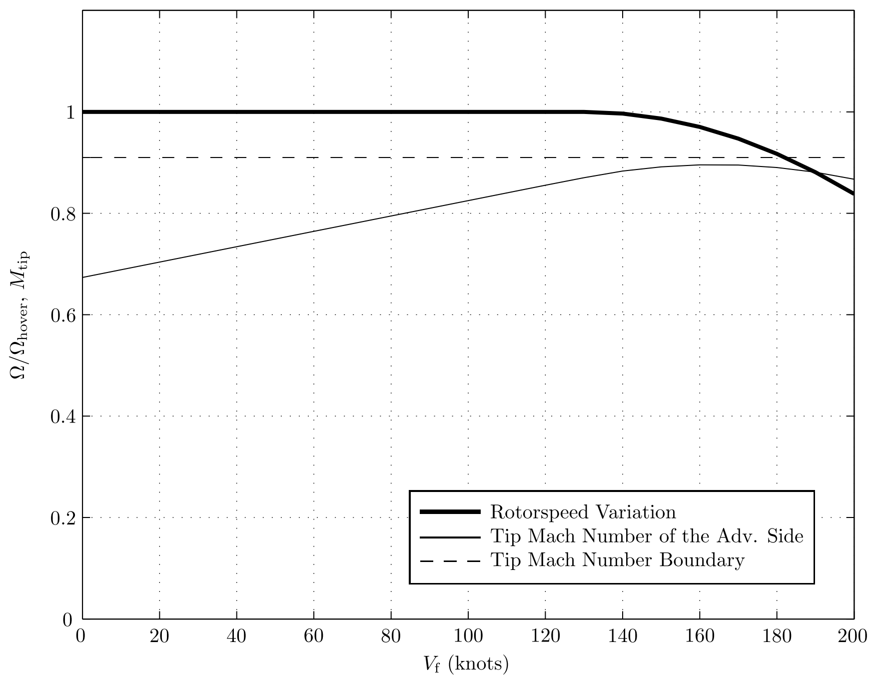

Figure 3.6: HCH Configurations Variation of Rotorspeed.

rotor's speed is gradually lowered, as seen in Figure 3.6, to avoid the advancing side of the disc approaching drag divergence.

3.3 Trim Analysis

The starting point of any meaningful analysis of a helicopter configuration is to trim the model. From the trim condition the helicopter's dynamic stability, performance, manoeuvrability and handling qualities can all be assessed. With the design of the compound helicopter configurations finalised, then the aircraft configurations can be trimmed. Concerning the BL configuration, the trim algorithm calculates the four control angles, roll and pitch angles which result in zero translational and angular accelerations acting at the aircraft's centre of gravity. In addition, the angular rates, sideslip velocity and glideslope angle are set to zero for all the trim calculations presented in this study. Essentially, there are six trim targets which are

$$X - W \sin\Theta = 0 \tag{3.6}$$

$$Y + W \cos\Theta \sin\Phi = 0 \tag{3.7}$$

$$Z + W \cos\Theta \cos\Phi = 0 \tag{3.8}$$

$$L = 0 \tag{3.9}$$

$$M = 0 \tag{3.10}$$

$$N = 0 \tag{3.11}$$

which correspond to the condition of steady level flight. Clearly, finding the four control angles, roll and pitch angles to trim the BL configuration, thereby satisfying the six trim targets Equations (3.6) - (3.11), is not a trivial task. The unknowns cannot be calculated analytically, therefore a numerical technique, as described fully in Appendix B, is used. This numerical method has proven to be a flexible and robust algorithm for the conventional helicopter. However, due to the introduction of extra control(s) to the compound helicopter configurations the trim algorithm requires a slight amendment. One solution to this issue is to add another equation(s) to the six trim targets, Equations (3.6) - (3.11), to match the number of unknowns. Alternatively, an additional vehicle state could be prescribed to reduce the number of unknown controls. The following describes the approach to the trim of the CCH and HCH configurations.

One of the unique features of the CCH configuration is that a differential lateral cyclic control, which controls the lateral lift offset value, is introduced to the design. The CCH configuration therefore features a total of six controls: mean main rotor collective, differential main rotor control, two cyclic controls, propeller pitch and a differential lateral cyclic control. The approach taken to trim the CCH configuration is to prescribe an extra state as well as introduce an additional trim target. Presently, the extra state that is prescribed is selected to be the pitch attitude, Θ, as it directly impacts the amount of thrust the propeller is required to produce. One possibility is to set a fixed value of pitch to trim the helicopter at all flight speeds, for example $\Theta = 0$, fuselage level. However, this is not always desirable, as it would require an excessive level of propeller thrust at certain flight speeds. Another concern is that, in low-speed flight, there is no distinct advantage of having the propeller providing thrust, as it would unnecessarily increase the overall power consumption of the helicopter. Hence, rather than setting the pitch attitude to a fixed value for all flight speeds, a pitch schedule is developed to minimise the required propulsive force of the propeller. In terms of the additional trim target, this is the lateral lift offset value, which is given by Equation (3.1). The variation of the lateral lift offset value is selected to vary with flight speed in the following manner

$$LOS = AV_f^2 \tag{3.12}$$

so that no lateral offset is required in the hover but the value increases with speed. This trend of LOS across the flight envelope, Equation (3.12), is a typical variation of LOS which has been used on the Sikorksy X2 [82]. The lateral lift offset value is required to be within the range of 0.2 - 0.3 to avoid retreating blade stall in high speed flight [38]. In this study the coefficient A is selected so that the lateral lift offset value equals 0.2 at 200kt with all of the CCH configuration's results reflecting this. Therefore the trim algorithm calculates the seven unknowns to match the seven trim targets, which are Equations (3.6) - (3.11) and Equation (3.12), so that the CCH configuration is in steady level flight.

In relation to the HCH configuration, there are five controls: the main rotor collective, two cyclic controls, a mean propeller pitch control and a differential propeller pitch control. The approach taken to determine the control angles required to trim this aircraft configuration is to prescribe an additional state which results in six unknowns which match the six trim targets, Equations (3.6) - (3.11). Like the CCH configuration, the extra state which is prescribed is the pitch attitude as it directly impacts the level of thrust that the propellers are required to produce. In this design scheduling the pitch attitude is particularly useful as it allows for direct control of the wing lift. Hence, a pitch schedule is developed for the HCH configuration to reduce the required propeller thrusts in low speed flight. It should be noted that the HCH configuration could, in theory, be trimmed with a pitch attitude of zero at all flight speeds but there is an important issue that arises in low speed flight. In order to trim the HCH configuration in the hover, at a pitch attitude of zero, a large amount of negative thrust is required from the port propeller. As forward speed increases and the port propeller continues to create large amounts of negative thrust, to maintain a level fuselage, the forward velocity and the induced velocity of the port propeller travel in opposite directions. When their magnitudes are similar there would be no well defined slipstream and eventually the vortex ring state would be reached at some flight speed, resulting in the solutions from momentum theory being no longer valid [2]. Hence the pitch attitude is scheduled in such a manner that avoids the port propeller providing large amounts of negative thrust in low speed flight. It was originally found that this manner of pitch scheduling

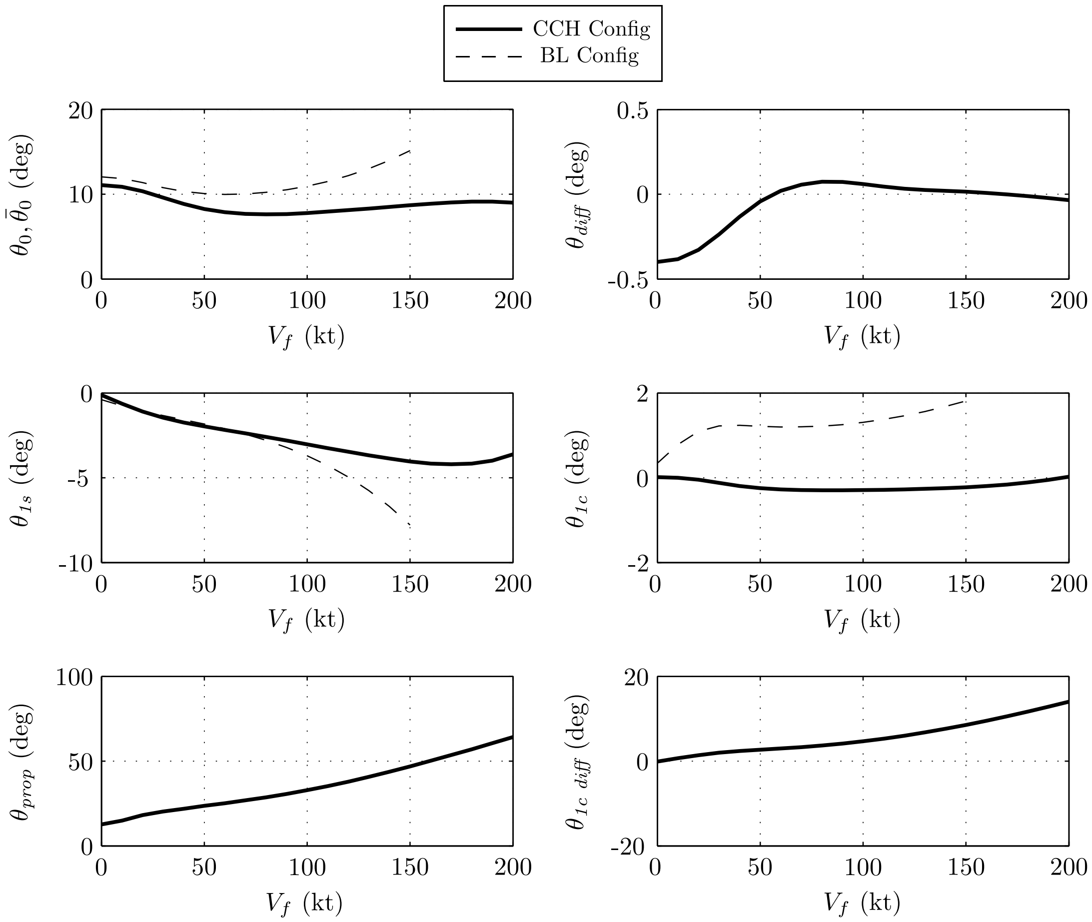

Figure 3.7: Trim results of the BL and CCH configurations.

does impose the penalty of increasing the pitch attitude in the hover, from 4.3° for the BL configuration to 8.4° for the HCH configuration. The reason for this increase in pitch attitude is that the starboard propeller provides a significant thrust to provide the anti-torque moment and the main rotor is required to flap backwards to oppose this force. However, this high pitch attitude setting in low speed flight can be attenuated by an appropriate selection of the rotor shaft tilt. Selecting a shaft tilt angle, γ_s, of zero results in more favourable pitch attitudes in low speed flight. For the trim problem, the pitch attitude is set close to zero after 150kt to maximize the lift produced by the wing. A combination of setting the pitch attitude to zero after 150kt as well as a fixed wing pitch setting of 7° maximises the lift of the wing, with the the wing's lift coefficient, C_L, being approximately 0.5, whilst maintaining an adequate stall margin. Although there is a temptation to completely offload the main rotor at 200kt, flight tests of winged compound helicopters have showed that the wing providing the entire lifting force of the vehicle is not the most efficient lift sharing ratio [32].

Coaxial Compound Helicopter (CCH) Configuration Trim Results

Figure 3.7 shows the trim results of the CCH and BL configurations. In hover, the coaxial inflow model, Equations (2.69) and (2.70), result in higher induced velocities through the lower rotor than that of the upper rotor. Therefore, the induced power loss of the lower rotor is greater than the upper rotor if the upper and lower thrust coefficients are equal. Hence, to provide a torque balance, the upper rotor must create more thrust than the lower rotor to match the lower rotor torque, with the thrust sharing ratio of the upper and lower rotors being 1.32 in hover. Another consequence of the higher induced velocities of the lower rotor is the reduced blade incidence of the lower rotor blades if $\theta_{0u} = \theta_{0l}$. Therefore, to compensate for the strong inflow through the lower rotor, the lower rotor's collective is slightly higher than that of the upper rotor in low-speed flight. This partitioning of the rotor thrusts and the higher pitch of the lower rotor are both consistent with findings from other trimmed coaxial rotors in hover [53, 83, 84]. As the CCH configuration moves away from hover, the thrust sharing ratio tends toward unity and θ_{diff} tends toward zero as the aerodynamic interference between the rotors lessens as μ begins to dominate the coaxial inflow, Equations (2.69) and (2.70). The differential lateral cyclic control is almost linear, increasing with flight speed to match the required lateral lift offset value in Equation (3.12). Another interesting feature of the trim results is the difference between the lateral cyclic required for both configurations. In a conventional helicopter, a large amount of lateral cyclic is required between 0 and 50kt, as can be seen with the BL configuration. As the conventional helicopter moves into forward flight, the rotor wake skews backward, lowering the local angle of attack at the rear of the rotor disk. This effect causes the helicopter to roll to starboard (for a helicopter rotor that rotates anticlockwise when viewed from above). To counteract this rolling moment, a large amount of lateral cyclic is required to trim the helicopter. This effect still exists in the coaxial rotor, but the two rotors flap in opposite directions, requiring little lateral cyclic. For speeds above 150kt, the propeller produces the majority of the axial thrust requiring a small amount of lateral cyclic θ_{1c} to balance the propeller torque. The lack of tail rotor and the fin not being angled relative to the fuselage centre-line reduces the side force that the helicopter produces from hover to 200kt, which consequently reduces the bank angle of the fuselage significantly.

The propeller pitch setting is also shown in Figure 3.7 with the control varying with flight speed in a linear manner. In low speed flight, the propeller does not produce a significant amount of axial thrust. However, the pitch schedule, which is shown

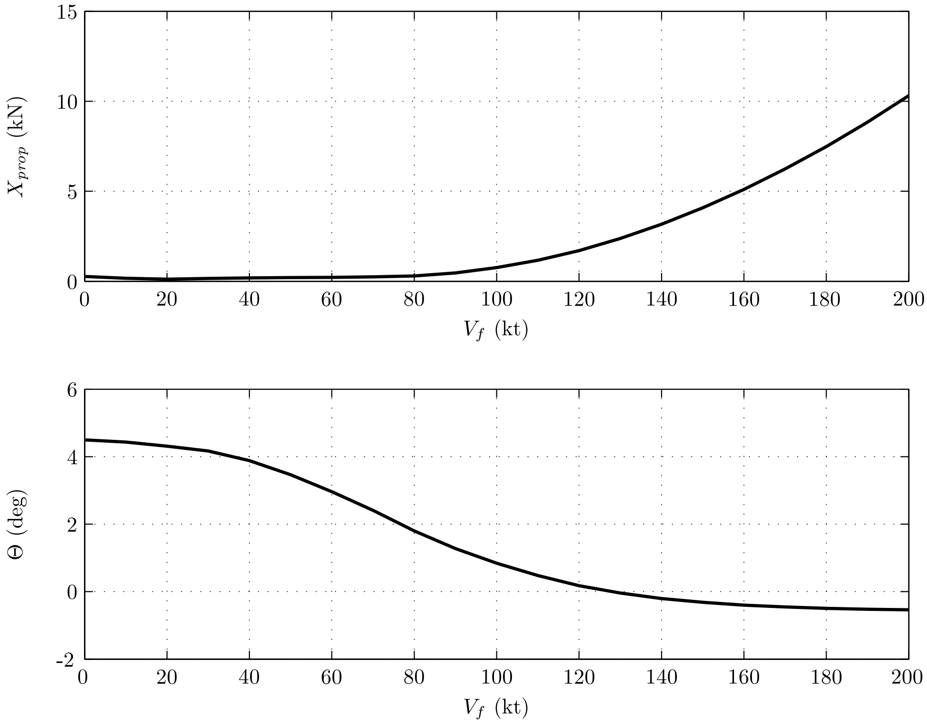

Figure 3.8: Propeller Thrust and Pitch Schedule for the CCH Configuration.

in Figure 3.8, is developed so that in high speed flight the propeller offloads the coaxial rotor of its propulsive duties. After 80kt, the axial thrust from the propeller increases significantly, producing over 10kN of thrust at 200kt, as seen in Figure 3.8. The amount of axial thrust produced by the propeller also impacts on the predicted values of longitudinal cyclic. Referring to Figure 3.7, there is little difference between the two longitudinal cyclic results (negative longitudinal cyclic tilts the rotor disk forward) until a flight speed of approximately 80kt, where the propeller begins to provide axial thrust, reducing the longitudinal cyclic required. As expected, the amount of stick forward, negative θ_{1s}, after 80kt reduces when compared to the BL configuration due to the contribution of the propeller to the propulsive force.

Figure 3.9 illustrates the effectiveness of the lateral lift offset coaxial rotor system at a speed of V_f = 150kt. The benefit of lateral lift offset is that the advancing sides of the discs provided the majority of the overall vehicle lift. Figures 3.9(a) and 3.9(b) show the lift distribution of the upper and lower rotor discs at a lateral lift offset value of 0.15. Recall that the upper rotor rotates in an anti-clockwise direction when viewed from above whereas the lower rotor rotates in the opposite direction. Of course, the advancing sides of the rotor discs provide the majority of lift with Figures 3.9(a) and 3.9(b) showing that they produce opposing rolling moments, thereby having the

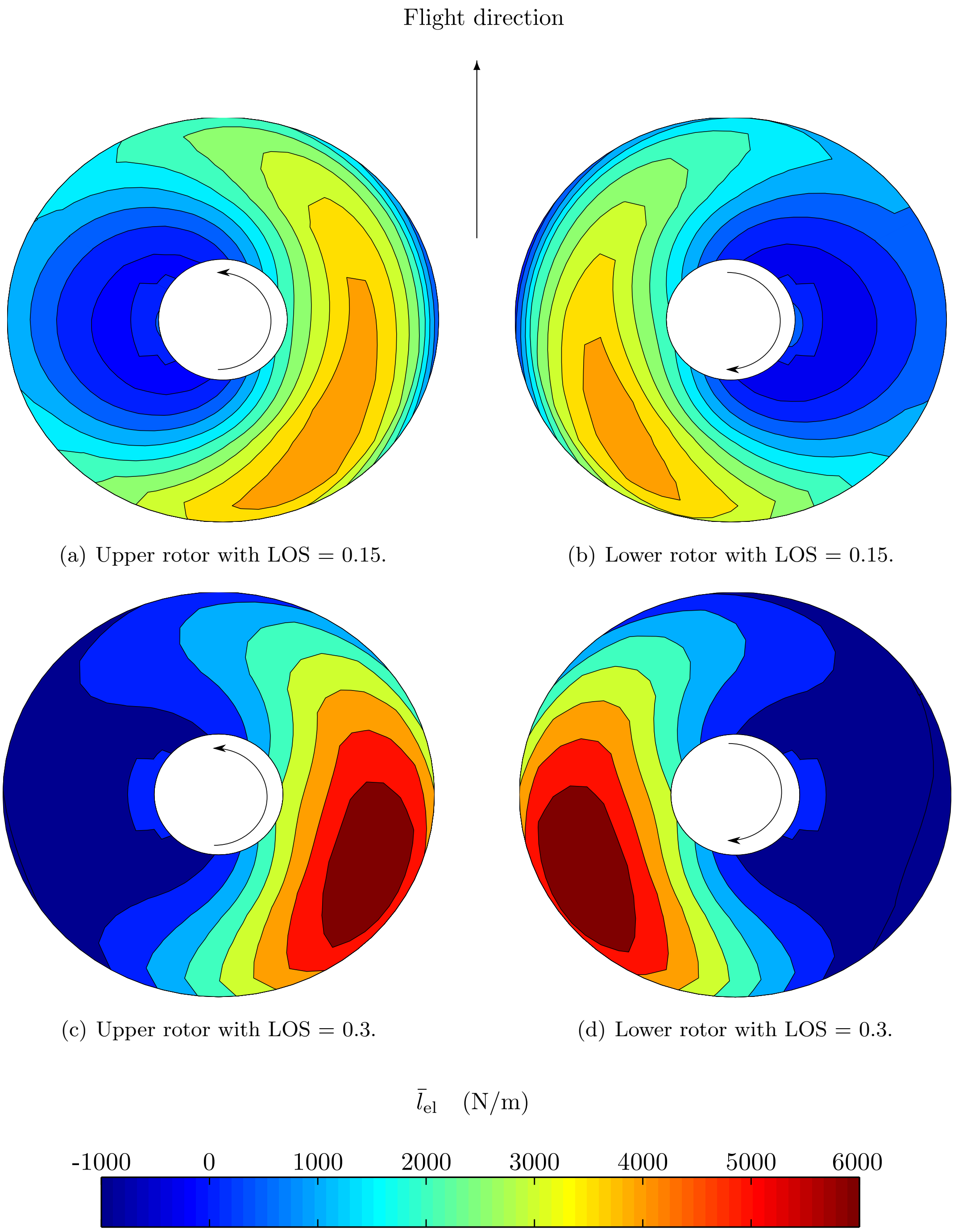

(a) Upper rotor with LOS = 0.15.

(b) Lower rotor with LOS = 0.15.

(c) Upper rotor with LOS = 0.3.

(d) Lower rotor with LOS = 0.3.

Figure 3.9: Lift distribution across the upper and lower main rotor discs of the CCH configurations with different LOS values at $V_f = 150$kt.

net effect of rolling hub trim. In addition, Figures 3.9(c) and 3.9(b) present the lift distributions of the upper and lower rotors with a greater value of lateral lift offset of 0.3. As expected, there is greater loading on the advancing sides of the rotor discs thereby

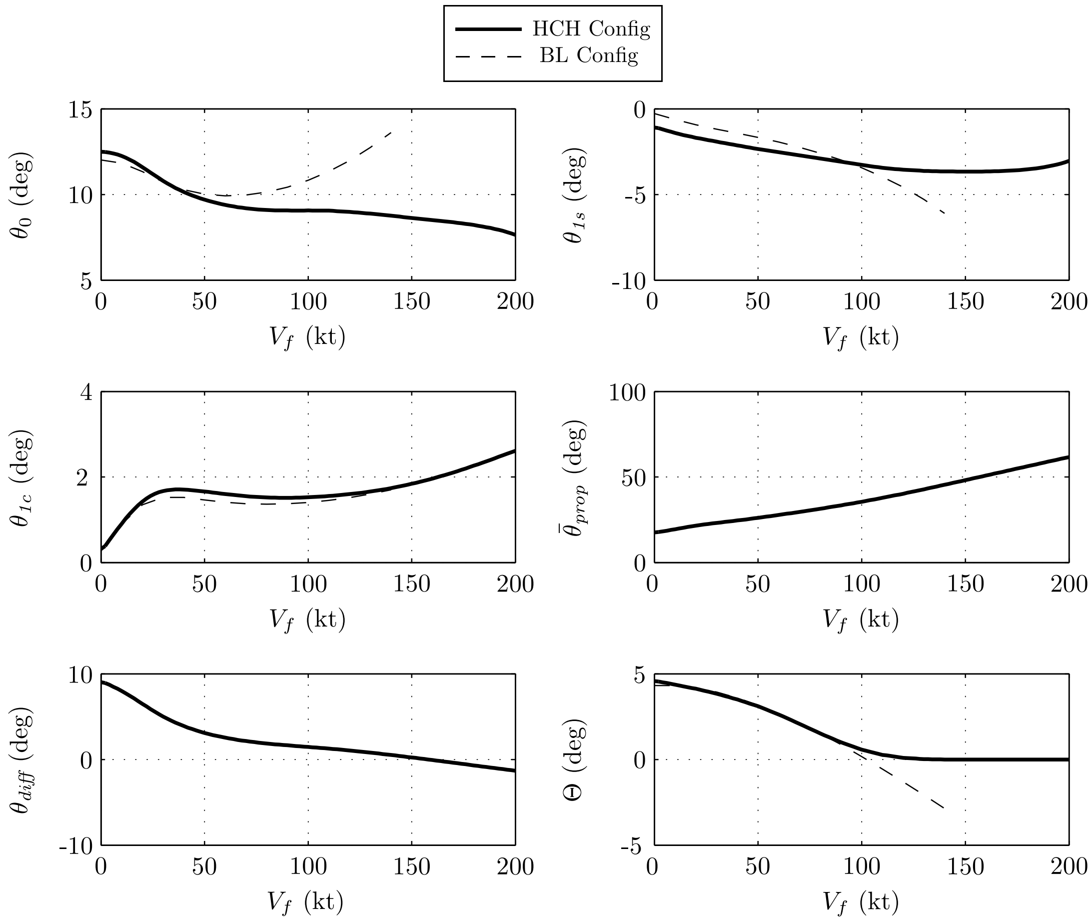

Figure 3.10: Trim Results of the HCH and BL Configurations.

providing a greater portion of the overall vehicle when compared to Figures 3.9(a) and 3.9(b). At this lateral lift offset value the retreating side of the rotor discs is almost completely offloaded. The highest lateral lift offset setting which is realistic depends on the structural properties of the rotor blades and the hub [80]. An additional concern is the separation distance between the two rotors to accommodate the lateral flapping of the two rotors [38].

Hybrid Compound Helicopter (HCH) Configuration Trim Results

The trim results of the HCH and BL configurations are shown in Figure 3.10. The first result to note is the difference between the collective settings. As the speed approaches 50kt, the collective setting of the HCH configuration begins to reduce as the wing begins to offload the main rotor, whereas with the BL configuration, the collective begins to increase, tending toward the limiting case of retreating blade stall. There is little difference between the longitudinal cyclic values of the two configurations until 100kt.

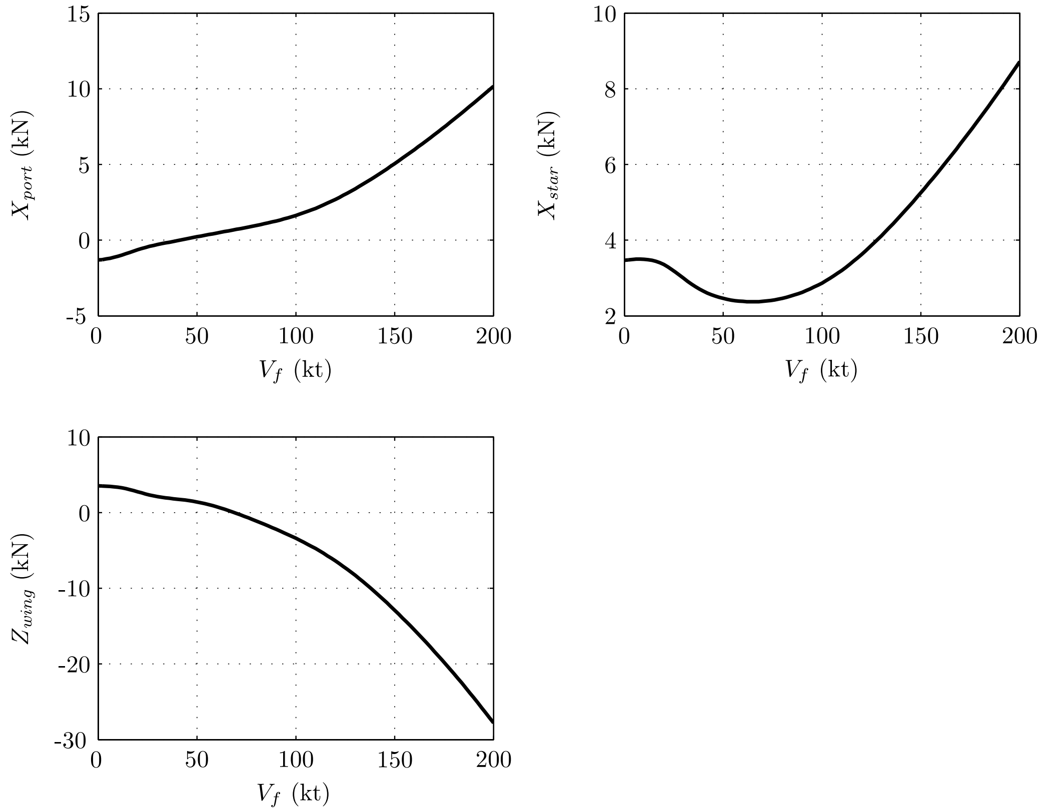

Figure 3.11: Wing's Lifting Force and Propeller Thrusts of the HCH Configuration.

However, after 100kt, the two propellers begin to supply the propulsive force; therefore, the rotor disk is no longer required to be tilted forward to provide the propulsive force but to maintain the pitch attitude required. The lateral cyclic results of the two configurations are of similar form throughout the speed range. In terms of the attitudes, the absence of a tail rotor reduces the bank angle of the fuselage for all flight speeds. The differential propeller collective is at its highest in low-speed flight to provide the anti-torque moment. As forward speed increases, the anti-torque moment duties are shifted toward the fin as it provides a side force, which results in the propeller differential setting lowering as speed increases. At flight speeds in excess of 150kt, the main rotor controls alter significantly due to the reduction of the main rotor's speed, in order to avoid compressibility effects. Hence, the wing offloads the main rotor to a greater extent with the rotor producing only 30% of the overall vehicle lift at 200kt. At this flight speed, it is possible that the control of the vehicle would transition from main rotor controls to fixed-wing controls, similar to that of a tilt-rotor aircraft, with conventional aircraft controls such as as ailerons, elevator, and a rudder.

Figure 3.11 presents the propeller forces, wing force and pitch schedule corresponding to trim conditions shown in Figure 3.10. In low speed flight the two propellers are providing modest levels of thrust to maintain the torque balance. Note that the port propeller is providing reverse thrust until a speed of 40kt. As flight speed increases, the thrust of the two propellers increase significantly, with the two propellers providing the majority of propulsive force to overcome the airframe drag in high speed flight. Also shown in Figure 3.11 is the variation of wing's lift throughout the speed range. As expected, the wing provides a download of approximately 8% of the rotor thrust in the hover which is consistent with experimental tests of other winged helicopters [74]. In low speed flight, the contribution of the main rotor's wake and the low dynamic pressure across the wing, result in the wing providing a download force until 60kt. However as flight speed increases the wing loading increases with the wing producing 28kN of the lifting force at 200kt, 70% of the overall lifting force for the entire vehicle.

Figures 3.12(a) and 3.12(b) compare the lift contours of the BL and HCH configurations at V_f = 150kt. With a conventional helicopter there is a decrease of the local angle of attack at the advancing side of the rotor disc and an increase over the retreating side of the disc as forward speed increases [38]. At a flight speed of 150kt, the angles of attack across the retreating side are high to balance the rolling moments of the advancing and retreating sides of the disc. At this flight condition the conventional main rotor disc is tilted forward at this speed so that a component of the rotor thrust vector provides a propulsive force to overcome the airframe drag. Therefore, the lift contours at the rear of the main rotor disc of the BL configuration, Figure 3.12(a), are greater than the lift at the front of the disc. In relation to the HCH configuration, the wing provides 25% of the overall vehicle lift at this forward speed, consequently offloading the main rotor as seen in Figure 3.12(b). As speed increases to the assumed maximum speed of 200kt, the loading across the wing increases thereby offloading the main rotor to a greater extend. The combination of a higher local dynamic pressure across the wing and the reduction of the main rotor's rotorspeed, increases the wing's contribution to the overall lift of the vehicle.

3.4 Model Validity Discussion

Before concluding this chapter, it seems appropriate to return and discuss the issue of model validity. The level of modelling used throughout this Thesis falls into the level 1 modelling category of Padfield's threefold hierarchy of rotor simulation models [36], and the limitations of this type of model were discussed in Chapter 2. One of the main limitations of the main rotor model is its inability to model nonlinear aerodynamics

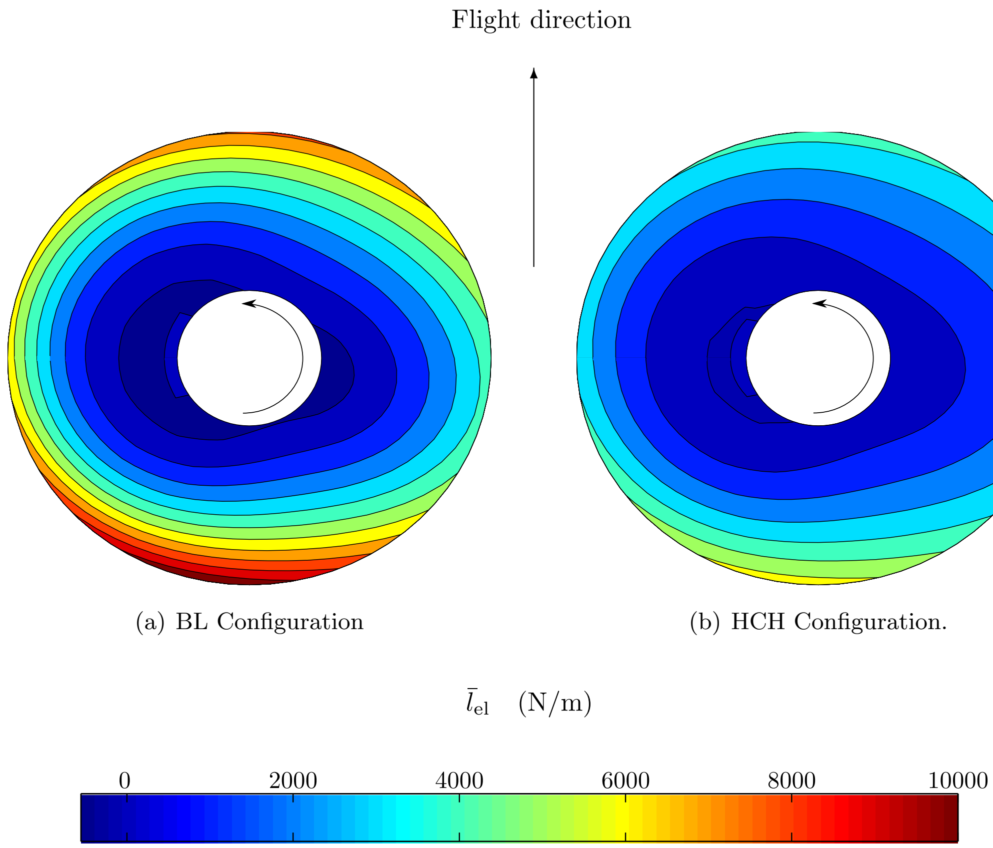

Figure 3.12: Lift distribution across the main rotor discs of the BL and HCH configurations at $V_f = 150$kt.

such as blade stalling. Due to this feature it is fair to postulate that the current level of modelling will produce unrealistic results if the compound helicopter configurations were taken to the edge of their flight envelopes. Consequently, the results presented within this Thesis are limited to flight speeds under 200kt, below the perceived edge of the compound helicopter's flight envelope, so that the modelling assumptions can be considered valid. Blade stalling is not modelled, but care has been taken to trim the compound helicopter configurations in a manner where blade stalling is unlikely to occur. For example, at 200kt the HCH configuration is trimmed at a flight condition where the wing produces 70% of the total vehicle lift, thereby offloading the main rotor significantly. Due to this offloading, the main rotor is well clear from its limiting state of retreating blade stall. In terms of the CCH configuration, the lateral lift offset concept is used to offload the retreating sides of the rotor discs in high speed flight. It is acknowledged that nonlinear aerodynamics have a greater effect with regards to the CCH configuration as there is no source of lift compounding for this vehicle. However, the use of a lateral lift offset of 0.2 at 200kt, avoids retreating blade stall across the rotor disc according to various studies [38, 85]. By avoiding blade stall, through the use of the lateral lift offset trim strategy, then the results from the CCH configuration can be viewed as of sufficient fidelity so that meaningful insights can be gained from the model. In terms of future work, it is recognised that there may be a need for high fidelity models, which take into account nonlinear aerodynamics, to support this flight mechanics study. Therefore, it is recommended that these types of models should be considered in future work to supplement the conclusions made in this Thesis. The main benefit of high fidelity modelling techniques is that the compound helicopter's flight dynamic characteristics could be assessed at the edge of its perceived flight envelope, at a flight speed in the region 250kt.

3.5 Chapter Summary

This Chapter detailed the development of the two compound helicopter configurations. These two configurations represent two compound helicopters which are of interest to the rotorcraft community and are being taken seriously by their respective manufacturers. The result is three aircraft configurations - the two compound helicopters and a baseline configuration providing an effective comparison vehicle. It was highlighted this is not a design study but a study to investigate the impacts of compounding. Therefore, the fuselage shape and size of all three vehicles is maintained so that the effects of compounding are isolated from other factors. However, the addition of a coaxial rotor, propellers and wing to the conventional helicopter do require some preliminary design considerations. The Chapter discussed these elementary design considerations.

With the aircraft configurations developed then the vehicles are trimmed using a numerical algorithm. As the compound helicopter configurations feature some level of control redundancy, the trim algorithm was amended to calculated the trimmed states of the vehicles. This algorithm was shown to successfully calculate the control angles required to trim the CCH and HCH configurations. This was achieved by the addition of extra trim target(s) as well as by prescribing the pitch attitude throughout the speed range. The trim results of the two compound helicopter configurations highlight some of the benefits of compounding. In terms of the CCH configuration, the main conclusions are as follows

- The effect of thrust compounding to the CCH configuration is to reduce the amount of stick forward required to trim the aircraft after 80kt. After 80kt the propeller provides a significant amount of propulsive force, divorcing the main rotor from its propulsive duties.

- The results not only highlight the influence of compounding but also demonstrate the potential of the coaxial rotor ABC concept. The lateral lift offset rotor is capable of providing the lifting force of the vehicle, without any additional source of lift compounding, in high speed flight unlike that of the single main rotor of the BL configuration. This is due to exploiting the lift potential of the advancing sides of the rotor discs in high speed flight using lateral lift offset. Without lateral lift offset the aircraft is incapable of obtaining speeds greater than 150kt.

In relation to the HCH configuration, the main conclusions from this Chapter are

- The trim results of the HCH configuration show a reduction of collective required after 50kt as the wing begins to offload the main rotor. In low speed flight, the wing provides an aerodynamic download due to a contribution of the main rotor's wake and the low dynamic pressure across the wing. At 200kt the wing provides 70% of the total lifting force.
- The differential propeller collective control required is at its highest in low speed flight as it provides the anti-torque moment. However as the aircraft transitions into forward flight, the control decreases as the fin is now capable of providing the anti-torque moment.
- There is also less longitudinal cyclic required after 100kt as the propellers provide the propulsive force to overcome the airframe drag. The two propellers allow the fuselage's pitch attitude to be controlled, resulting a near level fuselage in high speed flight which results in a significant lifting force from the wing.

Chapter 4

Performance Analysis

The performance of an aircraft is a critical aspect of the vehicle's design. Generally, the design process of any new aircraft is driven by the performance, cost, reliability, safety, maintainability, external noise and manoeuvrability of the vehicle [1]. However, perhaps the two most important design drivers generally tend to be the performance and cost of the aircraft. The performance of the vehicle must be able to satisfy or exceed the expectations of the potential customer. Economically, the aircraft needs to be affordable and profitable to the operator. In relation to the performance of the compound helicopter, the vehicle is expected to have a greater range and dash speed than that of a conventional helicopter. Due to the resurgence of interest in the compound helicopter design, performance studies of this type of vehicle have begun to be published. It is important to understand how these recent studies compare with the approach taken in this current work. Hence, before stating the aims of this performance work it is necessary to examine the recent compound helicopter performance studies.

The performance of the conventional helicopter is well understood and is explained in most standard helicopter textbooks [1, 3, 5, 7, 38]. However, recently more performance studies of compound helicopters have began to appear in the literature. In particular, due to the development of the Sikorsky X2 aircraft, there has been an increase of interest in the coaxial rotor arrangement with Johnson exploring the performance of the rotor system [85]. The comprehensive rotorcraft analysis (CAMRAD II) [72] package was used in this particular study to examine the performance of a coaxial rotor. With the vehicle weighing 150000lb and a coaxial rotor system optimised for cruise performance, the maximum lift-to-drag was calculated to be 6.2. Although Johnson hypothesises that this result may be somewhat optimistic, it does indicate that a coaxial compound helicopter could efficiently operate at 250kt. Regarding another recent study of lift-offset rotors, Yeo and Johnson investigated the maximum blade loading of such a rotor system [80]. The results show that the thrust capability of the lift-offset rotor is significantly greater than that of the conventional rotor due to the system fully exploiting the lift potential of the advancing side of the rotor.

In terms of a single main rotor compound helicopter, Yeo and Johnson investigated the optimum design of a single main rotor compound helicopter weighing 100,000lb [28]. The study concluded that the optimum performance occurred when the wing was producing the majority (≈90%) of the vehicle lift and that the main rotor blade twist strongly influenced the aircraft performance. Another study by Moodie and Yeo, conceptually designed a slowed-rotor compound helicopter to achieve the best cruise performance [27]. Their compound helicopter configuration was similar in layout to that of the Lockheed Cheyenne, with the tail rotor and propeller mounted at the rear of the aircraft. The main rotor is slowed at high speeds, in order to avoid adverse compressibility effects, with a highly nonlinear twist distribution to minimise power. The maximum take-off weight of the aircraft was calculated to be 36,851lb, in order to carry a payload of 4015lb, with the maximum lift-to-drag ratio at the cruise condition of 250kt computed to be 7. This result suggests that this particular configuration has a significant performance advantage when compared with a conventional helicopter. However, Moodie and Yeo were keen to stress that further work is required to assess how such a configuration would perform low speed manoeuvres as the large wing could present some challenges in this flight regime.

It is clear that the emergence of the compound helicopter has resulted in more performance studies of the vehicle. These studies have assessed the performance of the Advancing Blade Concept design as well as the design of a single main rotor compound helicopter [27, 28, 85]. These recent performance studies sized the compound helicopter's design parameters from a given mission specification. By using this approach, the performance benefits of the compound helicopter were highlighted [27, 28]. In contrast, the strategy of this work is to take a different approach from these studies to isolate the effects of compounding from the performance of the aircraft class. It is worth highlighting again that this is not a design exercise, but a study to determine the effects of compounding on the performance of the rotorcraft. Therefore, the results from this study should be viewed in this context. Although not a design study, it is likely that the results will highlight some design issues relating to the compound helicopter.

The performance results in this Chapter are all computed by using the appropriate trim algorithms which were introduced in Chapter 3. The Chapter begins by presenting the power required in steady level flight for each compound helicopter configuration. Recall that there are two compound helicopter configurations which are named the Coaxial Compound Helicopter (CCH) and the Hybrid Compound Helicopter (HCH), Figures 3.1(a) and 3.1(b). In addition, the Baseline (BL) helicopter serves as a comparison vehicle. The Chapter also investigates the effect of compounding on the maximum speed, hover ceiling, range and endurance of the compound helicopter. The Chapter concludes by examining the compound helicopter configurations when flying standard helicopter missions.

4.1 Power Required in Steady Level Flight

The power required to operate an aircraft in steady level flight is important in any helicopter design. It is the goal of the designer to minimise the power required in steady level flight to maximise aircraft performance as well as provide an adequate power margin for the aircraft to perform manoeuvres. Figure 4.1 compares the predicted power of the HCH and BL configurations in steady level flight at mean sea level (MSL). Throughout the speed range the HCH configuration requires greater power when compared with the BL configuration. In the hover, the HCH configuration requires greater rotor power to overcome the aerodynamic download of the wing and the anti-torque moment is provided by the port and starboard propellers. The power of the tail rotor, in the hover, is 133kW whereas the starboard and port propellers require 109kW to retain the torque balance. Hence, the effect of thrust compounding is advantageous in this regard. As flight speed increases, a notch appears in the HCH configuration's rotor power at 50kt due to wing stalling. After a speed of 80kt, combination of the wing offloading the main rotor and the main rotor slowing down to avoid adverse compressibility effects, reduces the main rotor power. However, this is met with an increase of power required by the two propellers, to overcome the fuselage drag and to maintain a near level pitch attitude to promote a favourable wing angle of attack. The net effect is that the power of the HCH configuration is greater than that of the BL configuration throughout the speed range. After 163kt the total power required exceeds the power available from the engines. This result, as expected, indicates that further optimisation of the design is required, particularly to reduce the airframe drag with technology such as active flow control [86]. The introduction of a low drag design would reduce the propulsive power required by the propellers and therefore lower the total power of the

HCH configuration. Additionally, the results highlight that it would be necessary to increase the installed engine power of a compound helicopter relative to a conventional helicopter of similar size. A similar conclusion was made during the investigation of the powerplant of a lift and thrust compounded Lynx demonstrator [21].

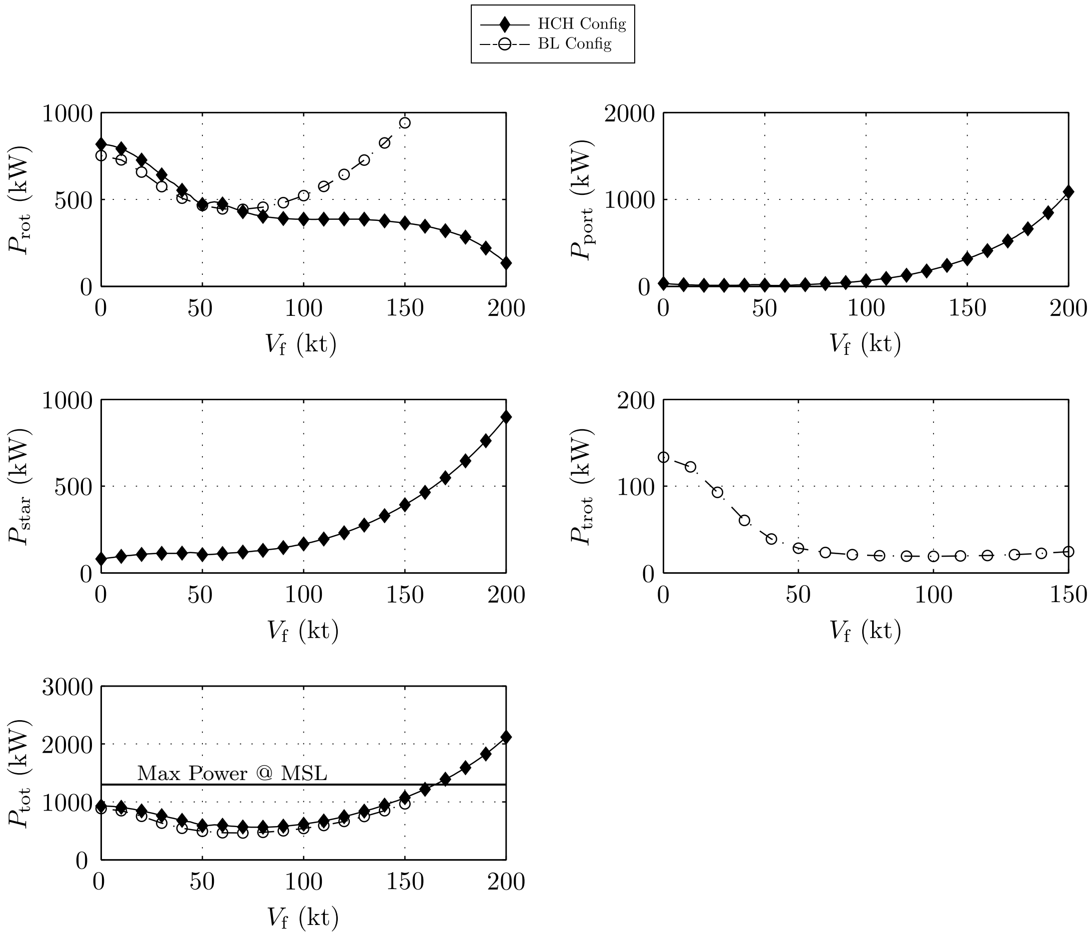

Figure 4.1: Predicted Power Required for the HCH and BL Configurations in Steady Level Flight at MSL

In relation to the CCH configuration, it has been a contentious issue whether or not a single main rotor design with a tail rotor is more efficient than a coaxial rotor design. To address this issue Kim and Brown [52, 53] used the vorticity transport model (VTM), which is a comprehensive rotor model, to compare the performance of a single rotor to that of a coaxial rotor. One important issue that Kim and Brown [52] highlight is that care must be taken when comparing a single rotor to that of a coaxial to ensure that a fair comparison can be made. Kim and Brown argue that to properly compare these two rotor systems the conventional single rotor must consist of an equal number of geometrically identical blades to those used in the coaxial rotor [52]. The

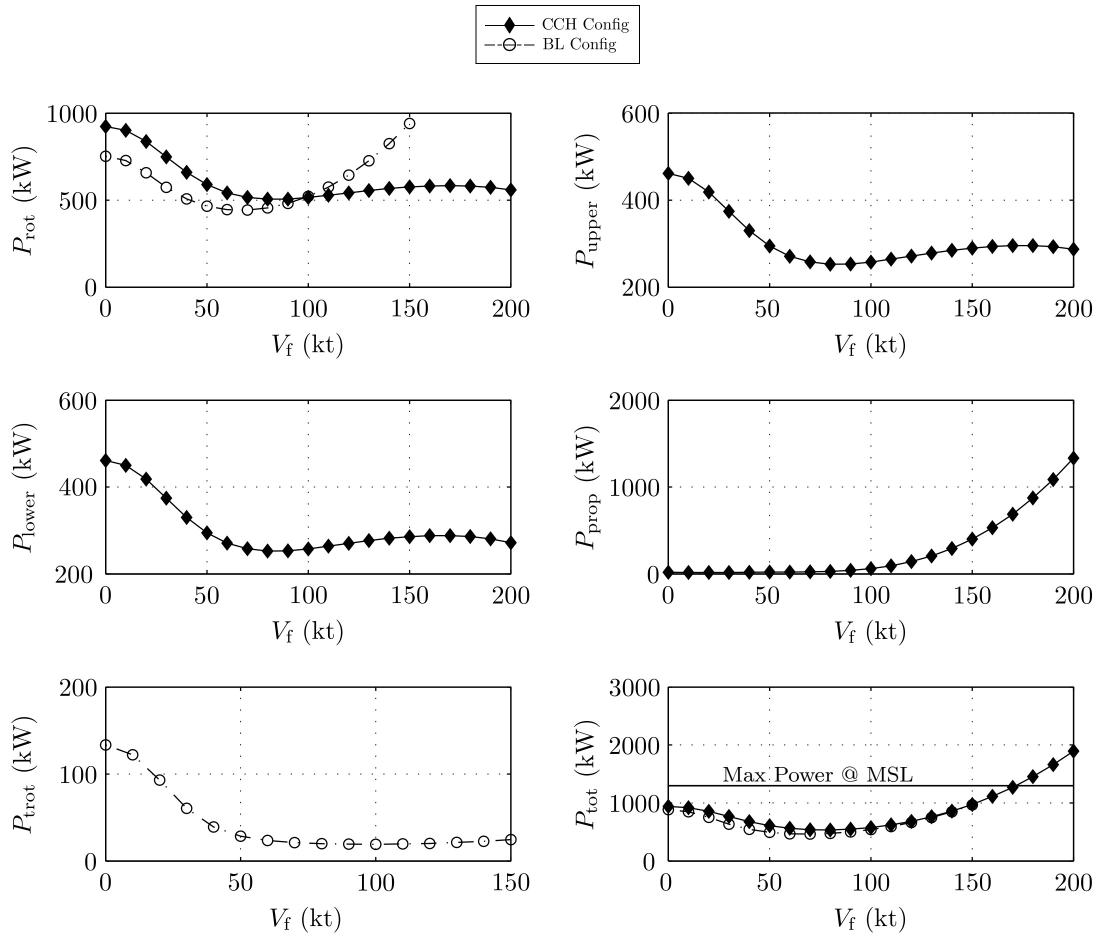

Figure 4.2: Predicted Power Required for the CCH and BL Configurations in Steady Level Flight at MSL

reasoning for this approach is so that the differences between the two rotor systems are confined to the vertical separation of the rotors and not to the geometric differences of the rotor blades [52]. With this comparison method defined, Kim and Brown conclude that a coaxial rotor system consumes slightly less power than that of a single main rotor, a conclusion that is supported by Johnson [38]. Regarding the current modelling of the coaxial rotor, which is described in a flight dynamics investigation of compound helicopters by Ferguson and Thomson [87], the comparison of a coaxial rotor to that of a single rotor gives similar power predictions. This is perhaps due to the rudimentary nature of the coaxial inflow model which does not take into account the radial contraction of the upper rotor wake. However, the coaxial rotor model has shown to agree well [87] with the coaxial hover results provided by Harrington [55] and forward flight results by Dingeldein [56].

The power of the CCH and BL configurations are shown in Figure 4.2. The predicted main rotor hover power of the BL and CCH configurations is 765kW and 922kW, respectively. The CCH configuration's rotor power is greater than that of the single rotor in the hover. This result is slightly misleading as it could be interpreted to suggest that the single main rotor is more efficient than the coaxial rotor. As mentioned in the previous discussion, to compare fairly the merits of the two rotor systems the single rotor must have the same number of identical blades to that of its coaxial rotor counterpart [52]. The coaxial rotor has a solidity of 0.127, which is based on the XH-59A demonstrator aircraft [79], whereas the conventional single rotor's solidity is 0.077. Hence, the coaxial rotor requires greater power in the hover due to its increased solidity which raises profile power losses. The high level of solidity featured on the XH-59A's main rotor was likely due to high speed design considerations. This design concept does not feature wing compounding, hence the coaxial rotor is responsible for providing the necessary lifting force at high speeds. The lateral lift offset fully exploits the high dynamic pressure on the advancing side of the rotor disc. However, on the opposite side of the rotor disc, the retreating side, a significant portion of the disc operates in reverse flow and therefore is incapable of contributing to the lifting force. This effectively reduces the rotor disc area and a high level of solidity is required to maintain the lifting force at high speeds. Returning to the presented results, the CCH configuration's rotor power reduces as it transitions into forward flight like that of the BL configuration. As the conventional helicopter moves into forward flight, the power begins to decrease reaching a minimum value at 68kt. After this flight condition the power begins to rise due to the significant increase of airframe drag, requiring a large amount of propulsive power. This is generally one factor limiting the maximum speed of the helicopter as the power available is insufficient to overcome that due to the airframe drag, which is proportional to V_f^3. In contrast, notice after 80kt that the coaxial rotor power does not increase significantly unlike the single main rotor. This is due to a combination of the propeller providing the propulsive power and the introduction of the lateral lift concept so that the lifting capability of the advancing sides of the coaxial rotor is realised. The total power of the CCH configuration is slightly greater than the BL configuration under 100kt. After this flight speed the total power between the two configurations is comparable. The excess power of the CCH configuration becomes zero at approximately 170kt suggesting that for the aircraft to operate in this speed range requires an increase in installed engine power. Therefore the two compound helicopter configurations predict that a significant increase of installed engine power is required to operate these aircraft at high speed.

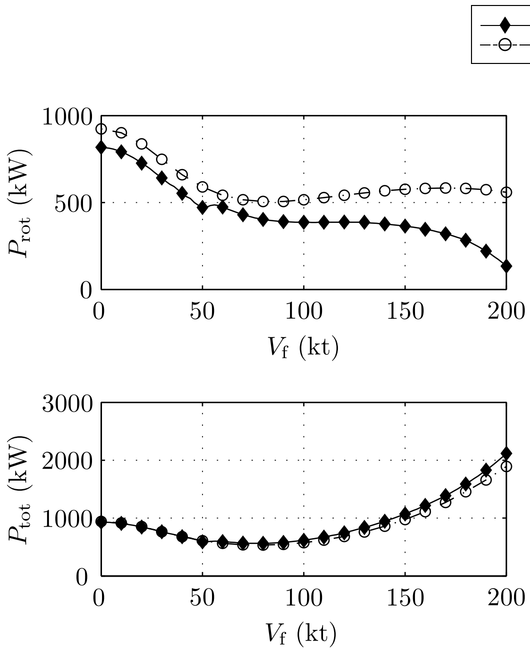

Figure 4.3: Predicted Power Required for the HCH and CCH Configurations in Steady Level Flight at MSL

Figure 4.3 compares the predicted rotor, propeller and total power of the two compound configurations in steady level flight. Throughout the speed range, the CCH configuration requires greater rotor power. At high speeds the rotor of the HCH configuration is significantly offloaded by the wing whereas with the CCH configuration the rotor is required to provide the lifting force as well as a portion of the propulsive force. As the coaxial rotor system provides a portion of the propulsive thrust to overcome the airframe drag, the necessary propeller power is lower than that of the two propellers featured in the HCH configuration.

It is also interesting to present the propeller(s) propulsive power as a percentage of the total power required. Figure 4.4 presents the propulsive power scaled by the total power for both HCH and CCH configurations. In the hover, the propeller of the CCH configuration consumes only 2% of the total power as the propeller is not required to produce any thrust. At this flight condition the propeller blades are rotating but the blades are feathered so that no thrust is required. Consequently, the propeller is not required to accelerate air rearwards, therefore the majority of propeller power at this point is due to profile power. In contrast, the two propellers of the HCH configuration occupy 12% of the total power in the hover. In this particular configuration the two propellers require power to provide the anti-torque moment. As the HCH configuration moves into forward flight, the power of the two propellers increases and there is a notch

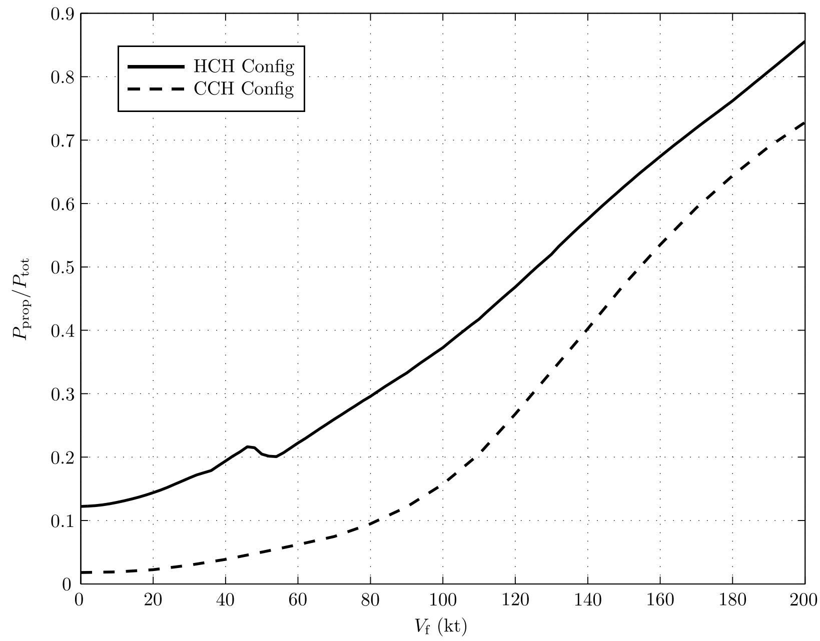

Figure 4.4: Ratio of the Propeller(s) Power Against the Total Predicted Power at MSL

at approximately 50kt due to the wing stalling which alters the amount of main rotor power required to compensate for the greater aerodynamic download the wing provides. In relation to the CCH configuration, after 100kt there is a steep rise in the percentage of propulsive power as the propeller divorces the main rotor of its propulsive duties. At 200kt, the propeller of the CCH configuration is responsible for 73% of the total power. Whereas for the HCH configuration the two propellers occupy 85% of the total power for that particular vehicle.

4.2 Maximum Speed

The maximum speed of a conventional helicopter is restricted due to aerodynamic limitations, installed engine power and airframe drag [1]. Due to these restrictions, the maximum speed of a conventional helicopter may typically be limited to approximately 150kt. However, the compound helicopter design aims to surpass this flight speed by the use of compounding to alleviate the aerodynamic limitations of the main rotor system. In this case the aircraft's speed may be limited by the installed power rather than retreating blade stall. Hence, for this analysis, it is assumed that the only restriction to the forward speed of the compound helicopter is the installed engine power. By making this assumption, the maximum speed of each compound configuration is determined by a Newton-Raphson technique which calculates the flight speed whereby the power available matches the power required by the vehicle.

Although the HCH and CCH configuration design parameters were determined in the development of the respective configurations [87], certain design parameters can be changed in order to observe their influence on aircraft performance. The design parameters which are of most interest are the installed engine power, mass and airframe drag of the configurations. It has been previously predicted that the compound configurations would need an increase of installed engine power relative to the BL configuration which would inevitably increase the mass of the vehicle. Therefore the effect of increasing the aircraft mass is of interest. Also, one of the main perceived advantages of the compound helicopter is that it has the ability to operate at high speeds where airframe drag becomes excessive. A conventional helicopter's fuselage is not as aerodynamically clean when compared to a fixed wing aircraft [37], therefore incurring a high drag penalty at high speeds. There are various sources of airframe drag which include the main rotor hub attachment, installation of the engine as well as the basic fuselage shape [88]. Hence, it seems likely that a successful compound helicopter design would feature a low drag rotor hub and fuselage design. There is a practical limit to which the fuselage drag could be reduced since the fuselage is required to hold the payload for various missions. Generally, the airframe drag is modelled by the equivalent flat plate drag area which represents both the fuselage and rotor hub drag. Therefore, the airframe drag is given by the simple relationship

$$D = \frac{1}{2}\rho V^2 f_e \tag{4.1}$$

For the present study, the same fuselage shape and size is assumed for all of the three aircraft configurations, with its equivalent flat plate area approximately equal to 1.9m^2. However, due to drag reduction techniques, statistical data discussed by Ormiston [23], suggests that the equivalent flat plate area of a a low airframe drag design can be approximated with

$$f_e = 2.5\left(\frac{W}{1000}\right)^{2/3} \tag{4.2}$$

Using this relationship and the current aircraft weight suggests that the airframe drag could be reduced by 25%. This low drag fuselage design can be modelled simply by multiplying the original airframe drag force, X_{fus}, by 0.75. Table 4.1 gives an overview of the design cases studied. The design parameters of Case E reflect, in all probability, what a compound helicopter would feature: an increase of engine power to operate the aircraft at a high speed range with a low drag airframe design. Also the mass is increased by a factor of 1.1 to compensate for additional installed power and the inclusion of propellers to the original design.

Case A	Case B	Case C	Case D	Case E
Standard Case	$P_{avail} = 1.4P_{base}$	$X_{base} = 0.75X_{fus}$	$M_a = 1.1M_{base}$	$P_{avail} = 1.4P_{base}$ $X_{base} = 0.75X_{fus}$ $M_a = 1.1M_{base}$

Table 4.1: Compound Helicopter Design Cases

The maximum speeds of the two compound helicopter configurations and design cases are shown in Table 4.2. Restricting the analysis to the HCH configuration, the maximum speed of case A is 163kt which is a modest increase relative to the 140kt maximum speed of the BL configuration [89]. Although the wing offloads the main rotor, the power of the two propellers increases to provide the propulsive power and to maintain a near level fuselage attitude. Consequently, the maximum speed of the HCH configuration, case A, is only slightly greater than that of the BL configuration. With the greater installed engine power, case B, there is an increase of maximum speed to 188kt which is a 25kt increase relative to case A. The reduction of fuselage drag, case C, increases the maximum speed by 15kt. With case D, the increased mass case, the maximum speed is lowered as the rotor power is increased to compensate for the additional weight of the vehicle. The greatest maximum speed is achieved by case E due to the combination of the increase of engine power and the reduction of airframe drag.

In terms of the CCH configuration, for case A the maximum speed is 172kt which is greater than its HCH configuration counterpart. This result is consistent with Figure 4.3, which indicates that at flight speeds in the region of 160kt that the CCH configuration's power setting is lower than the HCH configuration. This consequently

	Maximum Speed (kt)				
Configuration	Case A	Case B	Case C	Case D	Case E
HCH	163	188	178	161	202
CCH	172	197	189	170	216

Table 4.2: Maximum Speeds of the Compound Helicopter Cases

allows the CCH configuration to achieve a greater maximum speed. The cases of the CCH configuration exhibit a similar trend to the HCH configuration with the maximum speed of cases B, C and E rising when compared to case A. Case E achieves the greatest speed of 216kt which is significantly higher than the maximum speed of the HCH configuration. This result suggests that the one propeller vehicle, which is featured in the CCH configuration, is more suitable as a high speed design concept than the other compound helicopter. The maximum speed of the HCH configuration is limited by the excessive power to drive the two propellers to overcome the airframe's drag.

4.3 Hover Ceilings

The high speed aspect of the compound helicopter design is an attractive performance benefit, however the ability to efficiently hover is also key if the vehicle is to fulfil various missions and roles. One performance metric to indicate the hover efficiency of the helicopter is the hover ceiling. In order to predict the hover ceilings of these three aircraft configurations, each configuration is trimmed in the hover and their altitude increased until the power required matches the power available, within some given tolerance. The hover ceilings are estimated by the use of a simple Newton-Raphson numerical technique, to ensure rapid convergence. For the following analysis it is assumed that the power available, as described by Keys [90], is given by

$$P_{avail} \approx P_{MSL}\frac{\delta}{\theta} \tag{4.3}$$

where δ is the pressure ratio, approximated by

$$\delta = (1 - 6.876 \times 10^{-6}h)^{5.265} \tag{4.4}$$

The temperature, in the units of °F, can be calculated by

$$T = 59 - 3.57\left(\frac{h}{1000}\right) \tag{4.5}$$

The temperature ratio, θ, which is simply the ratio between the local temperature and the temperature at mean sea level can be determined easily. Similar to that of the maximum speed analysis, design parameters are altered to investigate their effect on

	Hover Ceilings (m)		
Configuration	Case A	Case D	Case F
BL	3210	2280	
HCH	2786	1849	3143
CCH	2529	1583	

Table 4.3: Hover Ceilings of Compound Helicopter Cases A, D and F

the hover ceilings, with only cases A and D being considered. The power available can be increased like that of cases B and E, however is it found that with this high level of power available the helicopter configurations reach an altitude whereby the collective angles of the two main systems are excessive and therefore approaching stall. Since the modelling does not take into account non-linear aerodynamics it is reasonable to expect the results from these particular cases to be unreliable, hence the results of these cases are not presented. Of course, case C is also not studied as there is no parasitic drag arising from the fuselage in the hover.

The hover ceilings of the three aircraft configurations are shown in Table 4.3. As the BL configuration features the lowest power setting of each of the aircraft configurations in the hover, see Figures 4.1 and 4.2, it achieves the greatest hover ceiling of 3210m. Considering the HCH configuration, the hover ceiling is less than that of the BL configuration primarily due to the aerodynamic download of the wing which results in increased rotor power to compensate. Although the wing is beneficial at high speeds to offload the main rotor, in hover and low speed flight it provides a significant download reducing low speed performance. This problem of aerodynamic download was encountered in the development of the tilt-rotor and the use of flaps was shown to ameliorate the wing download in low speed flight [24]. Therefore, case F represents the case where the wetted area of the wing is reduced by 60% by the use of flaps. The wing still provides an aerodynamic download, an inevitable consequence of lift compounding, but the power of the two propellers, to provide the anti-torque moment, is smaller than that of the conventional helicopter's tail rotor. The net effect is that the use of flaps results in comparable hover ceilings.

The CCH configuration achieves the lowest hover ceiling of the three aircraft configurations of 2529m. This is due to this configuration requiring the greatest power in the hover of the three configurations which results in the lowest hover ceiling. The effect of thrust compounding does not influence this result as the propeller only requires small levels of power in the hover. It should be stressed that this coaxial rotor system is not an optimum system such as that on the Sikorsky X2 which features non-linear twist of the rotor blades. In order to minimise the induced power losses from the coaxial rotor system the twist of the lower rotor blade is required to be of double hyperbolic form, as shown by Leishman and Ananthan [51]. This is due to the radial contraction of the upper rotor's wake upon passing through the lower rotor. The rudimentary nature of this coaxial rotor inflow model used within this current study assumes no radial contraction of the upper rotor's wake and therefore is unsuitable to predict the performance benefit that nonlinear twist throughout the lower rotor blades offers. However, the coaxial rotor inflow model has been validated in previous compound helicopter work [87]. Perhaps a higher level of modelling and optimisation of the coaxial rotor system would predict reduced levels of power than the results presented here.

4.4 Range and Endurance

The range and endurance of a helicopter indicate the capability of the aircraft to perform various missions and roles. There are various methods to predict these performance metrics but the approach presented in the following is given by Johnson [2]. Firstly, focusing on range, the range of a helicopter can be found by integrating the specific range over the total fuel weight, which is mathematically stated as

$$R = \int_0^{m_{fuel}} \frac{dR}{dm_{fuel}} dm_{fuel} \tag{4.6}$$

The specific air range, dR/dm_{fuel} (SAR), is given by the following

$$\frac{dR}{dm_{fuel}} = \frac{1}{SFC} \frac{V_f}{P_{tot}} \tag{4.7}$$

where SFC is the specific fuel consumption and V_f/P_{tot} is the optimum speed to power ratio to maximise range. The specific fuel consumption is a function of fuel flow rate and the power required, hence

$$SFC = \frac{\dot{m}_{fuel}}{P_{tot}} \tag{4.8}$$

In order to determine the specific fuel consumption, the fuel flow rate through the engine is required. The relationship between the fuel flow rate and power can be approximated with

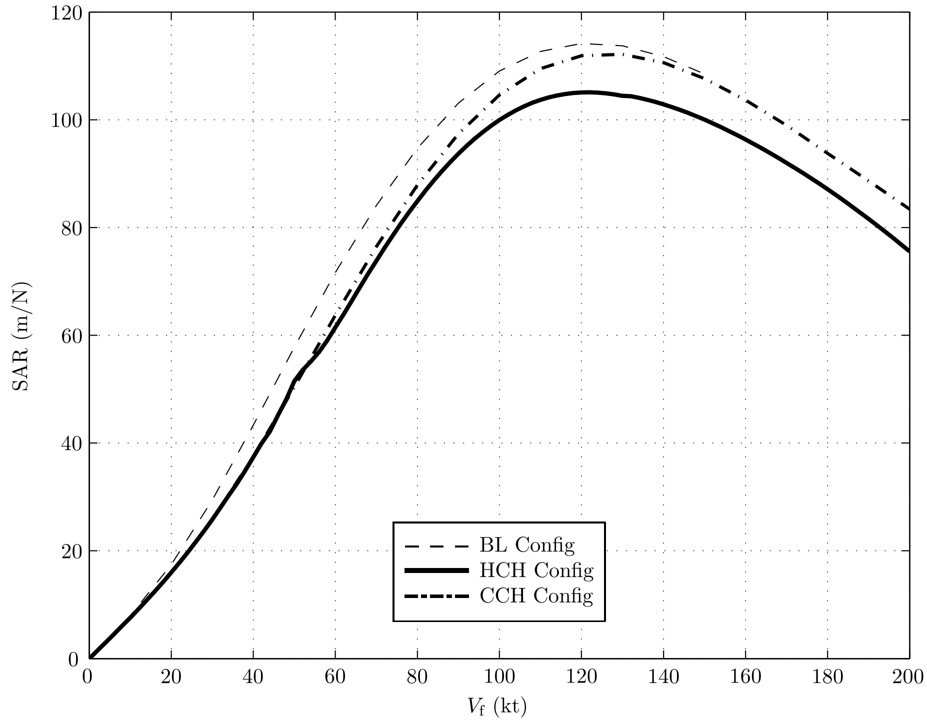

Figure 4.5: Predicted Specific Range of the Three Aircraft Configurations

$$\frac{\dot{m}_{fuel}}{\delta\sqrt{\theta}} = N_E A_E + 1.341 B_E \frac{P_{tot}}{\delta\sqrt{\theta}} \tag{4.9}$$

where N_E is the number of engines and both A_E and B_E define the engine's fuel flow with their units being lb/hr and (lb/hr)/HP, respectively. Using data relating to the conventional aircraft's engine [91], the value of A_E is approximated to be 67.5, whereas B_E is estimated to be 0.34. To determine the range of these aircraft the mass of fuel must be known. Since these are fictitious configurations it seems convenient to express the predicted range results in specific range form, so that the range can be determined by the product of the SAR and fuel mass. For the current analysis it is assumed that the specific fuel consumption and V_f/P_{tot} are independent of the vehicle weight. Furthermore, it is assumed that the ratio V_f/P_{tot} does not change over time, although in reality the optimum ratio of speed to power would be a function of altitude and vehicle weight. With these assumptions the SAR for the three aircraft configurations is shown in Figure 4.5. As expected, the BL configuration achieves the greatest specific air range of 114m/N at a speed of approximately 120kt. The maximum SAR of the CCH configuration is slightly less than that of the BL configuration which is achieved at 130kt. The results estimate that HCH configuration achieves the lowest SAR of

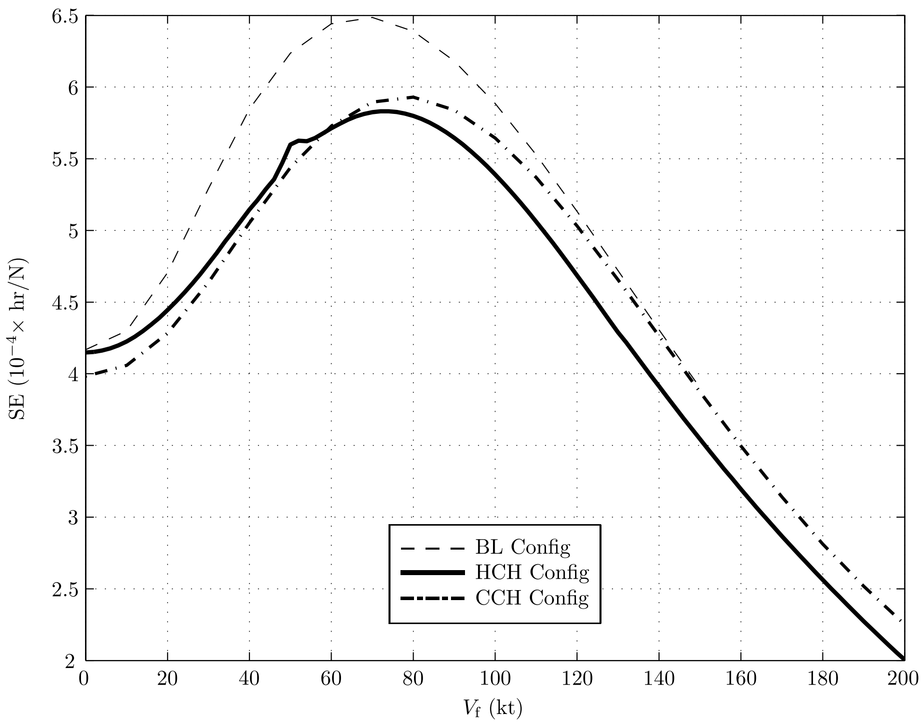

Figure 4.6: Specific Endurance

Figure 4.7: Predicted Specific Endurance of the Three Aircraft Configurations

104 m/N however an inherent advantage of a winged helicopter is the opportunity of carrying more fuel which would be factored into the design process.

As the helicopter is commonly used for scouting missions, the endurance of the aircraft is particularly important to maximise search time. The endurance of an aircraft is given by

$$E = \int_0^{m_{fuel}} \frac{dE}{dm_{fuel}} dm_{fuel} \tag{4.10}$$

where the specific endurance, dE/dm_{fuel} (SE), is

$$\frac{dE}{dm_{fuel}} = \frac{1}{\dot{m}_{fuel}} \tag{4.11}$$

Figure 4.6 shows the predicted specific endurance of the BL, HCH and CCH configurations. Similar to the specific air range, the endurance can be determined by the product of the specific endurance and weight of the aircraft fuel. The maximum endurance of each of the configurations is achieved when their respective power is at its

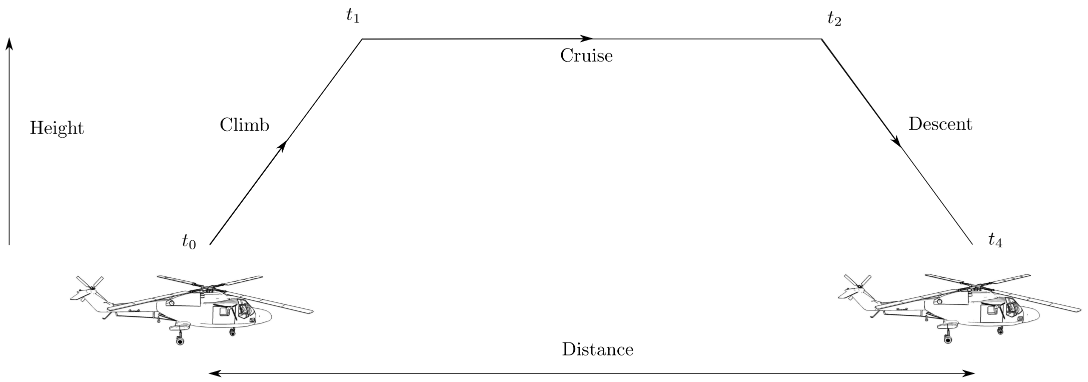

Figure 4.8: Mission Profile

lowest, which can be determined from Figures 4.1 and 4.2. Consequently, the BL configuration achieves the lowest power setting of the three configurations at 67kt, whereas the best endurance speeds of the HCH and CCH configurations are 74 and 82kt, respectively. It is interesting to note that despite the addition of compounding to both compound helicopters, the shape of the SE curve is similar to that of a conventional helicopter. Comparing the BL configuration to the two compound helicopters, the estimated endurance of the BL configuration is greater due to lower power requirements predicted in Figure 4.1. At this speed, between 60 and 80kt, the combination of the BL configuration's main rotor providing both the lifting and propulsive forces as well as the fin offloading the tail rotor allows the vehicle to achieve a lower power setting than the two compound helicopters. The maximum endurance of the two compound configurations is similar, although the endurance of the CCH configuration is slightly higher, which is consistent with Figure 4.3. Within this speed range the addition of thrust compounding is not particularly beneficial, as the propeller(s) require power but not much propulsive force is needed.

4.5 Mission Performance

The performance of a helicopter flying a given mission is of major interest to the operator of the aircraft. The helicopter is designed to be capable of performing various missions such as anti-tank, anti-submarine and search and rescue. Each mission is unique with some missions requiring the helicopter to hover for sustained periods of time whereas with other missions the helicopter operates at a high speed for a considerable time. The following analysis estimates the performance of the three aircraft configurations flying standard helicopter missions.

Loiter Mission

The first mission is a standard mission, as shown in Figure 4.8, with the helicopter beginning at the runway and flying for some specified distance or time to reach its destination. The helicopter can successfully perform search and surveillance operations due to its unique ability to hover and land in demanding environments. For these particular types of missions the helicopter's crew search or patrol large areas whilst operating the aircraft at the lowest possible power setting to maximise endurance. Of course, maximising the endurance of the helicopter is of key interest to any operator so that the helicopter can successfully patrol an area for an extended period of time without the need to refuel.

The loiter mission is split into five main sections, namely, the start up, climb, cruise, descent and shut-down portions. Each of these respective sections is discretised into small time increments, typically 25s, to take into account the fuel burn and its effect on the vehicle's mass which consequently alters the power requirements throughout the mission. An additional advantage of this approach is that the change of density due to altitude changes can be modelled easily. The total length of the mission is two hours and it is assumed that the helicopter accelerates to its best endurance flight speed at the take-off site before climbing to the cruise altitude of 2km. In the loiter mission it is assumed that the flight speed does not vary throughout the mission. In the climb section of the mission, it is assumed that each of the aircraft configurations take 4 mins to reach their cruise altitude. This corresponds to the vehicles climbing at a climb angle of $\approx 10°$, so that the configurations reach their specified altitudes in a timely manner without exceeding the power available. However, in the descent segment of the mission the climb angle is set to a constant value of -3° to avoid the respective main rotors reaching their autorotational conditions. Moreover, it is assumed that all of the three aircraft configurations operate at their maximum continuous power settings for a small period of time at the start up and shut down segments, with five minutes being a typical time for these sections [90], to take into account the fuel burned whilst performing procedural checks.

Table 4.4 shows the power and the fuel burned throughout the loiter mission for the three helicopter types. The power of all three configurations rises in the climb portion of the mission, relative to their cruise power settings, as each configuration requires greater induced rotor power in order to climb to an altitude of 2km. The BL configuration operates at the lowest power setting of 438kW in the cruise segment of the mission whereas the two compound configurations operate at comparable power settings. The

	BL Config $V_{cruise} = 75$kt $t = 2$ hr		HCH Config $V_{cruise} = 81$kt $t = 2$ hr		CCH Config $V_{cruise} = 87$kt $t = 2$ hr	
Mission Phase	Power (kW)	Fuel Burned (kg)	Power (kW)	Fuel Burned (kg)	Power (kW)	Fuel Burned (kg)
Start up	1300	27.27	1300	27.27	1300	27.27
Climb	899	16.8	979	17.96	955	17.6
Cruise	438	243.5	516	271.84	524	274.7
Descent	277	18.9	356	21.3	370	21.7
Shut down	1300	27.27	1300	27.27	1300	27.27
Total Fuel Burned		333.74		365.44		368.24

Table 4.4: Power and Fuel Burned Throughout the Loiter Mission

power settings of the HCH and CCH configurations in the cruise portion are 516kW and 524kW, respectively. This is consistent with Figure 4.6 which predicts comparable endurance performance between the two compound helicopter configurations at mean sea level. As the vehicles operate at the cruise condition for the majority it follows that the HCH and CCH configurations burn a greater amount of fuel relative to the BL configuration. The BL configuration requires 334kg of fuel to complete this mission whereas the two compound helicopter configurations burn approximately 10% more.

Range Mission

Another typical mission that a helicopter performs is the so called range mission. This is a mission whereby the helicopter carries payload from a particular starting point to a destination, that is a specified distance away. If the distance is significant then a fixed wing aircraft would be commonly used to fulfil the mission whilst managing to carry a much greater payload than a helicopter. However, the helicopter's unique ability to operate safely at low speeds and land in demanding environments makes it suitable for various missions, such as ship replenishment. Furthermore, one of the perceived roles of the compound helicopter, due to its greater speed, is that it could perform flights in the civil market, i.e. city-hops. A light fixed wing aircraft would perform the mission quicker than that of a compound helicopter but the helicopter has the additional advantage of being able to land in a populated city environment rather than an airport, which could subsequently reduce travel time.

The main aim of the loiter mission is to minimise fuel burn whereas the range mission is concerned with maximising the distance travelled for a given quantity of fuel [90]. The time of the range mission can be simply calculated by defining the climb, cruise and descent flight speeds and using the specified distance that the aircraft is to travel. Similar to that of the loiter mission, it is assumed that the aircraft begins at the take-off site at its climb speed before commencing its ascent to a cruise altitude of 2km. The aim of the range mission is to maximise the distance travelled per unit fuel, hence the cruise flight speed should correspond to the condition where the ratio P_{tot}/V_f is at a minimum. Whilst this is true, the SAR curve (Figure 4.5), is relatively flat where the ratio P_{tot}/V_f is at a minimum. Hence, a greater flight speed can be chosen without adversely reducing the range of the aircraft [38, 74]. Therefore, whilst in the cruise segment of the mission each of these aircraft configurations travel at their maximum operating speeds to reduce travel time. Generally, the time taken to complete the mission and the fuel burn are of equal importance to operators. However, in the climb stage of the mission the aircraft configurations operate at their minimum endurance speeds, where the maximum climb rate is achieved, so that they can ascent to the cruise altitude as quickly as possible.

Table 4.5 shows the predicted power and fuel burn of the BL, HCH and CCH configurations performing a 400km range mission. The three aircraft configurations reach the cruise altitude of 2km in 4 mins which requires a significant amount of power for each configuration. In terms of the descent portion of the mission, the power of all three configurations reduce, relative to the power in cruise, as expected. During the

	BL Config $V_{cruise} = 140$kt $t = 1.65$ hr		HCH Config $V_{cruise} = 161$kt $t = 1.46$ hr		CCH Config $V_{cruise} = 168$kt $t = 1.40$ hr	
Mission Phase	Power (kW)	Fuel Burned (kg)	Power (kW)	Fuel Burned (kg)	Power (kW)	Fuel Burned (kg)
Start up	1300	27.27	1300	27.27	1300	27.27
Climb	899	16.8	979	17.96	955	17.6
Cruise	724	278.5	1056	324.56	1052	308.8
Descent	278	19.3	352	21.2	366	21.8
Shut down	1300	27.27	1300	27.27	1300	27.27
Total Fuel Burned		369.14		418.26		402.74

Table 4.5: Power and Fuel Burned Throughout the Range Mission

cruise stage of the mission the conventional Lynx helicopter travels at its maximum operating speed of 140kt, which is stated in Ref [89], consequently requiring 369kg of fuel to complete the mission. Although the BL configuration requires the least amount of fuel, it does take the longest time of 1.65hr to to complete the mission. One of the main perceived benefits of the compound helicopter is to operate at greater speeds than the conventional helicopter by avoiding the main rotor's inherent aerodynamic restrictions. Of course, this increased speed would reduce the time the vehicle would take to complete various missions and roles. The results presented here do capture this benefit with both the HCH and CCH configurations completing the mission in a shorter span of time relative to the BL configuration. The CCH configuration takes 1.40hr whereas the HCH configuration completes the mission in 1.46hr. However, there is penalty with regards to the amount of fuel required. This is primarily due to the conventional helicopter operating at lower power setting of 724kW in the cruise whereas the compound helicopter configurations require ≈45% more power at this stage. When comparing the compound helicopter configurations, the CCH configuration requires 15.5kg less fuel than the HCH configuration. Although the power in the cruise of the two configurations is comparable, the higher cruise speed of CCH configuration results in less fuel being burned.

4.6 Chapter Summary

This Chapter has examined the effect of compounding and its influence on the performance of compound helicopter configurations. Recall that this was not a design exercise where the available power, weights and main rotor design were sized to fulfil a particular mission requirement. The approach taken, to quantify the performance of the two compound helicopters, was to retain the same vehicle shape and size as with the conventional helicopter. The motivation for this approach is so that the effects of compounding were isolated from other factors, thereby ensuring that the three sets of results could be compared fairly. Therefore, the results from this Chapter should be interpreted within this context. The main conclusions of this Chapter are listed below:

- The results confirm that the conventional helicopter's fuselage shape is not suitable for a high speed design and that a compound helicopter would require an optimised airframe design to reduce drag at high speed.
- The results also predict that a compound helicopter would require significantly more power than a conventional helicopter of similar mass. This increase of

installed engine power is needed so that the compound helicopter can operate in high speed flight.

- As expected, the addition of wing compounding to the HCH configuration reduces the main rotor power at high speeds. However, the power of two propellers, which provide the thrust compounding, increase with air speed to produce the propulsive force to overcome the airframe drag. The net result is that the HCH configuration requires greater power than the BL configuration across the speed range.

- Concerning the CCH configuration, the addition of thrust compounding does not significantly influence the performance of the vehicle below flight speeds of 100kt as the propeller is not required to produce axial thrust. Consequently, at these flight speeds it is the coaxial rotor that determines the performance of this vehicle. However, after 100kt the propeller provides a significant portion of axial thrust to divorce the coaxial rotor from its propulsive duties. The results predict that the BL configuration requires greater power than the CCH configuration between speeds of 100 and 150kt.

- With the assumption that the three aircraft configurations are of the same vehicle shape and mass, the compound helicopter configurations show modest increases of maximum speed relative to the BL configuration. However, the maximum speeds of the compound configurations can be significantly increased by a combination of airframe drag reduction and increasing the installed engine power. Hence, as expected, the addition of compounding can increase the maximum speeds of the vehicles if the design is further optimised.

- In terms of the hover ceilings of the three configurations, the BL configuration achieves the greatest hover ceiling whilst the HCH configuration achieves a lower hover ceiling due to the aerodynamic download of the wing. Regarding the CCH configuration, the level of modelling presented within predicts that it obtains a hover ceiling of 2529m. The addition of thrust compounding has a minor influence regarding this result as the propeller is pitched to provide a limited amount of thrust. Hence, it is the design of the coaxial rotor which determines the vehicle's hover ceiling. It is logical to assume that further optimisation of the design through nonlinear rotor blade twist would enhance the hover ceiling estimated in this study.

- The predicted maximum ranges of the BL and CCH configurations are similar. The estimated maximum range of the HCH configuration is 6% less than the

CCH and BL configurations. However it is highlighted that the inclusion of wing compounding to the HCH configuration's design opens the possibility to store additional fuel provisions. In terms of the endurance results, the BL configuration is capable of the longest endurance. The predicted maximum endurance of the two compound helicopter configurations are similar. The maximum endurances occur at speeds between 70 - 80kt, where the benefit of either thrust or wing compounding is not fully realised.

- Concerning the loiter mission, the BL configuration burns the least fuel of the three configurations. The BL configuration burns 334kg of fuel whereas the CCH and HCH configurations burn approximately 366kg of fuel. This result is consistent with the specific endurance results presented. With the range mission, the CCH configuration operates at the highest cruise speed, allowing the vehicle to complete the mission in 1.4hr, which is quicker than both the BL and HCH configurations. The addition of thrust and wing compounding to the compound helicopters do indicate that significant reductions in mission time can be achieved. However, this must be balanced with the penalty of burning more fuel than a conventional helicopter of the same vehicle shape and size. In can be concluded, with some confidence, that with further optimisation of the compound helicopter design further gains can be made in terms of flight time reduction whilst minimising the fuel burn.

Chapter 5

Stability Analysis of Compound Helicopter Configurations

5.1 Introduction

The previous Chapters have examined the effect of compounding on the trim and performance results of the vehicle. The next logical step, following on from these analyses in Chapters 3 and 4, is to assess the stability of the aircraft configurations. This will provide an insight to the broad effects of lift and thrust compounding on the stability of the helicopter. The starting point of a stability analysis is to take the nonlinear equations of motion and reduce them to linear form. Generally, there are two methods to linearise the aircraft equations of motion [36]. The first approach is to use a numerical linearisation algorithm which involves the perturbation of the aircraft's forces and moments about the trim condition, thereby allowing the calculation of the stability and control derivatives through numerical differentiation. Conversely, a system identification approach is commonly used to fit a linear simulation model's response to that of a nonlinear model [92]. The approach used within this study is the numerical linearisation approach which has been detailed within the literature to assess the stability of both rotary and fixed wing aircraft [93, 94].

The main aim of this Chapter is to assess the dynamic stability of compound helicopters and compare their stability to a conventional helicopter, then investigate how the addition of compounding to the configurations influences the helicopter's stability characteristics. In terms of the structure of this Chapter, it begins with a brief overview of the numerical linearisation approach with Appendix C supporting the discussion by providing a more detailed description. Following this discussion, the salient stability and control derivatives of the three aircraft configurations are presented. Moreover, with the nonlinear equations reduced to linear form, the natural modes of motion of the configurations are discussed. The Chapter concludes with a summary of the main findings.

5.2 Linearisation Process

The helicopter equations of motion are inherently nonlinear and can be conveniently represented in the form

$$\dot{\mathbf{x}} = \mathbf{F}(\mathbf{x}, \mathbf{u}) \tag{5.1}$$

With the application of a linearisation algorithm, which is fully described in Appendix C, the nonlinear equations can be reduced to the form of

$$\dot{\mathbf{x}} = \mathbf{A}\mathbf{x} + \mathbf{B}\mathbf{u} \tag{5.2}$$

where the state and control vectors are perturbations from the trimmed state. The system matrix, **A**, contains the stability derivatives whereas the control derivatives define the control matrix, **B**. The structure of these matrices, corresponding to a conventional helicopter simulation, are shown in Appendix C, Equations (C.11) and (C.12).

5.3 Stability Derivatives

Nonlinear models play an important role in helicopter flight simulation, however one of their drawbacks is that it is difficult to isolate what causes the complex flight behaviour of the aircraft. In contrast, greater understanding of the vehicle's motion can be obtained by using simplistic linear models. This is one reason why the nonlinear equations of motion are commonly reduced to linear form. The stability derivatives are particularly useful and represent how the helicopter responds following a small perturbation to a vehicle state. Hence, to understand the effect of thrust and lift compounding on the stability of a compound helicopter, the important stability derivatives between the three aircraft configurations are presented and compared.

Translational Velocity Derivatives

In the majority of cases, a velocity perturbation from the trimmed state alters the loading across the helicopter's main rotor blades with the magnitude and direction of the rotor thrust vector changing as a consequence. There are also additional effects from the other components of the aircraft, however in several cases the contribution of the main rotor dictates the values of the stability derivatives. A perturbation of forward speed, u, increases the lift across the advancing side of the rotor disc whereas it decreases the lift across the retreating side. Additionally, there is an increase of the airframe's drag due to the perturbation. In terms of the drag damping derivative, X_u, its variation across the speed range tends to be linear, representing the airframe's drag force following a perturbation [36]. This derivative is important as it is associated with the damping of the phugoid mode. Figure 5.1 presents the predicted drag damping derivatives of the three aircraft configurations as a function of flight speed. The addition of the propeller to the Coaxial Compound Helicopter (CCH) configuration has increased the level of drag damping when compared to the Baseline (BL) configuration. A positive perturbation of u, reduces the propeller's thrust. As a consequence the propeller contributes to reducing the axial force following a perturbation of u, hence the negative value of X_u. This effect also occurs in the Hybrid Compound Helicopter (HCH) configuration, but with greater impact due to the addition of the two propellers to the design. Hence, out of three aircraft configurations it is predicted that the HCH configuration has the greatest drag damping, Figure 5.1. In addition to the two propeller's influence to X_u, the wing also provides greater drag with a positive perturbation of u creating greater drag from the wing. One distinguishing feature of the HCH configuration is the rather unusual change of X_u between hover and 40kt, Figure 5.1. The two propellers and wing are the reason for this result. In terms of the propellers, the loading across the two discs alters significantly in low speed flight to balance the main rotor's torque. Furthermore, the port propeller provides reverse thrust in low speed flight which alters the direction of the induced velocity as it flows through the propeller disc. At approximately 40kt, the port propeller begins to provide forward thrust, hence changing the direction of the induced velocity. The direction of the induced velocity and the magnitude of propeller thrust influence the drag force following a perturbation of forward speed. The wing also contributes to the rather unusual appearance of X_u in low speed flight. In the hover, the local wing angle of attack is approximately -90° , due to the influence of the rotor wake. The wing is sensitive to a perturbation of u in low speed flight due to two reasons. Firstly, a forward perturbation of u causes the rotor wake to skews rearwards, it lowers the mean induced velocity v_0, thereby altering the local wing of angle of attack.

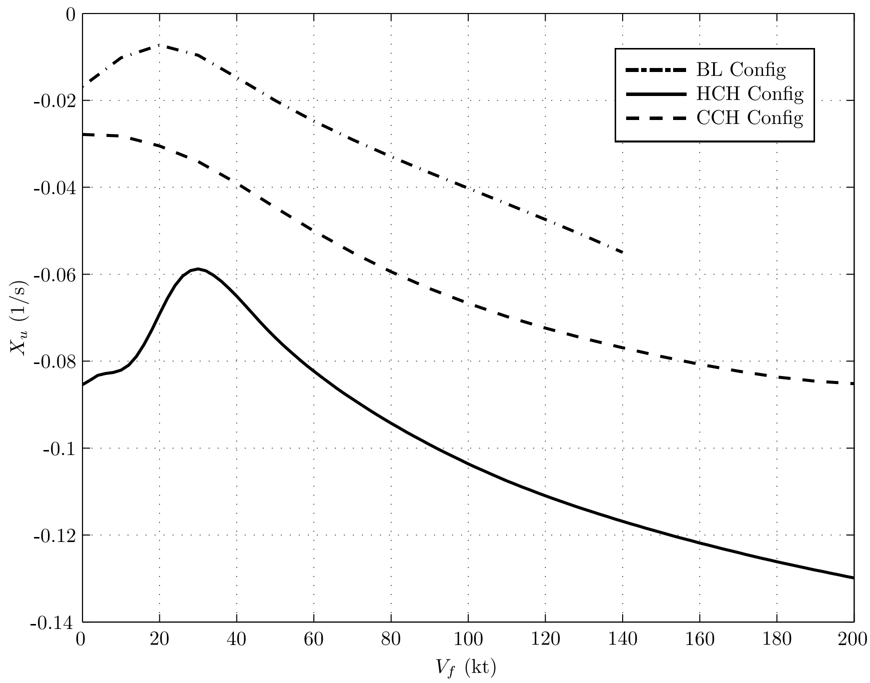

Figure 5.1: X_u Stability Derivative

Secondly, in low speed flight the perturbation of u changes the local airflow direction significantly. Neglecting wing pitch and the main rotor's contribution, the wing's angle of attack in low speed flight is approximately equal to $\tan^{-1}(W/U)$. Hence, even a small change of forward speed, in low speed flight, has a powerful impact on the local angle of attack value. As a consequence, in this flight regime the perturbation of u changes the direction of the wing force vector significantly. The net effect is that the combination of the wing and the two propellers provide a rather unusual shape of X_u in low speed flight.

One distinguishing feature of the conventional helicopter is cross-coupling - that is where a single axis control input or disturbance results in the aircraft responding in multiple axes [36]. This cross-coupling behaviour of the conventional helicopter is primarily due to the main rotor [36]. For example, a main rotor collective input increases the rotor thrust but also provides a yaw reaction due to the changes in torque. Another source of cross-coupling arises due to the effect of the rotor wake. The influence of the rotor wake can be observed by examining the stability derivative Y_u. For a fixed wing aircraft this derivative is essentially zero as there is little change in side force due to a perturbation in forward speed. However, with a helicopter in low speed flight a perturbation in forward speed gives a large change in the main rotor's wake skew angle [36]. This effectively reduces the local blade angle of attack at the rear of the

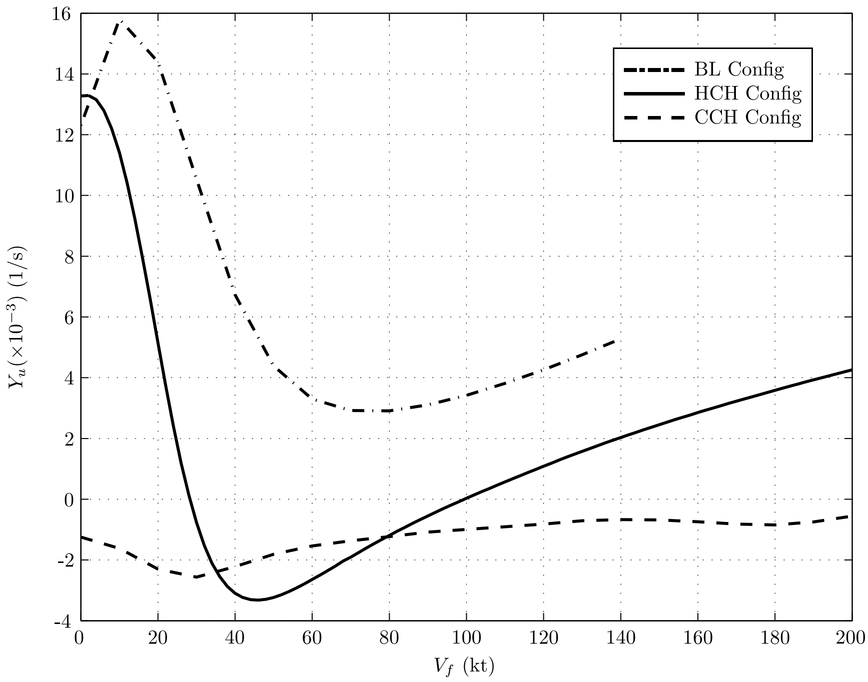

Figure 5.2: Y_u Stability Derivative

rotor disc. If the main rotor is rotating anti-clockwise, when viewed from above, then the forward speed perturbation tilts the main rotor to the starboard side, thereby changing the amount of side force. Figure 5.2 shows the predicted values of Y_u for the three aircraft configurations. The derivative is surprisingly high for the BL and HCH configurations, in low speed flight. However, for the CCH configuration this derivative, Y_u, is very small across the speed range. For this configuration, the perturbation in forward speed lowers the local blade angle of attack in low speed of the upper and lower rotor discs, with the upper rotor disc flapping to the starboard side whereas the lower rotor disc flaps to the port side. The flapping of the rotor discs in opposing directions effectively cancels out the side force, resulting in a lower value of Y_u. This result suggests that the CCH configuration is likely to have less cross-coupling than a single main rotor helicopter, a view that is supported by Johnson [38].

The heave damping derivative, Z_w, represents the change of rotor thrust following a perturbation in heave velocity. For a conventional helicopter this value generally tends to be negative throughout the speed range as a positive perturbation of heave velocity increases the angle of attack of the rotor disc, which results in greater rotor thrust [36]. For a conventional helicopter, the value of the heave damping derivative is dependent on the rotor blade loading - the ratio between the aircraft mass and the disc area. Figure 5.3 presents the predicted values of Z_w for all three aircraft configurations.

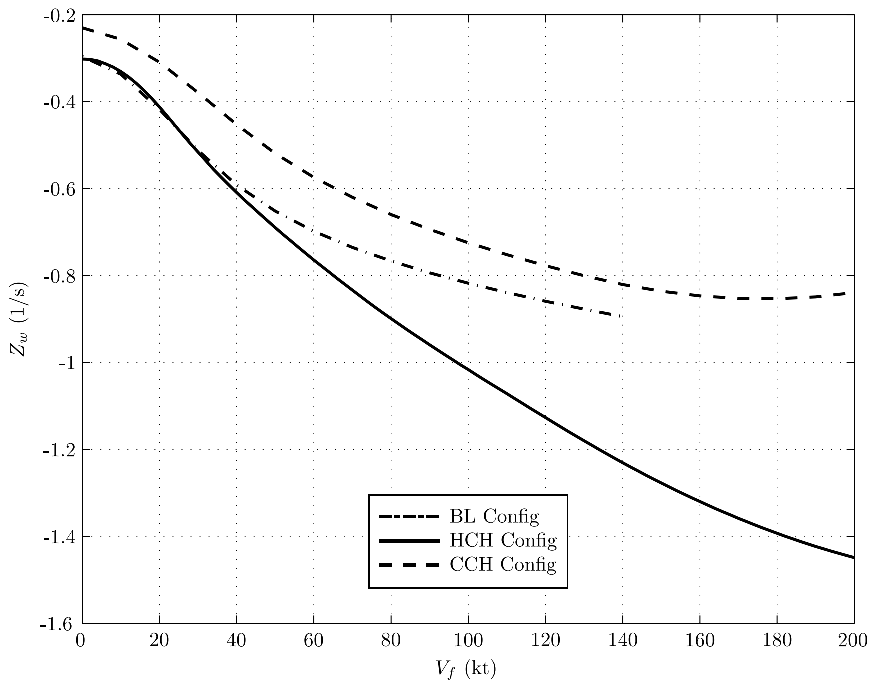

Figure 5.3: Z_w Stability Derivative

Concerning the CCH configuration, the estimated value of the Z_w in the hover differs from that of the BL and HCH configurations due to the differences in blade loading. As the vehicles move into forward flight, the change in main rotor inflow, as well as the contribution of other aircraft components such as fuselage and empennage begin to alter the value of Z_w. In terms of the two aircraft which feature no source of lift compounding, the BL and CCH configurations, the Z_w derivatives follow a similar trend across the speed range. The predicted values of Z_w for the BL and HCH configurations are comparable in low speed flight as the two aircraft feature identical rotor systems. However, after 60kt the stability derivative Z_w begins to decrease significantly for the HCH configuration as the wing begins to contribute to Z_w. In high speed flight following a perturbation of w both the rotor and the wing respond by producing greater lift, hence lowering the value of Z_w.

Two important derivatives in the aircraft's pitch axis are the M_u and M_w derivatives, commonly referred to as the speed and incidence static stability derivatives. The estimated speed derivatives of the aircraft configurations are compared in Figure 5.4. All three aircraft configurations exhibit a stable response with the fuselage of each of the configurations pitching up thereby decreasing the forward velocity. The perturbation of forward speed increases lift across the advancing side of the rotor disc whereas it reduces the lift across the retreating side. The flapping response of the rotor disc

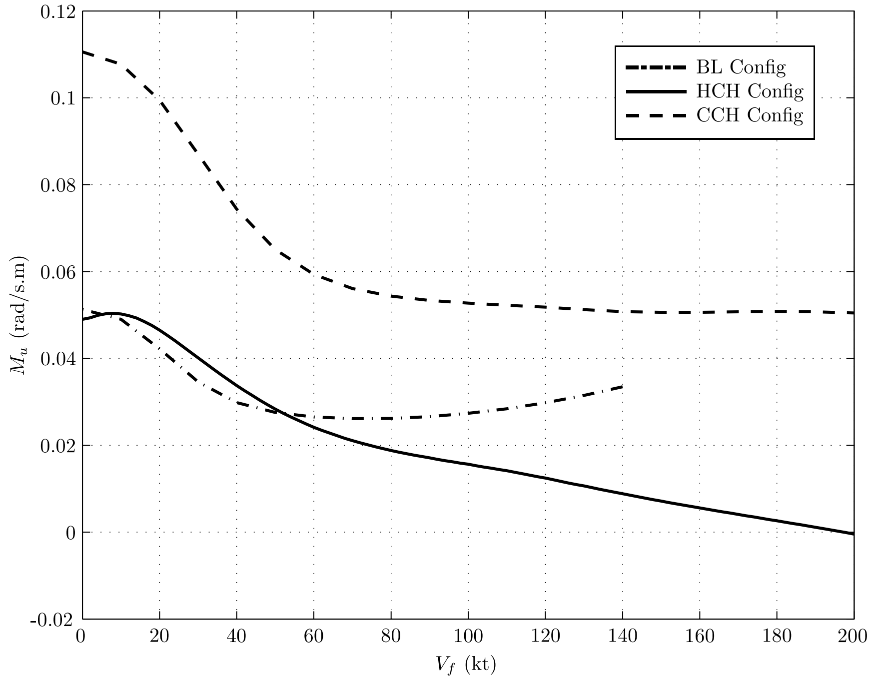

Figure 5.4: M_u Stability Derivative

occurs approximately between 60 - 90° out of phase with the aerodynamic changes, depending on the structural properties of the rotor blades, hence the forward perturbation has the net effect of tilting the rotor disc backward and pitching the aircraft up. The magnitude of the M_u derivative for the CCH configuration is greater than that of the two other configurations, due to its higher rotor hub stiffness. The values of M_u for the BL and HCH configurations are comparable up to a speed of 50kt. In terms of the BL configuration, M_u is fairly insensitive to flight speed after 50kt. In contrast, the HCH configuration's M_u values begin to reduce in a linear manner as the aircraft reaches speeds that exceed 50kt. In high speed flight, the wing of the HCH configuration provides a significant lifting force which also generates a powerful pitching moment as the quarter chord point of the wing is located aft of the centre of mass. As a result, a positive perturbation of forward speed increases lift and therefore the wing provides a nose-down pitching moment. At 200kt, M_u is effectively zero as the contribution of the wing, main rotor and tailplane balance each other.

Figure 5.5 shows variation of the incidence stability derivatives for the helicopter configurations with flight speed. This derivative, M_w, contributes significantly to the longitudinal short period modes of the helicopter and the vehicle's handling qualities [36, 95]. Typically, the tailplane provides a stabilising contribution to the derivative M_w, in high speed flight, with the perturbation of w producing a negative pitching down moment from the tailplane. Therefore the tailplane's size contributes significantly to M_w with Blake and Alansky highlighting its importance to the short period modes and handling qualities of the YUH-61A aircraft [95]. Conversely, the fuselage produces a nose-up pitching moment following a positive perturbation of w as its aerodynamic centre generally tends to be ahead of the centre of gravity position [36]. Hence, the effect of the fuselage on M_w is generally destabilising. For most conventional helicopters, the contributions of the fuselage and the tailplane have a tendency to cancel each other [36], resulting in the main rotor providing the most significant contribution to M_w. With reference to Figure 5.5, the stability derivative M_w for all three aircraft configurations is positive throughout the speed range and therefore destabilising. The values of M_w for the BL and CCH configurations follow the same trend, with the derivative increasing with flight speed. However, the CCH configuration's derivative is greater than the BL configuration's due to the stiffer hingeless rotor system. In terms of the HCH configuration, in low speed flight M_w is greater than the BL configuration due to the greater rotor loading across the HCH configuration's rotor disc to counteract the aerodynamic download of the wing. The greater loading causes the rotor disc to flap backwards, following a perturbation of w, to a greater extent, hence increasing the value of M_w when compared to the BL configuration. As the HCH configuration approaches high speed flight, the wing begins to contribute to the stability derivative

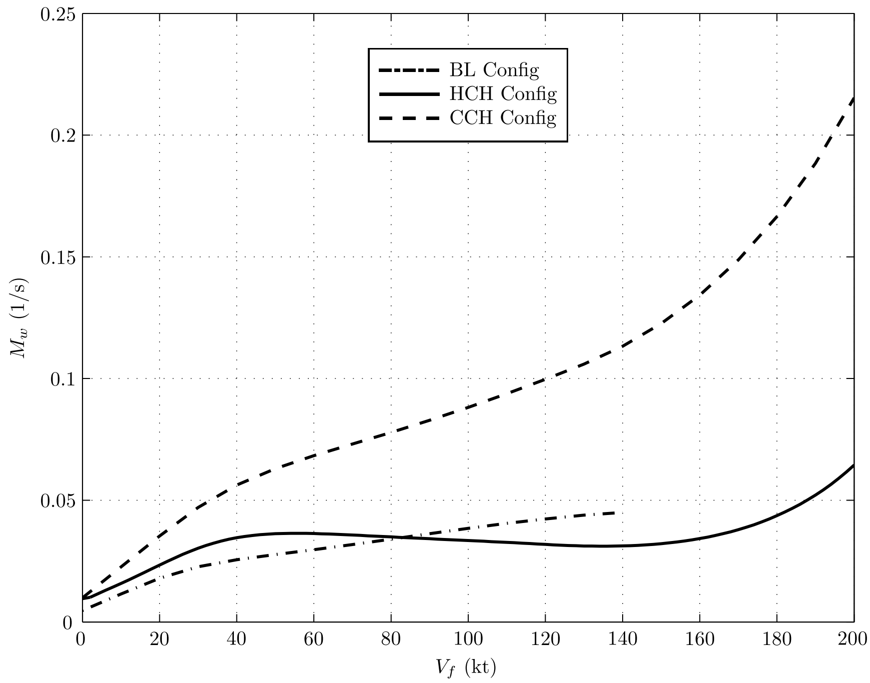

Figure 5.5: M_w Stability Derivative

M_w. In this flight regime, where the wing offloads the main rotor, the wing provides a stabilising contribution to M_w as the effective wing lift vector is located aft of the centre of mass. However, the wing's contribution is still insufficient to ensure that the pitching moment of the entire vehicle is stabilising following a perturbation of w. For the two compound helicopters, it may be necessary to include large tailplanes in their designs to counteract the destabilising values of M_w in high speed flight.

Angular Velocity Derivatives

There are two main components from the main rotor which provide pitching and rolling moments. These are namely the tilting of the rotor thrust vector and the hub moment due to the stiffness of the main rotor blades [36]. All three aircraft configurations feature very stiff rotor blades, which generate powerful pitching and rolling moments from the main rotor due to the blades' resistance to the flapping motion, $K_\beta \beta$. Neglecting the contribution of the tilt of the rotor thrust vector, the pitching moment around the rotor hub is shown by Padfield [36] to be

$$M_h = -\frac{N_b}{2}\Omega^2 I_\beta \left({\lambda_\beta}^2 - 1\right) \beta_{1c} \tag{5.3}$$

where I_β is the flapping moment of inertia and β_{1c} is the longitudinal flapping angle. The symbol ${\lambda_\beta}^2$ represents the flapping frequency of the rotor, and is given by

$${\lambda_\beta}^2 = 1 + \frac{K_\beta}{I_\beta \Omega^2} \tag{5.4}$$

In a similar manner, the rolling moment arising from the rotor stiffness is

$$L_h = -\frac{N_b}{2}\Omega^2 I_\beta \left({\lambda_\beta}^2 - 1\right) \beta_{1s} \tag{5.5}$$

where β_{1s} is the lateral flapping angle in the non-rotating frame. The flapping derivatives given by Padfield [36], can be used to approximate the stability derivatives L_p and M_q:

$$\frac{\partial \beta_{1c}}{\partial q} = \frac{\partial \beta_{1s}}{\partial p} = \frac{1}{\Omega(1 + S_\beta^2)}\left(S_\beta + \frac{16}{\gamma}\right) \tag{5.6}$$

where S_β is referred to as the stiffness number and given by the expression

$$S_\beta = \frac{8\left(\lambda_\beta^2 - 1\right)}{\gamma} \tag{5.7}$$

and γ is the classical Lock number. Consequently, approximate expressions representing the rotor hub derivatives are

$$L_p \approx -\frac{N_b S_\beta I_\beta \Omega}{I_{xx}}\left(1 + S_\beta \frac{\gamma}{16}\right) \tag{5.8}$$

$$M_q \approx -\frac{N_b S_\beta I_\beta \Omega}{I_{yy}}\left(1 + S_\beta \frac{\gamma}{16}\right) \tag{5.9}$$

Clearly the structural properties of the rotor blades, which are represented by S_β, I_β, K_β and λ_β^2 , have a significant influence on these two stability derivatives presented in Equations (5.8) - (5.9). It is important to highlight that the CCH configuration features very stiff rotor blades with a flapping frequency of 1.4 1/rev, which is required to maintain appropriate flapping clearance between the two rotor discs. Consequently, the CCH configuration's stiffness number, S_β, is greater than the other two vehicles. This increase in rotor stiffness significantly alters the prediction of the L_p and M_q derivatives. Figure 5.6 presents the predicted L_p derivatives for all three aircraft configurations. The BL configuration's L_p is insensitive to airspeed and is approximately -10 1/s across the speed range. The result is consistent with the results produced by Padfield [36]. In contrast, for the two compound helicopter configurations, the stability derivative L_p is strongly influenced by flight speed. The CCH configuration has the greatest roll damping in the hover reflected by its higher solidity and greater stiffness number, which is an inherent quality of the ABC rotor system. The estimated derivative L_p is fairly constant up to to 120kt and is approximately -17.7 1/s. However, above speeds of 120kt the the magnitude of roll damping begins to decrease as the main rotor slows down to avoid adverse compressibility effects in high speed flight. With inspection of Equation (5.5), it is evident that lower rotorspeeds reduce the amount of roll damping which is shown in Figure 5.6. In relation to the HCH configuration, L_p is also sensitive to flight speed although the cause is different from that of the CCH configuration. The large change of L_p for the HCH configuration across the speed range is due to the contribution of the wing. As the wing begins to offload the main rotor the stability derivative L_p decreases significantly, reducing to its lowest value of -17.7 1/s at 200kt. With a fixed wing aircraft, L_p always tends to be negative and therefore stabilising. A positive perturbation of roll rate increases the angle of attack across the starboard

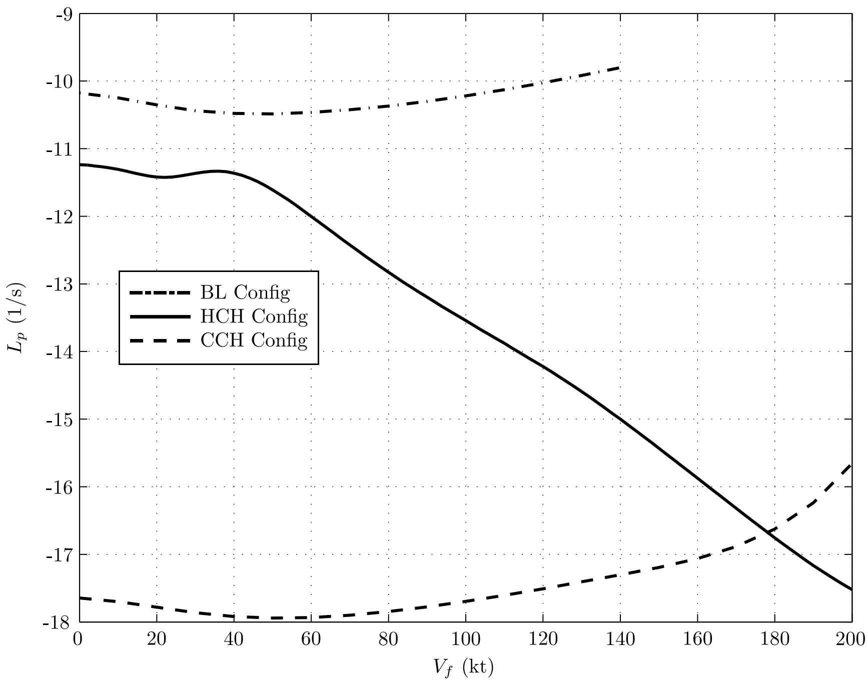

Figure 5.6: L_p Stability Derivative

wing whereas it reduces the angle of attack across the port wing [96]. The net effect is that the contribution of the wing is stabilising by rolling the aircraft back towards its initial trim condition. For the HCH configuration, the wing's contribution to L_p is added to the main rotor's natural tendency to provide a stabilising rolling moment following a perturbation of roll rate, which explains the significant change of L_p across the speed range.

Figure 5.7 shows the estimated values of the M_q for all three aircraft configurations. The BL configuration's pitch damping derivative changes in a linear manner with flight speed, reaching its lowest value of -2.7 1/s at 140kt. The contribution of the stiffness of the main rotor to M_q, Equation (5.3), is constant across the speed range. However, the tailplane at the rear of aircraft configurations influence this stability derivative as flight speed increases. Due to the significant lever arm from the tailplane's aerodynamic centre to the aircraft's centre of mass position, a perturbation of pitch rate increases the local angle of attack across the tailplane therefore providing a stabilising pitching moment contribution to M_q in high speed flight. In terms of the CCH configuration, its pitch damping derivative is lower than the two other configurations due to its main rotor design. Recall, that the ABC concept requires very stiff rotor blades with a flap frequency of approximately 1.4 1/rev to maintain appropriate flapping clearance between the two rotors. Hence, the CCH configuration's greater rotor stiffness which is

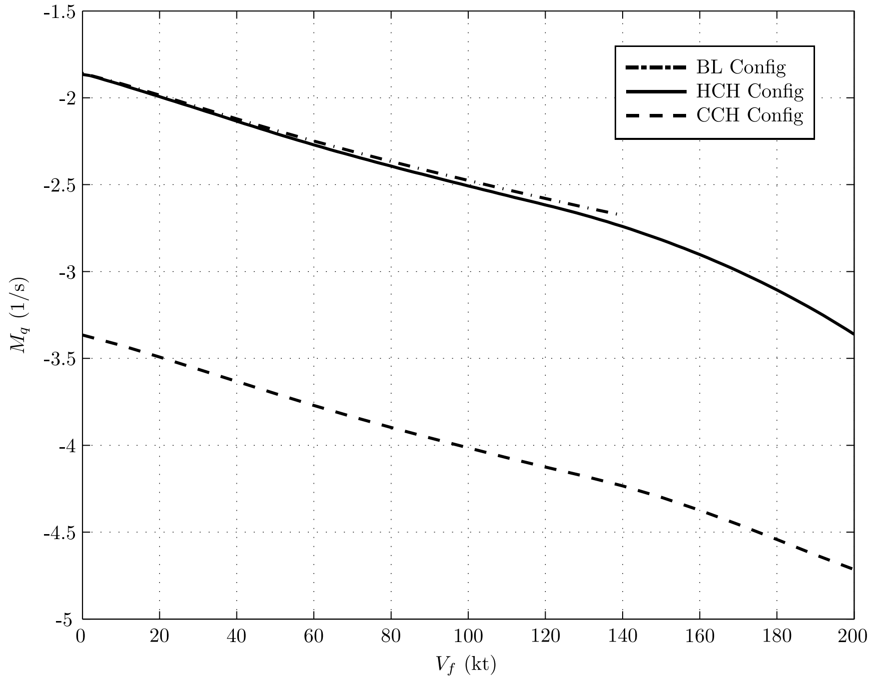

Figure 5.7: M_q Stability Derivative

reflected in the stiffness number, S_β, results in a lower value of M_q which is predicted by Equation (5.9). Its stability derivative M_q is -3.4 1/s in the hover and gets larger in magnitude as speed increases due to the contribution of the tailplane.

Another important stability derivative is the yaw damping derivative, N_r. This derivative represents the yawing moment following a perturbation of yaw rate with a negative value indicating a stable tendency. The predicted values of the stability derivatives of N_r for all three aircraft configurations are shown in Figure 5.8. For a conventional helicopter the contribution to N_r stems mainly from the fin and tail rotor located at the rear of the aircraft. The presence of the tail rotor in the BL configuration increases the yaw damping throughout the speed range. The result is that the BL configuration has greater yaw damping when compared to the compound helicopter configurations in Figure 5.8. Following a positive perturbation of r, the side force of the tail rotor increases having the effect of the yawing the aircraft's nose to the left, thereby providing a stabilising contribution. In addition, the fin provides a stabilising contribution as a positive perturbation of r increases the amount of side force the fin produces. The combination of the fin and the tail rotor provide significant yaw damping for the BL configuration. In contrast, the two compound helicopter configurations feature low levels of yaw damping when compared with the BL configuration. The compound helicopters do not feature a conventional tail rotor as the anti-torque moment

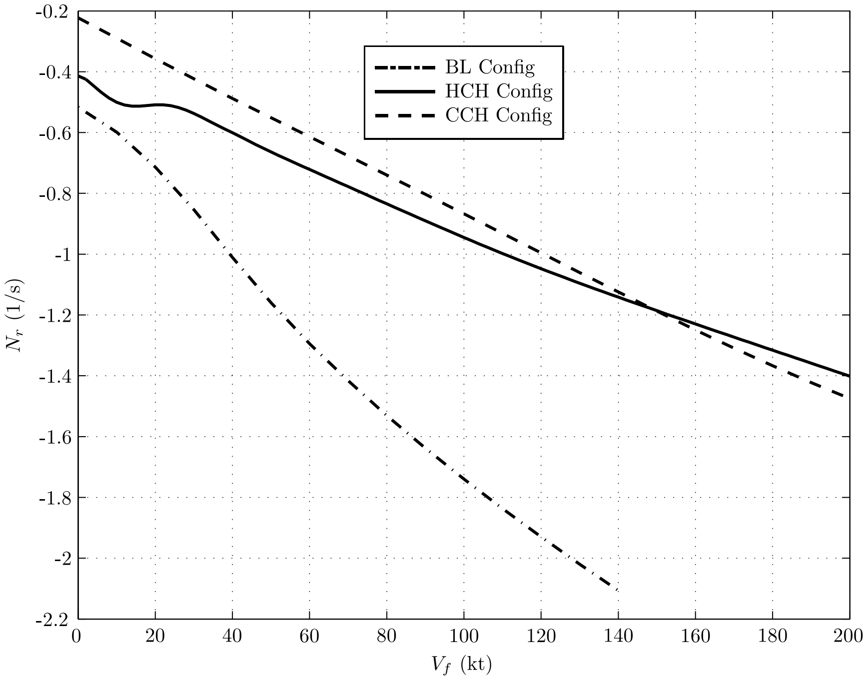

t!]

Figure 5.8: N_r Stability Derivative

is provided by other aircraft components. Due to the omission of a tail rotor, the fin is the major contributor to N_r for the two compound helicopter configurations. The result is that the predicted values of N_r for the HCH and CCH configurations are similar across the speed range. Although the estimated derivatives for these configurations do exhibit a stable tendency it may be necessary to increase the size of the fin in a compound helicopter design. This would naturally increase the stabilising contribution from the fin following a perturbation in yaw rate. Other options include the implementation of a stability augmentation system if the designer felt that the relatively low levels of yaw damping were an issue.

5.4 Control Derivatives

The preceding discussion highlighted some of the important stability derivatives and how these values changed with the introduction of compounding. The control derivatives are able to present some insight to the response of the vehicles and therefore answer this question. The control derivatives of conventional helicopters are discussed by Padfield [36], however it is logical to assume that the introduction of compounding may alter these derivatives. Additionally, a distinguishing feature of the two compound helicopter configurations is the need for additional control(s), hence increasing the size of the control matrices. This section focuses on some of the new control derivatives which arise from compounding the helicopter, with the derivatives presented and discussed.

Figure 5.9 presents the $X_{\bar{\theta}_{prop}}$ and $X_{\theta_{prop}}$ control derivatives which represent the change of axial force following a perturbation of propeller pitch for the HCH and CCH configurations, respectively. The introduction of thrust compounding allows the pilot to increase the vehicle's propulsive force without excessive pitch attitude changes. As expected, a positive perturbation of the propeller pitch control increases axial thrust which is reflected in the positive values shown in Figure 5.9. In low speed flight, the CCH configuration is trimmed so that its propeller does not produce significant amounts of thrust as it would increase the power consumption of the vehicle unnecessarily. Hence, the magnitude of the control derivative $X_{\theta_{prop}}$ is at its lowest in low speed flight and increases with flight speed as the loading across the CCH configuration's propeller disc increases to offload the coaxial rotor of its propulsive responsibilities. A similar situation occurs with the HCH configuration although the two propellers are required to provide different levels of thrust to maintain yaw trim, in low speed. When comparing the derivatives of the two compound configurations, Figure 5.9, the HCH configuration's derivative is approximately twice the magnitude of the CCH configuration's. Recall that the HCH configuration features two propellers compared with the one propeller of

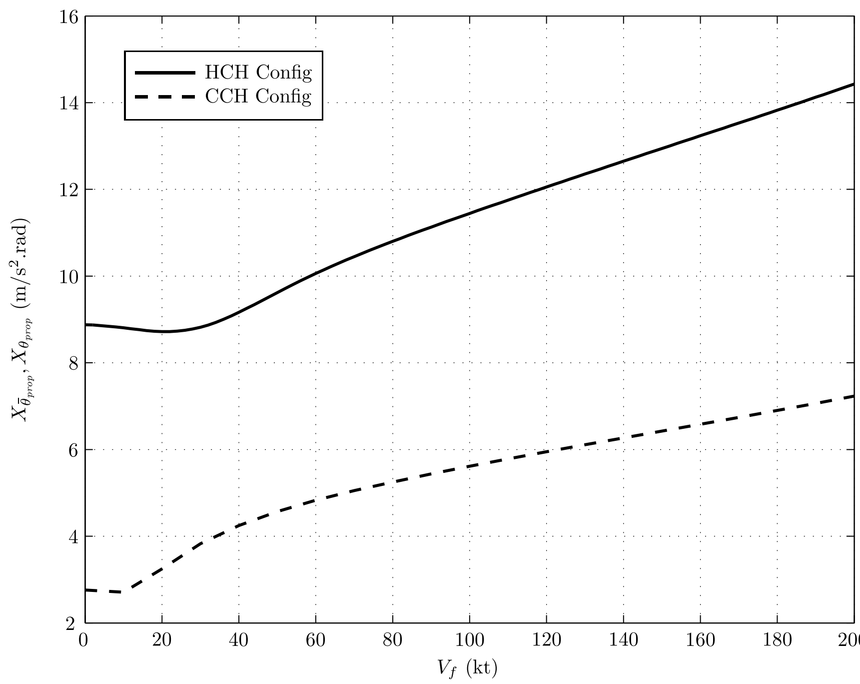

Figure 5.9: $X_{\bar{\theta}_{prop}}$ and $X_{\theta_{prop}}$ Control Derivatives

the CCH configuration. This is the reason why there is approximately a factor of two between the results presented in Figure 5.9.

A distinguishing feature of the three aircraft configurations is the different mechanisms which provide the yaw control of the vehicles. The BL configuration uses the standard helicopter layout with the tail rotor mounted at the rear of the aircraft to balance the torque of the main rotor. In contrast, the CCH configuration does not feature a tail rotor as the torque balance is naturally maintained by the upper and lower rotors rotating in opposite directions. In relation to the HCH configuration, yaw control is achieved by a differential propeller pitch control. A unit step input of this control increases the propeller pitch of the starboard propeller by one degree, whereas it decreases the propeller pitch across the port propeller by one degree. Figure 5.10 presents the change in yawing moment due to a positive perturbation of the yaw control for each configuration. In terms of the BL and HCH configurations, a positive perturbation of the yaw control has the effect of yawing the vehicle's nose to the port side, hence the negative values shown in Figure 5.10. Although the yaw control is achieved by different mechanisms, the values of $N_{\theta_{diff}}$ for the BL and HCH configurations are similar and follow the same trend with flight speed. Concerning the CCH configuration, in low speed flight, the positive value of $N_{\theta_{diff}}$ shows that the nose of the aircraft has a

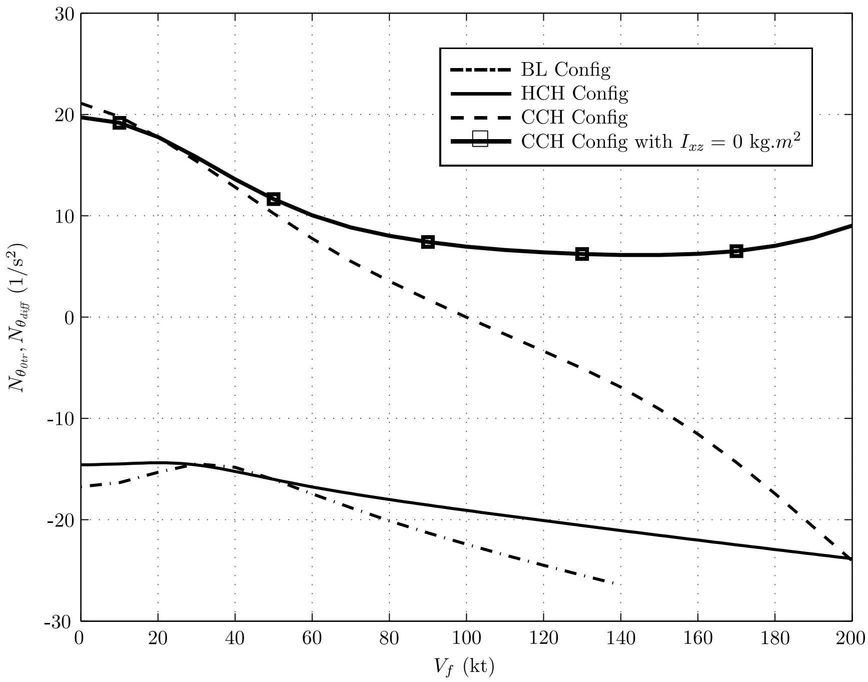

Figure 5.10: $N_{\theta_{0tr}}$ and $N_{\theta_{diff}}$ Control Derivatives for the BL, HCH and CCH Configurations

tendency to yaw to the starboard side following a perturbation of the yaw control. The upper rotor rotates anti-clockwise, when viewed from above, whereas the lower rotor rotates in the opposite direction. Hence, a positive perturbation of $N_{\theta_{diff}}$ has the net effect of yawing the aircraft's nose to the right in low speed flight. However, as the aircraft exceeds 100kt the direction of yaw, following a perturbation of θ_{diff}, reverses. This clearly is an undesirable characteristic and would degrade handling qualities of the aircraft, if uncorrected. It is logical to assume that the accurate modelling of the aerodynamic interaction between the upper and lower rotors becomes critical in determining this control derivative. In high speed flight, the forward velocity skews the two rotor wakes backward and a portion of the upper rotor's wake is not ingested through the lower rotor [57]. Clearly this is a complex aerodynamic environment and to model this successfully would require high fidelity modelling techniques. These techniques would need to be supported with a series of appropriate experimental data to validate the modelling approach. A control input of θ_{diff} increases the torques and thrusts of both rotors, thereby altering the local aerodynamic environment and changing the nature of the upper and lower wakes. The current modelling approach does not take into account these complex aerodynamic interactions, hence in the absence of suitable validation data the predicted value of $N_{\theta_{diff}}$ should be treated with a sense of caution. However, an explanation of why the current modelling strategy predicts this reversal is given. Recall that in high speed flight, the lift vector of each rotor is shifted towards the advancing sides of the discs. In trimmed flight, the upper and lower rotors create rolling moments which are equal in magnitude but opposite in direction. The net result is that the overall rolling moment is balanced. However, following a control input of θ_{diff} this rolling moment balance is lost, with the upper rotor's advancing side generating more lift than the lower rotor's advancing side. Therefore a perturbation of this control induces a powerful negative rolling moment. This rolling moment creates a significant negative roll acceleration around the aircraft's centre of mass. The equation which represents the yawing motion of the helicopter is

$$\dot{R} = \left(\frac{I_{xx} - I_{yy}}{I_{zz}}\right) PQ + \frac{I_{xz}}{I_{zz}}(\dot{P} - QR) + \frac{N}{I_{zz}} \tag{5.10}$$

which shows that a strong roll rate, coupled with a high product of inertia, I_{xz}, can alter the yaw rate of the aircraft. To reinforce this conclusion, Figure 5.10 shows the predicted $N_{\theta_{diff}}$ values with the vehicle's product of inertia equal to zero. Throughout the speed range, a perturbation of $N_{\theta_{diff}}$ yaws the helicopter's nose to the right, with no reversal occurring. Therefore, the use of the lateral lift offset concept with a relatively high product of inertia is a possible explanation of why the mathematical model predicts a reversal of sign for the $N_{\theta_{diff}}$ derivative in high speed flight.

For the conventional helicopter, cross-coupling appears from various sources and clearly influences the handling qualities of the vehicle. The previous discussion highlighted that with the CCH configuration there is a significant rolling moment produced due to a positive perturbation of the differential main rotor collective control. Figure 5.11 shows the predicted values of the control derivative, $L_{\theta_{diff}}$, which represents the CCH configuration. This derivative captures the rolling moment produced due to a perturbation of the differential main rotor collective control. Clearly, the derivative is strongly dependent on flight speed, with the value decreasing as the forward speed increases. As mentioned previously, the CCH configuration uses lateral lift offset, via a differential lateral cyclic control, so that the advancing sides of the upper and lower rotor discs exploit the high local dynamic pressure to provide the required lifting force. A positive perturbation of θ_{diff} increases blade incidence around the upper rotor's disc whereas it has the opposite effect around the lower rotor's disc. This perturbation creates greater lift across the advancing side of the upper rotor. Conversely, this perturbation reduces the lift produced by the advancing side of the lower rotor disc with the net effect of the rolling the aircraft to the port side, which is reflected in Figure 5.11. This characteristic was also observed in the flight tests of the XH-59A

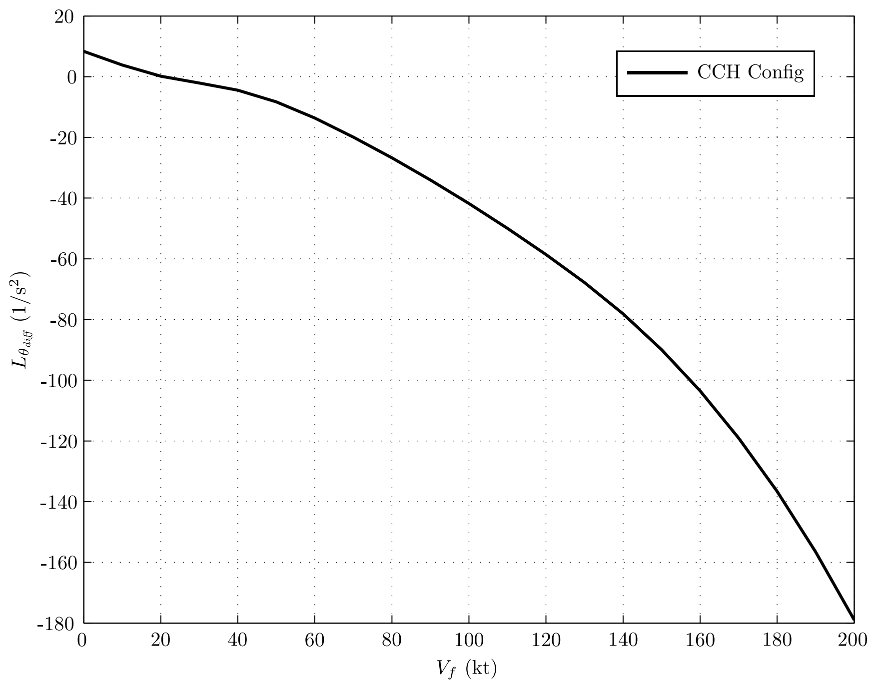

Figure 5.11: $L_{\theta_{diff}}$ Control Derivatives

aircraft [97]. Clearly, this is an undesirable feature of the lateral lift offset concept as it would degrade handling qualities and increase pilot workload if the issue was not addressed. Potential solutions to this issue are the introduction of a control system as well as the possibility of “washing out” the differential main rotor collective control by replacing it with a rudder control in high speed flight.

5.5 Natural Modes of Motion

The reduction of the nonlinear equations of motion to linear form result in a system matrix of ninth order. The application of small perturbation theory predicts nine natural modes of motion which are given by eigenvalues which describe the nature of the mode. For example, if the natural mode of motion is described by a pair of complex conjugates, then the mode is oscillatory with a certain damping ratio value. In terms of a fixed wing aircraft, these natural modes of motion are well understood with Cook [96] providing an overview of these modes. The names of the fixed wing aircraft modes such as the phugoid and roll subsidence modes, are also used when describing the modes of a helicopter. However, the nature and source of a fixed wing aircraft’s modes are entirely different from that of a rotorcraft. Within his book, Padfield compares the predicted natural modes of motion, determined through simulation, with flight estimates [36]. The flight estimates, determined by the work of AGARD [98, 99], compare well with the predicted eigenvalues, highlighting the effective nature of mathematical models. Furthermore, Houston also successfully validated a high order individual rotor blade model by comparing the predicted natural modes of motion with flight test estimates [100]. Again, with AGARD providing the validation data [101]. It is therefore evident that simulation models can successfully predict the natural modes of motion. The next logical step from assessing the salient stability and control derivatives is to determine the natural modes of motion for all three aircraft configurations. By comparing the three sets of results the effects of compounding on the natural of modes can be determined.

Predicted Stability of the HCH Configuration

Figure 5.12 shows the roll subsidence, pitch subsidence, and Dutch roll modes of both the BL and HCH configurations. Firstly, consider the roll subsidence mode. The eigenvalues of the roll subsidence mode are well predicted by the stability derivative, L_p, shown in Figure 5.6. For the BL configuration, the roll damping does not change

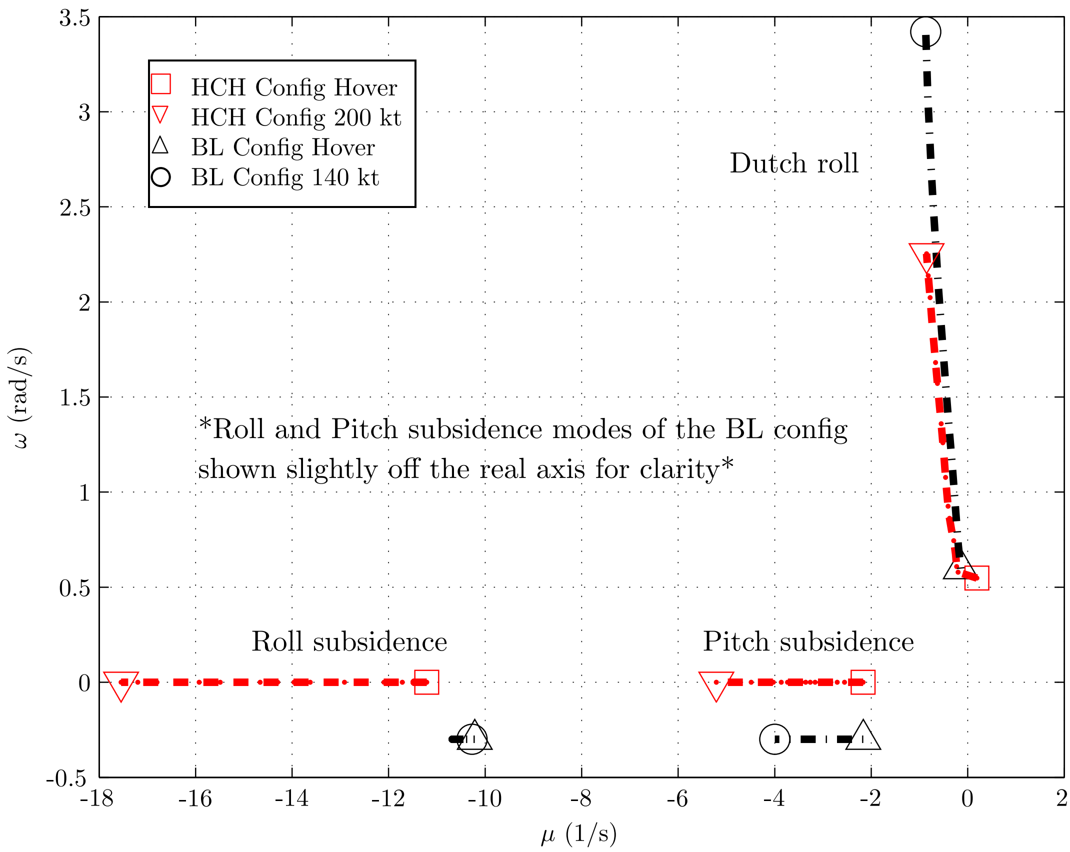

Figure 5.12: The Dutch roll, Roll Subsidence and Pitch Subsidence Modes of the HCH and BL Configurations

significantly from hover to 140kt and is dominated by the stiffness of the rotor. However, the roll damping eigenvalues of the HCH configuration range from -11 1/s in the hover to -18 1/s at 200kt. As discussed previously, the wing produces a significant portion of the overall lift of the helicopter in high speed flight. A positive perturbation in roll rate increases the angle of attack of the starboard wing and decreases the angle of attack of the port wing [96], thus producing a stabilising rolling moment. This effect also occurs in the HCH configuration and is now added to the roll damping produced by the hingeless rotor. The wing's contribution to L_p increases with flight speed as the wing loading increases to offload the main rotor. It is important to highlight that this study is not a design exercise as it is assumed that the BL and HCH configurations have identical moments of inertia values. In reality, the addition of a wing to the HCH configuration would, in all probability, increase the moment of inertia about the x_b axis, I_{xx}, which would lower the magnitudes of the roll damping derivatives for the HCH configuration. In effect, shifting the roll damping eigenvalues of the HCH configuration closer towards the imaginary axis. In the context of this study, the main finding is not

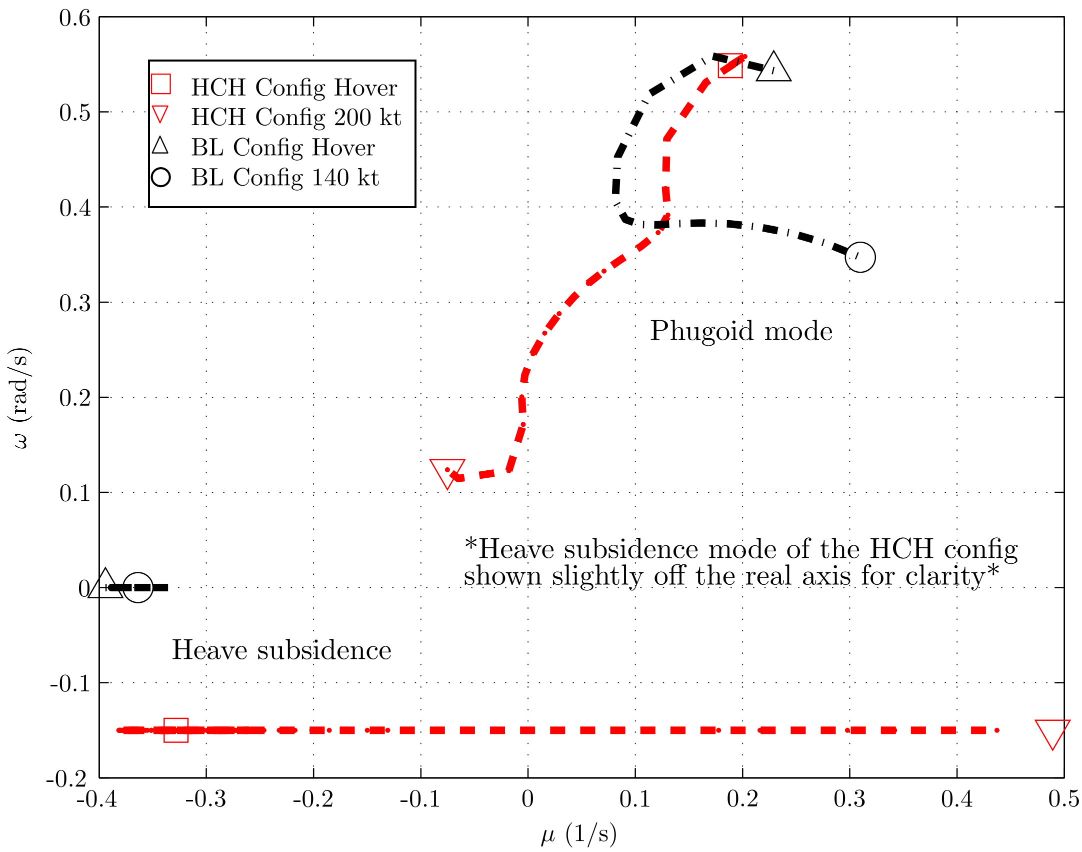

Figure 5.13: The Phugoid and Heave Modes of the HCH and BL Configurations

the numerical values of L_p as such, but rather the behaviour of the derivative as the HCH configuration moves into forward flight. The damping of the roll mode increases as the vehicle moves into forward flight due to the stabilising aerodynamic contribution of the wing. With the pitch subsidence modes, the estimated eigenvalues of both the HCH and BL configurations are comparable throughout the speed range, Figure 5.12.

The eigenvalues of the lateral oscillation, the so-called "Dutch roll" are similar for the two aircraft configurations in low speed flight. For the BL and HCH configurations, the damping of the Dutch roll mode is insensitive to flight speed with the results predicting a lightly damped oscillation for each configuration. The only major difference between the two sets of the results is the estimated frequency for each of the rotorcraft configurations. The frequencies of the Dutch roll modes at 140kt for the BL and HCH configurations are estimated to be 3.5 rad/s and 1.7 rad/s, respectively. At this flight speed the frequency of the BL configuration's Dutch roll mode is twice than that of the HCH configuration. The difference in frequencies is due to the omission of a tail rotor in the HCH configuration's design.

λ_{sp}^2	1	$Z_w M_q - M_w (Z_q + U_e)$
λ_{sp}^1	$-(Z_w + M_q)$	0
λ_{sp}^0	$Z_w M_q - M_w (Z_q + U_e)$	

Table 5.1: Routh-Hurwitz Stability Criterion of the Short Period Modes

Figure 5.13 shows the phugoid and heave subsidence modes of the HCH and BL configurations. In the hover, the phugoid modes of the HCH and BL configurations are similar. However, as speed increases, the mode becomes more stable for the HCH configuration but with decreasing frequency. The oscillatory nature of the mode is reduced due to the contribution of M_u, with this derivative tending toward zero above 160kt, Figure 5.4. This is due to the wing providing a pitch down moment following a perturbation of forward velocity, effectively cancelling the pitch up moment response of the main rotor. The net effect is that the ratio of the pitching moment due to speed and pitch rate becomes very small, lessening the oscillatory nature of the phugoid. At 160kt, the eigenvalues of the phugoid mode cross the imaginary axis, predicting a stable mode. In high speed flight, the phugoid becomes stable due to the drag damping derivative X_u. For a conventional helicopter, X_u is always negative, as a perturbation in forward velocity results in an increase in drag force due to the fuselage and the rotor disc tilting backward. However, for the HCH configuration, the drag is increased following a perturbation in forward velocity due to the addition of the two propellers and wing. A perturbation in forward velocity reduces the blade incidence of the propeller blades, which creates a sizeable drag force. Additionally, the perturbation of u also increases the drag of the wing; hence, both contribute to lower the drag damping derivative X_u, which in turn stabilises the phugoid.

Returning to the short period modes, it was shown that there is little change between the eigenvalues of the pitch subsidence mode for both the HCH and BL configurations, Figure 5.12. However, the other short period mode, the heave mode as seen in Figure 5.13, is estimated to become unstable at high speeds. This result can be explained with the use of a reduced order model of the short period modes. Padfield [36] approximates the characteristic equation of the short period modes as

$$\lambda_{sp}{}^2 - (Z_w + M_q)\,\lambda_{sp} + Z_w M_q - M_w (Z_q + U_e) = 0 \tag{5.11}$$

Clearly, the eigenvalues of the short-period modes are primarily influenced by the stability derivatives Z_w, M_q, M_w as well as the flight speed. This reduced order model,

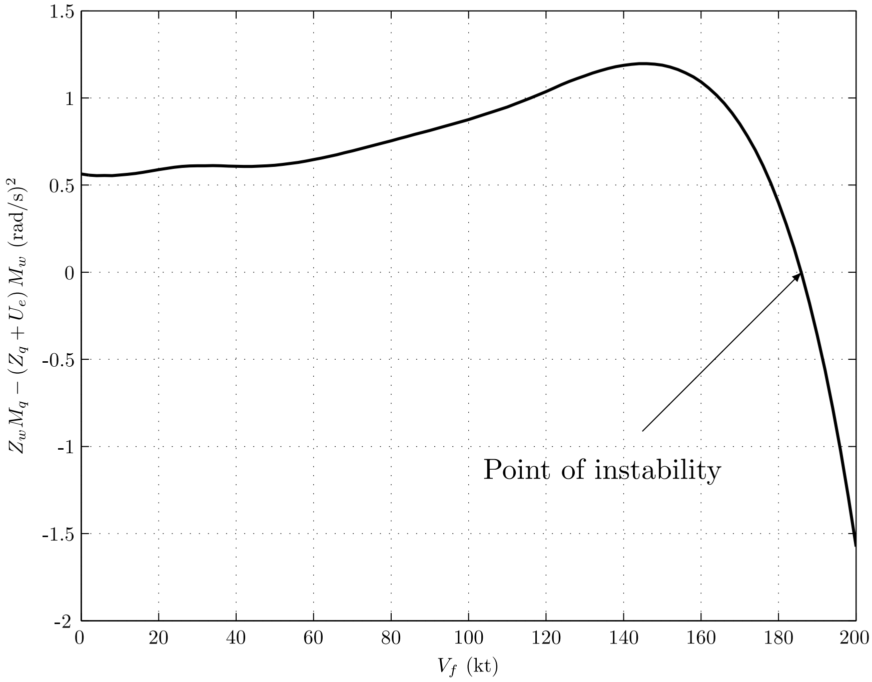

Figure 5.14: Spring Term of Equation (5.11)

Equation (5.11), is valuable and gives a good approximation to the short period eigenvalues. With the use of Equation (5.11), the stability conditions for the short period modes can be readily obtained by applying the Routh-Hurwitz stability criterion, as seen in Table 5.1. For the short period modes to be stable, all the values in the middle column of Table 5.1 are required to be positive. The term $-(Z_w + M_q)$ is always positive, as the vehicle's lifting force always increases due to a perturbation of normal velocity and the aircraft's response to a perturbation of pitch rate is stabilising. It is the last entry in the middle column, $Z_w M_q - M_w (Z_q + U_e)$, which has the greatest impact in terms of the stability of the short period modes. The term is required to be positive, for stability, which depends on the balance of the left and right terms. Neglecting the contribution of Z_q, as $U_e >> Z_q$ in high speed flight, the short period modes are predicted to be stable when $Z_w M_q > M_w U_e$. Figure 5.14 shows the variation of $Z_w M_q - M_w (Z_q + U_e)$ across the speed range. As the flight speed of 184kt is reached $M_w U_e$ becomes greater than $Z_w M_q$ therefore estimating a point of instability as seen in Figure 5.14. The result is that the eigenvalues of the heave mode cross the imaginary axis in high speed flight resulting in an unstable mode, Figure 5.13.

It should be noted that the eigenvalues of the spiral mode for all configurations are not shown within the presented results, as their eigenvalues are very similar, with the eigenvalues being small and negative, indicating stability for all the configurations.

Predicted Stability of the CCH Configuration

Figure 5.15 shows the roll subsidence, pitch subsidence, and Dutch roll modes of both the BL and CCH configurations. All three of these modes exhibit stability for both helicopter models. The damping of the roll subsidence mode of the CCH configuration has increased, slowing the roll response of the aircraft. The reason for this is due to a combination of the increased number of rotor blades, their stiffnesses, and the increased distance between the upper rotor's hub and the centre of gravity. The level of roll damping is estimated by L_p, and for the CCH configuration ranges between -16 and -18 1/s across the speed range. Throughout this work the L_p derivative is presented in semi-normalised form and is therefore scaled by I_{xx}. It is assumed that the CCH and BL configurations have the same moment of inertia values. However, with the design of a coaxial compound helicopter it may transpire that its I_{xx} value would be different to that of a conventional helicopter of similar mass. This could be due to additional blades featured in a coaxial compound configuration or due to a different fuselage shape. Clearly different values of I_{xx} would alter the magnitude of the L_p derivative. Regardless of the CCH configuration's I_{xx} value, the main conclusion from this work is that this type of helicopter will be heavily damped in roll and that the level of roll damping is likely to change in high speed flight due to the reduction of rotorspeed to avoid adverse compressibility effects. In terms of the Dutch roll mode, the main difference is the frequency of the two modes, with the CCH configuration exhibiting a smaller frequency, at high speeds, due to its empennage design. This can be seen by using Padfield's [36] approximation to the Dutch roll mode frequency in high-speed flight

$$\omega_{dr} \approx U_e N_v + L_v \left(\frac{g - N_p U_e}{L_p} \right) \tag{5.12}$$

The reduced Dutch roll frequency of the CCH configuration is due to the weathercock stability derivative N_v. For a conventional helicopter, N_v is generally positive for most flight speeds, with the tail rotor and fin playing the most prominent roles. Following a sideslip perturbation, the fin and tail rotor provide a side force that aligns the fuselage nose with the wind direction, thus providing a stabilising effect. However, for the CCH configuration, the lack of tail rotor reduces the yawing moment that the helicopter produces following a sideslip perturbation. The fin and fuselage are now the main contributors to N_v. The fuselage provides a destabilising moment following a sideslip perturbation due to the fuselage's aerodynamic centre being located forward of the centre of gravity position. In contrast, the fin's contribution is always stabilising. However, without the tail-rotor's contribution, the predicted N_v values of the CCH configuration are lower than that of the BL configuration. In forward flight, Equation (5.12) shows that a negative value of N_v reduces the Dutch roll frequency, which can be seen in Figure 5.15.

Figure 5.16 shows the phugoid and heave subsidence modes of the BL and CCH configurations. In the hover, the phugoid mode for both the BL and CCH configurations have similar frequencies, but the CCH configuration's eigenvalues are shifted closer to the imaginary axis. As speed increases, the frequency of the phugoid mode of the CCH configuration begins to decrease, with an unstable oscillation predicted under 150kt. The two aircraft feature hingeless rotor systems, and this is the primary reason for the instability [37]. The stiff rotors create large moments about the rotor hub due to the stiffness of the blades and large effective hinge offset. When the two helicopters are subject to a perturbation in forward speed, the two rotor systems flap

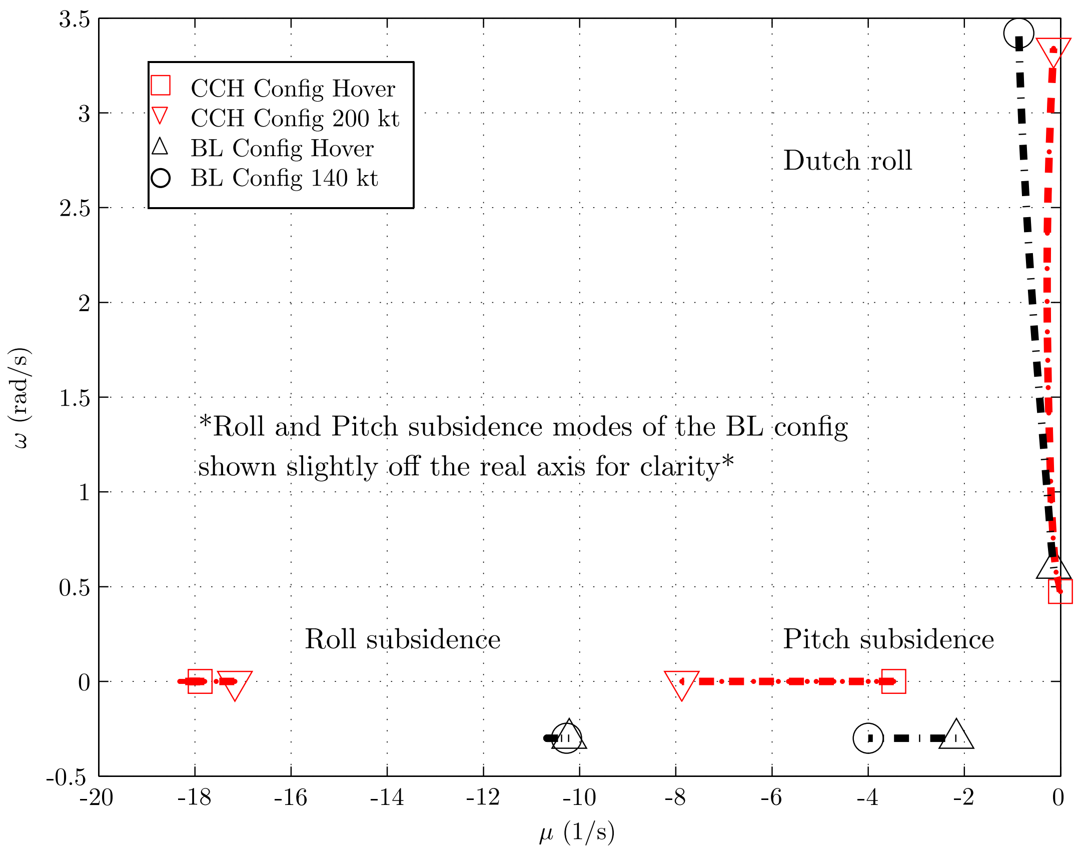

Figure 5.15: The Dutch roll, Roll Subsidence and Pitch Subsidence Modes of the CCH and BL Configurations

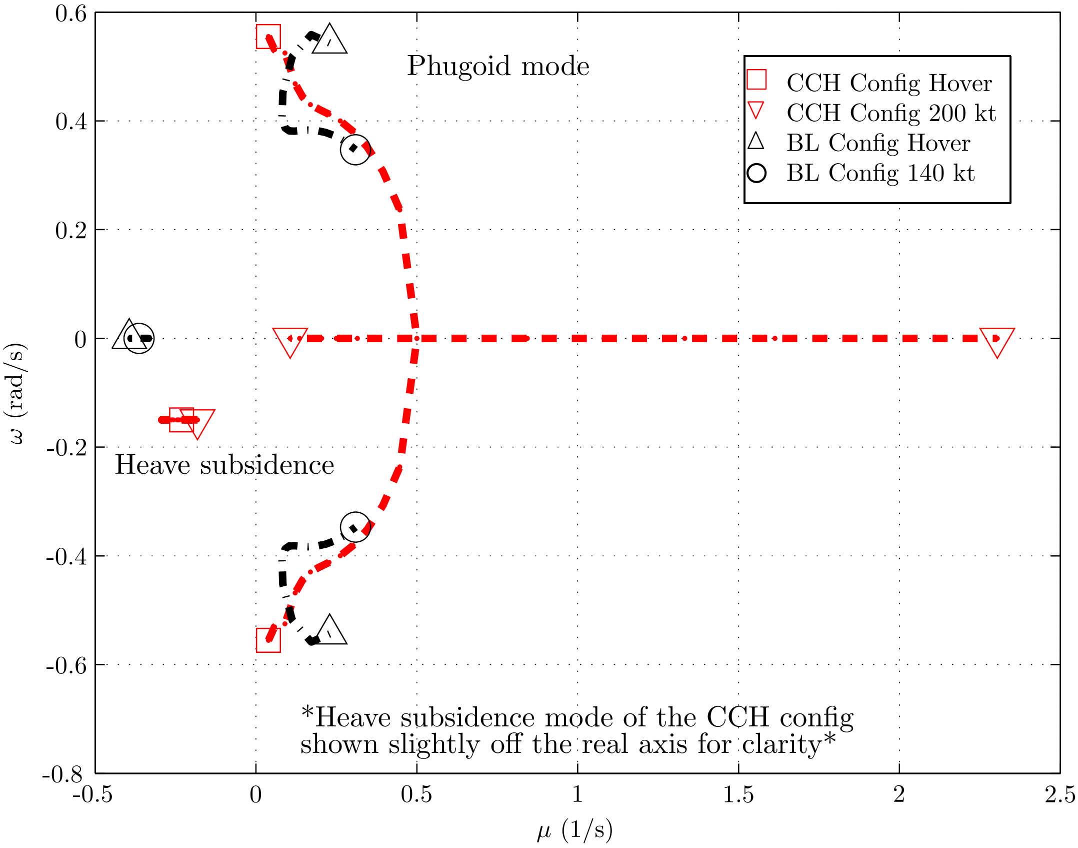

Figure 5.16: The Phugoid and Heave Modes of the CCH and BL Configurations

backward, resulting in the fuselage pitching up. As the fuselage pitches up, the main rotor provides a pitch down moment, with the stability derivative M_q being negative, with this oscillatory motion continuing with the amplitude steadily increasing. In the hover, the phugoid mode of the CCH configuration is close to the imaginary axis, due to an increase in drag damping. Following a perturbation in forward speed, the blade incidence of the propeller blades reduce, providing an extra drag force, lowering the value of X_u, but this is still insufficient to stabilise the phugoid oscillation. At 150kt, the eigenvalues of the phugoid mode branch off into the real axis and produce two divergent modes. This predicted instability clearly highlights an important flying qualities issue and it is likely that the flight control system would be configured to improve the aircraft's phugoid characteristics. Regarding the heave subsidence mode, there is little change between the two configurations.

5.6 Chapter Summary

Chapter 5 has investigated the effect of compounding on the stability of the compound helicopter configurations. This process began by trimming the respective compound helicopter configuration and then subsequently reducing the nonlinear equations of motion to linear form. With the equations of motion reduced to linear form, the stability and control derivatives were presented highlighting the effects of compounding. In addition, the predicted natural modes of motion of each aircraft configuration were presented highlighting the effect of compounding to the damping and frequency of the modes. The effect of compounding to the stability of the aircraft is as follows:

- The effect of thrust compounding increases the drag damping of the two compound helicopter configurations, which is reflected in the values of X_u. The HCH configuration has the greatest magnitude of drag damping, which is reflected in the values of X_u, as it features two propellers and a wing, both of which increase the level of drag following a perturbation of forward velocity.

- In relation to the speed stability derivative M_u, for each of the configurations the derivative is at its highest in the hover. For the BL and CCH configurations, this derivative decreases with flight speed and is fairly constant after 60kt. With the HCH configuration, M_u begins to reduce in a linear manner after 60kt due to the effect of lift compounding. The wing, which is situated behind the aircraft's centre of mass, provides a pitch-down moment following a perturbation of forward velocity. At high speeds, the contribution of the wing and the main rotor cancel each other out with the derivative almost equal to zero at 200kt.

- For all three aircraft configurations, the angle of attack stability derivative M_w is predicted to be unstable throughout the speed range. For the BL and CCH configurations, the contribution of the main rotors to this derivative is most significant with the two rotor systems flapping backwards following a perturbation of normal velocity. For the CCH configuration, M_w is greater than the values predicted for the BL configuration due to the greater rotor stiffness number. In terms of the HCH configuration, the effect of the wing provides a stabilising contribution to M_w. However, its contribution is still insufficient to stabilise M_w as the aircraft pitches upwards following a perturbation of w due to the powerful effect of the main rotor flapping backwards.

- The addition of lift compounding, as featured in the HCH configuration, increases the magnitude of roll damping as speed increases. This is due to the wing's natural tendency to provide a stabilising contribution to L_p. With the CCH configuration, L_p is fairly constant up to 120kt but the magnitude of roll damping begins to lower due to the reduction of rotorspeed to avoid adverse compressibility effects.

- As expected, the control derivatives of $X_{\bar{\theta}_{prop}}$ and $X_{\theta_{prop}}$ which correspond to the HCH and CCH configurations respectively, are positive throughout the speed range highlighting the increase of axial thrust following a perturbation to the propeller's control. These two control derivatives also increase with speed due to the higher propeller thrusts in high speed flight to offload the main rotors of their propulsive duties.

- The main differences between the HCH and BL modes of motion were the phugoid and roll subsidence modes. In high speed flight, the phugoid becomes stable for the HCH configuration due to the increase in drag damping, which is represented by a reduced value of X_u. In addition, the wing provides a pitch-down moment following a perturbation in angle of attack since its quarter chord position is slightly behind the centre of mass. This effect reduces the frequency of the oscillation. Therefore, the positioning of the wing can strongly influence the phugoid mode of the helicopter. In terms of the roll subsidence mode, the damping of the mode increases with flight speed due to the additional roll damping the wing provides.

- The main differences between the natural modes of motion of the CCH and BL configurations are the Dutch roll and roll subsidence modes. The frequency of the Dutch roll mode is less than that of the BL configuration's mode due to the lack of tail rotor, reducing the side force, following a sideslip perturbation. The differences between the roll subsidence modes are primarily due to the design of the main rotor systems. The increased number of rotor blades, their respective stiffnesses, and the increased distance between the upper rotor's hub to the centre-of-gravity position all contribute to increasing the roll damping, relative to the BL configuration.

Chapter 6

Manoeuvrability Assessment of Compound Helicopter Configurations

The previous chapters have investigated the effects of compounding to the trim, performance and stability results of the compound helicopter. One additional perceived benefit of compounding is the possibility of increasing the manoeuvrability of the vehicle. For example, it is possible that the addition of lift compounding to the design will allow a winged helicopter to achieve greater load factors than its conventional counterpart. To determine the influence of compounding to the manoeuvrability of this aircraft class, this Chapter continues with the theme of using the two compound helicopters, which were developed in Chapter 3, to assess the contribution of compounding to the manoeuvrability of the vehicle. The Chapter begins by discussing the relevant literature and then explaining the approach to assess the manoeuvrability of the compound helicopter configurations. The Chapter concludes by presenting the manoeuvrability results and main findings from the work.

6.1 Introduction

The success of the conventional helicopter is partly due to its unique ability to perform precise manoeuvres in Nap of the Earth (NoE) flight. One method of assessing the helicopter's ability to perform manoeuvres is inverse simulation. Inverse simulation reverses the conventional simulation approach by calculating the control activity required to force a vehicle along a particular trajectory [102]. The first inverse simulation algorithm, known as the differentiation method, was developed by Thomson and Bradley [103], to assess the agility of a six degree of freedom (DOF) rotorcraft model. The success of the inverse simulation results, as well as the increasing interest in handling qualities and pilot workload research, prompted further development of the algorithm. Subsequently, inverse simulation has been used for various applications, including investigating pilot control strategies, conceptual design analyses and handling qualities [104–107]. Despite the success of the differentiation method, there were some problems which consequently led to a new approach to inverse simulation. The major limitation of the differentiation method was that the mathematical model and the algorithm were strongly coupled, therefore even slight changes to the mathematical model required alterations to the algorithm itself. Realising this shortcoming, Hess, Goa and Wang developed a generalised technique of inverse simulation [108], often referred to as the integration method, which fully separates the mathematical model from the algorithm. Due to the robust and flexible nature of this technique, the integration method has become the most common approach [109].

Before proceeding, other methods of solving the inverse problem should be noted. Firstly, is the two time-scale method which was developed by Avanzini, de Matteis and de Socio [110, 111]. This method assumes that the rotational dynamics of an aircraft are much quicker than the translational dynamics, therefore permitting the assumption that the main rotor collective controls the translational dynamics whereas the cyclic and pedals influence the rotational dynamics. This method, similar to the other methods, use iterative schemes, such as the Newton-Raphson method, in order to solve the inverse problem. However, the Newton-Raphson method can be replaced with an optimisation algorithm to calculate the control angles, with Celi and de Matteis et al. [112, 113] successfully implementing optimisation algorithms in their respective approaches. The optimisation approach to inverse simulation is particularly useful to problems featuring control redundancy, however an appropriate cost function must be formed. Another method which could be used to calculate the appropriate control time histories is an inverse method using Adaptive Neural Networks (ANN). This approach has been used successfully in various rotorcraft control studies [114–119]. With this approach, the control action that is required is calculated by dynamic model inversion, which has proven to be a popular feedback linearisation technique [120]. However, the major disadvantage of this technique is the significant errors that occur between the predicted and actual response of the aircraft due to inaccuracies within the plant model. As neural networks have the ability to accurately predict nonlinear functions [121], ANN can be used to atone for these errors. Although dynamic inversion techniques using

ANN have considerable merit, the integration method of inverse simulation is used within this study due to its robust and flexible nature.

Manoeuvrability is an important design feature if the helicopter is to operate in tight Nap of the Earth (NoE) scenarios [122]. The ability of the helicopter to manoeuvre quickly and effectively enables the vehicle to quickly re-position. Furthermore, enhancing the manoeuvrability and agility of a helicopter can also aid its survivability with its ability to quickly turn or climb to avoid an attack. Traditionally, the design process has focused on performance and cost to drive the design of the helicopter. However, for the reasons previously stated, a high level of manoeuvrability has become a key design goal for most designers as it increases mission effectiveness [123]. As there is a demand for conventional helicopters to be manoeuvrable, it is reasonable to postulate that operators would expect the same for a compound helicopter. Therefore, this Chapter presents a manoeuvrability assessment method which is capable of quantifying the manoeuvrability of compound helicopter configurations.

Before continuing it is important to highlight that there are various definitions of the term manoeuvrability. Therefore it is necessary to define what is meant by manoeuvrability in this current work. Generally, most authors agree that manoeuvrability is the ability of the aircraft to change its flight path [122, 124] with Whalley [125] providing an overview of the various definitions proposed by authors. Whalley also concludes by stating his definition of manoeuvrability, which is the following

> *"Manoeuvrability is the measure of the maximum achievable time-rate-of-change of velocity vector at any point in the flight envelope."*

The aim of this current Chapter is to determine the maximum manoeuvring capability of three aircraft configurations, namely a conventional helicopter configuration and two compound helicopter configurations. Then to subsequently investigate if the compounding of the conventional helicopter offers an advantage in this regard. Hence, in this context, the term "manoeuvrability" and phrase "maximum manoeuvring capability" are used interchangeably throughout the remainder of this Chapter. Although not the primary aim the study, due to the use of inverse simulation the results from the work are likely to highlight some of the potential control actions that a pilot may use to fly a compound helicopter along a predetermined flight path. This Chapter continues with the theme of the previous chapters by using the two compound helicopters developed in Chapter 3. The Chapter compares the results to a conventional helicopter therefore isolating the broad effects of compounding to the helicopter. The approach in this work is to use inverse simulation to quantify the manoeuvrability of the aircraft configurations. This requires various elements such as helicopter mathematical models, an inverse simulation algorithm, models which represent typical helicopter manoeuvres and a manoeuvrability assessment method. The following section provides an overview of these required components.

6.2 Integration Method

Overview of the Integration Method

The inverse simulation algorithm used in this current study is the so called integration method. The integration method is explained widely within the literature by various authors [108, 109, 126], therefore only a brief description is provided within, with Figure 6.1 supporting the discussion. The integration method uses numerical integration and conventional simulation to calculate the controls required to move a vehicle through a desired trajectory. The first step is to calculate the control angles that trim the aircraft for the given starting flight speed. Generally, a helicopter can be in trimmed flight when climbing, descending or flying with a lateral velocity (sideslip). However, for this particular application the trimmed state corresponds to the condition whereby the aircraft is in steady level flight with the body accelerations and the attitude rates equal to zero. The next step, after the trim control angles have been calculated, is to define the manoeuvre. The manoeuvre is discretised into a series of time points, t_k, by specifying the time step and calculating the number of time points. Subsequently, the manoeuvre can be determined with matrix, $\mathbf{y}_{\mathrm{des}}(t_k)$ representing the flight path of the manoeuvre. The manoeuvre can be defined by polynomials that satisfy the requirements of the particular manoeuvre [127], with the mathematical modelling of these manoeuvres detailed later on. Starting from the trimmed condition, $\mathbf{u}_{\mathrm{e}}$ is the initial guess to calculate the control vector, $\mathbf{u}$, to force the helicopter to the position of the next time point. The current time point is represented by k, whereas m corresponds to the iteration number at a given time point. Therefore the general equation that describes the aircraft's state at a given time point or iteration number is

$$\dot{\mathbf{x}}(t_{\mathrm{k}})_m = \mathbf{f}(\mathbf{x}(t_{\mathrm{k}}), \mathbf{u}(t_{\mathrm{k}})_m) \tag{6.1}$$

The integration of Equation (6.1) calculates the state vector at the next time point. Commonly, a Runge-Kutta 4th order integration technique is used, which leads to an

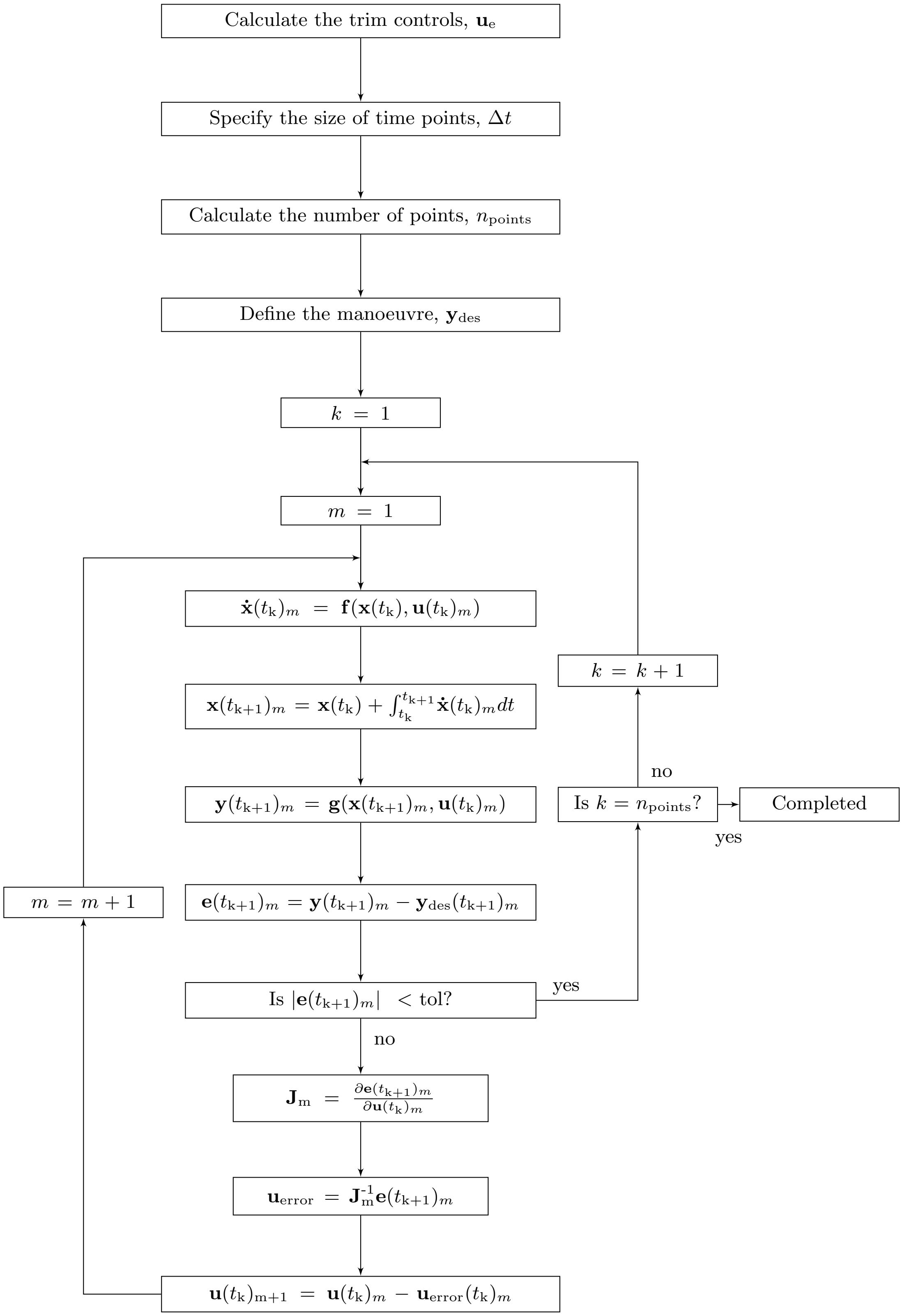

Figure 6.1: Flowchart Describing the Integration Method, Reproduced from [126]

estimate of $\mathbf{x}(t_{\mathrm{k+1}})$ by

$$\mathbf{x}(t_{\mathrm{k+1}})_m = \mathbf{x}(t_{\mathrm{k}}) + \int_{t_{\mathrm{k}}}^{t_{\mathrm{k+1}}} \dot{\mathbf{x}}(t_{\mathrm{k}})_m dt \tag{6.2}$$

With the calculation of $\mathbf{x}(t_{\mathrm{k+1}})_m$, by Equation (6.2), the output vector can be determined with

$$\mathbf{y}(t_{\mathrm{k+1}})_m = \mathbf{g}(\mathbf{x}(t_{\mathrm{k+1}})_m, \mathbf{u}(t_{\mathrm{k}})_m) \tag{6.3}$$

where $\mathbf{g}$ is a vector function relating the aircraft's state and controls to the required output vector. The expression, Equation (6.3), can then determine an error function such that

$$|\mathbf{e}(t_{\mathrm{k+1}})_m| = \mathbf{y}(t_{\mathrm{k+1}})_m - \mathbf{y}_{\mathrm{des}}(t_{\mathrm{k+1}})_m \tag{6.4}$$

A solution of the controls is reached when the error function is less than a predefined tolerance. If this transpires to be the case then the algorithm moves onto the next point. However, if the error function is greater than the tolerance then a new guess of the control vector, as shown by Hess, Gao and Wang [108], is made using the Newton-Raphson technique

$$\mathbf{u}(t_{\mathrm{k}})_{\mathrm{m\ +\ 1}} = \mathbf{u}(t_{\mathrm{k}})_m - \mathbf{J}_{\mathrm{m}}^{\text{-1}}\mathbf{e}(t_{\mathrm{k+1}}) \tag{6.5}$$

where, $\mathbf{J}$ is the Jacobian matrix describing the rate of change of the output vector with the control vector. If the number of controls, n_{con}, and number of error functions, n_{err}, are equal then the Jacobian is a square matrix of size $n_{\mathrm{con}} \times n_{\mathrm{err}}$. The entries of the Jacobian matrix are given by $j_{\mathrm{i,j}}$, where the subscripts i and k indicate the error and control numbers of the matrix,. The Jacobian is therefore

$$\mathbf{J} = \begin{bmatrix} j_{1,1}(t_{\mathrm{k}}) & \dots & j_{1,n_{\mathrm{con}}}(t_{\mathrm{k}}) \\ \vdots & \ddots & \vdots \\ j_{n_{\mathrm{err}},1}(t_{\mathrm{k}}) & \dots & j_{n_{\mathrm{err}},n_{\mathrm{con}}}(t_{\mathrm{k}}) \end{bmatrix} \tag{6.6}$$

where, an entry of the matrix is given by

$$j_{\mathrm{i,j}}(t_{\mathrm{k}})_m = \frac{\partial e_{\mathrm{i}}(t_{\mathrm{k+1}})_m}{\partial u_{\mathrm{j}}(t_{\mathrm{k}})_m} \tag{6.7}$$

A numerical method is used to calculate the partial derivatives as Equation (6.7) is typically not amenable to analytical differentiation. Therefore, the Jacobian entries are determined through central differencing, which is slightly different to the backward difference approach discussed in an another inverse simulation study [128], so that a given entry is

$$j_{\mathrm{i,j}}(t_{\mathrm{k}})_m = \frac{e_{\mathrm{i}}\left(t_{\mathrm{k}\,+\,1}, (u_{\mathrm{j}}(t_{\mathrm{k}}) + \Delta u_{\mathrm{j}}(t_{\mathrm{k}}))\right)_m - e_{\mathrm{i}}\left(t_{\mathrm{k}\,+\,1}, (u_{\mathrm{j}}(t_{\mathrm{k}}) - \Delta u_{\mathrm{j}}(t_{\mathrm{k}}))\right)_m}{2\Delta u_{\mathrm{j}}(t_{\mathrm{k}})_m} \tag{6.8}$$

Once the Jacobian matrix is calculated and the Newton-Raphson technique is applied, then typically there are only a few iterations required to converge towards a solution at each time point. Once a solution is found for the first time point, the algorithm moves onto the next time and calculates the control action required to satisfy Equation (6.4). The end result is the calculation of the control activity throughout the manoeuvre.

Features of the Integration Method

The Integration Method has proven to an effective tool in the area of flight dynamics and has been particularly suited to helicopter analyses as they are required to perform precision manoeuvres frequently [102]. However, a natural question that arises is does the inverse simulation algorithm (integration method in this case) compare well with flight test results? Inverse simulation has shown to compare favourably with flight test manoeuvres [102, 126], indicating that it is a useful tool. Despite its successes, it is important to highlight some of the features of the inverse simulation algorithm, in its current form. The current integration method does not have a pilot model. Consequently, the integration method calculates the control activity to force the helicopter along a pre-determined flight path, precisely. In reality, a human pilot will not be able to follow the flight path with such precision. The pilot is likely to overshoot or undershoot the desired position and there will be an inevitable error between the required and actual flight path position [125]. In addition, the current inverse simulation algorithm does not faithfully model the pilot's lag between sensing an error and generating an appropriate control input to compensate. This type of lag is sometimes referred to as a "neuromuscular lag" [107]. Modelling this type of human behaviour would require a pilot model [107]. However, as the work does not focus on handling qualities a pilot model is not required.

Due to the level of modelling featured in this study it is assumed that the movement of the pilot's controls has an instant effect on that aircraft component. For example, when there is a change of collective angle then there is an instantaneous change of rotor thrust. The level of modelling does not take into account the dynamic, or time-dependent, behaviour of rotor inflow. Another example, is that an application of propeller pitch immediately increases the propulsive thrust of the propeller. In reality, it takes time for the control signal to reach the appropriate actuator and then the propeller blade pitch changes. Within perhaps 0.1s, the blade pitch changes and the airflow through the propeller disc accelerates as a consequence. These types of time delays, between the control input and the aircraft component reaching its desired response, are not modelled in the current work. Although transport delays and actuator lags are important in terms of handling qualities, the assumption made in this work is that they these delays are not significant in the context of a manoeuvrability investigation.

6.3 Manoeuvre Modelling

Of course, to successfully implement inverse simulation, the trajectory the aircraft is to follow is required. In the early inverse simulation algorithms, the output vector $\mathbf{y}_{des}$, which describes the trajectory, was defined as follows:

$$\mathbf{y}_{des} = \begin{bmatrix} x_e & y_e & z_e & \Psi \text{ or } \beta \end{bmatrix}^{\mathrm{T}} \tag{6.9}$$

where x_e, y_e and z_e are the flight path co-ordinates and the additional constraint is either the heading or sideslip angle. As previously stated, the integration method is a flexible and robust approach to solve the inverse problem. However, the development of this approach provided new numerical instabilities, such as the control activity featuring "low-amplitude, high frequency oscillations superimposed on the low frequency waveform" as discussed by Hess, Gao and Wang [108]. Originally, the desired output vector was composed of the flight path co-ordinates with an additional constraint, either the heading or sideslip angles, as seen in Equation (6.9). However, Rutherford

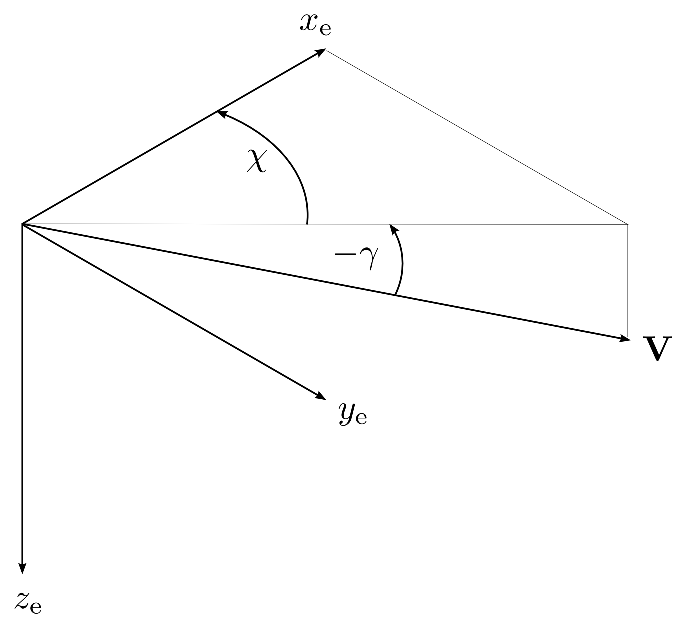

Figure 6.2: Trajectory Angles related to the Earth Axes

and Thomson showed that altering the output vector to be compose of inertial accelerations removed the high frequency oscillations of the control activity [126]. Therefore, modifying the output vector to the following

$$\mathbf{y}_{\mathrm{des}} = \begin{bmatrix} \ddot{x}_e & \ddot{y}_e & \ddot{z}_e & \dot{\Psi} \text{ or } \dot{\beta} \end{bmatrix}^{\mathrm{T}} \tag{6.10}$$

was shown to attenuate these oscillations [43]. Consequently, in this current work the output vector consists of the aircraft accelerations and heading or sideslip rate. The accelerations are determined by the differentiation of the velocities in Earth axes. The velocities, in Earth Axes, are conveniently described by the trajectory angles (glideslope and track angles) as seen in Figure 6.2. The velocities, are therefore given by

$$\dot{x} = V \cos\gamma \cos\chi \tag{6.11}$$

$$\dot{y} = V \cos\gamma \sin\chi \tag{6.12}$$

$$\dot{z} = -V \sin\gamma \tag{6.13}$$

leading to the following accelerations

$$\ddot{x} = \dot{V}\cos\gamma\cos\chi - V\dot{\gamma}\sin\gamma\cos\chi - V\dot{\chi}\cos\gamma\sin\chi \tag{6.14}$$

$$\ddot{y} = \dot{V}\cos\gamma\sin\chi - V\dot{\gamma}\sin\gamma\sin\chi + V\dot{\chi}\cos\gamma\cos\chi \tag{6.15}$$

$$\ddot{z} = -\dot{V}\sin\gamma - V\dot{\gamma}\cos\gamma \tag{6.16}$$

Therefore if γ, χ and V are all defined and their time derivatives calculated, then the accelerations can be determined, hence forming the output vector.

Selection of Manoeuvres

In theory, inverse simulation can be used to calculate the control activity required to fly any manoeuvre, with the assumption that an appropriate output vector, Equation (6.10), can be formed. There are a wide selection of manoeuvres which helicopters are required to perform routinely. However, as this is a study to examine the effects of compounding it seems necessary to restrict the analysis to certain manoeuvres where the addition of compounding is likely to have a significant influence. Conveniently, manoeuvres which represent real mission tasks [129], or so-called mission-task-elements (MTEs), are listed in the handling qualities performance standard of ADS-33 [130]. These are typical tasks which helicopters are required to perform safely, effectively and on a regular basis. Therefore, it seems prudent to select a manoeuvre from this library of MTEs. An additional benefit of selecting a manoeuvre based on a MTE is that it is likely that the mission-oriented framework of ADS-33 will be used to determine the handling qualities of compound helicopters. Therefore, in further studies, this current work could be taken further to assess the handling qualities of compound helicopters. The last factor in the selection of manoeuvres is the fidelity of the helicopter mathematical model. As discussed in Chapter 2, the current level of modelling is not suitable for flight regimes where the main rotor aerodynamics become highly nonlinear due to compressibility and reverse flow effects. Hence, the selected manoeuvres should begin and end when the helicopter is operating well within its Operational Flight Envelope (OFE). As a consequence, the modelling assumptions prohibit a manoeuvrability assessment of the compound helicopter at the edge of its perceived flight envelope. However, it is equally important to quantify the manoeuvrability of the compound helicopter in typical conventional helicopter flight regimes where the helicopter will spend a significant time operating.

To satisfy the these conditions, the manoeuvres selected are the Pullup-Pushover and the Accel-Decel manoeuvres which are described in the ADS-33 specification [130].

The main aim of the Pullup-Pushover manoeuvre is to test the aircraft's ability to avoid obstacles at flight speeds of 120 kt [130]. It is reasonable to expect that the addition of lift compounding would allow the aircraft to sustain greater load factors than a conventional helicopter. The addition of thrust compounding could also aid the manoeuvrability of the compound helicopter as the propeller(s) divorce the main rotor of its propulsive responsibilities. This manoeuvre satisfies the selection criteria, as outlined above, and therefore warrants an in-depth examination. The Accel-Decel manoeuvre is another well established manoeuvre in the ADS-33 specification which is used to test the pitch and heave handling qualities of a rotorcraft [130]. One undesirable effect of the conventional helicopter, is the large pitch excursions required to accelerate the aircraft. As the main rotor is the sole source of propulsion for a conventional helicopter, the rotor is required to tilt forward so that a component of the rotor thrust vector provides a propulsive force. This tilt of the main rotor also comes with the penalty of pitching the aircraft's nose down. However, the introduction of thrust compounding offers the potential of reducing the pitch excursion, as the propeller can provide the required propulsive force. As a consequence, the Accel-Decel manoeuvre is selected to investigate the influence of thrust compounding to the compound helicopter's manoeuvrability. The Accel-Decel begins in the hover and is therefore well within the region where realistic results can be expected.

Although only two manoeuvres are considered in this Thesis, it is possible that this work could be extended to investigate the manoeuvrability of compound helicopters in high speed manoeuvres. The natural consequence of compounding the helicopter is the expansion of the flight envelope, exposing the helicopter to unfamiliar flight conditions. Consequently, the compound helicopter will be able to perform high speed level turns or high-speed pull ups. These types of manoeuvres should be considered in future studies. An investigation of these types of manoeuvres would need to be supported by a high fidelity rotor model which is capable of modelling nonlinear aerodynamics such as retreating blade stall and compressibility effects. Lateral-directional manoeuvres, such as the slalom, could also be considered in future studies. The addition of propeller(s) to the helicopter's airframe will generate gyroscopic moments when the helicopter is pitching, rolling or turning. These moments could degrade the handling qualities of the vehicle and this type of study could provide some interesting results. Another issue is that compound helicopters typically do not have a conventional tail-rotor, meaning that the yaw control of the vehicle is provided by some other mechanism. Therefore, a manoeuvre like the slalom could potentially be used to compare the effectiveness of the devices which are used for yaw control.

ADS-33 Pullup-Pushover Manoeuvre

The Pullup-Pushover manoeuvre involves the aircraft achieving positive and negative load factors. The aircraft begins the manoeuvre at a trimmed condition at a flight speed equal to or less than 120 kt. The aircraft is required to achieve a sustained positive load factor in the pull up stage of the manoeuvre. Following this the aircraft is then to transition to a push over and achieve a negative load factor, then to recover to level flight as quickly as possible. The normal load factor is defined as

$$n_z = 1 - \frac{\ddot{z}}{g} \tag{6.17}$$

whereas the rearrangement of Equation (6.13) gives the standard definition of the glideslope angle

$$\gamma = -\sin^{-1}\frac{\dot{z}}{V} \tag{6.18}$$

The time derivative of the glideslope angle is therefore

$$\dot{\gamma} = \frac{-\dot{V}\sin\gamma - \ddot{z}}{V\cos\gamma} \tag{6.19}$$

Through the use of Equations (6.17) and (6.19), the time derivative of the glideslope angle can be expressed in terms of the normal load factor and flight speed

$$\dot{\gamma} = \frac{-\left(\dot{V}\sin\gamma + g - gn_z\right)}{V\cos\gamma} \tag{6.20}$$

The next step is to define the load factor distribution throughout the manoeuvre by applying manoeuvre boundary conditions. The ADS-33 document specifies the load factors to be attained throughout the manoeuvre [130]. To meet the desired standards of this manoeuvre, the maximum positive load factor must be attained after 1s of commencing the manoeuvre and sustained for a further 2s. Thereafter, the helicopter transitions from the positive load factor to the lowest load factor within 2s, and maintains this load factor for a further 2s. Figure 6.3 shows a typical load factor distribution which relates to the desirable standards set in the specification. The specification does

Table 6.1: Load Factor Boundary Conditions

Variable	$t_0 = 0s$	$t = t_1$	$t = t_2$	$t = t_3$	$t = t_4$	$t = t_5$	$t = t_6$
n_z	1	n_{max}	n_{max}	n_{min}	n_{min}	1	1
$\dot{n}_z$	0	0	0	0	0	0	0
$\ddot{n}_z$	0	0	0	0	0	0	0

not explicitly define an end time of the manoeuvre, a point raised by Celi [131], but does state that after the push over stage of the manoeuvre the aircraft should "*recover to level flight as rapidly as possible*". The assumption in this current work is that the manoeuvre ends when the aircraft's original flight speed is recovered at $t = t_5$ with the normal load factor returning to unity and sustained at this value for a further 2s until $t = t_6$. The approach taken to form the load factor distribution across the manoeuvre is to split the manoeuvre into six sections and apply manoeuvre boundary conditions, as seen in Table 6.1, between each of the manoeuvre segments. In each of the six segments, a fifth-order polynomial is formed to describe the load factor distribution. The Equations describing the variation of normal load factors throughout the manoeuvre are:

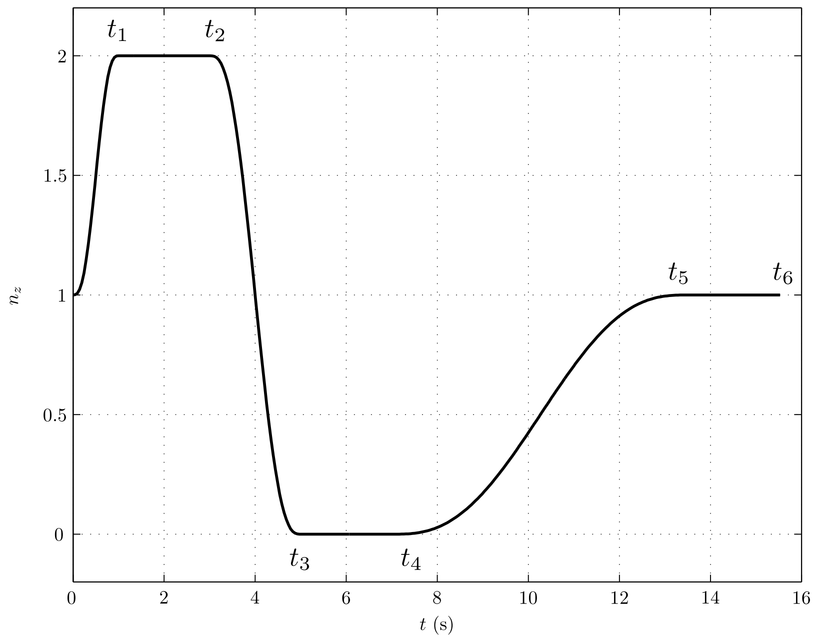

Figure 6.3: Desirable Load Factor throughout the Pullup-Pushover manoeuvre.

$$n_z = a_0 t^5 + a_1 t^4 + a_2 t^3 + a_3 t^2 + a_4 t + a_5 \qquad 0 < t < t_1 \tag{6.21}$$

$$n_z = n_{max} \qquad t_1 < t < t_2 \tag{6.22}$$

$$n_z = b_0 t^5 + b_1 t^4 + b_2 t^3 + b_3 t^2 + b_4 t + b_5 \qquad t_2 < t < t_3 \tag{6.23}$$

$$n_z = n_{min} \qquad t_3 < t < t_4 \tag{6.24}$$

$$n_z = c_0 t^5 + c_1 t^4 + c_2 t^3 + c_3 t^2 + c_4 t + c_5 \qquad t_4 < t < t_5 \tag{6.25}$$

$$n_z = 1 \qquad t_5 < t < t_6 \tag{6.26}$$

where the coefficients in Equations (6.21), (6.23) and (6.25) are determined by applying the boundary conditions between the start and end time of that manoeuvre segment, so that the normal load factor distribution in this portion of the manoeuvre is known. The end result is that there are six fifth-order piecewise polynomials, Equations (6.21) - (6.26), which describe the load factor distribution across the manoeuvre. These six polynomials are then pieced together so that the load factor distribution across the manoeuvre is known.

The next issue is to determine the variation of flight speed throughout the manoeuvre. One solution to this is to impose a predetermined profile of flight speed throughout the manoeuvre, however there is very little information regarding the variation of airspeed throughout this manoeuvre. The approach taken in this present work, in order to determine a flight speed profile, is to assume that there is a balance of potential and kinetic energy during the manoeuvre. For example, when the aircraft climbs there is a gain in potential energy which is balanced by a loss of kinetic energy. This is mathematically stated as

$$\frac{1}{2} m V^2 = m g z \tag{6.27}$$

and when differentiated with respect to time leads to

$$m V \dot{V} = m g \dot{z} \tag{6.28}$$

Recalling that $\dot{z} = -V \sin\gamma$, leads to the following equation

$$\dot{V} = -g \sin\gamma \tag{6.29}$$

Equation (6.29) describes the variation of airspeed throughout the manoeuvre. The result is that as the aircraft climbs, airspeed reduces whereas as the vehicle descends then airspeed increases. There are now two differential equations, Equations (6.20) and (6.29), which can be integrated to determine the flight velocity and climb angle throughout the manoeuvre, using the initial trimmed conditions. The track angle, χ, is set to zero since it is a longitudinal manoeuvre. Using the calculated values of V, $\dot{V}$, γ and $\dot{\gamma}$ the accelerations in the Earth axes set can be determined. Recall that the time derivative of the heading angle, $\dot{\Psi}$, is constrained throughout the manoeuvre and set to zero.

The inputs to inverse simulation are the parameters which define the flight path whereas the outputs are the vehicle's controls. As previously discussed, the flight path vector, $\mathbf{y}_{des}$, is composed of the accelerations of $\ddot{x}_e$, $\ddot{y}_e$ and $\ddot{z}_e$ relative to the Earth axes set. Generally speaking, the number of inputs must match the number of outputs to find a unique solution. Therefore, since the conventional helicopter features four controls then the condition of zero heading or sideslip is included so that the output vector contains four elements. However, the extra control(s) of the compound helicopter configurations presents an issue when attempting to calculate a unique solution of the control vector at each time point. Firstly, consider the HCH configuration which features five controls. One solution is to include an additional constraint in the output vector to match the five controls of the compound helicopter configuration. In terms of the Pullup-Pushover manoeuvre, the extra constraint is selected to be the time derivative of the fuselage angle of attack, $\dot{\alpha}_{fus}$. An alternative approach could have been to schedule a control such as θ_{1s} throughout the manoeuvre. However, the justification of the inclusion of the additional constraint, $\dot{\alpha}_{fus}$, is to ensure that the pilot adopts a control strategy which attempts to exploit the lifting capability of the wing in the pull up stage of the manoeuvre. It is found by experimenting with the simulation results that this approach of including $\dot{\alpha}_{fus}$ as an additional constraint, and appropriately scheduling this value over the duration of the manoeuvre, results in the wing's angle of attack increasing and decreasing in the respective pull up and push over stages of the manoeuvre. Figure 6.4 shows the distribution of the fuselage angle of attack, starting at its trim value of α_e before increasing to a value of 7° at 1s. After 1s, the fuselage angle of attack continues to increase, reaching a maximum value of approximately 17.5°. This increase of the fuselage angle of attack in the pull up stage of the manoeuvre increases the wing's angle of attack, helping the vehicle attain a positive load factor. Similarly in the push over stage of the manoeuvre the wing helps create a negative load factor. The fuselage angle of attack variation is described by a series of piece-wise fifth order

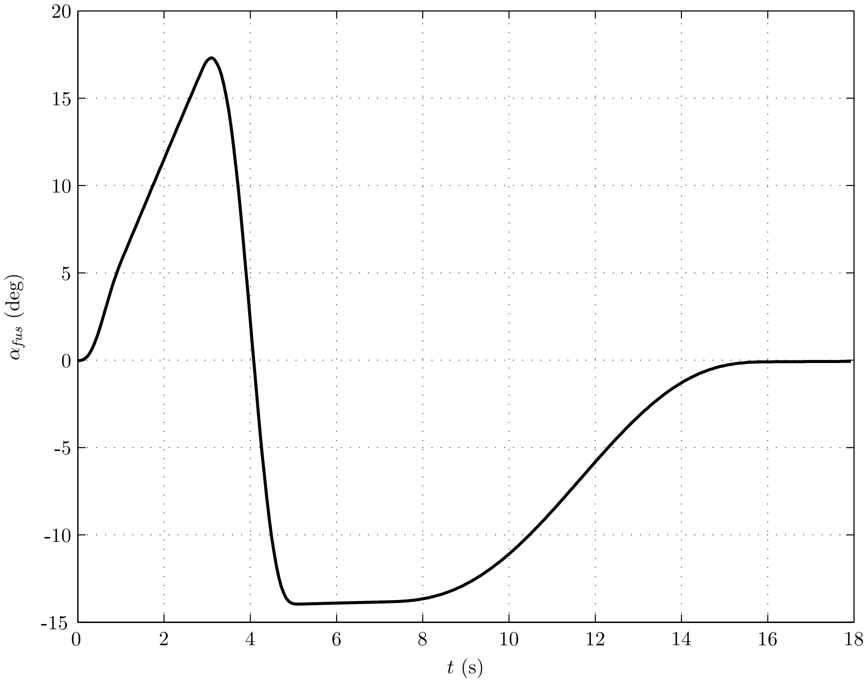

Figure 6.4: Fuselage Angle of Attack Variation throughout the Pullup-Pushover manoeuvre.

polynomials, similar in form to Equations (6.21) - (6.26), therefore the angle of attack time derivative, $\dot{\alpha}_{fus}$, is easily obtained through differentiation.

The previous discussion explained all the appropriate manoeuvre constraints to calculate the control action of the HCH configuration. As the CCH configuration features six controls then similar amendments to the flight path vector, $\mathbf{y}_{des}$, are required to determine the vehicle's control action. It is worth stating again, that the number of constraints must equal the number of controls so that the inverse simulation algorithm can determine the aircraft's control activity. The output vector, $\mathbf{y}_{des}$, for all three aircraft configurations is composed of the accelerations of $\ddot{x}_e$, $\ddot{y}_e$ and $\ddot{z}_e$ as well as the condition of zero heading rate. Clearly, two additional constraints are required, if the inverse simulation algorithm is to calculate all of the six unknown controls of the CCH configuration. Like the HCH configuration, one option is to prescribe the vehicle's fuselage angle of attack throughout the manoeuvre. The motivation for this approach was to utilise the wing's lifting capability in this particular aircraft arrangement. However, since the CCH configuration does not feature lift compounding, it is unlikely that a pilot would adopt a control strategy to maintain the required fuselage angle of attack. However, it is likely that a pilot would fly the manoeuvre in a manner which exploits the addition of thrust compounding. As a consequence, it is decided to schedule the

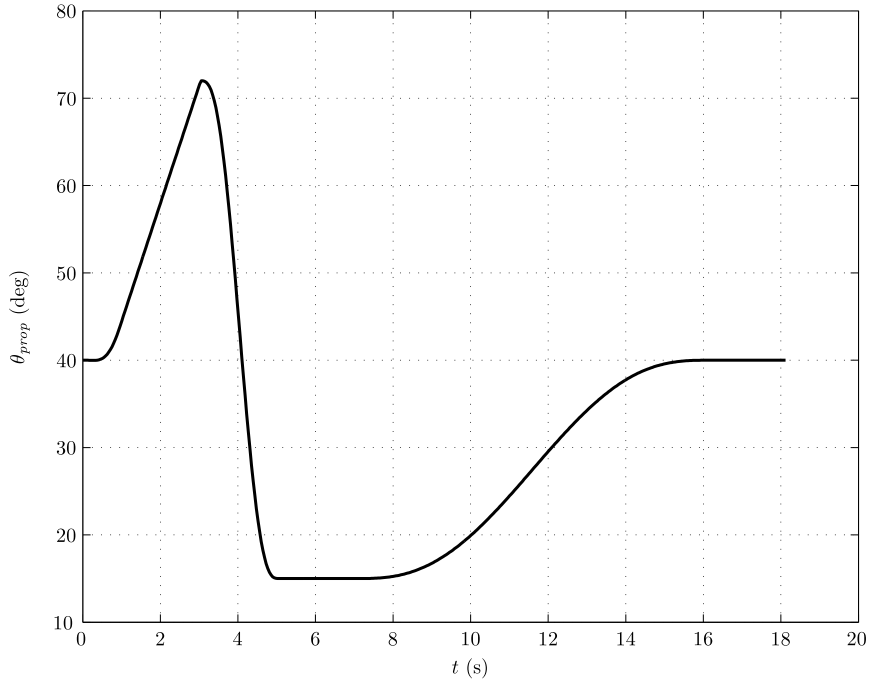

Figure 6.5: Propeller Pitch Variation throughout the Pullup-Pushover manoeuvre.

propeller pitch setting throughout the manoeuvre, which loosely resembles the load factor distribution. This approach ensures that the pilot uses the propeller to help achieve the required normal load factors. As a result, the number of unknown controls reduces to 5, as the propeller pitch setting is predetermined. The assumed variation of the propeller pitch setting is shown in Figure 6.5.

Another issue with the CCH configuration is how the differential lateral cyclic control, $\theta_{1c_{diff}}$, is used throughout the Pullup-Pushover manoeuvre. The use of differential lateral cyclic control promotes greater loading across the advancing sides of the rotor discs thereby offloading the retreating side of the discs. The manoeuvrability limit of the Pullup-Pushover manoeuvre is generally blade stalling, therefore it is likely that the lifting duties of the coaxial rotor would be shifted towards the advancing sides of the discs to delay the onset of retreating blade stall. To ensure that the CCH configuration is flown in this manner the lateral offset value, which is an input into the inverse simulation algorithm, is scheduled to vary with time as shown in Figure 6.6. In this manoeuvre, the LOS value begins at 0.09 (the value at the trimmed condition of 120 kt), then increases to 0.2 at 3s, where the manoeuvrability limit is expected to be reached. The choice of the maximum LOS value is chosen to offload the retreating side of the rotor discs but without the value being excessive. For example, Yeo and Johnson investigated LOS values up to 0.6, in their investigation of the lateral lift

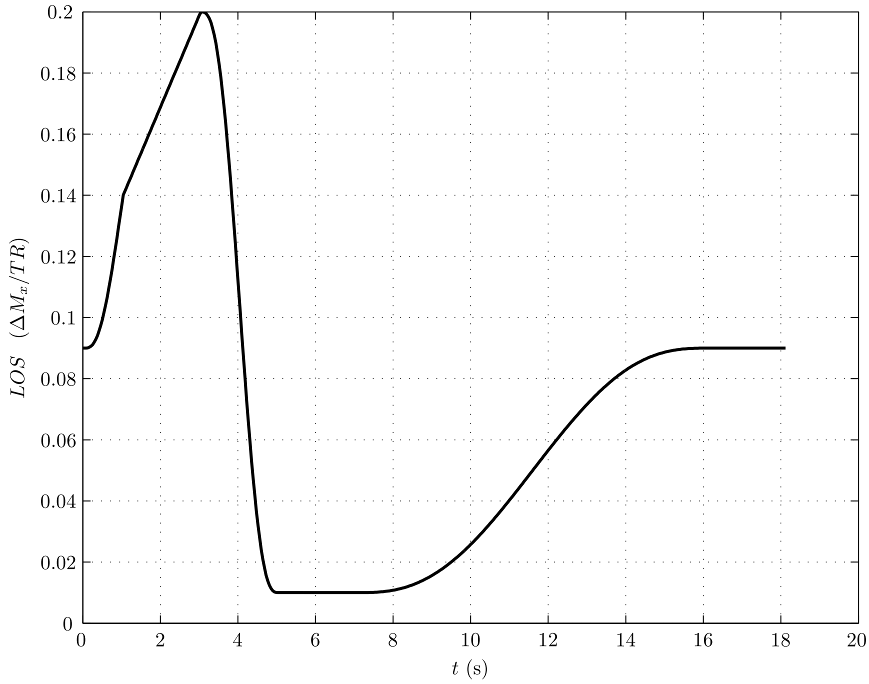

Figure 6.6: Lateral Offset Value (LOS) Variation throughout the Pullup-Pushover manoeuvre.

offset concept [80]. However, at these values of lateral lift offset the flapwise bending moment increases significantly [80]. Modelling high values of lateral lift offset, within the region of 0.6, would require a comprehensive rotorcraft modelling package which takes into account structural bending. This type of modelling would also have to be supported by detailed structural data of the rotor blades. Taking this into account, it seems appropriate to limit the lateral lift offset value to 0.2 in this manoeuvre, so that the lifting capability of the advancing side of the discs is exploited but within a region where the results can be considered valid. Returning to Figure 6.6, note that after the LOS reaches its maximum value of 0.2 it drops to 0.01 before returning to trim value of 0.09 at the end of the manoeuvre.

ADS-33 Accel-Decel Manoeuvre

The ADS-33 Accel-Decel manoeuvre starts with the aircraft in the stabilised hover with the aircraft accelerating to a flight velocity of 50 kt before aggressively decelerating back to a stabilised hover. The objective of this manoeuvre is to examine the pitch and heave axis handling qualities. Similar to that of the Pullup-Pushover manoeuvre the track angle and $\dot{\Psi}$ are set to zero throughout the manoeuvre. It is assumed that the maximum forward velocity of the aircraft is reached at the at half-way point of the manoeuvre.

In addition, the manoeuvre is completed when the helicopter returns to the hover. In total there are five boundary conditions of this manoeuvre which are given in Table 6.2. As a result, a fourth-order polynomial can be formed to describe the flight velocity

$$V(t) = d_0 t^4 + d_1 t^3 + d_2 t^2 + d_3 t + d_4 \tag{6.30}$$

According to the ADS-33 specification the altitude is to be held constant throughout the manoeuvre [130]. As a consequence, $\dot{z} = \ddot{z} = 0$ throughout the manoeuvre. Also recall that the heading rate, $\dot{\Psi}$, is held constant during the task. The end result is that the forward flight speed is given by $\dot{x} = V(t)$ where $\ddot{x}$ is readily obtained by the differentiation of Equation (6.30). The manoeuvre is defined by specifying the total manoeuvre time (or distance to be travelled) and the maximum flight speed, hence defining the output vector, $\mathbf{y}_{\text{des}}$.

Variable	$t = 0s$	$t = t_{\text{end}}/2$	$t = t_{\text{end}}$
V	0	50 kts	0
$\dot{V}$	0	-	0

Table 6.2: Accel Decel Boundary Conditions

The approach taken to calculate the control activity of the compound helicopter configurations throughout the Accel-Decel manoeuvre is to ensure that the number of manoeuvre constraints is equal to the number of controls. A logical question which arises with the compound helicopter configurations, flying an Accel-Decel manoeuvre, is how much of the propulsive force is provided by the thrust compounding device(s)? Conveniently, the fifth constraint for the Accel-Decel manoeuvre is selected to be the ratio between the propulsive force (i.e. the force in the x_e direction) produced by the propeller(s) and total propulsive force required. For a compound helicopter, it is likely that in the acceleration phase of the manoeuvre the pilot would adopt a control strategy which would actively use the propeller(s) to provide the required propulsive force. In terms of the HCH configuration, it is assumed that the two propellers provide 75% of the total force in the x_e direction at the point of maximum forward acceleration which is approximately $t_{end}/4$, Figure 6.7. Note that the entire propulsive force could be provided by the thrust of the propellers alone, however simulation runs showed that this strategy increases the power of the total vehicle excessively. The percentage of 75% is not an optimal value, however it is a compromise between fully exploiting the propulsive force of the propellers whilst keeping the power requirements, in the acceleration phase

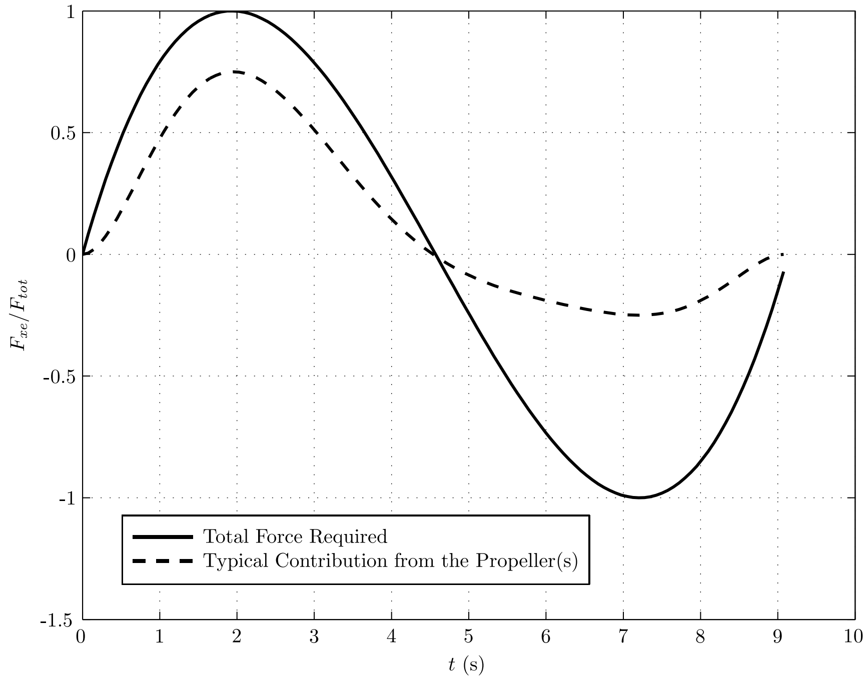

Figure 6.7: Contribution of the two propellers to F_{xe} throughout the Accel-Decel manoeuvre.

of the manoeuvre, within realistic values. Regarding the CCH configuration, it is assumed that the propeller provides 65% of the total propulsive force at the point of maximum forward acceleration. This value is chosen for similar reasons to those by the HCH configuration. An additional advantage of thrust compounding is the possibility of using the propellers to decelerate the aircraft by providing reverse thrust. It is fair to assume that the design of the the propulsor(s) would be optimized for high speed flight and not for reverse thrust purposes where the propellers operate in the windmill brake state. Hence it is assumed that for both configurations the thrust compounding device(s) are able to provide 25% of the entire reverse force required to decelerate the vehicle at the time of peak deceleration, $t \approx 3t_{end}/4$, as seen in Figure 6.7. The end result is that the majority of the force in the acceleration phase is provided by the thrust of the two propellers, whereas the deceleration phase involves more traditional helicopter like manoeuvring. The ratio of the propeller's propulsive force (i.e. the force in the x_e direction) and total propulsive force required is dependent on time, Figure 6.7, and is formed by the use of a eighth order polynomial

$$\frac{F_{prop}}{F_{tot}} = c_0 t^8 + c_1 t^7 \dots c_7 t + c_8 \tag{6.31}$$

where c_0, c_1, etc. are coefficients. For the HCH configuration, the manoeuvre is now fully described by five constraints: three accelerations, heading rate and the thrust the propellers are required to produce. These five constraints match the five unknown controls, which the inverse simulation algorithm calculates. In relation to the CCH configuration, an additional constraint is required to match the 6 unknown controls. This extra constraint is the lateral lift offset value required by the coaxial rotor. In this manoeuvre it is assumed that there is a simple flight control system which automatically controls the lateral lift offset value based on the vehicle's airspeed. This was the method used by Sikorsky in their flight tests of the Sikorsky X2 demonstrator. The distribution of the lateral lift offset across the speed range is loosely represented by

$$LOS = AV_f^2 \tag{6.32}$$

where the non-dimensional coefficient A is a constant and chosen so that LOS equals 0.2 at 200 kt. In the high speed range a value of 0.2 is required to avoid retreating blade stall [38], hence A is calculated to be 2×10^{-5}. In the context of the Accel-Decel manoeuvre, the desired lateral lift offset values are not significant across the manoeuvre. As it is a low speed manoeuvre, the power available is the limiting manoeuvring factor [1], so it is unlikely that large values of lateral lift offset would be used.

Before proceeding, it is necessary to highlight an important point about the inverse solution. In this manoeuvrability study, it is assumed that the pilot is continually using five or six controls (five for the HCH configuration, six for the CCH configuration) to control the aircraft. This would undoubtedly increase pilot workload throughout the manoeuvre. A solution to this issue could be a control system and interface, where the pilot has four available controls with a control system automatically altering the additional controls. For example, it is possible that a control system could be introduced so that the propeller pitch setting automatically increases once there is a forward displacement of the pilot's stick. Hence, a forward stick motion from the pilot would be met with an increase of axial thrust from the propeller(s). Such an investigation is not considered in the current work. However, it is clear that future studies would be required to explore the potential control systems which could be implemented in a compound helicopter design.

6.4 Manoeuvrability Assessment Method

The inverse simulation technique has been used to assess both the manoeuvrability and agility of helicopters [125, 132]. In this current study, a similar approach to Whalley's is adopted [125], in order to assess the maximum manoeuvring capability of three helicopter configurations. However, there are some differences. Firstly, the integration method is used within this work unlike the differentiation technique used by Whalley [125]. The integration method has proven to be a robust and flexible approach which separates the mathematical model and the inverse simulation algorithm. This method also permits the inclusion of high fidelity modelling techniques, such as individual rotor blade modelling, which are not included within this study of compound helicopters but could be in future work.

Another important difference between Whalley's work and the current approach is the definition of the limiting factor which determines the aircraft's ability to complete a manoeuvre. There are various limits which define the manoeuvrability of a rotorcraft, which include aerodynamic, power and control travel limits [1]. In Whalley's work [125] it is assumed that the maximum or minimum control angles are the limiting factor for the helicopter configuration to perform a particular manoeuvre. Indeed this can be selected to be the manoeuvrability limit in this work, however due to the assumption of

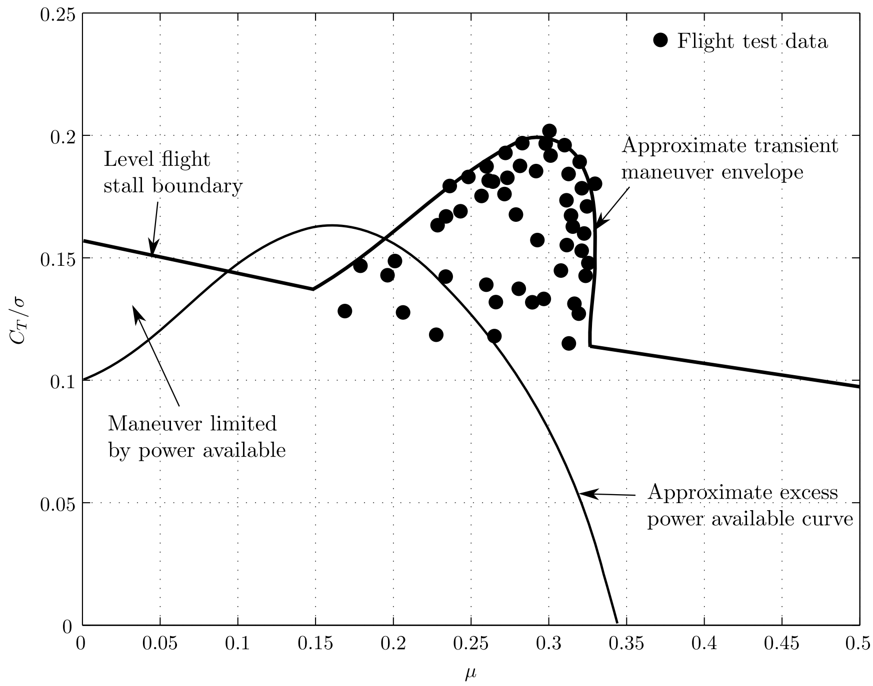

Figure 6.8: Manoeuvre capability adapted from Lappos and Padfield [133]

linear aerodynamics within the current rotor model and therefore not modelling blade stalling, the extreme limit of the main rotor collective can be reached producing an unrealistic amount of rotor thrust. The first solution to this is to assume that the aerodynamic limitations of the main rotor determine the maximum manoeuvring capability of the vehicle. Hence, it is assumed that the limiting factor of certain manoeuvres occurs when the main rotor blade loading, C_T/σ, reaches a maximum value. For transient manoeuvres, such as pull ups and turns, rotor blade stalling occurs at greater blade loading values than when compared to the helicopter in steady level flight [38]. This result has been confirmed by flight test data, see Figure 6.8, which was obtained from Lappos and Padfield [133]. The reason that the main rotor is able to delay the onset of retreating blade stall is due to the positive influence of the manoeuvre which effectively reduces the local angles of attack across the retreating side of the disc [38]. The flight test data obtained by Lappos and Padfield [133] can be conveniently used to approximate a transient manoeuvre boundary envelope, as seen in Figure 6.8. As this envelope has been established from flight test data, in the context of this study it is assumed that the limiting factor of certain manoeuvres occurs when the main rotor's blade loading reaches the transient manoeuvre boundary in Figure 6.8. This limitation is appropriate in forward flight manoeuvres, due to the high level of excess power available. However, for low speeds manoeuvres the manoeuvring capability is generally limited by excess power available [1], as seen in Figure 6.8. Therefore, in low speed manoeuvres it is appropriate to assume that the power available restricts the vehicle's ability to complete a manoeuvre. It is evident that the manoeuvrability limit could be due to the aerodynamic restrictions of the main rotor or power requirements. For these reasons, the manoeuvrability method allows the user to select their assumed limit which can be based on control travel limits, main rotor aerodynamic restrictions or the power available.

Figure 6.9 presents an overview of the Manoeuvrability Assessment Method (MAM). This iterative method uses inverse simulation to determine the maximum manoeuvring capability of the three aircraft configurations: the BL, HCH and CCH configurations. The method begins at the first iterative counter and subsequently defines the manoeuvre. Thereafter, the integration method calculates the control angles required to force the particular aircraft configuration along the desired flight path. With the controls and states calculated throughout the manoeuvre, the assumed limiting factor determining the vehicle's manoeuvrability can be calculated. If the limit is selected to be the aerodynamic restrictions of the main rotor then the main rotor blade loading at every time point is calculated. If $C_T/\sigma < (C_T/\sigma)_{max}$ at any time point throughout

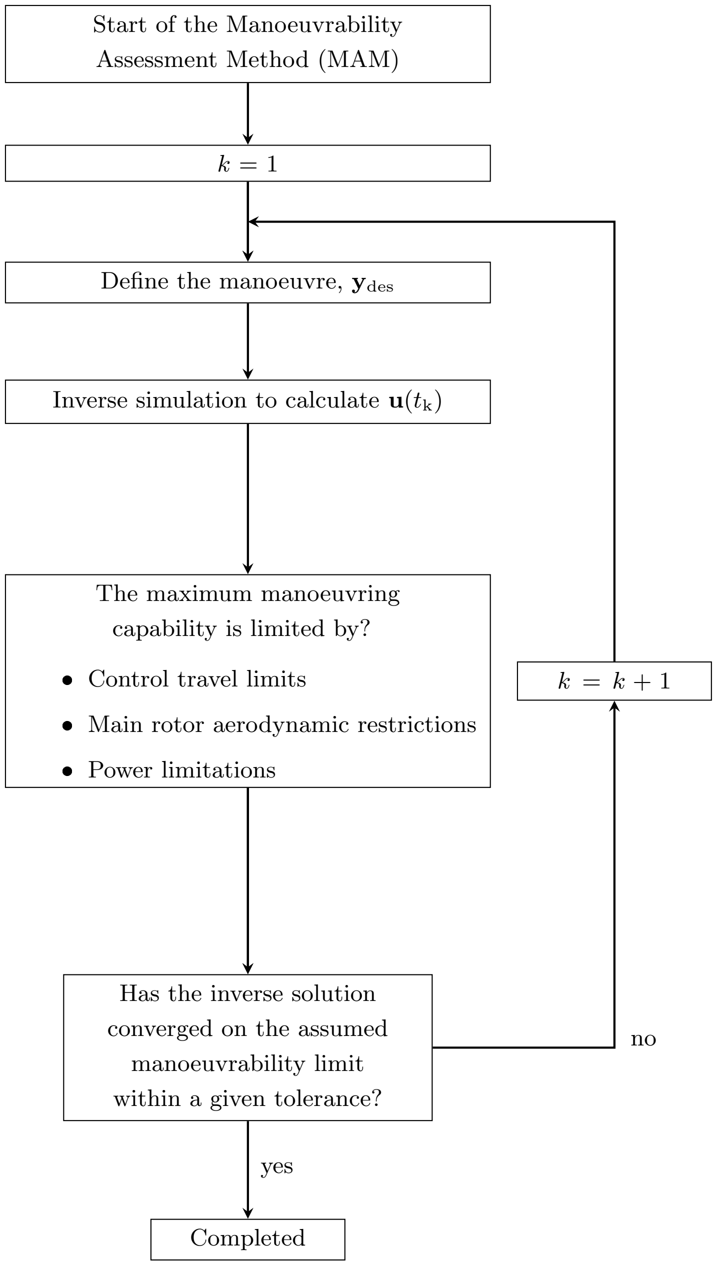

Figure 6.9: Flowchart Describing the Manoeuvrability Assessment Method.

the manoeuvre then the aggressiveness of the manoeuvre is redefined until this condition is satisfied. Conversely, if the power available is the limiting factor then the total power throughout the manoeuvre is calculated and then the manoeuvre is redefined until MAM converges towards a solution. In terms of the Pullup-Pushover manoeuvre, the maximum load factor, n_{max}, in the manoeuvre definition, is allowed to alter the aggressiveness of the manoeuvre and therefore converge towards the manoeuvrability limit. In contrast, with the Accel-Decel manoeuvre the distance travelled by the vehicles, S, is varied to converge towards a solution. The manoeuvrability limit is generally reached within 5 iterations.

6.5 Manoeuvrability Results

HCH Configuration Pullup-Pushover Results

With the methodology developed, MAM can now be used to predict the manoeuvrability of the three aircraft configurations. Consider the HCH and BL configurations first. For both configurations, flying the Pullup-Pushover manoeuvre, it is assumed that the limiting factors are the aerodynamic restrictions of the two main rotors. Hence, throughout the manoeuvres the aerodynamic blade loading of the main rotors, C_T/σ, is calculated and the aggressiveness of the manoeuvre refined until the maximum blade loading is reached. The Pullup-Pushover manoeuvre begins at an airspeed of 120 kt and as the aircraft climbs, airspeed begins to reduce due to a gain of potential energy. The maximum blade loading is likely to occur at 3s into the manoeuvre, since this is where the highest load factor is to be obtained with the lowest amount of translational kinetic energy. At this flight condition the flight speed drops to ≈100 kt, which corresponds to an advance ratio, μ, of approximately 0.22. With the use of Figure 6.8, which approximates a transient manoeuvre boundary, the maximum blade loading, $(C_T/\sigma)_{max}$, which can be expected at this flight speed is 0.17. As a consequence, it is assumed that the limiting factor for this manoeuvre is when $(C_T/\sigma)_{max} = 0.17$ for both aircraft configurations.

Figure 6.10 presents the blade loading values at each time point for both aircraft configurations. As expected, the predicted limiting state of the main rotors of the BL and HCH configurations occur at ≈3s. It is interesting to the note the large differences in blade loading between the two configurations at 2s. At this time point, for the BL configuration, $C_T/\sigma = 0.15$, whereas at the same time point $C_T/\sigma = 0.115$ for the HCH configuration. The difference is due to the wing offloading the main rotor significantly at this particular point in the manoeuvre. However, notice that there is a sharp rise in blade loading for the HCH configuration after 2.3s to increase the main rotor's thrust to sustain the positive load factor. The load distributions and height achieved by each vehicle are shown in Figure 6.11. The maximum load factors achieved by the HCH and BL configurations are 2.262 and 2.149, respectively. As a consequence the HCH configuration climbs to a greater height than the BL configuration. The HCH configuration reaches a height of 169m after 8.5s whereas the BL configuration's maximum height of 147m is attained at 8.2s. Although the HCH configuration is capable of climbing to a greater height than the BL configuration, the result may be viewed as somewhat surprising as one might intuitively think that the maximum load factor capability of a winged helicopter would significantly surpass the conventional helicopter's capability. This may indeed prove to be the case for high speed manoeuvres where the lifting capability of the wing is fully exploited due to high dynamic pressure values. Figure 6.12 presents the airspeed and the wing's angle of attack variation throughout the Pullup-Pushover manoeuvre. Figure 6.12 confirms that an effort is made to ensure that the Pullup-Pushover manoeuvre is flown in a manner which realises the lifting potential of the wing. For example, Figure 6.12(a) shows the wing's angle of attack increases significantly in the early stages of the pull up to increase the wing's lifting force, with the wing's angle of attack reaching a maximum value of 15° at 3s. The high angle of attacks in the pull up stage of the manoeuvre promote a lifting force and as a consequence the wing provides about 20% of the vertical force at 3s. This contribution towards the lifting force is ultimately limited by the relatively low airspeeds in which the manoeuvre is performed, shown in Figure 6.12(b). Recall that this manoeuvre begins at 120 kt which is a modest flight speed for a fixed wing aircraft. The airspeed drops after the manoeuvre has commenced as the aircraft climbs. Hence, the relatively low airspeeds coupled with a medium sized wing limit the lifting capability of the wing throughout the manoeuvre.

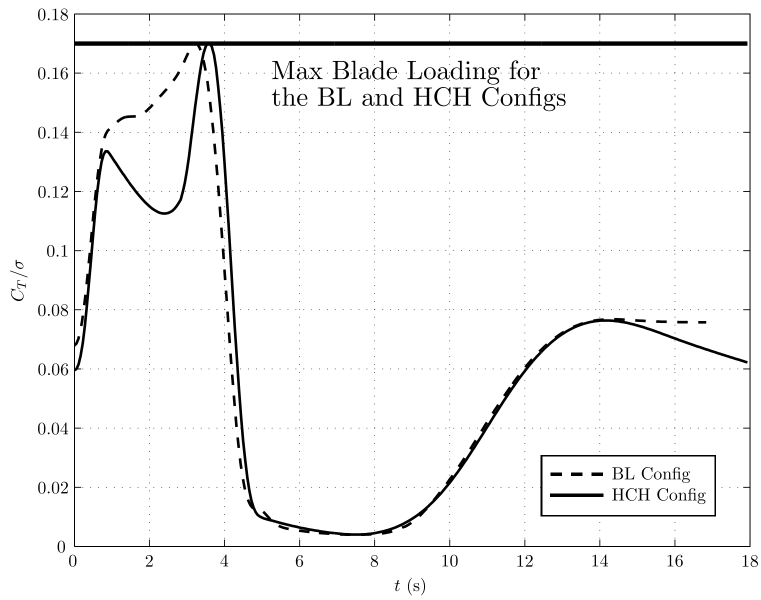

Figure 6.10: Blade Loading for the BL and HCH Configurations during the Pullup-Pushover manoeuvre.

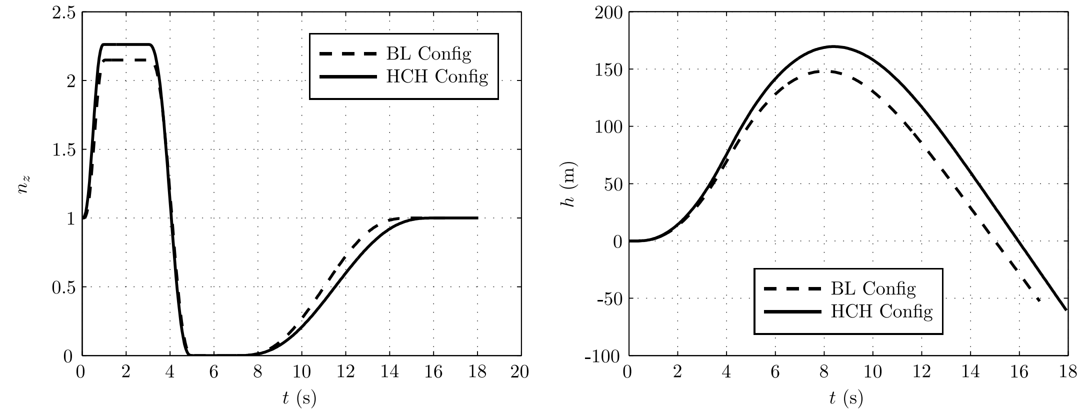

(a) Load Factor Distribution (b) Height

Figure 6.11: Load Factor and Height Variation throughout the Pullup-Pushover Manoeuvre.

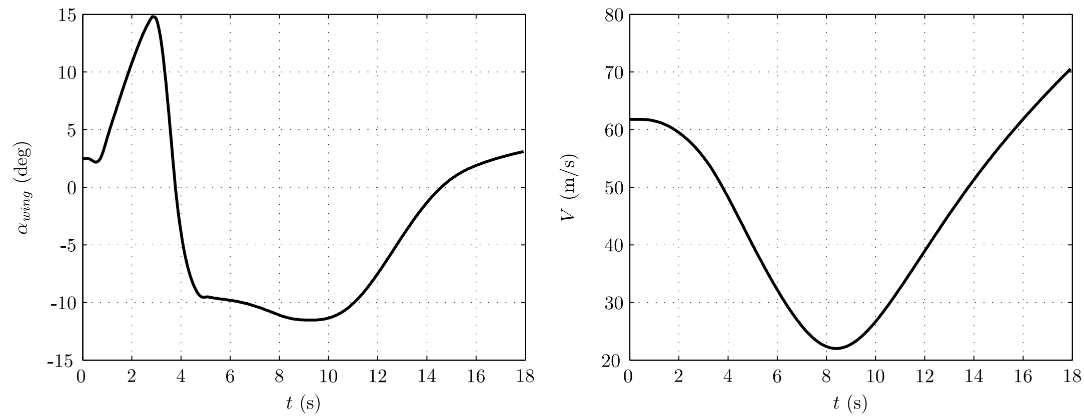

(a) Wing Angle of Attack (b) Airspeed

Figure 6.12: Airspeed and Wing's Angle of Attack Variation throughout the Pullup-Pushover Manoeuvre.

To properly interpret the results presented in Figure 3.10 it is convenient to inspect the forces that the HCH configuration's components produce. Figure 6.13 shows the main rotor, wing and propeller forces in the x_e and z_e directions of the Earth Axes set. Also shown in Figure 6.13 are the forces required by the aircraft components to complete the manoeuvre. Note that the forces produced by the fuselage, tailplane and fin are not shown for the purposes of clarity. The pull up stage of the manoeuvre is characterised by a reduction in airspeed as there is a drop in translational kinetic energy as the aircraft climbs. As a consequence, a significant amount of force in the negative x_e

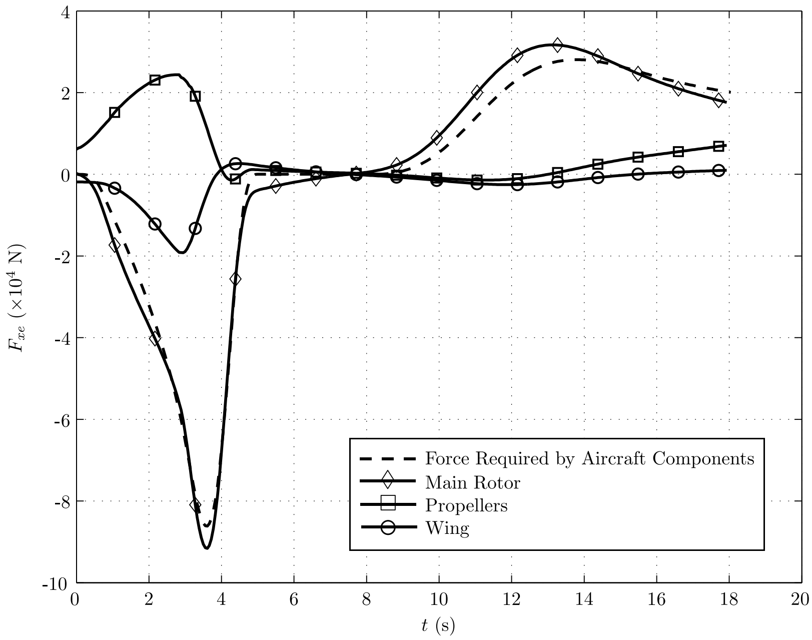

(a) Forces in the x_e axis

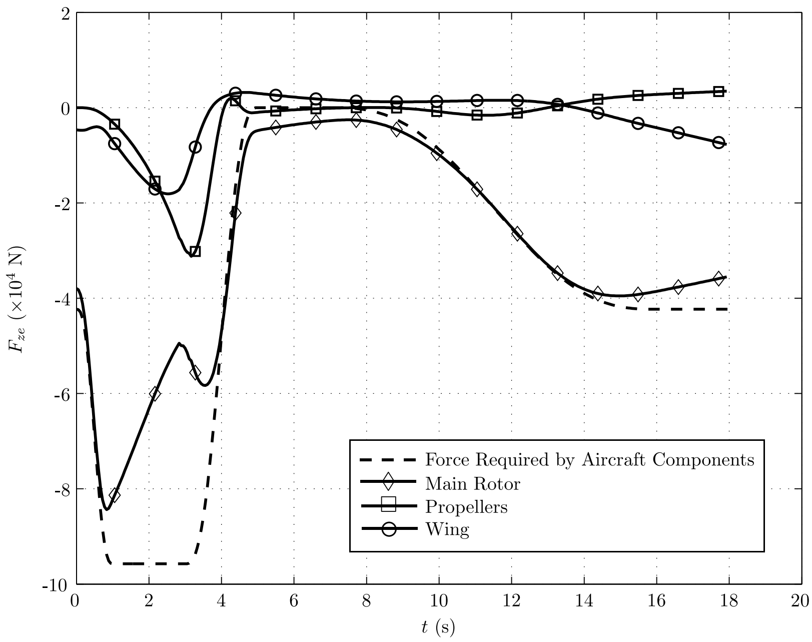

(b) Forces in the z_e axis

Figure 6.13: Main Rotor, Wing and Propeller Forces of the HCH Configuration in the x_e and z_e directions of the Earth Axes set during the Pullup-Pushover Manoeuvre.

direction is required, as seen in Figure 6.13(a), by the aircraft components to decelerate the vehicle. Figure 6.13(a) shows that the main rotor provides the majority of the force to decelerate and pitch the aircraft's nose up in the first part of the manoeuvre. At 2.5 seconds into the manoeuvre the wing provides 16kN in the negative x_e direction due to the aircraft's nose pitching up to attain the necessary load factor. In contrast, the two propellers provide a significant force in the positive x_e direction to overcome the airframe's drag and to maintain the required fuselage angle of attack. Figure 6.13(b) presents the forces required by the HCH configuration's components to provide the required vertical acceleration. In the early stages of the manoeuvre, up to 3s, the wing's lifting force sharply increases as the aircraft's nose pitches up, thereby increasing the wing's angle of attack. The wing produces 19kN of force in the vertical direction at 3s. However, after 3s the wing's lifting force in the z_e direction begins to deteriorate due to the piloting strategy to sharply reduce the fuselage's angle of attack to transition to the load factor of zero at 4s. It is also interesting to note that the propellers contribute significantly to provide the required normal load factor, with the propellers providing 31kN of useful force in the negative z_e direction at 3.5s into manoeuvre. At this time the vehicle's fuselage pitch angle is approximately 44°. Propellers generally create the majority of their propulsive thrust in the direction normal to the propeller disc plane, however due to the high fuselage pitch angle a significant amount of the propeller's propulsive force transforms into the z_e direction, thereby providing a useful force to obtain the highest load factor possible.

Figure 6.14 shows the predicted control displacements throughout the maximum Pullup-Pushover manoeuvres. In the first second of the manoeuvre, a large main rotor collective control input is required by the BL configuration to transition to a positive load factor. However, the collective lever of the HCH configuration is lower than of its conventional helicopter counterpart within the early stages of the manoeuvre. The differences in the large initial longitudinal stick inputs, up to 3s, are due to the contribution of the two propellers in the HCH configuration. There is a rapid rise in the mean propeller pitch setting, $\bar{\theta}_{prop}$, within the first second of the initial control input to increase the propulsive force of the two propellers. After 4s the trend of the longitudinal stick displacements are similar for the two aircraft configurations. As the vehicles transition to their minimum load factors, n_{min}, both assumed to be 0, the main rotor collective levers drop to lower the level of rotor thrust. The longitudinal cyclic of the BL configuration reaches its minimum value at 5s as it pitches the aircraft down to achieve a zero normal load factor. The propeller pitch control input increases consistently from the start of the manoeuvre until 3s to promote greater propulsive force to

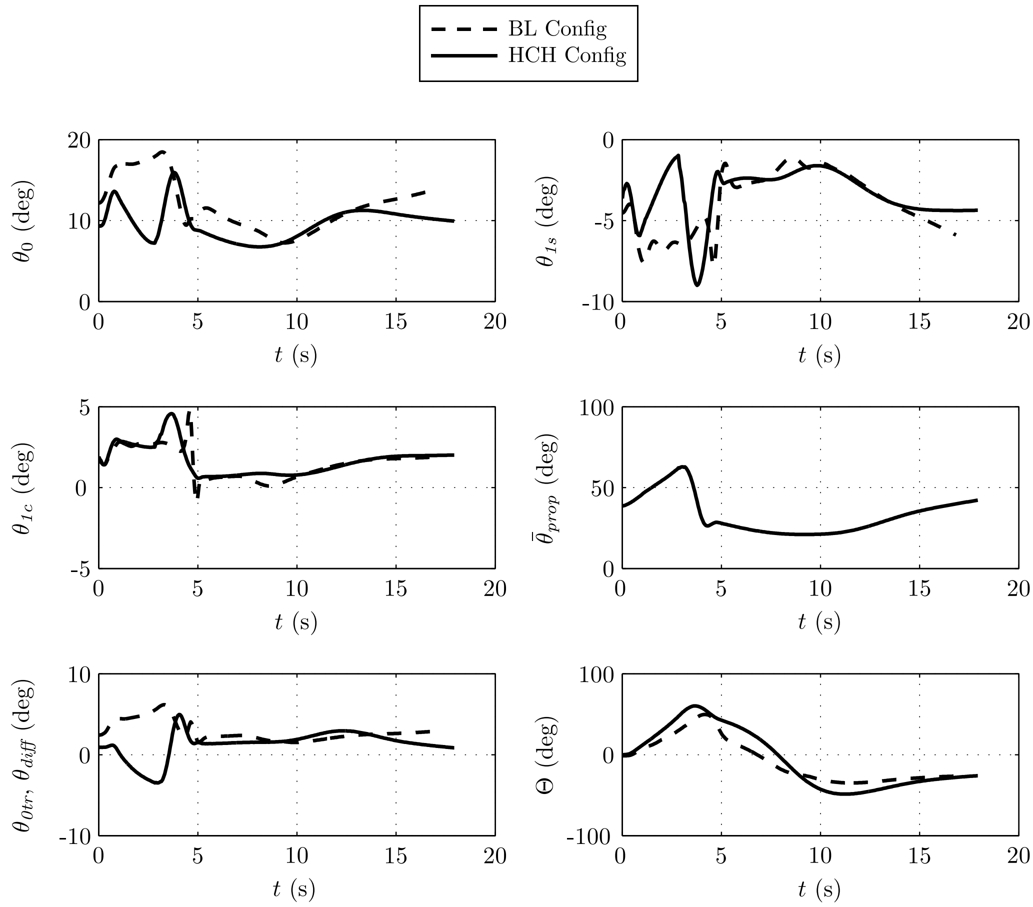

Figure 6.14: Maximum Manoeuvrability Control time histories of the HCH and BL configurations during the Pullup-Pushover manoeuvre.

supplement the contributions of the wing and main rotor to sustain the positive load factor. However, as the aircraft transitions to a push over the control input reduces significantly from 62° to a value of 27°. The control remains within this region until it is increased in the latter stages of the manoeuvre to recover the vehicle's original airspeed.

HCH Configuration Accel-Decel Results

For the Accel-Decel manoeuvre, the power available is assumed to be the limiting factor influencing the manoeuvrability of the two aircraft configurations. Figure 6.15 shows the power variation of the two configurations throughout the maximum Accel-Decel manoeuvre. The two configurations reach their limiting states, i.e. $P_{tot} = P_{av}$, at the point of maximum forward acceleration. It is assumed that the installed engine power of the HCH configuration is 2000kW, which is a significant increase from the 1300kW available for the BL configuration. Although this is not a design study, various other studies have concluded that the compound helicopter is expected to have significantly more power than a conventional helicopter [21, 134]. The compound helicopter is expected to operate at high speeds where parasite power, which is proportional to the cube of the airspeed, dominates the power required [38]. To overcome this parasite power penalty requires a significant reduction of airframe drag or a large increase of installed power. Although it is the goal of the designer to minimise drag there is a practical limit to which the rotorcraft's drag can be reduced. The result is that an increase of installed engine power for the compound helicopter configuration is required. Therefore, it seems reasonable to increase the HCH configuration's available power to assess the vehicle's potential manoeuvrability. The predicted result is that the HCH configuration is capable of completing the manoeuvre quicker than the BL configuration, as seen in Figure 6.16, with the BL and HCH configurations completing the manoeuvre in 8.9s and 10.1s, respectively. Figure 6.16 shows the longitudinal distance travelled by the two vehicles, with the BL configuration completing the manoeuvre over a distance of 139.8m, whereas the HCH configuration covers a total distance of 124.7m. This result suggests that the HCH configuration is capable of completing the manoeuvre quicker than the BL configuration but requires greater installed power to do so.

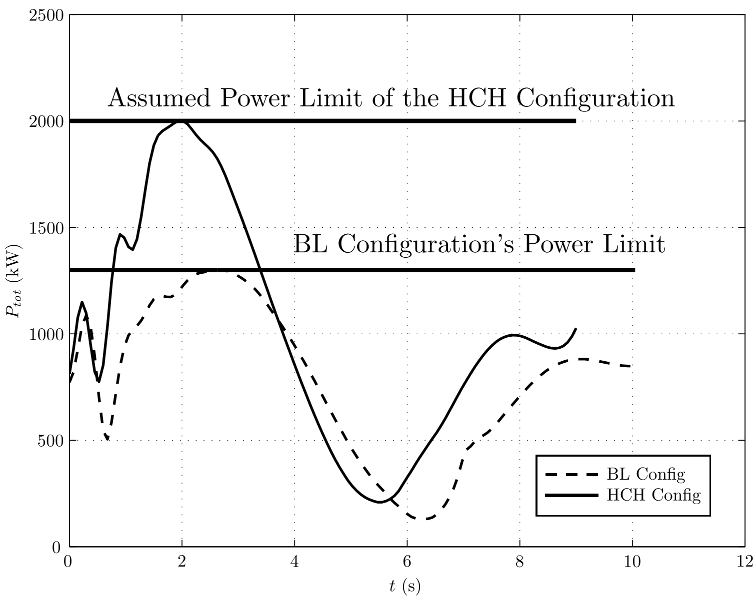

Figure 6.15: Power variation of the two configurations throughout the maximum Accel-Decel manoeuvre.

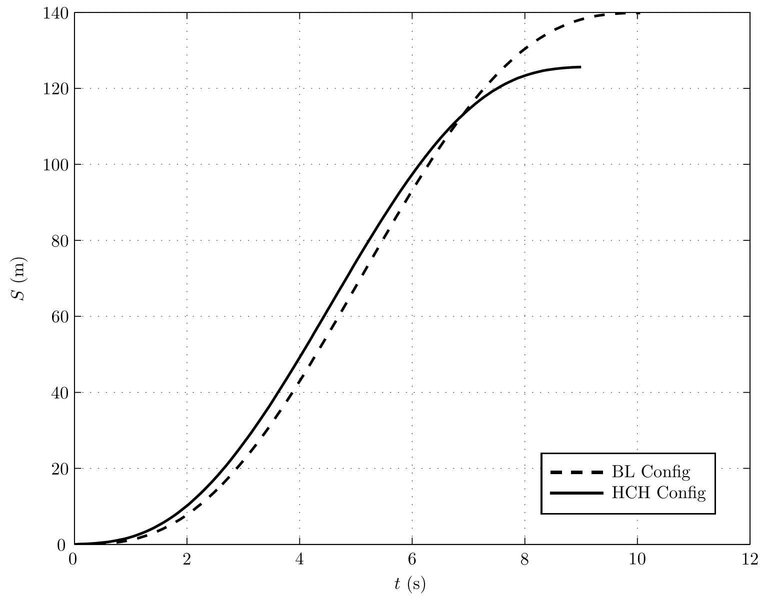

Figure 6.16: Flight path of the maximum Accel-Decel manoeuvres.

Figure 6.17 shows the forces produced by HCH configuration's main rotor, wing and propellers in the x_e and z_e directions of the Earth Axes set during the Accel-Decel manoeuvre. Recall that with the HCH configuration, the additional constraint imposed in the Accel-Decel manoeuvre is the amount of propeller thrust that provides the total propulsive force required throughout the manoeuvre. As expected, the two propellers provide 75% of the total propulsive force at the point of maximum forward acceleration, as seen in Figure 6.17(a). As the aircraft begins decelerating, the main rotor disc tilts backwards to slow the aircraft's flight speed. As the propellers provide 25% of the required reverse force, at the point of maximum deceleration, the HCH configuration decelerates by traditional helicopter manoeuvring, by the main rotor disc flapping backwards with the consequence of significantly pitching the vehicle's nose upwards. In terms of the forces in the z_e direction, the vertical force required by the aircraft components is simply the aircraft's weight, as the vehicle does not change height throughout the manoeuvre. Figure 6.17(b) presents the forces produced by the aircraft components of the HCH configuration in the z_e axis. As seen in Figure 6.17(b), the main rotor provides the majority of the lifting force throughout the manoeuvre. The addition of lift compounding to the HCH configuration's design is detrimental in this particular manoeuvre as the wing produces an aerodynamic download throughout the manoeuvre, Figure 6.17(b). Although the wing is beneficial at high speeds, as it offloads the main rotor, in the hover and low speed flight it provides a significant download,

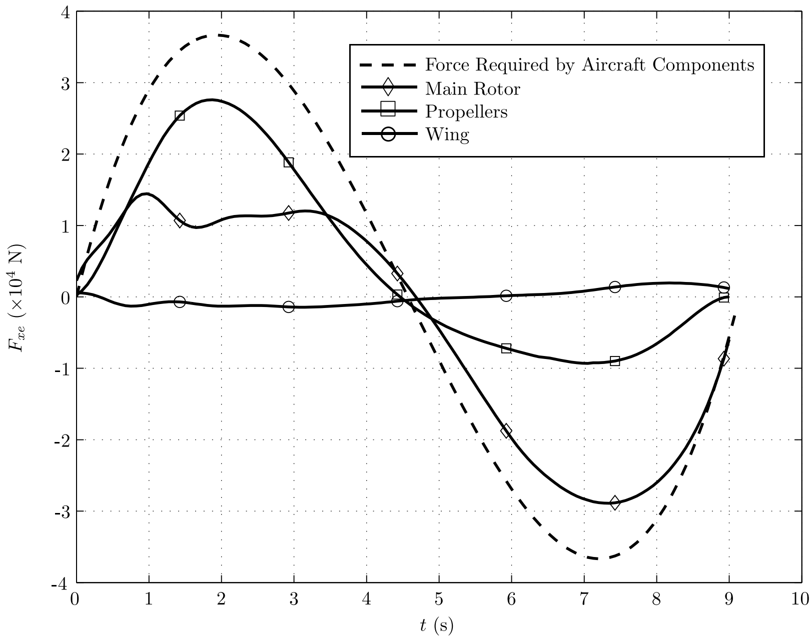

(a) Forces in the x_e axis

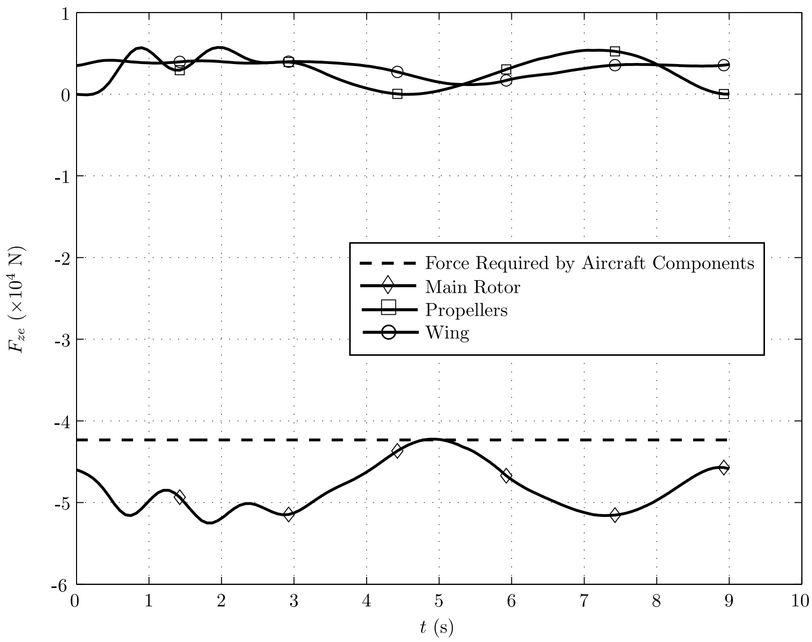

(b) Forces in the z_e axis

Figure 6.17: Main Rotor, Wing and Propeller Forces of the HCH Configuration in the x_e and z_e directions of the Earth Axes set during the Accel-Decel Manoeuvre.

reducing low speed performance. It is likely that a winged compound helicopter would implement the use of flaps which were used on the tilt-rotor aircraft [24]. However,

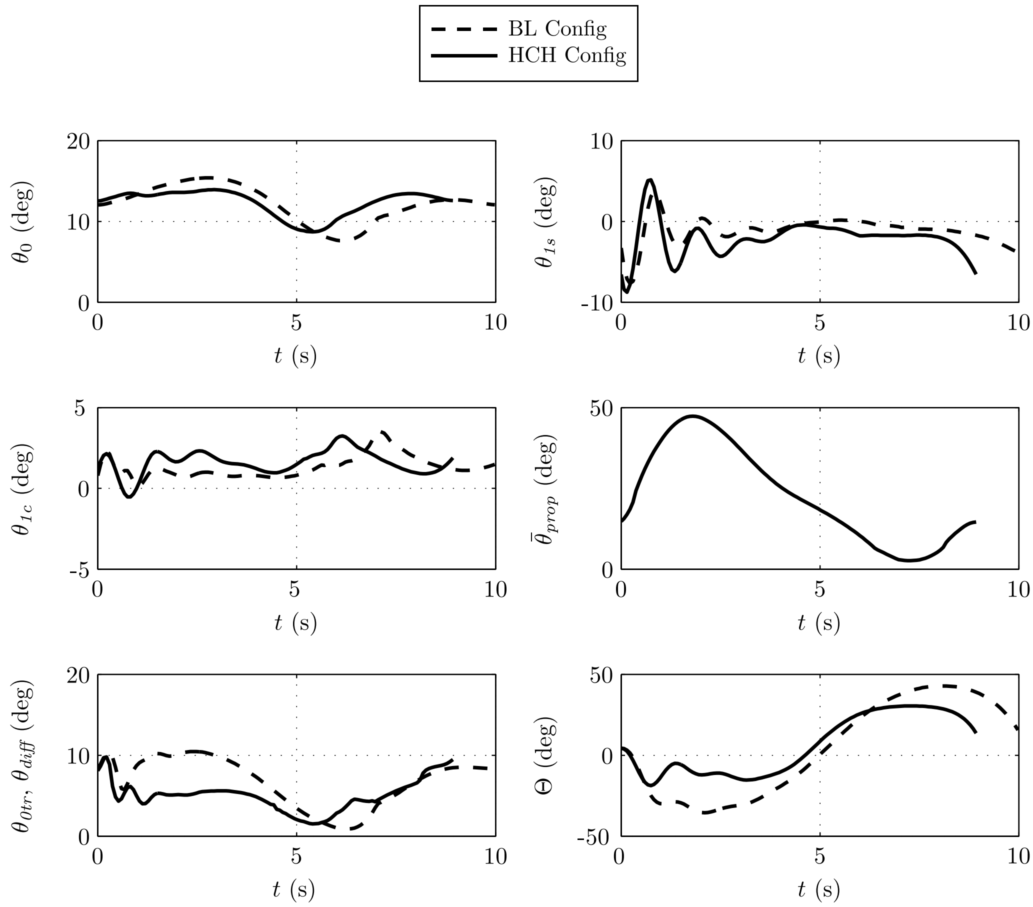

Figure 6.18: Maximum Manoeuvrability Control time histories of the HCH and BL configurations during the Accel-Decel manoeuvre.

even with the use of flaps the wing will still provide an aerodynamic download in low speed flight, which is an inevitable consequence of lift compounding.

Figure 6.18 presents the control time histories throughout the maximum Accel-Decel manoeuvres. As noted previously, there are five manoeuvre constraints which are the three accelerations, heading rate and the contribution of the thrust from the two propellers which make up the total propulsive force required. The inverse simulation algorithm calculates the control activity required for the aircraft to fly the manoeuvre in this particular manner. The advantage of using the final constraint is that the two propellers are actively used to provide the majority of propulsive force in the early stages of the manoeuvre. As a consequence, the two propellers provide 75% of the total force in the x_e axis, as seen in Figure 6.17(a), at the time where maximum forward acceleration is required. Therefore, the mean propeller pitch, $\bar{\theta}_{prop}$, increases significantly in the early stages of the manoeuvre, as seen in Figure 6.18. The trend of $\bar{\theta}_{prop}$ is similar to that of the propulsive force required by the propellers throughout the manoeuvre, with the control increasing in the first stage of the manoeuvre and reducing to provide some level of reverse thrust. At the starting position of the manoeuvre the main collective of the HCH configuration is greater than that of the BL configuration. This is due to the wing of the HCH configuration providing an aerodynamic download which requires additional collective input to offset the download force. As the manoeuvre commences, the main rotor collective of the BL configuration increases, to increase rotor thrust, with the control reaching its highest value at 4s. For the HCH configuration its highest collective setting is lower than that of the BL configuration. The main rotor is only required to provide 25% of the forward force in the x_e direction, at the time of peak forward acceleration, which consequently reduces the amount of collective input required. For a conventional helicopter the main rotor is responsible for both the propulsive and lifting capability of the vehicle [1]. One undesired quality of the helicopter is that in order to accelerate or decelerate a large pitch excursion is required. Due to the addition of thrust compounding, after 2s the main rotor disc of the HCH configuration does not have to tilt as much as the BL configuration in order to provide the propulsive force to the accelerate the vehicle. The net effect is that the pitch attitude is reduced, between 1-4s, when the pitch attitude of the two configurations are compared, highlighting one of the benefits of thrust compounding. As the propellers provide a modest level of reverse thrust, the HCH configuration decelerates by traditional helicopter manoeuvring. However, the peak pitch attitude of the HCH configuration is lower than that of the BL configuration, as a result of the reverse thrust the two propellers provide. The main rotor cyclic inputs are very similar throughout the manoeuvre. Both configurations exhibit large oscillatory longitudinal cyclic control inputs at the beginning of the manoeuvre. In terms of the anti-torque controls, θ_{0tr} and θ_{diff}, their control time histories are similar to the collective settings in order for the aircraft configurations to retain a constant heading.

CCH Configuration Pullup-Pushover Results

The fundamental premise of the Advancing Blade Concept is that it can overcome the aerodynamic restrictions which generally limit the lifting capability of a single main rotor. A recent study of the lateral lift offset concept concluded that the maximum lifting capability of this coaxial rotor system is greater than a conventional single rotor [80]. This is further reinforced by the flight tests of the XH-59A, which demonstrated that the aircraft was capable of reaching a blade loading value, C_T/σ, of 0.28 in a high speed manoeuvre at an advance ratio of 0.4 [135]. The lift potential of the advancing

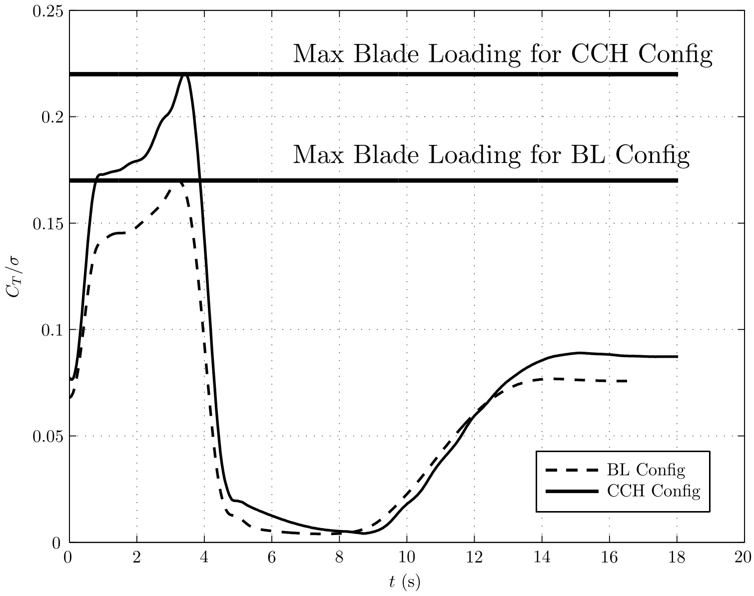

Figure 6.19: Maximum Blade Loadings of the BL and CCH Configurations

sides of the discs can be fully realised and the net rolling moment of the rotor system is maintained due to the counter rotating rotors. The end result is that stall boundary of a lateral lift concept rotor is greater than that of a single main rotor, which is well predicted by the classical McHugh lift boundary [136–138].

It is clear that the maximum lift capability of the coaxial rotor is greater than that of the conventional single main rotor for a given solidity. Consequently, it is appropriate to increase the maximum blade loading limit of the coaxial rotor, relative

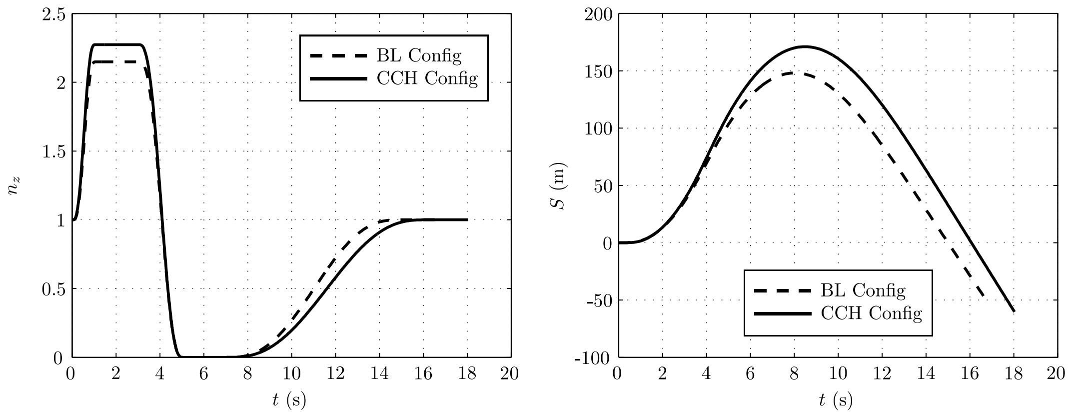

(a) Load Factor Distribution (b) Height Profile

Figure 6.20: Flight path during the Pullup-Pushover Manoeuvres.

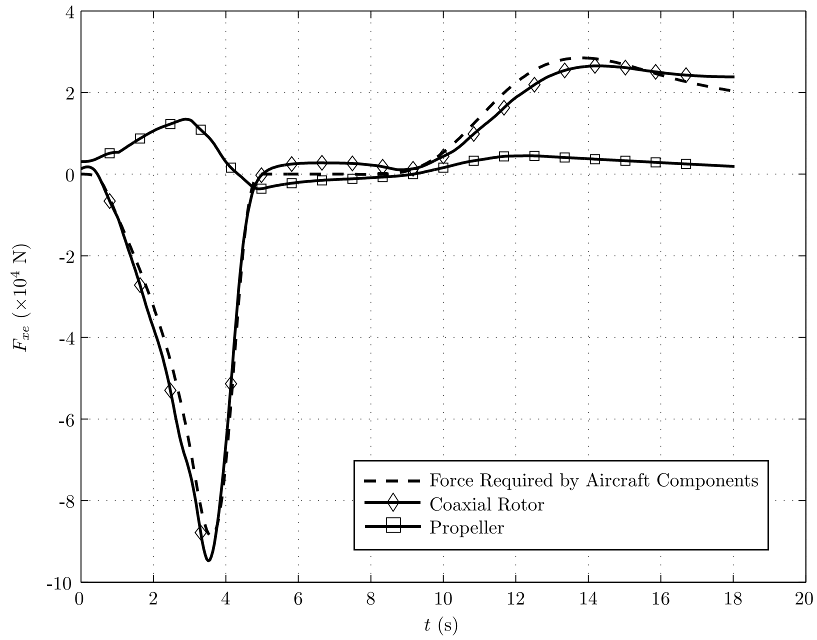

(a) Forces in the x_e axis

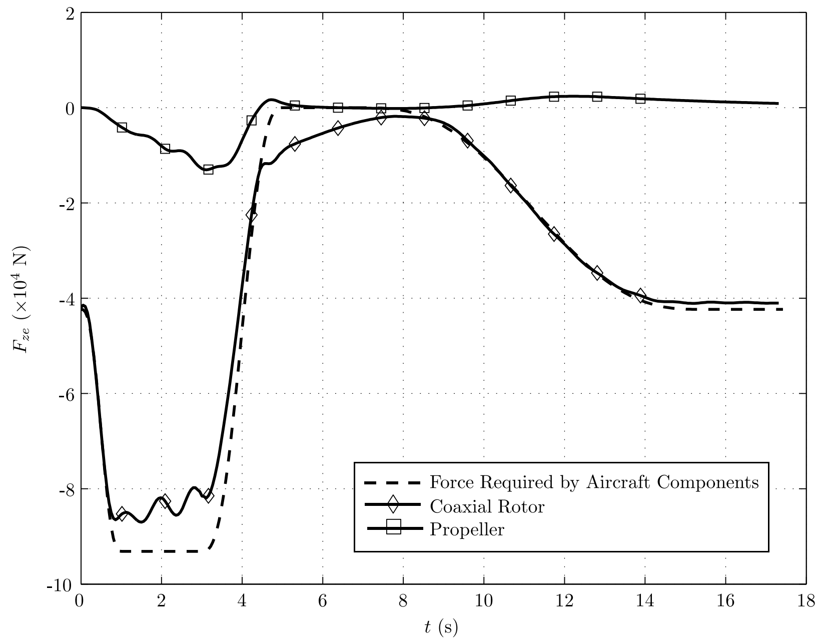

(b) Forces in the z_e axis

Figure 6.21: Coaxial Rotor and Propeller Forces of the CCH Configuration in the x_e and z_e directions of the Earth Axes set during the Pullup-Pushover Manoeuvre.

to the single main rotor. Therefore, using the results from Yeo and Johnson [80] and flight test data from Sikorsky flight tests [135] it is assumed that the maximum blade loading achievable by the coaxial rotor is 0.22. Figure 6.19 presents the variation of blade loading throughout the manoeuvre for both of the CCH and BL configurations. The appearance of C_T/σ throughout the manoeuvres is comparable with the aerodynamic blade loading of the two vehicles increasing sharply within the first second of the manoeuvre. The two aircraft climb to achieve the appropriate load factor, requiring an increase in rotor thrust. After the point where the maximum blade loading values are reached, there is an acute reduction of C_T/σ as the vehicle commences the push over stage of the manoeuvre. The end result is that the simulation estimates that the CCH configuration is capable of achieving a greater load factor than its conventional helicopter counterpart, Figure 6.20(a). It is predicted that the CCH configuration can obtain a load factor of 2.274, compared to 2.149 of the BL configuration. Therefore, the CCH configuration reaches a greater height than the BL configuration, Figure 6.20(b). The maximum height of the CCH configuration is 150m, which is a 20m increase over its comparison vehicle.

The results can be further scrutinised by inspecting the forces that the CCH configuration produces during the manoeuvre, as seen in Figure 6.21. In particular, Figure 6.21(a) presents the forces produced by the vehicle in the x_e direction of the Earth axes set. Recall that the forces of the fuselage, fin, tailplane are not shown for the purposes of clarity. The coaxial rotor is required to provide a large amount of force in the negative direction of the x_e axis, until 5s. The greatest force of approximately -95kN is required at 3s, to pitch the aircraft's nose up to achieve the necessary load factor. As expected, the propeller provides a positive component of force in the first 3s of the manoeuvre. This force is required to overcome the drag of the vehicle's airframe. Concerning the forces in the z_e direction, Figure 6.21(b) presents the appropriate results. In the early stages of the manoeuvre, until 3s, the coaxial rotor provides the majority of the force in the z_e direction. From the initial stages of the manoeuvre the force produced by the propeller increases, reaching its lowest value of -16kN at about 3s, with the propeller contributing to achieve the required vertical acceleration. This shape of the propeller's z_e force in the first 3s of the manoeuvre reinforces the fact that the manoeuvre is flown in a manner which exploits the benefit of thrust compounding. After the aircraft achieves the maximum load factor the vehicle transitions to a push over. Consequently, the vertical force produced by the coaxial rotor is very low between 5 and 7s, so that the aircraft's normal load is appropriately 1. As the end of the manoeuvre the force produced by the coaxial rotor is approximately 40kN, matching the aircraft's weight so that a load factor of unity is achieved.

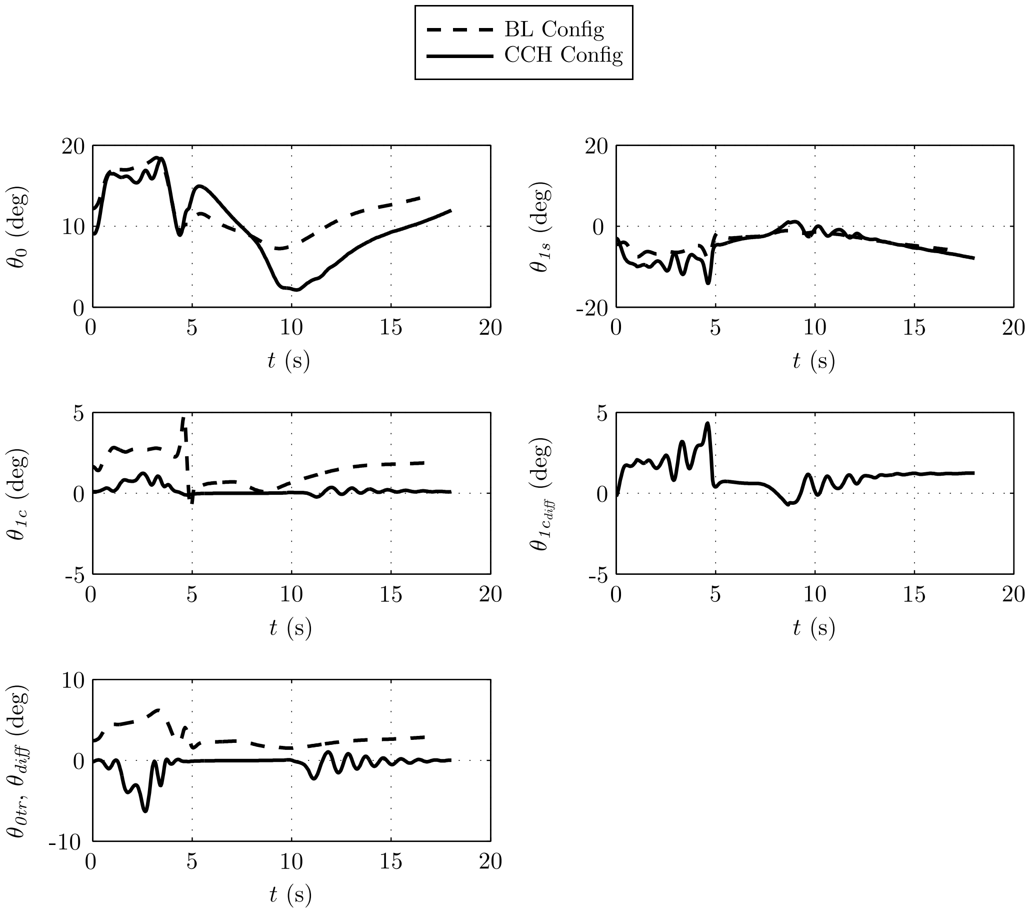

Figure 6.22: Maximum Manoeuvrability Control time histories of the CCH and BL configurations during the Pullup-Pushover manoeuvre.

Figure 6.22 presents the control action of the coaxial rotor when flying the Pullup-Pushover manoeuvre. In the pull up stage of the manoeuvre, the trend of the main rotor collective settings of the BL and CCH configuration is similar. The increase in collective input is required to increase the rotor thrust to attain the necessary load factor. In relation to the longitudinal stick inputs of the two aircraft configurations, the appearance of the two results is comparable throughout the manoeuvre. For the CCH configuration, there is very little lateral cyclic control action required throughout the manoeuvre as the rolling moments from the upper and lower rotors have a natural tendency to cancel each other out. Recall that there are 6 available controls in the CCH configuration, one of which is differential lateral cyclic which controls the distance between the rotor hub and the effective lift vector of each of the rotor discs. In effect, it controls how much of the rotor lift is shifted towards the advancing sides of the rotor discs. The highest differential lateral cyclic values are calculated to occur in the pull up stage of the manoeuvre. In this portion, the manoeuvre is flown in a manner which transfers the lifting capabilities of each rotor disc towards the advancing sides, avoiding the onset of retreating blade stall. In terms of the yaw control of the CCH configuration, there is a large control input of approximately -6° at 3s. At this stage of the manoeuvre the propeller disc is highly loaded with the propeller producing a significant amount of axial force. The consequence of this is that the helicopter has a tendency to yaw, if uncorrected, due to the coupling of the highly loaded propeller blades and the steep climb angle of the vehicle. This effect is best explained by using a single propeller driven fixed wing aircraft, which is in climbing flight, as an example. For this particular configuration, there is a tendency of this aircraft to yaw due to a moment normal to the plane of rotation, which is referred to as the p-factor [61]. As the aircraft climbs, the loading across the propeller blade which tip points along the starboard wing is different to that of the blade which points along the port wing. This difference is due to a high value of heave velocity, W, which alters the magnitude and direction of airflow between the right and left hand sides of the propeller disc. The difference in aerodynamic loading, creates a yawing moment which is not insignificant [61]. The effect occurs in the CCH configuration when the airframe is climbing and the propeller is producing a significant amount of axial thrust. This yawing moment produced by the propeller at 3s is counteracted by the application of θ_{diff} to ensure that the vehicle remains on the required heading.

For the CCH configuration, one of the assumed knowns throughout the manoeuvre is the propeller pitch setting, as seen in Figure 6.23. This propeller control is scheduled in a manner which exploits the benefit of the compounding as discussed previously. The maximum application of propeller pitch occurs at 3s, with the control reaching a maximum value of 72°, thereby promoting a substantial amount of propeller thrust. After 3s the propeller pitch control is scheduled to reduce the amount of propulsive thrust to supplement the aircraft to transition to a push over. In addition, Figure 6.23 shows the pitch attitude variation throughout the Pullup-Pushover manoeuvre. For the two aircraft configurations, this variation across the manoeuvre is similar. In the early stages of the manoeuvre, the nose of the two aircraft pitch up to create the required vertical acceleration, $\ddot{z}$. The peak pitch attitudes for the two configurations is reached at approximately 4s. Thereafter, a combination of the collective and longitudinal stick control inputs pushes the aircraft's nose down to reduce the vehicle's vertical acceleration.

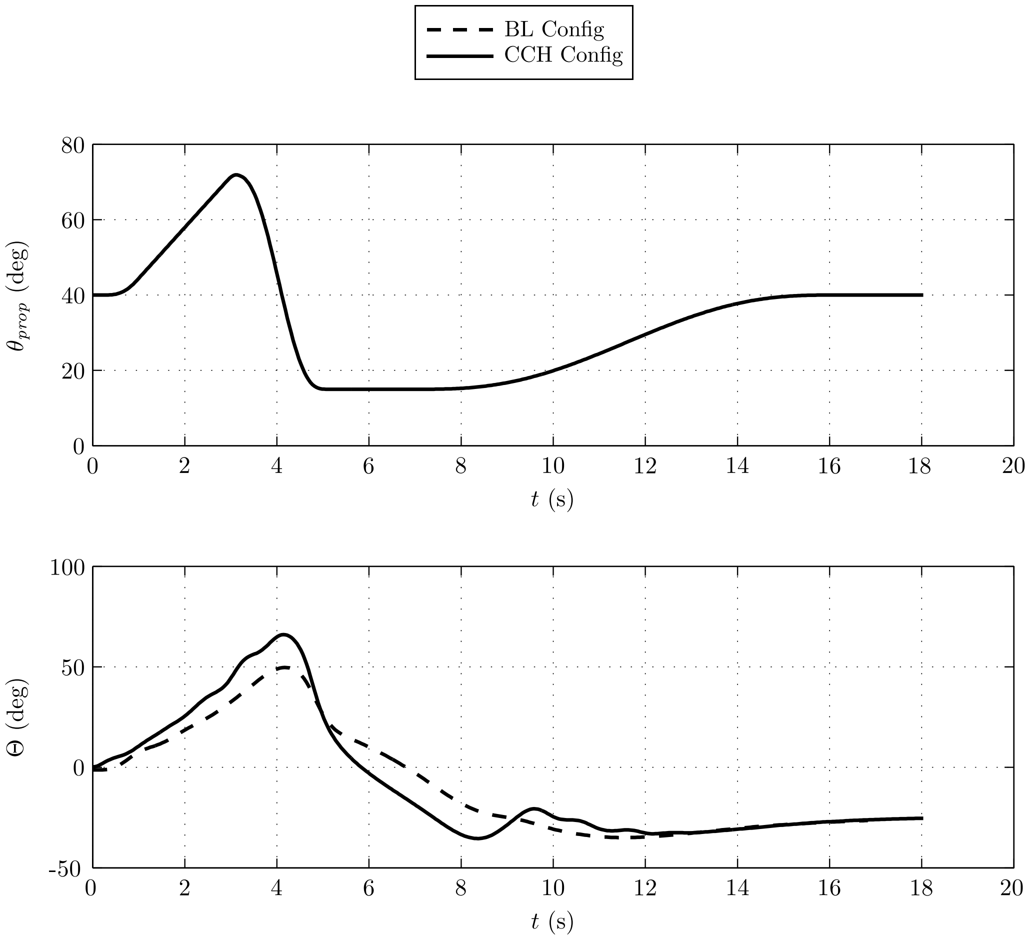

Figure 6.23: Maximum Manoeuvrability Control time histories of the CCH and BL configurations during the Pullup-Pushover manoeuvre.

CCH Configuration Accel-Decel Results

The Manoeuvrability Assessment Method (MAM) is now applied to the CCH configuration to estimate its maximum manoeuvring ability whilst flying the Accel-Decel manoeuvre. Like the HCH configuration, the assumption made here is that the power available for the CCH configuration is greater than its conventional helicopter counterpart. Figure 6.24 presents the power variation of the CCH and BL configurations throughout their maximum Accel-Decel manoeuvres. Both of the configurations reach their limiting states at the point of maximum forward acceleration where the greatest propulsive force is required. For the CCH configuration, there are two major components of power which arise from the coaxial rotor and propeller. The propeller is actively used by the pilot during this manoeuvre to provide the necessary propulsive forces and therefore this aircraft component requires significant engine power. Additionally, the coaxial rotor consumes a significant amount of power as it provides the lifting force and an element of the propulsive force throughout the manoeuvre. Notice that there is a sharp drop in power, for both aircraft configurations, in the second stage of the manoeuvre as the pilot drops the collective lever to decelerate the vehicles.

Figure 6.25 shows the predicted flight path of the BL and CCH configurations during their maximum Accel-Decel manoeuvres. The end result is that the CCH configuration is able to complete the manoeuvre in a distance of 133.7m, compared with the 139.8m of that of the BL configuration. The result here is that the addition of thrust compounding to the CCH configuration is capable of improving the manoeuvrability of the vehicle whilst performing an Accel-Decel manoeuvre, but it is likely that such an aircraft arrangement would require a significant amount of installed engine power. It is possible that, with further optimisation of the design, further manoeuvrability benefits would result.

Figure 6.26 shows the predicted forces produced by the CCH configuration during the Accel-Decel manoeuvre. One of the benefits of thrust compounding is that it can offload the main rotor of its propulsive duties. In the forward acceleration part of the manoeuvre, the CCH configuration's propeller provides 65% of the required propulsive force at the point of maximum acceleration, Figure 6.26(a). At the same point, $\approx$ 2s, the coaxial rotor provides 14kN of force in the x_e direction. Like the HCH configuration, it is assumed that the propeller is capable of providing 25% of the total deceleration

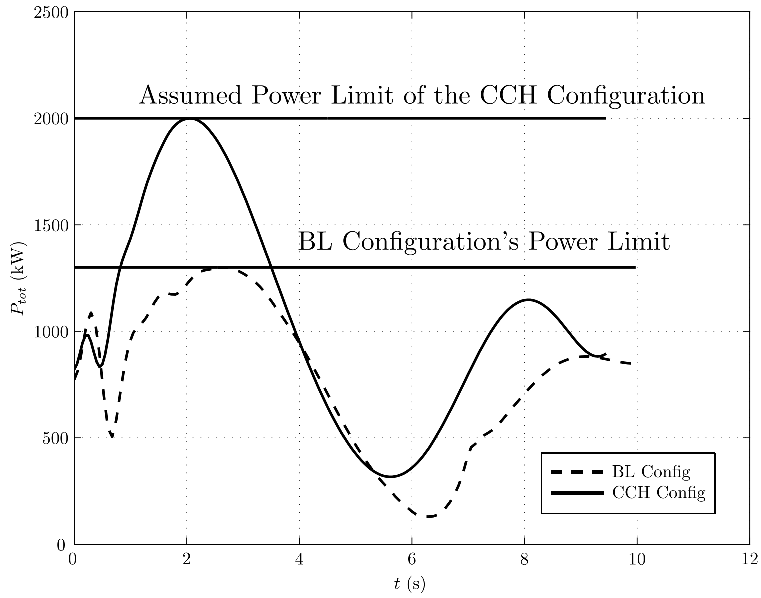

Figure 6.24: Power variation of the two configurations throughout the maximum Accel-Decel manoeuvres.

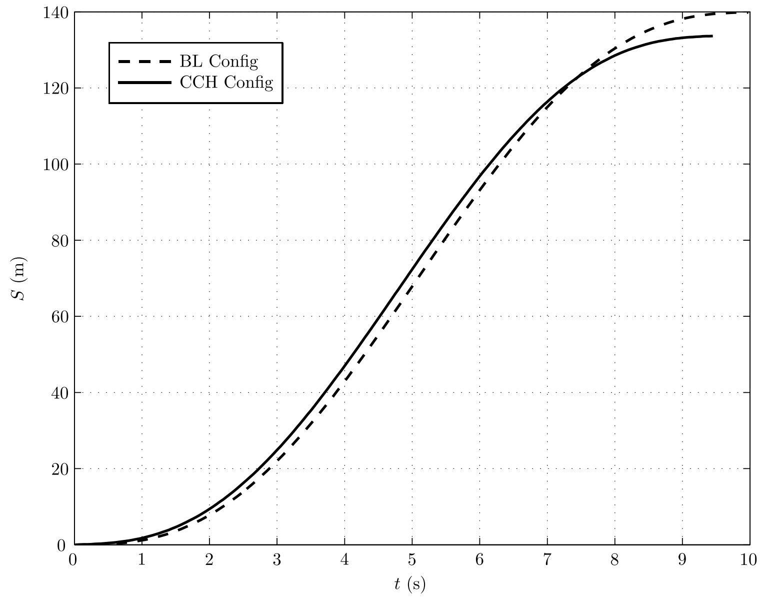

Figure 6.25: Flight path of the BL and CCH Configurations during the Accel-Decel Manoeuvres.

force at the point of maximum deceleration, $\approx$ 7.7s. As a result, the propeller provides 8.7kN of reverse force to decelerate the vehicle. In terms of the forces produced in the z_e axis, Figure 6.26(b), the coaxial rotor provides the majority of lifting force, as expected. Of course, this lifting force is approximately equal to the weight during the manoeuvre. However, the propeller provides a portion of the force in the z_e direction, particularly at the points of maximum acceleration and deceleration. At these distinct points, the propeller produces a significant amount of force normal to the propeller's disc plane. However, due to the fuselage's pitch attitude at these points, a relatively significant amount of force is produced in the z_e direction.

Figure 6.27 shows the CCH configuration's coaxial rotor control action throughout the Accel-Decel manoeuvre. The main rotor collectives of the two vehicles follow a similar trend during the manoeuvre. As expected, the peak main rotor collective of the two aircraft occurs at the point of maximum forward acceleration. As the propeller of the CCH configuration provides 65% of the propulsive force at this point, the coaxial rotor collective input is less than that of the BL configuration. The collective levers of the main rotor controls also drop significantly to orientate the rotor thrust vector backwards to decelerate the respective aircraft configuration back to a stabilised hover. For both configurations there are large longitudinal stick inputs at the beginning of the manoeuvre which are similar in magnitude. The control inputs of the lateral cyclic stick are also comparable during the manoeuvre. Regarding the CCH configuration,

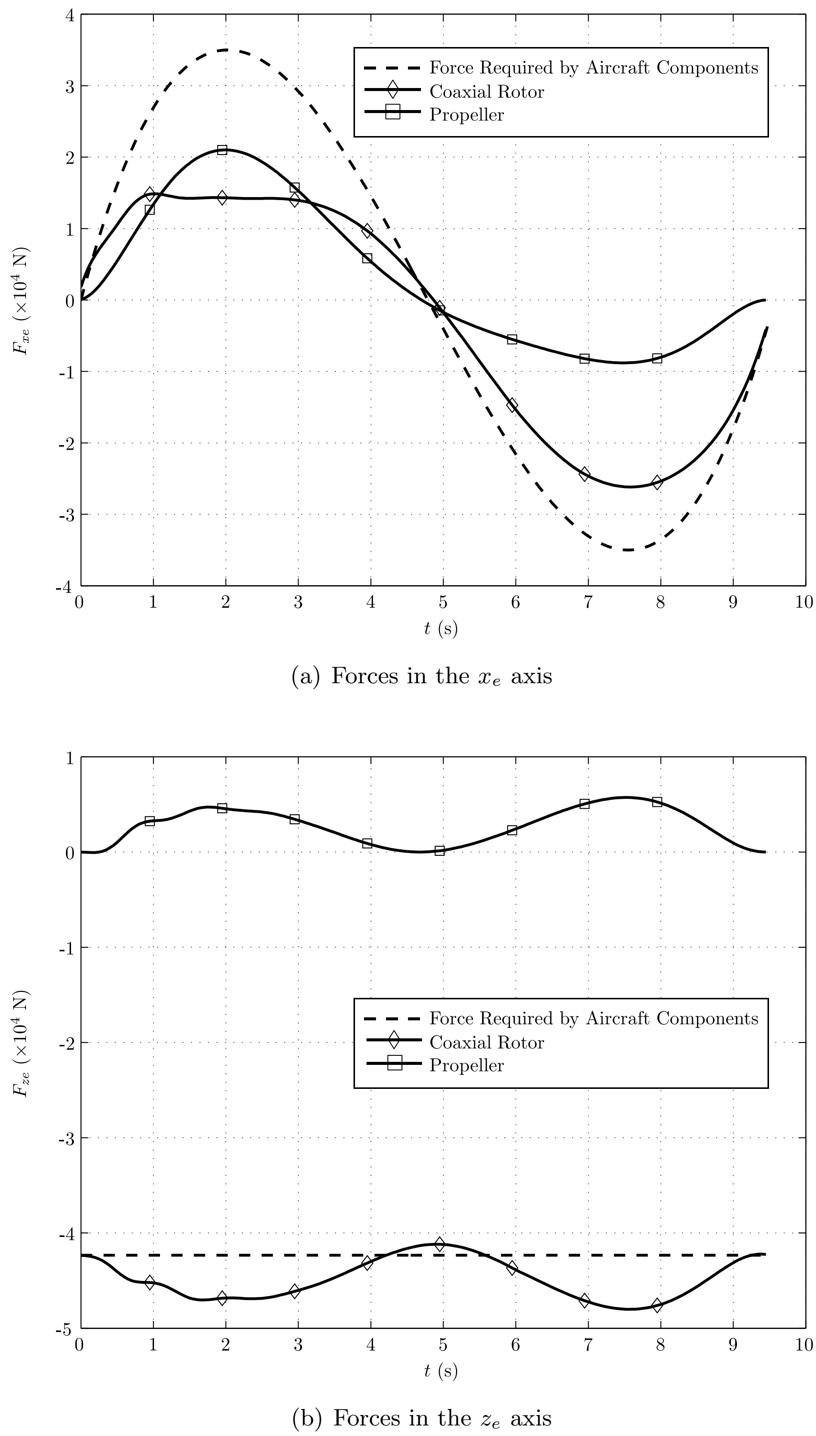

Figure 6.26: Coaxial Rotor and Propeller Forces of the CCH Configuration in the x_e and z_e directions of the Earth Axes set during the Accel-Decel Manoeuvre.

recall that one of the additional constraints for this manoeuvre is the level of lateral lift offset that the coaxial rotor is required to achieve at each time point. The lateral

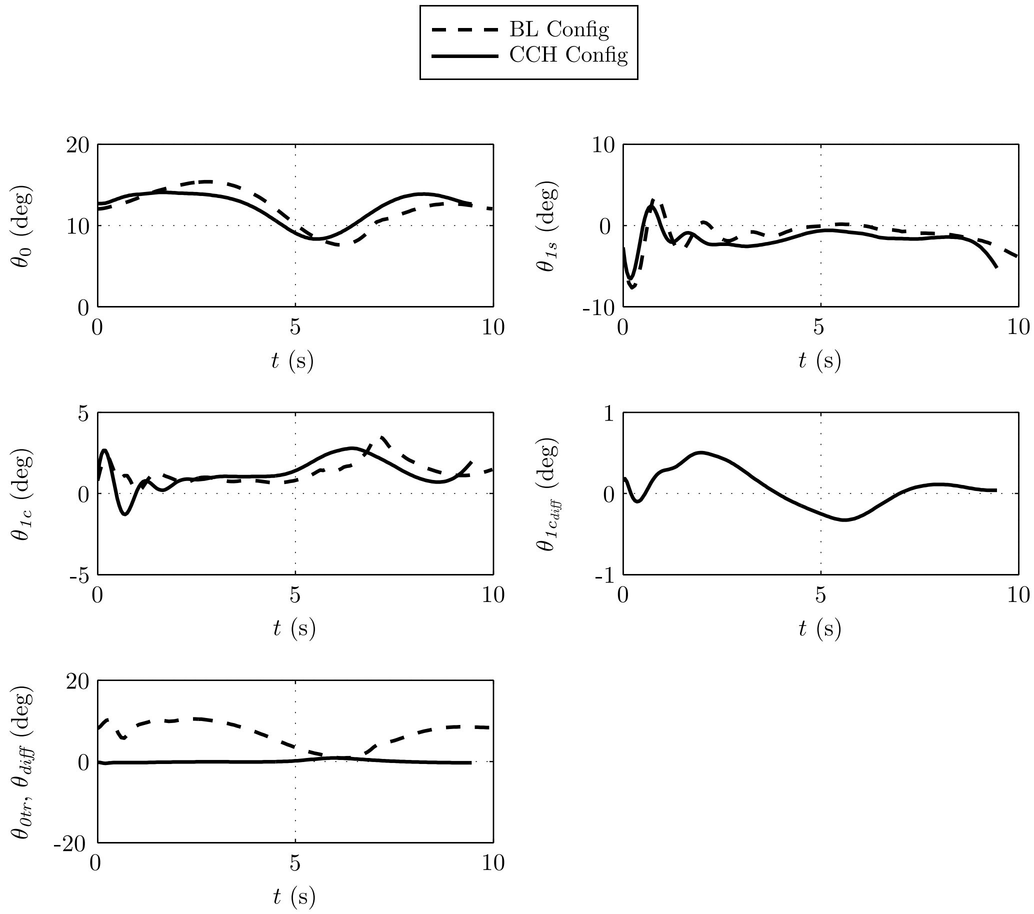

Figure 6.27: Maximum Manoeuvrability Control time histories of the CCH and BL configurations during the Accel-Decel manoeuvre.

lift offset value was selected to increase with airspeed to promote greater aerodynamic loading across the advancing side of the discs during the forward acceleration stage of the manoeuvre. However, excessive amounts of lateral lift offset were not used as blade stalling does not generally limit the vehicle's manoeuvrability in low speed flight. Figure 6.27 presents the differential lateral control to maintain the desired the lateral lift offset value. For this control, only small control inputs are required to achieve the necessary lift offset values. The final control inputs presented in Figure 6.27 are the anti-torque controls. The large differences between these controls is mainly due to the method which provides the anti-torque moment for each configuration. For the BL configuration, the tail-rotor provides the yaw control whereas the CCH configuration features a differential collective control to yaw the helicopter.

Concerning the CCH configuration, the other available control to the pilot is the propeller pitch, θ_{prop}. Effectively, the inverse simulation calculates this control value based on the amount of propulsive force the propeller is required to produce, which is

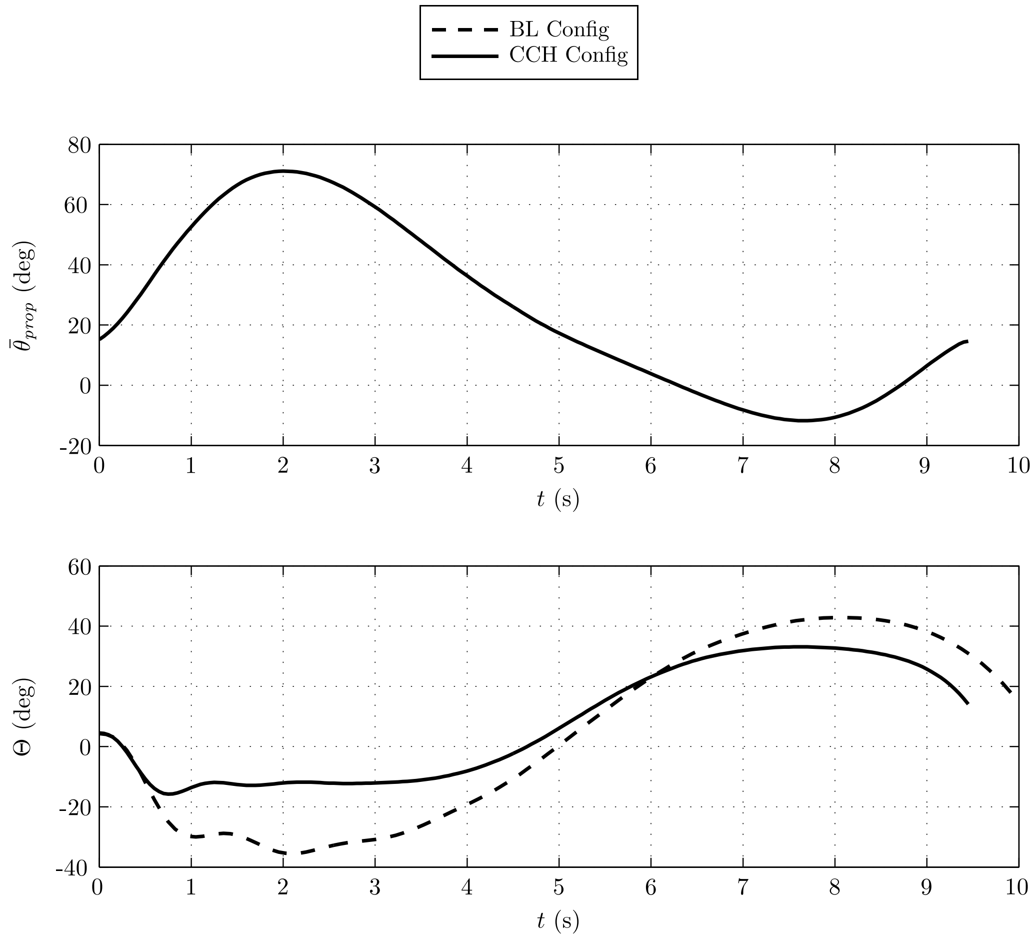

Figure 6.28: Maximum Manoeuvrability Control time histories of the CH and BL configurations during the Accel-Decel manoeuvre.

dictated by Equation (6.31). Figure 6.28 presents the propeller pitch and the resulting pitch attitude of the fuselage through the Accel-Decel manoeuvres. The trend of the propeller pitch setting follows the amount of propulsive force that the propeller is required to produce, which is seen in Figure 6.26(a). The control increases in the initial stages of the manoeuvre, and reaches its maximum value of 63° at 2.015s. Thereafter, the propeller pitch setting reduces after the point of maximum forward acceleration, reaching its lowest value of -12° where the propeller is required to provide 8.7kN of reverse thrust to slow the aircraft's speed. One of the positive consequences of the thrust compounding is shown in Figure 6.28. An undesirable quality of the conventional helicopter is the significant pitch excursions required to accelerate the aircraft. The addition of the propeller to the design attenuates this issue, as seen in Figure 6.28. For example, the lowest pitch of the BL configuration is -37° compared with -17° of the CCH configuration. Note, that throughout the deceleration stage of the manoeuvre the CCH configuration's nose pitches upwards, in a similar fashion to that of the BL configuration, as it is assumed that propeller is only capable of providing 25% of the decelerating force. Although not shown here, it is possible for the CCH configuration to accelerate forward without the aircraft's pitch attitude changing. However, this can only be achieved if the acceleration distance is relatively large, otherwise the coaxial rotor and propeller require an excessive amount of power.

6.6 Chapter Summary

This Chapter has investigated the effects of compounding on the manoeuvrability of two compound helicopter configurations. The Chapter began by introducing the inverse simulation algorithm. Subsequently, additional manoeuvre constraints were developed so that the inverse simulation algorithm could calculate the control action required by the pilot. Although the primary aim of this Chapter was to examine the influence of compounding to the manoeuvrability of the helicopter it has also highlighted some of the potential control strategies that pilots may use to fly a compound helicopter. The conclusions of this Chapter are best summarised by focussing on each compound helicopter separately.

Focusing on the HCH configuration, it is predicted that this vehicle is capable of reaching greater load factors than the conventional helicopter. The wing is beneficial in attaining normal load factors, however its contribution is limited by the small wing area and the relatively low airspeeds in which the manoeuvre is flown. When flying the Accel-Decel manoeuvre, it was shown that the HCH configuration was capable of completing the manoeuvre in a quicker time than the conventional helicopter. However, this came at the expense of greater installed engine power. The active use of the propellers in the acceleration and decelerations stages of the manoeuvre reduce the fuselage's pitch attitude which is a clear advantage of thrust compounding.

The results from this Chapter also highlighted some positive aspects of the CCH configuration. Firstly, the CCH configuration was predicted to able to reach a load factor of 2.273 due to the combination of the coaxial rotor and the propeller. The coaxial rotor is able to avoid blade stalling until greater blade loading values which allows the vehicle to attain larger load factors than a single main rotor machine. In addition, the propeller has a beneficial contribution flying the Pullup-Pushover manoeuvre. It is therefore concluded that a vehicle which is similar to the CCH configuration would be able to attain greater normal load factors than a conventional helicopter of similar size and mass. The downside of achieving this is the introduction of additional complexity into the helicopter design. With the Accel-Decel manoeuvre, the CCH configuration is able to complete the manoeuvre in a quicker time than the BL configuration. The introduction of thrust compounding was beneficial in this manoeuvre with the propeller providing a significant amount of propulsive force which reduces fuselage pitching.

As a whole, the conclusion from this Chapter is that the addition of thrust and lift compounding do have the potential to make the rotorcraft more manoeuvrable, when compared with a conventional helicopter. However, it should be stressed that to achieve these manoeuvrability benefits requires careful design of the vehicle. For example, the wing was shown to be beneficial in the Pullup-Pushover manoeuvre, but its positive influence could be negated by the increase of helicopter weight required to add a wing to the helicopter design. Undoubtedly, reducing the weight of the compound helicopter will be a key design goal. Another design issue is the importance of installing greater power to fully exploit the benefits of the axial force that a propeller provides. In addition it can be concluded, with some confidence, that thrust compounding does offer a manoeuvrability benefit in terms of reducing fuselage pitching when the vehicle is required to accelerate.

Chapter 7

Handling Qualities of Compound Helicopter Configurations

7.1 Introduction

The preceding Chapters have identified some of the fundamental flight mechanics characteristics of compound helicopter configurations. More specifically, the effects of compounding on the trim, performance, stability and manoeuvrability of two compound helicopter configurations have been examined. Another critical component of the compound helicopter configuration, which has not been addressed yet, is its handling qualities. The addition of compounding to the aircraft design introduces control redundancy and changes the response characteristics of the vehicle. It also expands the flight envelope of the aircraft, enabling it to operate in new flight regimes. All three of these elements are important and will strongly influence the handling qualities of this aircraft class. To address the issue of handling qualities, this Chapter departs from the theme of using the HCH and CCH configurations to investigate the merits of the compound configurations. Instead, this Chapter takes a broader view at handling qualities and the issues that need to be addressed to quantify the handling qualities of a compound helicopter configuration. To this end, the main aim of this Chapter is to examine the existing conventional helicopter handling qualities specification and determine whether it is applicable to compound helicopters. In the areas where the current handling qualities standards are deemed to be deficient, then some suggestions will be offered to account for these inadequacies. It is important to stress that the aim of this Chapter is not to develop new handling qualities criteria. Such an activity is beyond the scope of the work and would, in all probability, take several years due to the volume of studies which would be required. Extensive flight tests would be essential. With the aim of the current work stated, the Chapter begins by highlighting the importance of handling qualities in modern helicopters. This is followed by a brief history of how the existing handling qualities criteria were formed. This set of criteria are then examined to determine if they are suitable to assess the handling qualities of high-speed compound helicopter configurations. Where the existing handling qualities design criteria are determined to be insufficient, incomplete or inappropriate, then some suggestions are offered. The Chapter ends by listing the main conclusions from the work.

7.2 Handling Qualities

The conventional helicopter has to fulfil various roles, both in civil and military environments, such as search and rescue, ship replenishment and scouting missions. The ability of the helicopter to complete these missions, often referred to as mission effectiveness, depends on the handling qualities of the vehicle. The handling qualities of a rotorcraft depend on various factors such as the vehicle's response, operational environment, the SCAS (Stability and Control Augmentation System) and the mission task [139]. In a scenario where the pilot is attempting to complete a mission, particularly a mission that involves NoE manoeuvres, pilot workload is generally high due to the volume of tasks the pilot must perform. These primary tasks, which of course affect pilot workload, can be categorised into navigation, guidance and stabilisation tasks [140]. In addition, there are other potential duties that the pilot may also have to perform which include: weapon deployment, instrument monitoring and communication tasks. All of these demands increase pilot workload and as a consequence it is widely recognised that rotorcraft require excellent handling qualities to ensure that pilots can routinely complete missions effectively and safely.

Before continuing further, it is necessary to highlight that there is no universal agreement on the definition of the term "handling qualities". The original definition of handling qualities was coined by Cooper and Harper [141] and is

> *"Those qualities or characteristics of an aircraft that govern the ease and precision with which a pilot is able to perform the tasks required in support of an aircraft role."*

This definition is still considered valid, however Padfield proposes that handling qualities consist of two components - internal and external influences [36]. The internal components consist of the vehicle's response to control inputs and cockpit elements such as pilot displays. The external component includes elements such as weather conditions, the visual environment and the mission task. Consequently, Padfield uses the terms flying and handling qualities interchangeably, arguing that there is no need to decouple flying from handling qualities [36]. In contrast, Key proposed a slightly different definition of the terms flying and handling qualities [142]. Key's definition states that the aircraft's stability and control characteristics can be described under the bracket flying qualities whereas handling qualities refers to the mission task element and the external environment. Although the definition of handling qualities is not critical to this Chapter, the author has chosen to adopt Padfield's opinion of the term. The motivation behind this choice is so that the term handling qualities describes a broad range of helicopter attributes.

It is clear that the helicopter, regardless if it used for civil or military purposes, requires excellent handling qualities so that it can operate safely in all flight regimes where it is expected to function. To design a helicopter that satisfies the demand for high safety standards requires an assessment method to quantify the handling qualities of the vehicle. The most popular handling qualities scale is the Cooper-Harper scale [141], as shown in Figure 7.1. The Cooper-Harper scale is used to derive a Handling Qualities Rating (HQR) based on the opinion of the pilot flying the manoeuvre. The pilot is asked to navigate the decision tree, Figure 7.1, and assign a HQR based on their judgement of the task performance and the level of pilot workload [36]. Within this scale, the quality rating spans three levels with Level 1 corresponding to an acceptable rating for normal operation throughout the OFE (Operational Flight Envelope). If this is the pilot's conclusion, then a HQR between 1-3 is assigned. If the HQR rating is between 4-6, and therefore within the Level 2 category, then there are objectionable deficiencies with the handling qualities of the aircraft which are only acceptable in emergency situations. When the handling qualities of the aircraft are considered unacceptable, then the rating between 7-8 is assigned, which falls into the Level 3 class. The scale also includes a HQR between 9-10 when the pilot is unable to complete the manoeuvre. The Cooper-Harper ratings are by their nature subjective and therefore care must be taken when conducting a handling qualities assessment using this approach. To attenuate the subjective element of this approach it is recommended that multiple pilots (perhaps 5 or 6) should participate in the experiment to ensure that there is no significant scatter between the sets of results [36].

Although the Cooper-Harper rating has proven to be a valuable assessment method, the HQRs are inherently subjective and therefore must be supplemented with additional

Figure 7.1: Cooper-Harper Handling Qualities Rating Scale. (Figure has been removed due to Copyright restrictions.)

quantifiable metrics. The main issue with the scale is that if the aircraft is found to be difficult to handle during a task then there is little information to isolate the problems which are responsible for the poor HQRs. This problem can be remedied by acquiring the pilot's comments about the task and asking the pilot to complete a questionnaire that describes the flight test [143]. However, quantifiable metrics allows the fundamental handling qualities issues to be identified, aiding the design process. An additional advantage of objective criteria is that they form design targets for the handling qualities engineer to satisfy. Objective criteria, which can be readily calculated, also allow the aircraft designer to demonstrate that the vehicle complies with the handling qualities regulations [36]. For these reasons, it is recognised that the subjective assessment of a pilot needs to be supported by measurable and quantitative criteria [36]. Clearly, a successful handling qualities specification needs to amalgamate the benefits of subjective pilot opinions with objective design criteria.

7.3 Progress in Rotorcraft Handling Qualities

The first specification of Rotorcraft Handling Qualities was the MIL-H-8501 document [144] which was published in 1952 [145]. This specification focused on timedomain parameters such as the response of the rotorcraft due to a step input and the control power requirements were based on the vehicle's weight. This specification was revised in 1961 (MIL-H-8501A) and was continually used until its cancellation in 1995. The handling qualities of the UH-60 and the AH-64 were developed using the requirements from MIL-H-8501A. Despite its successes, the shortcomings of the MIL-H-8501A requirements were ever present and widely known [145]. For example, Ashkenas and Walton identified some of the inconsistencies of the specification by the late 1960s [146]. One of the main drawbacks was the lack of clarity in the requirements, with the specification continually using subjective terminology such as "excessive" and "objectionable". The respective meanings of these terms were inherently ambiguous and open to interpretation. The requirements also did not take into account cross-couplings, which are ever present in the helicopter, which was another shortcoming of MIL-H-8501A. There were other issues regarding the specification, such as the lack of basic structure [145].

The shortcomings of the MIL-H-8501A requirements were evident, and it was clear that a new specification was required. To support the development of a new performance standard it was recognised that a substantial handling qualities database was required. Flight simulators played a key role in developing a significant database which allowed for the creation of substantial quantitative criteria [139]. The US Army also issued multiple contracts to various agencies with the broad aims to develop a new specification format, to incorporate the existing criteria into this framework and to identify any gaps in the current standards [139]. It was clear that by the early 1980s, a significant effort had commenced to create a specification to replace MIL-H-8501A. Initially this new standard was to be named MILH-8501B, with the idea that the specification would be an upgrade from the existing MIL-H-8501A standard [139]. After the progress review of MILH-8501B, the US Army announced its intention to develop a performance standard to supplement the development of a light helicopter, the RAH-66 Comanche [139, 145]. By 1988, the subsequent result was the development of the first generic rotorcraft performance standard named the Aeronautical Design Standards (ADS-33B). Improvements have been made to this standard since it was formed and have continued with the current updated version of these requirements (ADS-33E-PRF) published in 2000 [130]. This performance standard is still currently in use in the United States. Since the publication of the various versions of the ADS-33 specifications, greater attention has been shown to handling qualities in the design stages of the helicopter [36].

7.4 Aeronautical Design Standard (ADS)

The mission-orientated framework of the ADS-33 specification provides a comprehensive set of handling qualities criteria for military rotorcraft in the United States [147]. This specification is the most popular within the rotorcraft community as it has proven to be effective in improving the handling qualities of various rotorcraft [139]. For example, the benefits of the ADS-33 performance specification have been observed in conventional helicopters, such as the MH-47G [148], as well as the German Army's CH-53G cargo helicopter [149]. One of the most distinguishing features of the ADS-33 requirements is that it does not separate helicopters based on their weight or size. The only distinction made between helicopter types is based on the primary role that the vehicle is expected to fulfil. In the most updated version of the standard, ADS-33E-PRF, there are four categories of helicopter type: attack, scout, utility and cargo helicopters. The type of rotorcraft determines the manoeuvres that the vehicle is expected to complete, at a certain level of agility, to comply with the regulations. As a whole the ADS-33 specification is significantly different from that of its predecessor, the MIL-H-8501A specification [144], with various key and innovative features [36]. These key features include: the mission-task-element, the usable cue environment and the response type. The following sections presents some of the important elements of the ADS-33 performance standard.

Frequency-Amplitude Manoeuvre Chart

The fundamental premise of the ADS-33 specification is that the handling qualities of the rotorcraft can be obtained by focusing on the mission the vehicle is required to complete. Unlike MIL-H-8501A, the ADS-33 requirements separate handling qualities criteria depending on the manoeuvre of interest. Typically, speeds under 45kt are defined as low speed manoeuvres whereas speeds greater than this are classed as forward flight manoeuvres. Additionally, the dynamic response criteria within the specification is separated by the aircraft dynamic response in terms of the frequency and amplitude parameters, Figure 7.2. There are four important regions within the frequency-amplitude chart, shown in Figure 7.2. These regions can be conveniently split into stability and agility criteria. The stability criteria are isolated to low amplitude manoeuvres, where low frequencies are characterised by the open loop response of the aircraft, whereas high frequencies correspond to flight conditions where the pilot can close the loop [150]. The former can be quantified by the frequency and damping of the aircraft's motion whereas the latter is measured by response bandwidth.

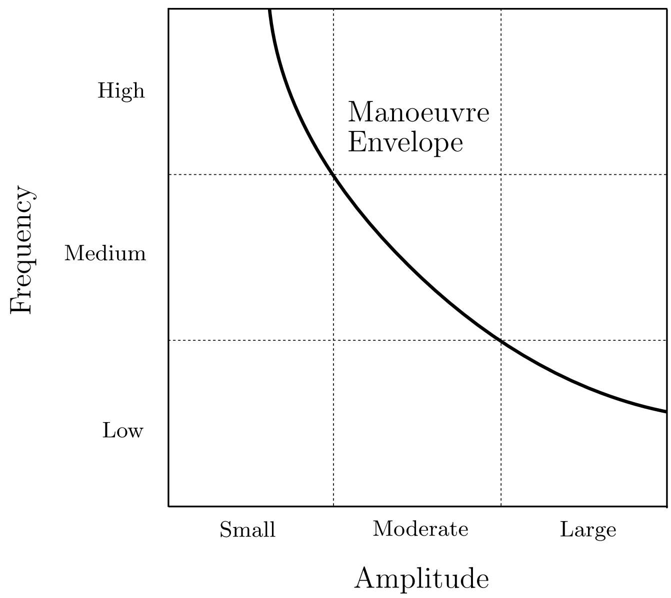

Figure 7.2: Frequency-Amplitude Manoeuvre Chart

The agility of the helicopter is characterised by moderate to large amplitude manoeuvres. Large amplitude manoeuvres can be quantified by the control power, with the yaw control power an example within the ADS-33 performance standard [130]. In contrast, moderate amplitude manoeuvres can be measured using the "quickness" criterion. The term moderate normally conforms to attitude changes between 10 and 60°. Essentially, the quickness parameter is a measure of how quickly an attitude change can be achieved [150]. This parameter is the ratio of the peak attitude rate achieved and the change of the attitude. It is generally desirable for the helicopter to exhibit high values of quickness so that the vehicle can manoeuvre quickly with poise [139]. Note that this quickness parameter is discussed in more detail in subsequent sections.

Response Types

One of the important features of the ADS-33 specification is the response type of the aircraft, at a given flight condition. The response type defines the character of the vehicle's response following a step control input [36]. Figure 7.3 shows the four different response types: Rate Command (RC), Attitude Command (AC), Translational Rate Command (TRC) and Acceleration Command (AC). The relationship between the time and the attitude of RC response is of linear form. In terms of Attitude Command (AC) and Translational Rate Command (TRC), the attitude loop is automatically closed [36] which is advantageous in certain flight conditions. For example, consider a pilot performing a low speed manoeuvre or a precision hover in a degraded visual

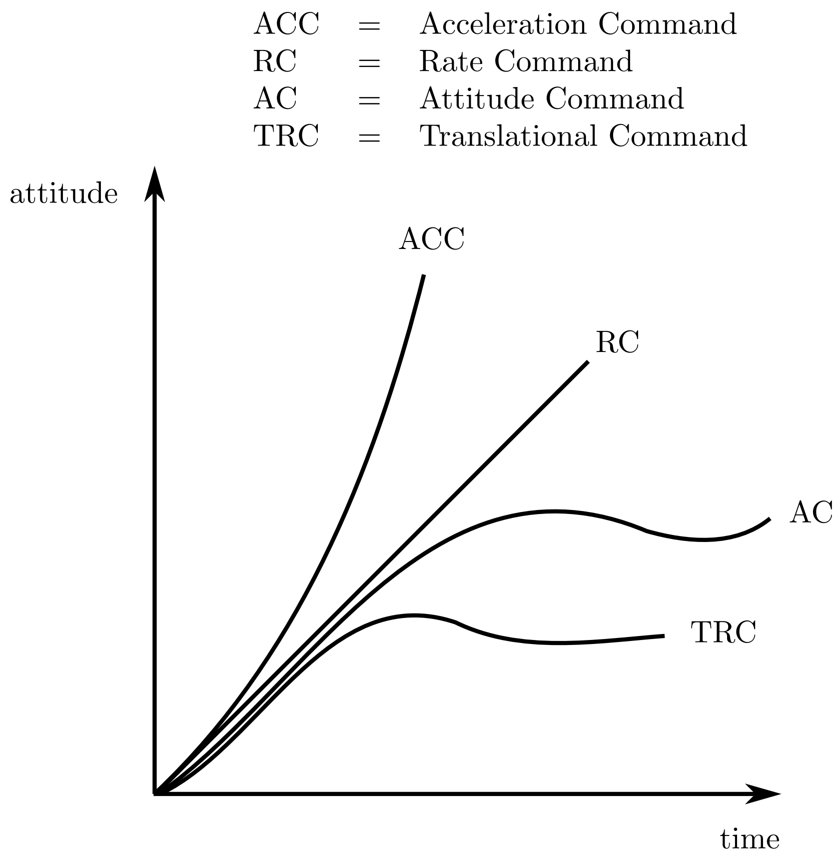

Figure 7.3: Response Type

environment. For this type of flight condition and task the pilot's workload is generally high due to the lack of visual cues [151]. Hence, in this flight environment it is beneficial for the aircraft to exhibit a TRC response to relieve the pilot of the stabilisation task, so that the pilot can focus on guiding the vehicle safely. In contrast, for good visual environments it is favourable for the aircraft to exhibit a RC response type so that the vehicle can be manoeuvred quickly and effectively. Recognising that the required response type is dependent on the given flight condition, the ADS-33 explicitly specifies the response types that are required based on the applicable MTE and Usable Cue Environment (UCE).

Mission-Task-Elements

One of the most critical aspects of the ADS-33 specification is the definition of the MTE. In its current form, there is a library of suggested MTEs within the ADS-33E-PRF performance specification. These are all well established manoeuvres which have been refined due to the results from various studies [152–154]. These manoeuvres are shown in Table 7.1 with the symbol ✓ indicating that the specification requirement

MTE	Required Agility	Rotorcraft Category				Externally Slung Load
		Attack	Scout	Utility	Cargo	
Tasks in GVE						
Hover	L	✓	✓	✓	✓	✓
Landing	L	✓	✓	✓	✓	
Slope Landing	L	✓	✓	✓	✓	
Hovering Turn	M	✓	✓	✓	✓	
Pirouette	M	✓	✓	✓	✓	
Vertical Manoeuvre	M	✓	✓	✓	✓	✓
Depart/Abort	M			✓	✓	✓
Lateral Reposition	M			✓	✓	✓
Slalom	M	✓	✓	✓	✓	✓
Vertical Remask	A	✓	✓			
Accel/Decel	A	✓	✓			
Sidestep	A	✓	✓			
Decel to Dash	A	✓	✓	✓		
Transient Turn	A	✓	✓	✓		
Pullup/Pushover	A	✓	✓	✓		
Roll Reversal	A	✓	✓	✓		
Turn to Target	T	✓	✓			
High Yo-yo	T	✓	✓			
Low Yo-yo	T	✓	✓			
Tasks in DVE						
Hover	L	✓	✓	✓	✓	✓
Landing	L	✓	✓	✓	✓	
Hovering Turn	L	✓	✓	✓	✓	✓
Pirouette	L	✓	✓	✓	✓	✓
Vertical Manoeuvre	L	✓	✓	✓	✓	✓
Depart/Abort	L			✓	✓	✓
Lateral Reposition	L			✓	✓	✓
Slalom	L	✓	✓	✓		
Accel/Decel	L	✓	✓			
Sidestep	L	✓	✓			
Tasks in IMC						
Decel Approach	L	✓	✓	✓	✓	✓
ILS Approach	L	✓	✓	✓	✓	✓
Missed Approach	L	✓	✓	✓	✓	
Speed Control	L	✓	✓	✓	✓	

Table 7.1: Mission-Task-Elements (MTEs) from ADS-33 [130]

is applicable. The required agility during a particular MTE depends on the aircraft configuration and the visual environment. Recall that there are four rotorcraft configurations considered in the specification which include: attack, scout, utility and cargo helicopters. Also the specification suggests MTEs for helicopters with externally slung loads. The type of visual environment is split into three categories. The first two categorises represent a good visual environment (GVE) and a degraded visual environment (DVE). In addition, the specification includes standards for instrument meteorological conditions (IMC) where the rotorcraft is controlled without the aid of visual cues and with reference only to the onboard aircraft instruments [130]. The required level of agility is denoted by L, M, A or T, which correspond to limited, moderate, aggressive agility and target acquisition respectively. Each of these MTEs, Table 7.1, is supplemented with a set of guidelines defining how the mission task should be set-up.

7.5 Structure of ADS-33

Clearly the ADS-33 performance standard encompasses many innovative features over its predecessor, the MIL-H-8501A specification. One of the critical components of ADS-33 is that it has a well defined structure. Figure 7.4 presents the structure of the ADS-33 specification and how the various innovative features of ADS-33 combine to attempt to deliver a helicopter with high mission effectiveness and low pilot workload. The starting point of the specification is to define the operational missions by analysing what what the rotorcraft is expected to do. Subsequently, mission-task-elements can then be selected which are based on the perceived operational requirements of the vehicle. The tailoring section of the specifications also requires a selection of the desired agility and the operational environment of the rotorcraft.

The UCE is a key element in the ADS-33 specification. The UCE defines the required response type of the vehicle, as seen in Figure 7.4. As mentioned previously, some flight conditions require greater stabilisation than others. Fundamentally, the UCE defines what response type, and therefore level of stabilisation, is required [145]. Figure 7.4 shows that the required agility, which depends on the relevant MTE, is an input into the quantitative criteria of the specification. The end result is that a combination of the required agility, based on the MTE, and the response type define the applicable quantitative criteria. The quantitative criteria may be in the form of the attitude quickness parameter, bandwidth or phase delay depending on various factors including the UCE and MTE.

The next step, within the framework of the handling qualities process, is to define the OFE and Service Flight Envelope (SFE) of the rotorcraft. Thereafter, the aim is to obtain data to determine which boundary the aircraft falls within to predict the levels of handling qualities [155]. In addition, the structure of ADS-33, Figure 7.4,

Figure 7.4: Handling Qualities Process using ADS-33. (Figure has been removed due to Copyright restrictions.)

allows for qualitative evaluations based on the HQRs assigned by the test pilots when attempting to fly a MTE. The most preferred method to achieve this, but most costly, is flight testing. Flight simulation is another method which plays an important role within the structure of ADS-33. The flight simulator allows mission-task-elements to be flown, at a relatively low cost, by test pilots to gauge the handling qualities of the vehicle. Simulators can provide meaningful handling qualities assessments if the flight model is of high fidelity and the visual and motion environment is modelled accurately. Another benefit of simulation is that it can be useful in assessing changes to the vehicle, particularly the control system functionality. These qualitative evaluations form the "assigned levels of handling qualities" part of the process. Is also important to highlight that the handling qualities process, Figure 7.4, also allows the designer to alter the characteristics of the helicopter. This can be done by changing the vehicle's bare airframe or control system to comply with the performance standards.

7.6 Flight Control System of the Compound Helicopter

For the conventional helicopter, the flight control system plays a critical role in determining the vehicle's handling qualities [147]. Typically, the bare-airframe handling qualities of a helicopter fall into the Level 3 category [36]. The strong cross-couplings, which are ever present in the helicopter, make the piloting task of the bare-airframe challenging [36]. However, the presence of a properly designed flight control system relieves pilot workload and allows the helicopter to achieve Level 1 handling qualities, in certain flight conditions. In terms of the compound helicopter, the design of the flight control system, to ensure that the vehicle's handling qualities are satisfactory across the OFE, may prove difficult. One challenge is that it is likely that compound helicopters will exhibit unfamiliar control and response characteristics, particularly in high speed flight. Consider a winged helicopter which also features thrust compounding. In high speed flight, the main rotor is slowed to avoid adverse compressibility effects whereas the wing and propeller(s) combine to offload the main rotor of its lifting and propulsive duties. In this flight regime, the contribution of the wing and propeller(s) may be significant, so that the response of the aircraft may be distinctly different from that expected of a conventional helicopter. Although Chapter 5 predicted the stability of the HCH and CCH configurations, future research is required to quantify the response characteristics of these types of vehicles at greater flight speeds. This work is required because the results will form the basis of the SCAS design. Secondly, the bare-airframe response characteristics need to be known so that the vehicle can be controlled in the event of a flight control system failure [36].

There are other issues which the flight control system must overcome. The compound helicopter requires additional propulsive and/or lifting devices to expand the OFE of the vehicle. As a result, the compound helicopter designs will feature some level of control redundancy. This may be viewed as a beneficial aspect of the compound, as the additional control(s) can be used to improve the aircraft's performance. For example, a winged helicopter could feature flaps which could be deployed to improve deceleration performance. However, the flight control system and the pilot interface will have to be designed to ensure that the additional control(s) available to the pilot do not adversely increase pilot workload. A successful compound helicopter must require low levels of pilot workload in good visual environments so that the vehicle can complete missions effectively and safely. The flight control system must achieve this goal whilst ensuring that the aircraft exploits the potential advantages offered by compounding to improve performance.

Continuing with the theme of the compound helicopter's flight control system, it is possible that such a vehicle will feature multiple sets of flight controls, particularly with a winged compound helicopter. In hover and low speed flight, the aircraft will operate in helicopter-like mode with standard swashplate controls. However, as the compound helicopter transitions into high speed forward flight the main rotor is slowed and the aircraft controls could be transferred to other components of the aircraft such as the wing, fin and tailplane. In effect, the controls in this flight regime would be analogous to that of a fixed wing aircraft with elevator, aileron and rudder controls. A similar situation occurs in the tilt-rotor aircraft [1]. Clearly, the flight control system will need to harmonise these two set of controls, particularly when the aircraft transitions from helicopter controls to another set of controls.

7.7 Applicability of ADS-33 to Compound Helicopters

The success of ADS-33 is widely recognised, with the benefits of the specification observed in various rotorcraft designs including the RAH-66, MH-47G and the CH-53K [148, 156, 157]. Due to the accomplishments of the specification, it is reasonable to expect that the handling qualities guidelines for the compound helicopter will be based upon the mission-orientated framework of ADS-33. However, the development of the ADS-33 framework was focused on the conventional helicopter and it is evident that there are some areas, within the specification, that do not address the handling qualities of high-speed rotorcaft. This view is supported by a European based programme, named the Rotorcraft Handling Interactions and Load Prediction (RHILP), which has identified that there is no generic handling qualities specification which is appropriate to the tilt-rotor aircraft [158, 159]. Consequently, one of the primary aims of the RHILP project was to develop a set of handling qualities criteria suitable for the tilt-rotor aircraft. The project used the mission orientated framework approach, like that of ADS-33, to develop handling quality standards for the aircraft configuration [158]. Some progress has been made to extend the ADS-33 specification to include handling qualities criteria for this particular aircraft class [158, 159]. However, it is important to highlight that although initial studies have begun, no comprehensive handling criteria have been formed to date. The compound helicopter is similar to the tilt-rotor in the sense that one of the primary advantages of the vehicle is the expansion of the flight envelope, relative to the conventional helicopter. It is therefore evident that similar handling qualities studies, relating to the compound helicopter, are required. Generally speaking, the development of handling qualities criteria is a lengthy and iterative process [158], requiring research in terms of rotorcraft modelling, flight tests and flight simulations. For example, it took a period of 15 years to upgrade the original ADS-33 to the newer version ADS-33E. Similar time-scales can be expected as the rotorcraft research community attempts to develop handling qualities criteria relating to compound helicopters.

A successful compound helicopter will have to exhibit satisfactory handling qualities across its OFE. However, developing handling qualities criteria for compound helicopters will pose a challenging task due to a variety of issues. Upon examining the current ADS-33 performance standard, ADS-33E-PRF, there are two notable gaps in the requirements which do not take into account the compound helicopter. Two of the important omissions of the current ADS-33, are listed below:

- There are no Mission-Task-Elements which consider high speed missions which a compound helicopter is likely to perform regularly.
- There are no handling qualities criteria which are applicable to high speed manoeuvres.

The subsequent sections describe these areas where ADS-33 is deficient, in more detail.

Examination of Mission-Task-Elements

The menu of MTEs presented in the ADS-33E-PRF specification are listed in Table 7.1. Upon inspection of these recommended flight test manoeuvres, there are no MTEs which take into the high speed element of a rotorcraft design. For example, the descriptions of the Deceleration to Dash, Transient Turn, Pullup-Pushover and Roll Reversal MTEs all state that the test should be conducted with the helicopter at a speed equal to or less than 120kt [130]. The main perceived benefit of compounding the helicopter is to expand the vehicle's OFE, so that the helicopter can achieve speeds in excess of 200kt. As a consequence, it is likely that the currents MTEs will have to be altered, or alternatively new MTEs designed, to asses the handling qualities of a compound helicopter in high speed flight. Recall that MTEs are formed by the operational missions that the vehicle is expected to perform [36]. Essentially, a MTE is a test manoeuvre which represents a phase in a typical operational mission [36]. Hence, if new test manoeuvres are required, a close inspection of the compound helicopter perceived operational missions would be necessary.

The previous discussion highlighted that the MTEs in the existing performance standard do not take into account the high speed element of the compound helicopter. However, this does not mean that all the current MTEs, in the ADS-33E-PRF specification, are not appropriate to the compound helicopter. The compound helicopter is expected to have similar hover and low speed performance to that of the conventional helicopter. As a result, it is likely that the hover and low speed test manoeuvres may be applicable to assess the compound helicopter's handling qualities. Consider the Vertical Remask test manoeuvre as described in ADS-33E-PRF [130]. The primary aim of this manoeuvre is to check the rotorcraft's ability to manoeuvre, in low speed flight, close to the ground. This attribute is an important quality as the compound helicopter may need to avoid enemy fire in low speed flight. The only issue with this manoeuvre, in relation to compound helicopters, is that the performance standards may need to be tailored to account for the presence of a wing on a compound helicopter. However, the Vertical Remask does seem applicable to a compound helicopter. The fundamental premise of the compound helicopter is that it can achieve high speed whilst maintaining hover and low speed manoeuvring capability. Therefore, it may transpire that the majority of low speed test manoeuvres, listed in table 7.1, may prove applicable to a compound helicopter configuration.

Case Study - Deceleration to Dash

The following is an example of how an existing MTE may be altered to suit a compound helicopter. In this case study the test manoeuvre in question is the Deceleration to Dash MTE. One of the main benefits of the compound helicopter is its greater speed capability. In various scenarios this type of aircraft will have to decelerate frequently from its dash speed to its loiter speed. For example, consider a combat situation. The compound helicopter travels at its dash speed, to reach the appropriate area, and then is required to decelerate to its loiter speed to inspect or engage a potential threat. After this engagement the pilot realises that the helicopter may be vulnerable to an attack and therefore commences a sharp acceleration to reach the vehicle's dash speed to avoid an attack. This type of situation may occur frequently in a military environment. Consequently, within the ADS-33 specification, an MTE that aims to check the vehicle's handling qualities as the aircraft decelerates from its maximum to loiter speed, then sharply accelerates back to its initial airspeed, seems appropriate. For a compound helicopter, the acceleration and deceleration of the vehicle could involve the application of a propeller control to reduce or increase axial thrust. Additionally, the main rotor's speed may change significantly as it is required to be slowed, in high speed flight, to avoid adverse compressibility effects. For a winged helicopter, the main rotor is also offloaded, so a test manoeuvre involving a sharp deceleration could inspect the vehicle's handling characteristics as the lift across the wing alters significantly. There

	Deceleration to Dash
a	**Objectives**
•	Check for poor engine governing or overly complex power management requirement.
•	Check pitch, heave, and yaw axis handling qualities for aggressive manoeuvring.
•	Check for undesirable coupling between the longitudinal and lateral-directional axes, and between the heave axis and longitudinal and lateral-directional axes, for manoeuvres requiring large power changes.
•	Check for harmony between the heave, pitch, and directional axis controllers.
•	Check for adequate rotor response to aggressive collective inputs.
b	**Description of the manoeuvre**
	From level unaccelerated flight at the lesser of V_H or 120 knots, perform a level deceleration-acceleration. Adjust the pitch attitude to maintain altitude with a full down collective position. As the airspeed decreases to approximately 50 knots, aggressively assume the attitude for maximum acceleration and rapidly increase power to approximately the maximum, and maintain that power until the initial airspeed is reached.
c	Description of the test course
	Any reference line on the ground will serve as an adequate test course for this manoeuvre.
d	The entire manoeuvre shall be conducted below 200 ft.

Table 7.2: Description of the ADS-33E-PRF Deceleration to Dash MTE

could also be the option of the pilot to use flaps to improve the deceleration performance of the vehicle. Clearly, there are a variety of control issues in this type of manoeuvre which a compound helicopter will be expected to perform regularly. Hence, it seems appropriate to include a similar test manoeuvre in a performance standard relating to a compound helicopter. The existing "Deceleration to Dash" MTE, which is shown in Table 7.2, is similar to this type of manoeuvre. However, further analysis suggests that the airspeed values, stated in Table 7.2, do not seem appropriate for a compound helicopter. The dash speed in the current specification is limited to 120kt, whereas the compound helicopter's maximum speed is perceived to be much greater than this value. The dash speed of a compound helicopter is expected to be in the region of 220kt. The objectives of the test manoeuvre are also listed in Table 7.2. As these were based on a conventional helicopter, it does not check the handling qualities that may arise due to the addition of the compounding device(s). Additionally, the performance standards of the "Deceleration to Dash", which are separated into desired and adequate metrics, were developed using the conventional helicopter. These standards may or may not be applicable to the compound helicopter.

Due to the greater speed capability of the compound helicopter, it is possible that the "Deceleration to Dash" may need to be amended to accommodate this design

	Deceleration to Dash
a	**Objectives**
•	Check for poor engine governing or overly complex power management requirement.
•	Check pitch, heave, and yaw axis handling qualities for aggressive manoeuvring.
•	Check for undesirable coupling between the longitudinal and lateral-directional axes, and between the heave axis and longitudinal and lateral-directional axes, for manoeuvres requiring large power changes.
•	Check for harmony between the heave, pitch, and directional axis controllers.
•	*Check for adequate rotor response to aggressive collective inputs and the variation of rotorspeed.*
•	*Check for harmony between the thrust compounding controls and the other helicopter controls.*
•	*(Winged Compound Only) Check for harmony between the response of wing due to response of aggressive control inputs.*
b	**Description of the manoeuvre**
	From level unaccelerated flight at the lesser of V_H or 220 knots, perform a level deceleration-acceleration. The deceleration of the aircraft can be achieved through a combination of pitching the vehicle's nose up, the application of reverse thrust from the propeller(s), and by the application of speed brakes on a winged rotorcraft. As the airspeed decreases to approximately 80 knots, aggressively apply the control inputs for maximum acceleration and rapidly increase power to approximately the maximum, and maintain that power until the initial airspeed is reached.
c	Description of the test course
	Any reference line on the ground will serve as an adequate test course for this manoeuvre.
d	The entire manoeuvre shall be conducted below 200 ft.

Table 7.3: Possible Amended Version of the ADS-33E-PRF Deceleration to Dash MTE Suitable for Compound Helicopters

attribute. An amended version of the "Deceleration to Dash" test manoeuvre, applicable to the compound helicopter, may look like the description presented in Table 7.3. The proposed major changes to this test manoeuvre include the change of the initial airspeed when this MTE commences. The recommended manoeuvre begins at an airspeed less than or equal to 220kt, which is more applicable to expected flight speeds of a compound helicopter. The aircraft is required to decelerate to an airspeed of 80kt, then to accelerate to its initial speed. The description of the manoeuvre also states that the deceleration phase of the manoeuvre may be achieved through a variety of mechanisms. The perceived compound helicopter design could decelerate by typical helicopter manoeuvring (pitching the aircraft's nose up), or through the application of propeller reverse thrust or through the use of speed brakes on a winged compound vehicle. Clearly, with the addition of compounding to the rotorcraft there are a variety of piloting strategies that could be used to fly this particular manoeuvre. Consequently, this type of test manoeuvre would have additional objectives, relative to the conventional helicopter. Some of these additional objectives are stated in Table 7.3. This MTE would check how the main rotor of the compound helicopter responds due to strong control inputs which would result from this manoeuvre. With the types of airspeeds suggested in Table 7.3, the rotorspeed of the main rotor could vary significantly, (the rotor is required to be slowed in high speed flight) altering the response characteristics of the aircraft. Altering the rotorspeed is a task that the flight control system would be required to do, in effect regulating the rotorspeed with the given flight condition. This manoeuvre would check the control system's ability to achieve this. The test manoeuvre would also check for harmony between the thrust compounding controls (most probably propeller controls) with the standard helicopter controls. It is possible that multi-mode mixing would be adopted. For example, the propeller control could be mixed directly with the longitudinal stick so that forward stick tilts the rotor disc forward as well as increases the propeller's axial thrust. Again, this manoeuvre would check for harmony between these two controls. The last addition to the objectives concerns the wing's contribution, if applicable, to the handling qualities. The lifting capability of the wing is strongly dependent on flight speed. The rapid deceleration of a winged helicopter would significantly deteriorate the lifting force across the wing, requiring an increase of rotor thrust to maintain height. The reverse situation occurs as the aircraft accelerates. The proposed amendment to the "Deceleration to Dash" would examine the wing's effect on the handling qualities of the aircraft.

Handling Qualities Criteria

An important component of the mission based framework of ADS-33 is the set of quantitative criteria, as seen in Figure 7.4. Although, the opinion of the pilot is generally the conclusive factor [36], quantitative criteria are required as they form design goals and can be used to demonstrate compliance during the design stages [36]. Although design criteria for the conventional helicopter has been well established, and included in the publication of ADS-33, there remains a challenge to develop handling qualities design criteria which are appropriate for compound helicopters. The natural consequence of compounding the helicopter is the expansion of the flight envelope, exposing the helicopter to unfamiliar flight conditions. For the conventional helicopter, the ADS-33 specification conveniently splits the quantitative criteria into two sections; namely the hover and low speed and forward flight requirements. The hover and low speed requirements correspond to airspeeds below 45 kt. Conversely, the forward flight requirements

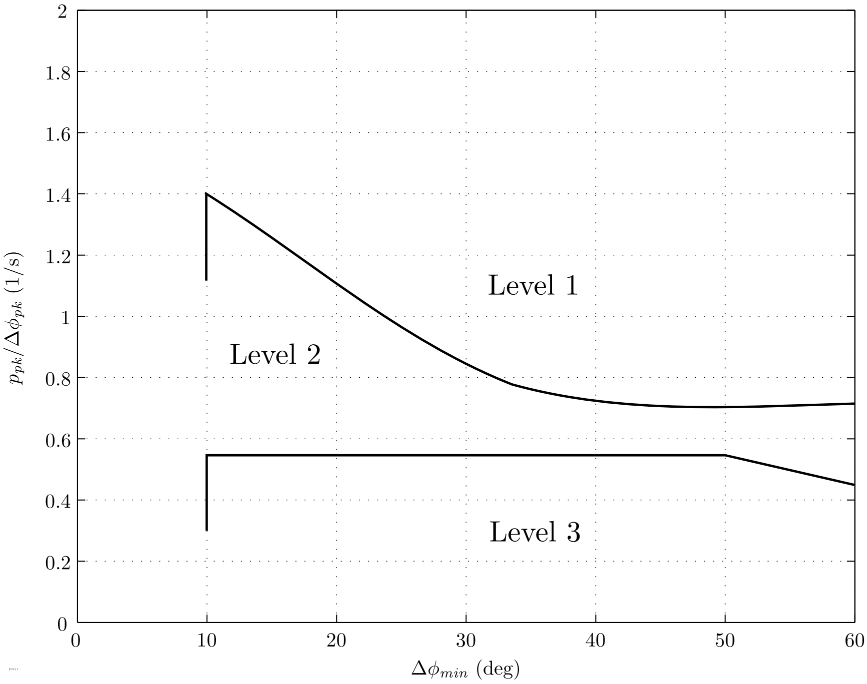

Figure 7.5: Roll Attitude Quickness Criteria for Forward Flight (MTEs expect Target Acquisition and Tracking) [130]

are applicable to flight speeds over 45 kt.

The compound helicopter will be expected to operate in flight conditions which cannot be achieved by the standard helicopter design. With the expansion of the flight envelope it may be necessary, within the handling qualities criteria, to make a distinction between “mid-speed flight” and “high speed flight”. The “mid-speed flight” range could be a speed range within 45 - 140kt whereas the term “high-speed flight” would correspond to airspeeds in excess of 140 kt. The high speed range would be where the compounding device(s) would be fully exploited, to overcome the limitations of the conventional helicopter, leading to unfamiliar response characteristics. Consequently, the boundary lines, which discriminate between Levels 1, 2 and 3, in the ADS-33 specification may need to be redefined in the high speed range. For example, consider the roll attitude quickness criterion for forward flight MTEs, excluding target acquisition and tracking MTEs, shown in Figure 7.5. Figure 7.5 introduces the “roll attitude quickness” parameter which is shown on the y-axis. This parameter is the ratio of the peak roll rate and the peak change of roll angle

$$Roll\ Attitude\ Quickness = \frac{p_{pk}}{\Delta\phi_{pk}} \tag{7.1}$$

The quantity ϕ_{min} is the minimum bank angle achieved in the manoeuvre. The boundaries in Figure 7.5 were determined by Roger Hoh, a key contributor to the ADS-33 performance standard, with the use of flight test data [139]. It may transpire that the boundaries presented in Figure 7.5 may not be appropriate to a compound helicopter in high speed flight. This would need to examined by a series of flight tests or flight simulations in the high speed range. It is important to highlight that compound helicopter designs are likely to have significant roll control power, with significant roll rates expected to be achieved by a combination of lateral cyclic and some other control. Consider a winged compound helicopter in high speed flight. The maximum theoretical bank angle could be greater than that of a conventional helicopter as higher bank angles could be attained by the application of both lateral cyclic and aileron controls across the wing. As a result, simulations or flight tests involving test pilots flying a compound helicopter may conclude that the Level 1 handling qualities boundary may need to be moved in a different region to that presented in Figure 7.5. However, it must be stressed that a decisive conclusion can only be reached after tests have been conducted.

In a similar manner to the roll quickness parameter, it may be necessary to refine the boundaries of the pitch quickness in high speed flight. The definition of the pitch quickness parameter is analogous to roll quickness, with the term described by the following relationship

$$Pitch\ Attitude\ Quickness = \frac{q_{pk}}{\Delta\theta_{pk}} \tag{7.2}$$

For a conventional helicopter, high pitch rates can be achieved by longitudinal cyclic and/or collective inputs. In relation to a compound helicopter, the pilot may be able to create greater pitch rates by the application of control inputs to the thrust compounding device. Although there are various proposed compound helicopter designs, one common theme is the additional source of thrust compounding which is likely to be supplied by a propeller. Depending on the rotorcraft's design, the pilot may be able to exploit the benefits of thrust compounding to achieve greater pitch rates than a conventional helicopter counterpart. Another issue is the contribution of the wing, if the vehicle features lift compounding. In high speed flight, the wing will offload the main rotor of its lifting responsibilities. As a consequence, the lifting force from the wing added with suitable main rotor control inputs could allow the aircraft to achieve significant pitch rates. For these reasons, the boundaries of Level 1, 2 and 3 may need to be altered.

Another issue with compound helicopter designs are the methods in which the anti-torque moment is provided. For example, with the Eurocopter X^3 the yaw control is provided by the two propellers, mounted on earlier side of the fuselage, and not by a standard tail-rotor. Considering the Sikorsky X2, the application of differential collective control allows the helicopter to yaw. There is the additional possibility that the yaw control of the compound helicopter will be shifted to a rudder control, in high speed flight. As a consequence, both the yaw control power and yaw axis quickness boundaries may need to be re-examined. Again, it is important to stress that calculating these boundaries is beyond the scope of this work, with the primary aim of the work to identify some of the potential handling qualities issues associated with compound helicopters.

In relation to the tilt-rotor aircraft, the RHILP programme showed that the fixed wing aircraft handling qualities criteria could be integrated with the tilt-rotor in aeroplane mode [159]. In particular, the RHILP showed that the short period mode of the tilt-rotor loosely conformed with the short period “thumbprint” criterion of fixed wing aircraft. Figure 7.6 shows the classical thumbprint chart of fixed wing aircraft [96]. For fixed wing aircraft, past experience shows that good short period handling qualities are obtained when the mode is heavily damped with a frequency of approximately 3rad/s [96]. Using this criterion, the tilt-rotor short period was determined to be in the “poor” and “acceptable” boundaries [159]. In the context of compound helicopters, the handling qualities of fixed wing aircraft could be used as quantitative criteria. However, there is an important distinction to make between the tilt-rotor vehicle and a compound helicopter design. In effect, the tilt-rotor operates as a turbo-prop aircraft in high speed flight, with the wing providing the entire lifting force. In contrast, with a compound helicopter featuring lift compounding, the wing and the main rotor combine to provide the lifting force. The response of the main rotor following a disturbance will be significant, as seen in Chapter 5, therefore the short period mode may not be similar to the damping and frequency range in the thumbprint criterion. Due the dominating nature of the main rotor, with its ability to produce significant pitching and rolling moments independent of the amount of rotor thrust, it is fair to postulate that in high sped flight the response of a compound helicopter would be different to that of a fixed wing aircraft. Therefore, it is the author’s opinion that fixed wing handling qualities will not play a significant role in the formation of compound helicopter handling qualities criteria.

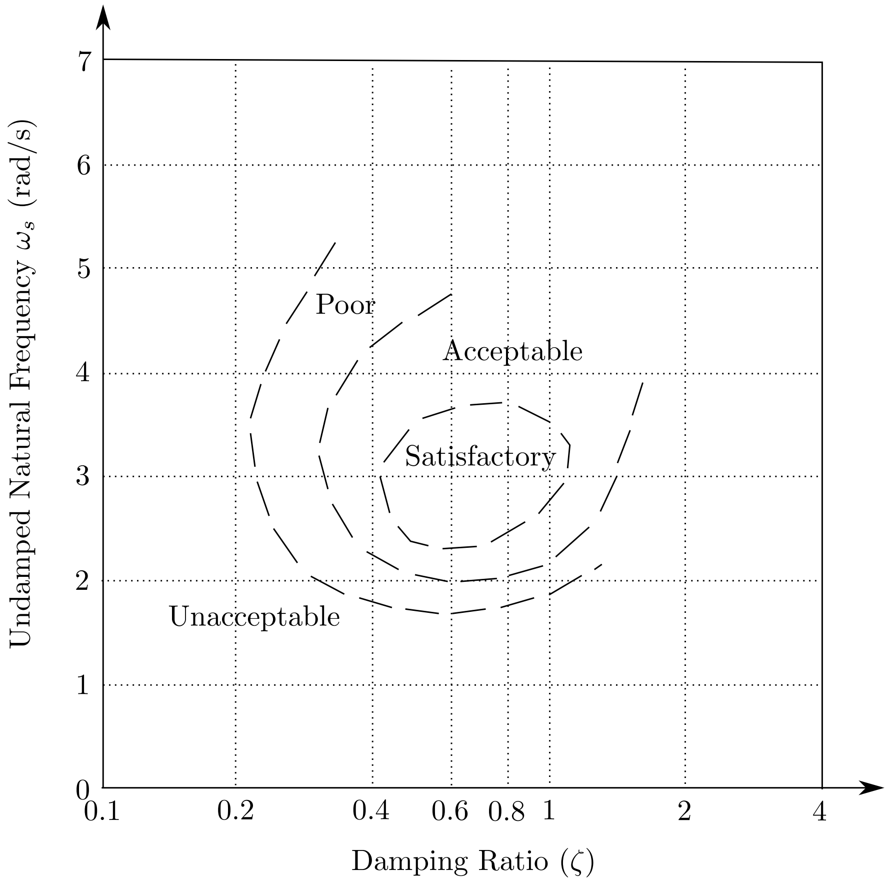

Figure 7.6: Short Period Thumbprint Chart [96]

7.8 Chapter Summary

This Chapter has examined the handling qualities criteria for conventional helicopters, primarily focusing on the ADS-33 performance standard. Clearly, the ADS-33 performance standard is a comprehensive set of handling qualities criteria which has improved the handling qualities of various rotorcraft. One of the key innovations of the standard is that it centres on the helicopter mission that is being conducted. Therefore, it can be described as a mission-oriented framework. Despite the inherent successes of the ADS-33 specification, it was demonstrated that there are some gaps within the requirements that do not take into account some of the important features of a compound helicopter. For example, the menu of MTEs within the current specification, ADS-33E-PRF, do not address the high speed element of the compound helicopter. All of the well established forward flight MTEs are limited to airspeeds under 120kt. To remedy this issue two solutions are suggested. The first solution is to take the existing MTEs and alter the appropriate test manoeuvres to take into account the high speed range of a compound helicopter. Ultimately, the altered MTE would be similar to the established

MTE, with the exception that the airspeeds or distances that the aircraft is expected to reach may be different due to differences in performance. By altering the MTE, it may be necessary to redefine the performance standards which accompany the test manoeuvre. An example of this approach was demonstrated in the Chapter by altering the existing “Deceleration to Dash” manoeuvre. The second solution is to develop new test manoeuvres based on the operational missions that the compound helicopter is expected to perform.

The Chapter also highlighted that low speed MTEs, within the ADS-33E-PRF performance standard, may still be applicable to a compound helicopter design. One of the obvious advantages of the compound helicopter is its greater speed capability. However, this rotorcraft configuration will be expected to perform hover and low speeds tasks such as ground surveillance and ship landings. Therefore the vehicle will be required to exhibit excellent handling qualities in low speed flight as well as high speed flight, to ensure that the aircraft can complete a wide variety of missions effectively. Consequently, it seems reasonable that the existing hover and low speed tests manoeuvres could be used to demonstrate that the compound helicopter has satisfactory handling qualities in this flight regime. In terms of dynamic response criteria, the Chapter introduced the typical parameters which assess the helicopter’s handling qualities. Examples of response parameters include the attitude quickness, control power and bandwidth. These form the basis of the dynamic response criteria with appropriate boundaries discriminating between Levels 1, 2 and 3 handling qualities. It is suggested that these boundaries may need to be amended to suit a compound helicopter, in forward speed flight. The introduction of compounding may allow the pilot to achieve greater or lower angular rates than the conventional helicopter. As a result, it may be necessary to redefine the boundary lines in the response criteria. However, it was stressed that a conclusive decision can only be reached by carrying out appropriate flight tests or simulations in future studies.

Chapter 8

Conclusions

8.1 Introduction

The main conclusions of this Thesis are summarised in this Chapter. The main aim of this Thesis was to make a contribution to the improved understanding of the flight dynamics of compound helicopters. To this end, this study investigated the effects of thrust and lift compounding and how they influence the flight mechanics of the helicopter configuration. As stated in Chapter 1, the motivation for this work arose from the resurgence of interest in the compound helicopter configuration. The study focussed on understanding the effects of compounding to the trim, performance, stability and manoeuvrability of the compound helicopter. Another objective was also to examine the handling qualities of the compound helicopter and the challenges which face the rotorcraft community in this area. The following lists the conclusions from each objective, which were stated in Chapter 1.

8.2 Research Conclusions

(i) **Mathematical Model Development**

The first objective was to develop a simulation package capable of modelling compound helicopter configurations. To model compound helicopter configurations, the existing conventional helicopter package has been enhanced to include propeller, wing and coaxial rotor models. The coaxial rotor and the propeller models were validated using available wind tunnel data. These encouraging results show that the models can accurately capture the behaviour of a coaxial rotor and a propeller for the purposes of flight dynamics research. The end result here is that a simulation package, which falls into the Level 1 rotorcraft modelling category, has been developed which is capable of assessing compound helicopters.

(ii) **Development of Compound Helicopter Configurations**

The second objective was to develop compound helicopter configurations using the simulation package. The study was influenced by industrial interest in two specific arrangements of the compound helicopter, namely the Eurocopter (now Airbus Helicopters) X^3 and the Sikorsky X2. Due to the interest in these rotorcraft configurations, it was decided to focus the research on these two vehicles. To model the two compound helicopters, an established conventional helicopter was taken and altered to represent two compound helicopter configurations. Hence, the study involves three aircraft configurations - a conventional helicopter and two compound helicopter configurations. The baseline (BL) helicopter was based on the AugustaWestland Lynx and the two other compound helicopters were referred to as the Hybrid Compound Helicopter (HCH) and Coaxial Compound Helicopter (CCH).

The second part of this particular objective was to trim the compound helicopters. This required altering the well-established trim algorithm to take into account the additional control(s) that compounding offers. The new trim algorithm was successful and it appears to be a useful flight dynamics tool. The results from the compound helicopter showed that controls required to trim the aircraft can change significantly due to influence of compounding. With a winged helicopter configuration, the main rotor collective reduces as the wing offloads the main rotor of its lifting duties. The addition of thrust compounding, reduces the amount of forward stick required as airspeed increases due to the axial thrust the propeller(s) provide. With the CCH configuration, differential lateral cyclic was shown to be able to offload the retreating sides of the rotor discs in high speed flight with the trim algorithm predicting that this control varies linearly with airspeed.

(iii) **Performance**

The next objective was to examine the effects of compounding to the performance of this aircraft class. Although this was not a design exercise, the results from this Chapter did highlight some important design aspects of the compound helicopter. The conclusions from this piece of work emphasise the importance of reducing airframe drag on this particular aircraft configuration. In addition, the work concludes that the presence of a wing is detrimental to the hover performance of a compound helicopter. Another conclusion is that it is likely that the compound helicopter will need a significant increase of engine power, relative to a conventional helicopter of similar mass, so that it can operate in the high speed range. In this flight regime, parasitic power becomes excessive and therefore requires a significant increase of power to compensate. Due to the modelling approach, it is difficult to broadly conclude whether or not a compound helicopter would have greater performance than a conventional helicopter. Such a conclusion can only be made with a parametric performance study which takes into account the powerplants, weights and sizing of various aircraft components. This type of study is a suggestion for future work.

(iv) **Dynamic Stability**

The stability of the compound helicopter configurations was examined in Chapter 5. The main conclusion from Chapter 5 is that the dynamic stability characteristics of the two compound helicopter configurations are broadly similar, although there are some differences, to the conventional helicopter. The reason for this is due to the powerful contribution of the main rotor to the stability attributes of the compound helicopter. It can be concluded, with some confidence, that the roll damping of a helicopter will increase in forward flight if a wing is added to the design. The roll damping of the lateral lift offset rotor will also be significant due to the coaxial rotor design. Another conclusion is that the drag damping of the compound helicopter will be greater than that of the the conventional helicopter. This is due to the contribution of the propeller(s), which increases the drag of the vehicle following a perturbation of forward speed. This result attempts to stabilise the phugoid mode of the respective aircraft, although the phugoid mode may still be unstable due to the main rotor's contribution. One important conclusion, is that the compound helicopter may exhibit an unstable longitudinal mode in high speed flight. For the HCH configuration, an unstable heave mode develops whereas the phugoid mode of the CCH configuration branches off to the real axis, producing a purely divergent mode.

(v) **Manoeuvrability**

The fifth objective of the study was to determine the influence of compounding on the manoeuvrability of the compound helicopter configurations. To achieve this the simulation tool of the inverse simulation was used. One of the achievements of this Chapter was the development of a Manoeuvrability Assessment Method which can predict the manoeuvrability of a compound helicopter. In the context of the Chapter, it is predicted that the two compound helicopters featured in the study are more manoeuvrable than the conventional helicopter when flying Accel-Decel or Pullup-Pushover manoeuvres. For these two manoeuvres, the conclusion is that it is likely that the compound helicopter will be more manoeuvrable that a conventional helicopter if the following conditions are met. The first condition is that the weights of the the conventional helicopter and compound helicopter are similar. The weight of the compound helicopter may be greater than the standard helicopter due to the additional weight of wings, propellers and additional engines. The second condition is that the installed power of the compound helicopter must be greater than its conventional counterpart to exploit the manoeuvrability potential of compounding. Therefore, it is unreasonable to conclusively state, in a broad sense, that a compound helicopter will be more manoeuvrable than a conventional helicopter. But it can be concluded, with some certainty, that the introduction of compounding does have the potential to be increase the manoeuvrability of this aircraft class.

(vi) **Handling Qualities**

The final objective of the study was to outline the challenges in developing handling qualities standards which are appropriate to compound helicopters. Chapter 7 highlighted some of the important omissions of the ADS-33E-PRF standard. The first conclusion is that none of the menu of mission-task-elements within the ADS-33E-PRF specification take into account the high speed element of the compound helicopter. The forward speed boundary of all of the mission-task-elements does not exceed 120kt. The compound helicopter is expected to operate at greater flight speeds, with an envisioned cruise speed being in the region of 220kt. Consequently, it is concluded that there are two options to address this shortcoming. The first option is to alter the current mission-task-elements to take into account high speed mission tasks that a compound helicopter will perform in its operational duties. Alternatively, new mission-task-elements could be formed which take into the account the operational roles that the compound helicopter will perform in high speed flight. Another conclusion from the Chapter is that it may be necessary to redefine the boundaries of the various dynamic response criteria when high speed flight conditions are considered. It might be appropriate to make a distinction between "mid-speed" and "high-speed" flight in the specification. The term "mid-speed" flight would represent speeds between 40 - 140kt, whereas "high-speed" flight would reflect airspeeds in excess of 140kt. The "high speed flight" bracket would consider flight speeds where the benefits of compounding are fully exploited to avoid the aerodynamic limitations which typically restrict the maximum speed of a conventional helicopter. These different speed categories are only a suggestion as it may transpire that the boundaries in the "high-speed" flight range may be similar or identical to the existing dynamic response criteria.

Appendix A

Linear Inflow Model

A.1 Glauert Inflow Model

Modelling the rotor wake is a complex aerodynamics problem. The modelling strategy used to approximate the behaviour of the rotor wake depends on the application. For example, for main rotor design studies high fidelity vortex wake models are typically used. However, for the purposes of flight dynamics simple linear inflow models are commonly used. The HGS package uses a linear inflow variation to model the induced velocity through the rotor disc. Although a rudimentary model, the linear inflow model has shown good correlation with wind tunnel data. One fundamental assumption of this type of model is that the inflow variation is of linear form

$$v_i = v_0 + v_{1s} r \sin\psi + v_{1c} r \cos\psi \tag{A.1}$$

Therefore, the induced velocity through the rotor disc is composed of three terms - a steady term represented by v_0, and two other terms which describe the induced velocity's variation across the rotor disc. The terms v_{1s} and v_{1c} represent the lateral and longitudinal contributions of the rotor inflow, respectively. Equation (A.1) is commonly presented in normalised form as

$$\lambda_i = \lambda_0 + \lambda_{1s}\bar{r} \sin\psi + \lambda_{1c}\bar{r} \cos\psi \tag{A.2}$$

where

$$\lambda_i = \frac{v_i}{\Omega R}$$

$$\lambda_{1s} = \frac{v_{1s}}{\Omega R}$$

$$\lambda_{1c} = \frac{v_{1c}}{\Omega R}$$

$$\bar{r} = \frac{r}{R}$$

By the application of steady momentum theory, the steady inflow term λ_0 can be calculated using the familiar expression of

$$\lambda_0 = \frac{C_T}{2\sqrt{\mu^2 + (\mu_z - \lambda_0)^2)}} \tag{A.3}$$

The term, μ, is the in-plane velocity at the rotor hub, where μ_z is the normal component of the velocity at the rotor hub. The thrust coefficient is also present in Equation (A.3) as denoted by C_T. Although in some special cases an analytical solution to Equation (A.3) can be found, the mean inflow component through the rotor disc is generally calculated numerically.

The next task is to calculate the lateral and longitudinal contributions to Equation (A.2). It is assumed that these terms are based on the rotor wake skew angle and the mean induced velocity through the disc. To determine the values of λ_{1c} and λ_{1s} it is necessary to introduce another axes set, called the wind axes set. The transformation between the rotor disc axes and the rotor wind axes is

$$\begin{bmatrix} \lambda_{\mathrm{1c}}^{\mathrm{disc}} \\ \lambda_{\mathrm{1s}}^{\mathrm{disc}} \end{bmatrix} = \begin{bmatrix} \cos\psi^{\mathrm{wind}} & -\sin\psi^{\mathrm{wind}} \\ \sin\psi^{\mathrm{wind}} & \cos\psi^{\mathrm{wind}} \end{bmatrix} \begin{bmatrix} \lambda_{\mathrm{1c}}^{\mathrm{wind}} \\ \lambda_{\mathrm{1s}}^{\mathrm{wind}} \end{bmatrix} \tag{A.4}$$

where

$$\psi^{\mathrm{wind}} = \tan^{-1}\left(\frac{\mu_x}{\mu_y}\right)$$

The longitudinal component of the rotor inflow, in rotor wind axes, can be approximated by the expression

$$\lambda_{1c}^{\text{wind}} = \lambda_0 \tan\frac{\chi}{2} \qquad \text{if} \qquad \chi < \frac{\pi}{2} \tag{A.5}$$

$$\lambda_{1c}^{\text{wind}} = \lambda_0 \cot\frac{\chi}{2} \qquad \text{if} \qquad \chi > \frac{\pi}{2} \tag{A.6}$$

One of the convenient results of transforming from the rotor disc axes to the rotor wind axes is that the lateral component of the inflow, in wind axes, is zero. As $\lambda_{1s}^{\text{wind}} = 0$, and by using Equations (A.1) - (A.6) the induced velocity through the rotor disc can be approximated.

Appendix B

Trim Algorithm

B.1 Newton-Raphson Trim Algorithm

The starting point of any meaningful analysis of a helicopter model is to trim the model. From the trim condition the helicopter's dynamic stability, open-loop response and handling qualities can all be assessed. The trim problem is to find the control angles to hold the helicopter in a flight condition were the body accelerations are exactly zero [36]. The helicopter can be in trimmed flight when turning, climbing or descending. In the condition of steady level flight then the angular velocities are set to zero as well as the sideslip velocity. Consequently, the aircraft will be steady level flight when the six Euler rigid body equations are:

$$\frac{X}{M_a} - g\sin\Theta = 0 \tag{B.1a}$$

$$\frac{Y}{M_a} + g\cos\Theta\sin\Phi = 0 \tag{B.1b}$$

$$\frac{Z}{M_a} + g\cos\Theta\cos\Phi = 0 \tag{B.1c}$$

$$L = 0 \tag{B.1d}$$

$$M = 0 \tag{B.1e}$$

$$N = 0 \tag{B.1f}$$

From Equations (B.1), it is evident that in this particular case there are six functions that must equal zero. A numerical method is used to calculate the control angles which satisfy the above set of equations. The method is the so-called Newton-Raphson method. A complete description of the numerical technique is detailed by Press et. al [160], with a brief summary given below. The discussion also shows how this method is used to trim the helicopter model.

The Newton-Rapshon method can be used for a problem where the number of function relationships equal the number of unknown quantities. In the general case, if there are N functions to be equal to zero, with the unknown variables denoted by x_i, then it can be said

$$F_i(x_1, x_2, ...x_N) = 0 \qquad\qquad i = 1, 2, ...N \tag{B.2}$$

Let the vector $\mathbf{x}$ contain the unknown values with the vector $\mathbf{F}$ denoting the functions. A Taylor series can be applied, resulting in

$$F_i(\mathbf{x} + \delta\mathbf{x}) = F_i(\mathbf{x}) + \sum_{j=1}^{N} \frac{\partial F_i}{\partial x_j}\delta x_j + O(\delta\mathbf{x}^2) \tag{B.3}$$

Equation (B.3) can be simplified by firstly noting that $\dfrac{\partial F_i}{\partial x_j}$ is a matrix of partial derivatives known as the Jacobian matrix, $\mathbf{J}$. In addition, the higher order derivatives can be neglected. Therefore, in matrix notation the equation becomes

$$\mathbf{F}(\mathbf{x} + \delta\mathbf{x}) = \mathbf{F}(\mathbf{x}) + \mathbf{J}.\delta\mathbf{x} \tag{B.4}$$

For the particular case of the conventional helicopter, with the assumption of constant rotorspeed, there are six unknowns. The unknown vector, $\mathbf{x}$, is therefore

$$\mathbf{x} = [\theta_0, \theta_{1s}, \theta_{1c}, \theta_{0tr}, \Theta, \Phi]^T \tag{B.5}$$

To further reinforce how the method works, Equation (B.4) may be written in expanded form. If the term F_1 represents Equation (B.1a), F_2 represents Equation (B.1b) and so forth, then

$$\begin{bmatrix} F_1(\mathbf{x_i}+\delta\mathbf{x_i}) \\ F_2(\mathbf{x_i}+\delta\mathbf{x_i}) \\ \vdots \\ F_6(\mathbf{x_i}+\delta\mathbf{x_i}) \end{bmatrix} = \begin{bmatrix} F_1(\mathbf{x_i}) \\ F_2(\mathbf{x_i}) \\ \vdots \\ F_6(\mathbf{x_i}) \end{bmatrix} + \begin{bmatrix} \frac{\partial F_1}{\partial \theta_0} & \frac{\partial F_1}{\partial \theta_{1s}} & \cdots & \frac{\partial F_1}{\partial \Phi} \\ \frac{\partial F_2}{\partial \theta_0} & \frac{\partial F_2}{\partial \theta_{1s}} & \cdots & \frac{\partial F_2}{\partial \Phi} \\ \vdots & \vdots & \ddots & \vdots \\ \frac{\partial F_6}{\partial \theta_0} & \frac{\partial F_6}{\partial \theta_{1s}} & \cdots & \frac{\partial F_6}{\partial \Phi} \end{bmatrix} \cdot \begin{bmatrix} \delta\theta_0 \\ \delta\theta_{1s} \\ \vdots \\ \delta\Phi \end{bmatrix} \tag{B.6}$$

The only major difficulty with this method is determining the values of the 36 particular derivatives (6 unknowns $\times$ 6 functions), such as $\frac{\partial F_1}{\partial \theta_0}$, etc. Due to the complexity of the helicopter equations of motion it is challenging, if not impossible, to analytically calculate the particular derivatives. As a result, the derivatives are calculated numerically by adopting a central differencing approach. The overall solution of the unknown vector is found when $\mathbf{F}(\mathbf{x}+\delta\mathbf{x}) = 0$. This equation, in matrix form, can therefore be written as

$$\delta\mathbf{x} = -\mathbf{J^{-1}}.\mathbf{F} \tag{B.7}$$

The $\delta\mathbf{x}$ vector is added to the solution vector to converge towards a solution

$$\mathbf{x_{i+1}} = \mathbf{x_i} + \delta\mathbf{x} \tag{B.8}$$

This is an iterative process with the algorithm continuing until convergence. If the initial guesses are of good quality then convergence is normally reached within five iterations. Generally, the convergence criterion is set by specifying a tolerance. That is to say that the process keeps iterating until

$$\mathbf{x_{i+1}} - \mathbf{x_i} < tol \tag{B.9}$$

This method has proven to be robust and reliable. It should be noted that the algorithm is easily amended to suit a given application. For example, the number of unknowns with $\mathbf{x}$ can be extended, with the assumption that an additional function is formed.

Appendix C

Linearisation Algorithm

C.1 Linearisation Algorithm

The following is an overview of the numerical linearisation algorithm to reduce the nonlinear equations of motion into linear form. One of the main fundamental assumptions of the numerical linearisation approach is that the vehicle's forces and moments can be expressed by a Taylor-series expansion. For example, using the X body force, this can be expressed as

$$X \approx X_{\mathrm{e}} + \frac{\partial X}{\partial u}\delta u + \frac{\partial X}{\partial w}\delta w \ldots h.o.t. \tag{C.1}$$

with the remaining forces and moments expanded in a similar manner. The δ term denotes a small change from the trimmed state. Equation (C.1) linearised the force of the X body equation, however the Taylor-series expansion can be conveniently applied to the entire rigid body equations. If the nonlinear equations of motion of the aircraft are given by

$$\dot{\mathbf{x}} = \mathbf{F}(\mathbf{x}, \mathbf{u}) \tag{C.2}$$

then a Taylor-series expansion of the nonlinear equations of motion, Equation (C.2), gives

$$\dot{\mathbf{x}} + \delta\dot{\mathbf{x}} = \mathbf{F}(\mathbf{x}, \mathbf{u}) + \frac{\partial \mathbf{F}}{\partial \mathbf{x}}\delta\mathbf{x} + \frac{\partial \mathbf{F}}{\partial \mathbf{u}}\delta\mathbf{u} \ldots h.o.t. \tag{C.3}$$

Additionally, Equation (C.3) can be reduced further by noting that at the trimmed state the time derivative of the state vector is zero, which is mathematically stated as

$$\dot{\mathbf{x}} = \mathbf{F}(\mathbf{x}, \mathbf{u}) = 0 \tag{C.4}$$

Therefore, the Taylor-series expansion of the equations of motion yield the following

$$\delta\dot{\mathbf{x}} = \frac{\partial \mathbf{F}}{\partial \mathbf{x}}\delta\mathbf{x} + \frac{\partial \mathbf{F}}{\partial \mathbf{u}}\delta\mathbf{u} \tag{C.5}$$

which with dropping the perturbation notation, is commonly expressed as

$$\dot{\mathbf{x}} = \mathbf{A}\mathbf{x} + \mathbf{B}\mathbf{u} \tag{C.6}$$

where the system matrix, $\mathbf{A}$, is form of the stability derivatives and the control matrix, $\mathbf{B}$, contains the control derivatives. The fully expanded form of the system and control matrices are shown in Equations (C.11) and (C.12), respectively. The structure of the state matrix is

$$\mathbf{x} = \begin{bmatrix} U, & V, & W, & P, & Q, & R, & \Phi, & \Theta \end{bmatrix}^T \tag{C.7}$$

whereas, the control matrix for the BL helicopter is of the form

$$\mathbf{u} = \begin{bmatrix} \theta_{0}, & \theta_{1s}, & \theta_{1c}, & \theta_{0tr} \end{bmatrix}^T \tag{C.8}$$

The derivatives contained in each of the matrices, Equations (C.11) and (C.12), are estimated through numerical differentiation. More specifically, a central difference approach is used to calculated the derivatives. For example, consider the first Euler Rigid Body equation

$$\dot{U} = -\left(WQ - VR\right) + \frac{X}{M_a} - g\sin\theta \tag{C.9}$$

For simplicity, Equation (C.9) is referred to as F_1. Clearly, the function F_1 is dependent on the vehicle's states and controls. In the trimmed condition, F_1 equals zero. It is best to explain the central difference approach, by an example. Focusing on the drag damping derivative X_u, it is calculated by applying small perturbations of forward velocity, u, to F_1. During these perturbations, all the states apart from u and the controls remain at their trim values. The drag damping derivative is therefore approximated by

$$X_u \approx \frac{F_1\left(U_e + u\right) - F_1\left(U_e - u\right)}{2u} \tag{C.10}$$

The perturbation size of u is chosen to be a small value. This process of central differencing occurs 64 times (8 states $\times$ 8 equations) to calculate the system matrix, Equation (C.11). To develop the control matrix it is used 32 times (8 states $\times$ 4 controls) to create the control matrix, Equation (C.12).

$$\mathbf{A} = \begin{bmatrix} X_u & X_v + R_e & X_w - Q_e & X_p & X_q - W_e & X_r + V_e & 0 & -g\cos\Theta_e \\ Y_u - R_e & Y_v & Y_w + P_e & Y_p + W_e & Y_q & Y_r + U_e & g\cos\Phi_e\cos\Theta_e & -g\sin\Phi_e\sin\Theta_e \\ Z_u + q_e & Z_v - P_e & Z_w & Z_p - V_e & Z_q + U_e & Z_r & -g\sin\Phi_e\cos\Theta_e & -g\cos\Phi_e\sin\Theta_e \\ L^{'}_{\mathrm{u}} & L^{'}_{\mathrm{v}} & L^{'}_{\mathrm{w}} & L^{'}_{\mathrm{p}} + k_1 Q_e & L^{'}_{\mathrm{q}} + k_1 P_e - k_2 R_e & L^{'}_{\mathrm{r}} - k_2 Q_e & 0 & 0 \\ M_u & M_v & M_w & M_p - 2P_e I_{xz} I_{yy} - R_e(I_{xx} - I_{zz}) I_{yy} & M_q & M_r + 2R_e I_{xz} I_{yy} - P_e(I_{xx} - I_{zz}) I_{yy} & 0 & 0 \\ N^{'}_{\mathrm{u}} & N^{'}_{\mathrm{v}} & N^{'}_{\mathrm{w}} & N_p - k_3 Q_e & N^{'}_{\mathrm{q}} - k_1 R_e - k_3 P_e & N^{'}_{\mathrm{r}} - k_1 Q_e & 0 & 0 \\ 0 & 0 & 0 & 1 & \sin\Phi_e\tan\Theta_e & \cos\Phi_e\tan\Theta_e & 0 & \Psi_e\sec\Theta_e \\ 0 & 0 & 0 & 0 & \cos\Phi_e & -\sin\Theta_e & -\Psi_e\cos\Theta_e & 0 \end{bmatrix} \tag{C.11}$$

$$\mathbf{B} = \begin{bmatrix} X_{\theta_0} & X_{\theta_{1s}} & X_{\theta_{1c}} & X_{\theta_{0tr}} \\ Y_{\theta_0} & Y_{\theta_{1s}} & Y_{\theta_{1c}} & Y_{\theta_{0tr}} \\ Z_{\theta_0} & Z_{\theta_{1s}} & Z_{\theta_{1c}} & Z_{\theta_{0tr}} \\ L_{\theta_0} & L_{\theta_{1s}} & L_{\theta_{1c}} & L_{\theta_{0tr}} \\ M_{\theta_0} & M_{\theta_{1s}} & M_{\theta_{1c}} & M_{\theta_{0tr}} \\ N_{\theta_0} & N_{\theta_{1s}} & N_{\theta_{1c}} & N_{\theta_{0tr}} \\ 0 & 0 & 0 & 0 \\ 0 & 0 & 0 & 0 \end{bmatrix} \tag{C.12}$$

Appendix D

System and Control Matrices

The following lists the system and control matrices of the BL, HCH and CCH configurations at various flight speeds.

D.1 BL Configuration Matrices

BL Configuration - Hover

A Matrix =

$$\begin{bmatrix} -0.0168 & -0.0104 & 0.0209 & -0.2794 & 0.3788 & -0.0195 & -0.0002 & -9.7866 & -0.0000 \\ 0.0123 & -0.0359 & -0.0001 & -0.4167 & -0.3240 & 0.1141 & 9.7731 & 0.0386 & 0.0000 \\ 0.0232 & -0.0051 & -0.2963 & -0.0250 & 0.0500 & -0.0034 & 0.5137 & -0.7377 & -0.0000 \\ 0.3123 & -0.2530 & 0.0204 & -10.1760 & -2.9769 & -0.7474 & -0.0007 & -0.0048 & 0.0000 \\ 0.0513 & 0.0509 & 0.0047 & 0.3291 & -1.8589 & 0.0155 & 0.0008 & -0.0002 & -0.0000 \\ 0.0569 & 0.0040 & 0.0063 & -1.8226 & -0.5928 & -0.5166 & -0.0001 & -0.0008 & -0.0000 \\ 0.0000 & 0.0000 & 0.0000 & 1.0000 & -0.0040 & 0.0754 & 0.0000 & 0.0000 & 0.0000 \\ 0.0000 & 0.0000 & 0.0000 & 0.0000 & 0.9986 & 0.0525 & 0.0000 & 0.0000 & 0.0000 \\ 0.0000 & 0.0000 & 0.0000 & 0.0000 & -0.0526 & 1.0015 & 0.0000 & 0.0000 & 0.0000 \end{bmatrix}$$

B Matrix =

$$\begin{bmatrix} 7.1616 & -10.2320 & 1.8096 & 0.0098 \\ -0.3794 & -1.2741 & -10.6350 & 6.1998 \\ -94.9680 & -0.7176 & 0.1265 & 0.0007 \\ 6.3393 & -30.3720 & -154.9300 & -1.2540 \\ 1.0500 & 26.6770 & -8.2320 & 0.4179 \\ 17.3080 & -5.5262 & -28.1860 & -16.7340 \\ 0.0000 & 0.0000 & 0.0000 & 0.0000 \\ 0.0000 & 0.0000 & 0.0000 & 0.0000 \\ 0.0000 & 0.0000 & 0.0000 & 0.0000 \end{bmatrix}$$

BL Configuration - 20 kt

A Matrix =

$$
\begin{bmatrix}
-0.0073 & -0.0069 & 0.0237 & -0.2433 & -0.3252 & -0.0431 & -0.0002 & -9.7883 & 0.0000 \\
0.0144 & -0.0660 & 0.0057 & 0.2732 & -0.2917 & -10.0930 & 9.7816 & 0.0262 & -0.0000 \\
-0.1635 & -0.0171 & -0.4178 & -0.0872 & 10.5060 & -0.0147 & 0.3613 & -0.7158 & 0.0000 \\
0.1308 & -0.2325 & 0.2366 & -10.3530 & -2.6124 & -0.8178 & -0.0007 & -0.0049 & -0.0000 \\
0.0422 & 0.0415 & 0.0179 & 0.2969 & -1.9845 & 0.0103 & 0.0008 & -0.0002 & -0.0000 \\
-0.0108 & 0.0194 & 0.0356 & -1.9892 & -0.4171 & -0.7134 & -0.0001 & -0.0009 & 0.0000 \\
0.0000 & 0.0000 & 0.0000 & 1.0000 & -0.0027 & 0.0731 & 0.0000 & 0.0000 & 0.0000 \\
0.0000 & 0.0000 & 0.0000 & 0.0000 & 0.9993 & 0.0369 & 0.0000 & 0.0000 & 0.0000 \\
0.0000 & 0.0000 & 0.0000 & 0.0000 & -0.0370 & 1.0020 & 0.0000 & 0.0000 & 0.0000
\end{bmatrix}
$$

B Matrix =

$$
\begin{bmatrix}
6.0074 & -9.7112 & 2.0886 & -0.0543 \\
-0.9434 & -1.5592 & -10.5260 & 5.6748 \\
-91.1470 & -6.5480 & 0.1715 & 0.0197 \\
9.3158 & -31.3720 & -154.2200 & -1.1495 \\
3.8329 & 26.7160 & -8.4239 & 0.4164 \\
15.9060 & -6.3149 & -27.6510 & -15.3150 \\
0.0000 & 0.0000 & 0.0000 & 0.0000 \\
0.0000 & 0.0000 & 0.0000 & 0.0000 \\
0.0000 & 0.0000 & 0.0000 & 0.0000
\end{bmatrix}
$$

BL Configuration - 40 kt

A Matrix =

$$
\begin{bmatrix}
-0.0147 & -0.0023 & 0.0294 & -0.1906 & -0.7637 & -0.0408 & -0.0002 & -9.7951 & 0.0000 \\
0.0067 & -0.1008 & 0.0025 & 0.7158 & -0.2396 & -20.2760 & 9.7923 & 0.0145 & -0.0000 \\
-0.1081 & -0.0153 & -0.5919 & -0.1730 & 20.6990 & -0.0259 & 0.2353 & -0.6152 & 0.0000 \\
-0.0368 & -0.1898 & 0.2482 & -10.4790 & -2.1681 & -0.8918 & -0.0007 & -0.0048 & -0.0000 \\
0.0298 & 0.0233 & 0.0256 & 0.2464 & -2.1208 & -0.0018 & 0.0008 & -0.0002 & -0.0000 \\
-0.0423 & 0.0551 & 0.0174 & -2.0001 & -0.2539 & -1.0106 & -0.0001 & -0.0009 & 0.0000 \\
0.0000 & 0.0000 & 0.0000 & 1.0000 & -0.0015 & 0.0628 & 0.0000 & 0.0000 & 0.0000 \\
0.0000 & 0.0000 & 0.0000 & 0.0000 & 0.9997 & 0.0240 & 0.0000 & 0.0000 & 0.0000 \\
0.0000 & 0.0000 & 0.0000 & 0.0000 & -0.0241 & 1.0017 & 0.0000 & 0.0000 & 0.0000
\end{bmatrix}
$$

B Matrix =

$$
\begin{bmatrix}
5.1977 & -9.1505 & 2.5294 & -0.0650 \\
-0.7720 & -1.9332 & -10.3630 & 5.4970 \\
-96.4010 & -12.9480 & 0.2053 & 0.0373 \\
20.8160 & -30.9960 & -153.2700 & -1.0944 \\
7.4274 & 26.9570 & -8.7445 & 0.2890 \\
14.6590 & -6.7807 & -27.1310 & -14.8270 \\
0.0000 & 0.0000 & 0.0000 & 0.0000 \\
0.0000 & 0.0000 & 0.0000 & 0.0000 \\
0.0000 & 0.0000 & 0.0000 & 0.0000
\end{bmatrix}
$$

BL Configuration - 60 kt

A Matrix =

$$
\begin{bmatrix}
-0.0248 & 0.0002 & 0.0304 & -0.1635 & -0.8715 & -0.0350 & -0.0003 & -9.8036 & 0.0000 \\
0.0033 & -0.1359 & -0.0016 & 0.8254 & -0.2125 & -30.4780 & 9.8017 & 0.0088 & -0.0000 \\
-0.0340 & -0.0155 & -0.6981 & -0.2865 & 30.8750 & -0.0352 & 0.1925 & -0.4599 & 0.0000 \\
-0.0508 & -0.1689 & 0.1995 & -10.4650 & -1.9817 & -0.9557 & -0.0007 & -0.0045 & -0.0000 \\
0.0265 & 0.0127 & 0.0297 & 0.2251 & -2.2487 & -0.0071 & 0.0009 & -0.0002 & -0.0000 \\
-0.0333 & 0.0853 & -0.0052 & -1.9493 & -0.1654 & -1.2942 & -0.0002 & -0.0009 & 0.0000 \\
0.0000 & 0.0000 & 0.0000 & 1.0000 & -0.0009 & 0.0469 & 0.0000 & 0.0000 & 0.0000 \\
0.0000 & 0.0000 & 0.0000 & 0.0000 & 0.9998 & 0.0196 & 0.0000 & 0.0000 & 0.0000 \\
0.0000 & 0.0000 & 0.0000 & 0.0000 & -0.0197 & 1.0009 & 0.0000 & 0.0000 & 0.0000
\end{bmatrix}
$$

B Matrix =

$$
\begin{bmatrix}
4.8651 & -8.6224 & 2.7190 & -0.0515 \\
-0.9386 & -2.1559 & -10.3330 & 6.4701 \\
-107.6300 & -20.9680 & 0.2162 & 0.0045 \\
23.1420 & -29.7590 & -152.8900 & -1.2536 \\
10.8590 & 27.5020 & -8.9120 & 0.1035 \\
12.7680 & -7.1380 & -26.7660 & -17.4370 \\
0.0000 & 0.0000 & 0.0000 & 0.0000 \\
0.0000 & 0.0000 & 0.0000 & 0.0000 \\
0.0000 & 0.0000 & 0.0000 & 0.0000
\end{bmatrix}
$$

BL Configuration - 80 kt

A Matrix =

$$\begin{bmatrix} -0.0329 & 0.0014 & 0.0287 & -0.1572 & -0.5158 & -0.0274 & -0.0003 & -9.8109 & 0.0000 \\ 0.0029 & -0.1699 & -0.0049 & 0.4659 & -0.1999 & -40.7070 & 9.8090 & 0.0050 & -0.0000 \\ 0.0069 & -0.0161 & -0.7668 & -0.4147 & 41.1000 & -0.0350 & 0.1954 & -0.2614 & 0.0000 \\ -0.0431 & -0.1654 & 0.1683 & -10.3700 & -1.8731 & -1.0059 & -0.0007 & -0.0041 & -0.0000 \\ 0.0262 & 0.0076 & 0.0340 & 0.2262 & -2.3662 & -0.0096 & 0.0009 & -0.0002 & -0.0000 \\ -0.0276 & 0.1064 & -0.0160 & -1.9021 & -0.0977 & -1.5309 & -0.0002 & -0.0008 & 0.0000 \\ 0.0000 & 0.0000 & 0.0000 & 1.0000 & -0.0005 & 0.0266 & 0.0000 & 0.0000 & 0.0000 \\ 0.0000 & 0.0000 & 0.0000 & 0.0000 & 0.9998 & 0.0199 & 0.0000 & 0.0000 & 0.0000 \\ 0.0000 & 0.0000 & 0.0000 & 0.0000 & -0.0199 & 1.0002 & 0.0000 & 0.0000 & 0.0000 \end{bmatrix}$$

B Matrix =

$$\begin{bmatrix} 4.5154 & -8.1655 & 2.7102 & -0.0474 \\ -1.2875 & -2.3102 & -10.4370 & 7.4623 \\ -117.1700 & -29.6400 & 0.2096 & -0.0135 \\ 22.2140 & -28.2750 & -153.0300 & -1.4309 \\ 14.1510 & 28.3040 & -8.9614 & 0.0171 \\ 11.6050 & -7.4262 & -26.5300 & -20.1030 \\ 0.0000 & 0.0000 & 0.0000 & 0.0000 \\ 0.0000 & 0.0000 & 0.0000 & 0.0000 \\ 0.0000 & 0.0000 & 0.0000 & 0.0000 \end{bmatrix}$$

BL Configuration - 100 kt

A Matrix =

$$\begin{bmatrix} -0.0402 & 0.0019 & 0.0264 & -0.1664 & 0.3989 & -0.0089 & -0.0003 & -9.8144 & 0.0000 \\ 0.0034 & -0.2033 & -0.0078 & -0.4588 & -0.1955 & -50.9400 & 9.8117 & 0.0005 & -0.0000 \\ 0.0319 & -0.0173 & -0.8178 & -0.5597 & 51.3360 & -0.0439 & 0.2306 & -0.0300 & 0.0000 \\ -0.0380 & -0.1728 & 0.1534 & -10.2190 & -1.7965 & -1.0548 & -0.0006 & -0.0035 & -0.0000 \\ 0.0273 & 0.0049 & 0.0384 & 0.2420 & -2.4760 & -0.0116 & 0.0009 & -0.0002 & -0.0000 \\ -0.0268 & 0.1218 & -0.0165 & -1.8623 & -0.0484 & -1.7398 & -0.0002 & -0.0007 & 0.0000 \\ 0.0000 & 0.0000 & 0.0000 & 1.0000 & -0.0001 & 0.0031 & 0.0000 & 0.0000 & 0.0000 \\ 0.0000 & 0.0000 & 0.0000 & 0.0000 & 0.9997 & 0.0235 & 0.0000 & 0.0000 & 0.0000 \\ 0.0000 & 0.0000 & 0.0000 & 0.0000 & -0.0235 & 0.9997 & 0.0000 & 0.0000 & 0.0000 \end{bmatrix}$$

B Matrix =

$$\begin{bmatrix} 4.1911 & -7.7602 & 2.5563 & -0.0544 \\ -1.6804 & -2.4421 & -10.6890 & 8.3242 \\ -125.1900 & -38.5460 & 0.1821 & -0.0225 \\ 21.5460 & -26.3260 & -153.7100 & -1.5912 \\ 17.4110 & 29.3460 & -8.9284 & -0.0194 \\ 11.7240 & -7.4138 & -26.4500 & -22.4220 \\ 0.0000 & 0.0000 & 0.0000 & 0.0000 \\ 0.0000 & 0.0000 & 0.0000 & 0.0000 \\ 0.0000 & 0.0000 & 0.0000 & 0.0000 \end{bmatrix}$$

BL Configuration - 120 kt

A Matrix =

$$\begin{bmatrix} -0.0474 & 0.0021 & 0.0248 & -0.1893 & 1.9112 & 0.0363 & -0.0002 & -9.8119 & 0.0000 \\ 0.0043 & -0.2367 & -0.0104 & -1.9908 & -0.1973 & -61.1500 & 9.8075 & -0.0069 & -0.0000 \\ 0.0499 & -0.0194 & -0.8591 & -0.7353 & 61.5490 & -0.0534 & 0.2944 & 0.2231 & 0.0000 \\ -0.0366 & -0.1894 & 0.1500 & -10.0260 & -1.7490 & -1.0997 & -0.0004 & -0.0026 & -0.0000 \\ 0.0298 & 0.0034 & 0.0423 & 0.2698 & -2.5795 & -0.0141 & 0.0010 & -0.0001 & -0.0000 \\ -0.0295 & 0.1331 & -0.0077 & -1.8291 & -0.0259 & -1.9296 & -0.0001 & -0.0006 & 0.0000 \\ 0.0000 & 0.0000 & 0.0000 & 1.0000 & 0.0007 & -0.0227 & 0.0000 & 0.0000 & 0.0000 \\ 0.0000 & 0.0000 & 0.0000 & 0.0000 & 0.9996 & 0.0300 & 0.0000 & 0.0000 & 0.0000 \\ 0.0000 & 0.0000 & 0.0000 & 0.0000 & -0.0300 & 0.9998 & 0.0000 & 0.0000 & 0.0000 \end{bmatrix}$$

B Matrix =

$$\begin{bmatrix} 4.0325 & -7.3367 & 2.2721 & -0.0734 \\ -2.0739 & -2.5739 & -11.1200 & 9.0956 \\ -132.4000 & -47.5290 & 0.1202 & -0.0290 \\ 21.9500 & -23.7210 & -155.0300 & -1.7391 \\ 20.6220 & 30.5930 & -8.8214 & -0.0320 \\ 13.2910 & -6.8587 & -26.5790 & -24.4990 \\ 0.0000 & 0.0000 & 0.0000 & 0.0000 \\ 0.0000 & 0.0000 & 0.0000 & 0.0000 \\ 0.0000 & 0.0000 & 0.0000 & 0.0000 \end{bmatrix}$$

BL Configuration - 140 kt

A Matrix =

$$\begin{bmatrix}
-0.0550 & 0.0020 & 0.0253 & -0.2251 & 4.0244 & 0.1332 & -0.0002 & -9.8023 & 0.0000 \\
0.0053 & -0.2705 & -0.0129 & -4.1385 & -0.2039 & -71.3060 & 9.7947 & -0.0193 & -0.0000 \\
0.0645 & -0.0223 & -0.8945 & -0.9656 & 71.7070 & -0.0635 & 0.3834 & 0.4891 & 0.0000 \\
-0.0378 & -0.2151 & 0.1553 & -9.8020 & -1.7351 & -1.1421 & -0.0000 & -0.0016 & -0.0000 \\
0.0335 & 0.0026 & 0.0450 & 0.3085 & -2.6768 & -0.0172 & 0.0010 & -0.0001 & -0.0000 \\
-0.0352 & 0.1411 & 0.0102 & -1.8031 & -0.0403 & -2.1065 & -0.0001 & -0.0004 & 0.0000 \\
0.0000 & 0.0000 & 0.0000 & 1.0000 & 0.0020 & -0.0499 & 0.0000 & 0.0000 & 0.0000 \\
0.0000 & 0.0000 & 0.0000 & 0.0000 & 0.9992 & 0.0391 & 0.0000 & 0.0000 & 0.0000 \\
0.0000 & 0.0000 & 0.0000 & 0.0000 & -0.0392 & 1.0005 & 0.0000 & 0.0000 & 0.0000
\end{bmatrix}$$

B Matrix =

$$\begin{bmatrix}
4.2036 & -6.7739 & 1.8519 & -0.1077 \\
-2.4504 & -2.7194 & -11.7650 & 9.8161 \\
-139.2800 & -56.5000 & 0.0194 & -0.0348 \\
23.6300 & -20.3100 & -157.1000 & -1.8817 \\
23.7230 & 31.9910 & -8.6356 & -0.0272 \\
16.4750 & -5.4953 & -26.9800 & -26.4420 \\
0.0000 & 0.0000 & 0.0000 & 0.0000 \\
0.0000 & 0.0000 & 0.0000 & 0.0000 \\
0.0000 & 0.0000 & 0.0000 & 0.0000
\end{bmatrix}$$

D.2 HCH Configuration Matrices

The structure of the HCH configuration's control matrix and vector are as follows

$$\mathbf{B} = \left[\begin{array}{c:c:c:c:c}
X_{\theta_0} & X_{\theta_{1s}} & X_{\theta_{1c}} & X_{\bar{\theta}_{prop}} & X_{\theta_{diff}} \\ \hdashline
Y_{\theta_0} & Y_{\theta_{1s}} & Y_{\theta_{1c}} & Y_{\bar{\theta}_{prop}} & Y_{\theta_{diff}} \\ \hdashline
Z_{\theta_0} & Z_{\theta_{1s}} & Z_{\theta_{1c}} & Z_{\bar{\theta}_{prop}} & Z_{\theta_{diff}} \\ \hdashline
L_{\theta_0} & L_{\theta_{1s}} & L_{\theta_{1c}} & L_{\bar{\theta}_{prop}} & L_{\theta_{diff}} \\ \hdashline
M_{\theta_0} & M_{\theta_{1s}} & M_{\theta_{1c}} & M_{\bar{\theta}_{prop}} & M_{\theta_{diff}} \\ \hdashline
N_{\theta_0} & N_{\theta_{1s}} & N_{\theta_{1c}} & N_{\bar{\theta}_{prop}} & N_{\theta_{diff}} \\ \hdashline
0 & 0 & 0 & 0 & 0 \\ \hdashline
0 & 0 & 0 & 0 & 0 \\ \hdashline
0 & 0 & 0 & 0 & 0
\end{array}\right] \quad \text{and} \quad \mathbf{u} = \begin{bmatrix} \theta_0 \\ \theta_{1s} \\ \theta_{1c} \\ \bar{\theta}_{prop} \\ \theta_{diff} \end{bmatrix} \tag{D.1}$$

HCH Configuration - Hover

A Matrix =

$$
\begin{bmatrix}
-0.0860 & -0.0169 & 0.0035 & -0.3063 & 0.4626 & -0.0837 & -0.0003 & -9.7857 & 0.0000 \\
0.0200 & -0.0272 & 0.0014 & -0.4080 & -0.4260 & -0.5159 & 9.7857 & -0.0021 & 0.0000 \\
0.0081 & -0.0013 & -0.3039 & -0.0075 & 0.5154 & -0.0015 & -0.0238 & -0.7512 & 0.0000 \\
0.4485 & -0.4161 & 0.0237 & -11.3480 & -4.9259 & -0.3767 & -0.0010 & -0.0075 & -0.0000 \\
0.0574 & 0.0743 & 0.0110 & 0.3561 & -1.9459 & -0.0017 & 0.0013 & -0.0004 & -0.0000 \\
0.0484 & -0.0714 & 0.0064 & -1.8893 & -0.9808 & -0.3826 & -0.0001 & -0.0013 & 0.0000 \\
0.0000 & 0.0000 & 0.0000 & 1.0000 & 0.0002 & 0.0768 & 0.0000 & 0.0000 & 0.0000 \\
0.0000 & 0.0000 & 0.0000 & 0.0000 & 1.0000 & -0.0024 & 0.0000 & 0.0000 & 0.0000 \\
0.0000 & 0.0000 & 0.0000 & 0.0000 & 0.0024 & 1.0029 & 0.0000 & 0.0000 & 0.0000
\end{bmatrix}
$$

B Matrix =

$$
\begin{bmatrix}
1.9692 & -11.2850 & 3.0828 & 8.9171 & 0.7810 \\
-0.0766 & -1.4605 & -14.8700 & -0.0026 & -0.0203 \\
-89.4550 & -0.2900 & 0.6799 & -0.0001 & -0.0001 \\
13.7490 & -30.9300 & -234.5500 & -0.3710 & -8.8082 \\
3.6743 & 28.0410 & -12.5190 & 0.4020 & -0.1629 \\
19.4830 & -5.2625 & -40.3710 & -1.0994 & -14.0400 \\
0.0000 & 0.0000 & 0.0000 & 0.0000 & 0.0000 \\
0.0000 & 0.0000 & 0.0000 & 0.0000 & 0.0000 \\
0.0000 & 0.0000 & 0.0000 & 0.0000 & 0.0000
\end{bmatrix}
$$

HCH Configuration - 20 kt

A Matrix =

$$
\begin{bmatrix}
-0.0736 & -0.0161 & -0.0127 & -0.2798 & -0.1870 & -0.0313 & -0.0003 & -9.7895 & 0.0000 \\
0.0113 & -0.0522 & 0.0127 & 0.2404 & -0.3766 & -10.2310 & 9.7889 & -0.0082 & 0.0000 \\
-0.1780 & 0.0040 & -0.4006 & -0.0882 & 10.7620 & -0.0011 & -0.1101 & -0.6992 & 0.0000 \\
0.2864 & -0.3851 & 0.3602 & -11.5060 & -4.3430 & -0.5716 & -0.0012 & -0.0078 & -0.0000 \\
0.0556 & 0.0733 & 0.0330 & 0.3326 & -2.0937 & -0.0059 & 0.0013 & -0.0004 & -0.0000 \\
0.0290 & -0.0620 & 0.0566 & -2.0663 & -0.7804 & -0.4972 & -0.0002 & -0.0014 & 0.0000 \\
0.0000 & 0.0000 & 0.0000 & 1.0000 & 0.0008 & 0.0714 & 0.0000 & 0.0000 & 0.0000 \\
0.0000 & 0.0000 & 0.0000 & 0.0000 & 0.9999 & -0.0113 & 0.0000 & 0.0000 & 0.0000 \\
0.0000 & 0.0000 & 0.0000 & 0.0000 & 0.0113 & 1.0025 & 0.0000 & 0.0000 & 0.0000
\end{bmatrix}
$$

B Matrix =

$$\begin{bmatrix} -0.1023 & -11.1140 & 3.1693 & 8.8473 & 1.0127 \\ -0.4992 & -1.7070 & -14.2740 & -0.0016 & -0.0181 \\ -88.2450 & -5.8481 & 15.5700 & -0.0023 & -0.0011 \\ 20.8350 & -32.1580 & -228.8100 & 0.1960 & -9.0968 \\ 6.8104 & 28.5030 & -13.3080 & 0.4114 & -0.1637 \\ 18.7380 & -6.1102 & -38.5410 & -1.3099 & -13.9830 \\ 0.0000 & 0.0000 & 0.0000 & 0.0000 & 0.0000 \\ 0.0000 & 0.0000 & 0.0000 & 0.0000 & 0.0000 \\ 0.0000 & 0.0000 & 0.0000 & 0.0000 & 0.0000 \end{bmatrix}$$

HCH Configuration - 40 kt

A Matrix =

$$\begin{bmatrix} -0.0636 & -0.0127 & -0.0107 & -0.2336 & -0.6303 & 0.0057 & -0.0004 & -9.7960 & -0.0000 \\ 0.0001 & -0.0764 & 0.0118 & 0.6915 & -0.2721 & -20.4700 & 9.7948 & -0.0097 & -0.0000 \\ -0.1619 & 0.0024 & -0.5797 & -0.1869 & 21.2100 & -0.0012 & -0.1515 & -0.6016 & -0.0000 \\ 0.0471 & -0.2938 & 0.4502 & -11.4310 & -2.9862 & -0.6136 & -0.0015 & -0.0080 & 0.0000 \\ 0.0438 & 0.0603 & 0.0511 & 0.2795 & -2.2494 & -0.0097 & 0.0013 & -0.0004 & 0.0000 \\ -0.0118 & -0.0413 & 0.0513 & -2.1745 & -0.4321 & -0.5867 & -0.0003 & -0.0015 & 0.0000 \\ 0.0000 & 0.0000 & 0.0000 & 1.0000 & 0.0010 & 0.0614 & 0.0000 & 0.0000 & 0.0000 \\ 0.0000 & 0.0000 & 0.0000 & 0.0000 & 0.9999 & -0.0155 & 0.0000 & 0.0000 & 0.0000 \\ 0.0000 & 0.0000 & 0.0000 & 0.0000 & 0.0155 & 1.0018 & 0.0000 & 0.0000 & 0.0000 \end{bmatrix}$$

B Matrix =

$$\begin{bmatrix} -1.9636 & -10.9560 & 2.8520 & 9.2723 & 0.7853 \\ -0.8036 & -2.1528 & -12.0610 & -0.0008 & -0.0135 \\ -94.4020 & -12.4100 & 25.7850 & -0.0055 & -0.0003 \\ 26.9090 & -32.9940 & -189.5900 & 1.2552 & -9.9503 \\ 10.3920 & 29.1390 & -12.6970 & 0.4563 & -0.2048 \\ 16.0220 & -7.0408 & -30.4040 & -0.7811 & -14.7240 \\ 0.0000 & 0.0000 & 0.0000 & 0.0000 & 0.0000 \\ 0.0000 & 0.0000 & 0.0000 & 0.0000 & 0.0000 \\ 0.0000 & 0.0000 & 0.0000 & 0.0000 & 0.0000 \end{bmatrix}$$

HCH Configuration - 60 kt

A Matrix =

$$
\begin{bmatrix}
-0.0768 & -0.0057 & -0.0147 & -0.1926 & -0.7062 & 0.0157 & -0.0004 & -9.8041 & -0.0000 \\
-0.0028 & -0.1011 & 0.0043 & 0.7875 & -0.2069 & -30.7280 & 9.8030 & -0.0073 & 0.0000 \\
-0.1076 & -0.0024 & -0.7296 & -0.2897 & 31.3710 & -0.0016 & -0.1495 & -0.4489 & -0.0000 \\
-0.0502 & -0.2231 & 0.3512 & -11.7720 & -2.1942 & -0.4902 & -0.0017 & -0.0078 & 0.0000 \\
0.0335 & 0.0354 & 0.0581 & 0.2191 & -2.3768 & -0.0116 & 0.0013 & -0.0004 & 0.0000 \\
-0.0270 & -0.0236 & 0.0135 & -2.2172 & -0.2121 & -0.7038 & -0.0004 & -0.0015 & 0.0000 \\
0.0000 & 0.0000 & 0.0000 & 1.0000 & 0.0007 & 0.0458 & 0.0000 & 0.0000 & 0.0000 \\
0.0000 & 0.0000 & 0.0000 & 0.0000 & 0.9999 & -0.0152 & 0.0000 & 0.0000 & 0.0000 \\
0.0000 & 0.0000 & 0.0000 & 0.0000 & 0.0153 & 1.0009 & 0.0000 & 0.0000 & 0.0000
\end{bmatrix}
$$

B Matrix =

$$
\begin{bmatrix}
-2.2167 & -10.6310 & 3.3538 & 9.9971 & 0.4646 \\
-1.0729 & -2.4676 & -10.9120 & -0.0009 & -0.0097 \\
-102.1500 & -19.7360 & 25.0810 & -0.0087 & 0.0014 \\
30.6470 & -31.6750 & -166.9100 & 2.5433 & -11.0620 \\
14.2270 & 29.6500 & -11.9650 & 0.5223 & -0.2544 \\
13.2150 & -7.6666 & -25.7580 & -0.0894 & -15.9350 \\
0.0000 & 0.0000 & 0.0000 & 0.0000 & 0.0000 \\
0.0000 & 0.0000 & 0.0000 & 0.0000 & 0.0000 \\
0.0000 & 0.0000 & 0.0000 & 0.0000 & 0.0000
\end{bmatrix}
$$

HCH Configuration - 80 kt

A Matrix =

$$
\begin{bmatrix}
-0.0883 & -0.0017 & -0.0214 & -0.1687 & -0.3648 & 0.0095 & -0.0004 & -9.8109 & -0.0000 \\
-0.0020 & -0.1273 & -0.0019 & 0.4558 & -0.1719 & -40.9980 & 9.8101 & -0.0039 & -0.0000 \\
-0.0816 & -0.0037 & -0.8615 & -0.3848 & 41.5330 & -0.0019 & -0.1301 & -0.2602 & -0.0000 \\
-0.0621 & -0.1897 & 0.2633 & -12.4560 & -1.8760 & -0.3218 & -0.0018 & -0.0073 & 0.0000 \\
0.0291 & 0.0200 & 0.0624 & 0.1798 & -2.4868 & -0.0108 & 0.0013 & -0.0004 & 0.0000 \\
-0.0280 & -0.0125 & -0.0135 & -2.2821 & -0.1006 & -0.8149 & -0.0004 & -0.0014 & 0.0000 \\
0.0000 & 0.0000 & 0.0000 & 1.0000 & 0.0004 & 0.0265 & 0.0000 & 0.0000 & 0.0000 \\
0.0000 & 0.0000 & 0.0000 & 0.0000 & 0.9999 & -0.0133 & 0.0000 & 0.0000 & 0.0000 \\
0.0000 & 0.0000 & 0.0000 & 0.0000 & 0.0133 & 1.0003 & 0.0000 & 0.0000 & 0.0000
\end{bmatrix}
$$

B Matrix =

$$\begin{bmatrix} -2.5403 & -10.2160 & 3.6707 & 10.6900 & 0.3000 \\ -1.5324 & -2.6644 & -10.3840 & -0.0011 & -0.0070 \\ -108.2400 & -27.2650 & 23.4820 & -0.0093 & 0.0026 \\ 29.1940 & -30.0500 & -159.0100 & 3.8074 & -12.0140 \\ 17.8640 & 30.3700 & -11.6400 & 0.5865 & -0.2886 \\ 10.5450 & -8.2209 & -24.1580 & 0.3582 & -17.0760 \\ 0.0000 & 0.0000 & 0.0000 & 0.0000 & 0.0000 \\ 0.0000 & 0.0000 & 0.0000 & 0.0000 & 0.0000 \\ 0.0000 & 0.0000 & 0.0000 & 0.0000 & 0.0000 \end{bmatrix}$$

HCH Configuration - 100 kt

A Matrix =

$$\begin{bmatrix} -0.0970 & 0.0003 & -0.0287 & -0.1590 & 0.2115 & 0.0006 & -0.0004 & -9.8139 & -0.0000 \\ -0.0008 & -0.1545 & -0.0069 & -0.1210 & -0.1472 & -51.2620 & 9.8133 & -0.0015 & 0.0000 \\ -0.0681 & -0.0047 & -0.9774 & -0.4823 & 51.7040 & -0.0024 & -0.1090 & -0.0955 & -0.0000 \\ -0.0609 & -0.1750 & 0.2094 & -13.1120 & -1.6847 & -0.1970 & -0.0018 & -0.0066 & -0.0000 \\ 0.0272 & 0.0121 & 0.0668 & 0.1597 & -2.5898 & -0.0100 & 0.0012 & -0.0004 & 0.0000 \\ -0.0275 & -0.0048 & -0.0276 & -2.3468 & -0.0273 & -0.9237 & -0.0004 & -0.0012 & 0.0000 \\ 0.0000 & 0.0000 & 0.0000 & 1.0000 & 0.0001 & 0.0097 & 0.0000 & 0.0000 & 0.0000 \\ 0.0000 & 0.0000 & 0.0000 & 0.0000 & 0.9999 & -0.0111 & 0.0000 & 0.0000 & 0.0000 \\ 0.0000 & 0.0000 & 0.0000 & 0.0000 & 0.0111 & 1.0000 & 0.0000 & 0.0000 & 0.0000 \end{bmatrix}$$

B Matrix =

$$\begin{bmatrix} -2.9095 & -9.7856 & 3.7303 & 11.3190 & 0.2219 \\ -2.1154 & -2.8496 & -10.0310 & -0.0015 & -0.0049 \\ -113.9300 & -35.0210 & 21.9450 & -0.0061 & 0.0032 \\ 26.6310 & -28.4130 & -155.5800 & 5.1113 & -12.8010 \\ 21.4020 & 31.3700 & -11.4360 & 0.6489 & -0.3128 \\ 8.5702 & -8.7009 & -23.5040 & 0.6754 & -18.0970 \\ 0.0000 & 0.0000 & 0.0000 & 0.0000 & 0.0000 \\ 0.0000 & 0.0000 & 0.0000 & 0.0000 & 0.0000 \\ 0.0000 & 0.0000 & 0.0000 & 0.0000 & 0.0000 \end{bmatrix}$$

HCH Configuration - 120 kt

A Matrix =

$$\begin{bmatrix}
-0.1037 & 0.0014 & -0.0356 & -0.1540 & 0.7049 & -0.0054 & -0.0004 & -9.8144 & -0.0000 \\
0.0003 & -0.1822 & -0.0117 & -0.6213 & -0.1221 & -61.5170 & 9.8140 & -0.0003 & 0.0000 \\
-0.0621 & -0.0065 & -1.0828 & -0.5860 & 61.8820 & -0.0035 & -0.0896 & 0.0039 & -0.0000 \\
-0.0593 & -0.1671 & 0.1773 & -13.7230 & -1.5109 & -0.0910 & -0.0017 & -0.0059 & -0.0000 \\
0.0259 & 0.0080 & 0.0716 & 0.1480 & -2.6920 & -0.0090 & 0.0012 & -0.0003 & 0.0000 \\
-0.0276 & 0.0016 & -0.0345 & -2.4180 & 0.0318 & -1.0285 & -0.0004 & -0.0011 & 0.0000 \\
0.0000 & 0.0000 & 0.0000 & 1.0000 & -0.0000 & -0.0004 & 0.0000 & 0.0000 & 0.0000 \\
0.0000 & 0.0000 & 0.0000 & 0.0000 & 1.0000 & -0.0091 & 0.0000 & 0.0000 & 0.0000 \\
0.0000 & 0.0000 & 0.0000 & 0.0000 & 0.0091 & 1.0000 & 0.0000 & 0.0000 & 0.0000
\end{bmatrix}$$

B Matrix =

$$\begin{bmatrix}
-3.1786 & -9.2524 & 3.6397 & 11.9070 & 0.1798 \\
-2.8480 & -3.1035 & -9.6551 & -0.0024 & -0.0025 \\
-119.4800 & -42.9190 & 20.7450 & -0.0013 & 0.0033 \\
24.1240 & -26.7890 & -153.2800 & 6.5165 & -13.5050 \\
24.9410 & 32.5980 & -11.2850 & 0.7121 & -0.3329 \\
6.9182 & -9.1263 & -23.0860 & 0.9530 & -19.0480 \\
0.0000 & 0.0000 & 0.0000 & 0.0000 & 0.0000 \\
0.0000 & 0.0000 & 0.0000 & 0.0000 & 0.0000 \\
0.0000 & 0.0000 & 0.0000 & 0.0000 & 0.0000
\end{bmatrix}$$

HCH Configuration - 140 kt

A Matrix =

$$\begin{bmatrix}
-0.1094 & 0.0021 & -0.0429 & -0.1439 & 1.0331 & -0.0086 & -0.0003 & -9.8143 & 0.0000 \\
0.0012 & -0.2101 & -0.0175 & -0.9617 & -0.0870 & -71.7680 & 9.8140 & 0.0001 & 0.0000 \\
-0.0632 & -0.0090 & -1.1848 & -0.6937 & 72.0590 & -0.0050 & -0.0726 & 0.0536 & 0.0000 \\
-0.0591 & -0.1649 & 0.1537 & -14.5460 & -1.2506 & 0.0382 & -0.0016 & -0.0053 & -0.0000 \\
0.0250 & 0.0055 & 0.0789 & 0.1187 & -2.8216 & -0.0074 & 0.0012 & -0.0003 & -0.0000 \\
-0.0283 & 0.0069 & -0.0392 & -2.5290 & 0.1062 & -1.1242 & -0.0004 & -0.0010 & 0.0000 \\
0.0000 & 0.0000 & 0.0000 & 1.0000 & -0.0000 & -0.0055 & 0.0000 & 0.0000 & 0.0000 \\
0.0000 & 0.0000 & 0.0000 & 0.0000 & 1.0000 & -0.0074 & 0.0000 & 0.0000 & 0.0000 \\
0.0000 & 0.0000 & 0.0000 & 0.0000 & 0.0074 & 1.0000 & 0.0000 & 0.0000 & 0.0000
\end{bmatrix}$$

B Matrix =

$$\begin{bmatrix} -3.3672 & -8.4782 & 3.4973 & 12.4750 & 0.1507 \\ -3.8398 & -3.5402 & -9.0756 & -0.0047 & 0.0020 \\ -121.9800 & -50.1890 & 19.3800 & 0.0035 & 0.0032 \\ 20.4510 & -26.1610 & -150.2300 & 8.0223 & -14.1540 \\ 28.7700 & 34.0330 & -11.3910 & 0.7821 & -0.3605 \\ 4.8967 & -9.7318 & -22.4970 & 1.2284 & -19.9580 \\ 0.0000 & 0.0000 & 0.0000 & 0.0000 & 0.0000 \\ 0.0000 & 0.0000 & 0.0000 & 0.0000 & 0.0000 \\ 0.0000 & 0.0000 & 0.0000 & 0.0000 & 0.0000 \end{bmatrix}$$

HCH Configuration - 160 kt

A Matrix =

$$\begin{bmatrix} -0.1147 & 0.0028 & -0.0520 & -0.1242 & 1.3611 & -0.0107 & -0.0003 & -9.8140 & -0.0000 \\ 0.0020 & -0.2385 & -0.0252 & -1.3107 & -0.0335 & -82.0180 & 9.8137 & 0.0002 & -0.0000 \\ -0.0728 & -0.0120 & -1.2950 & -0.8017 & 82.2190 & -0.0070 & -0.0554 & 0.0928 & -0.0000 \\ -0.0608 & -0.1711 & 0.1282 & -15.8530 & -0.7845 & 0.2268 & -0.0017 & -0.0049 & 0.0000 \\ 0.0249 & 0.0034 & 0.0923 & 0.0429 & -3.0051 & -0.0044 & 0.0013 & -0.0003 & 0.0000 \\ -0.0296 & 0.0109 & -0.0435 & -2.7108 & 0.2234 & -1.2076 & -0.0005 & -0.0009 & 0.0000 \\ 0.0000 & 0.0000 & 0.0000 & 1.0000 & -0.0001 & -0.0095 & 0.0000 & 0.0000 & 0.0000 \\ 0.0000 & 0.0000 & 0.0000 & 0.0000 & 1.0000 & -0.0056 & 0.0000 & 0.0000 & 0.0000 \\ 0.0000 & 0.0000 & 0.0000 & 0.0000 & 0.0056 & 1.0000 & 0.0000 & 0.0000 & 0.0000 \end{bmatrix}$$

B Matrix =

$$\begin{bmatrix} -3.4477 & -7.3252 & 3.2771 & 13.0350 & 0.1261 \\ -5.1824 & -4.2615 & -8.1550 & -0.0105 & 0.0106 \\ -118.6100 & -55.6600 & 17.3680 & 0.0098 & 0.0032 \\ 13.8300 & -27.6440 & -145.1000 & 9.5852 & -14.7160 \\ 33.3880 & 35.8610 & -12.0070 & 0.8692 & -0.4080 \\ 2.1246 & -10.6570 & -21.4890 & 1.5002 & -20.8380 \\ 0.0000 & 0.0000 & 0.0000 & 0.0000 & 0.0000 \\ 0.0000 & 0.0000 & 0.0000 & 0.0000 & 0.0000 \\ 0.0000 & 0.0000 & 0.0000 & 0.0000 & 0.0000 \end{bmatrix}$$

HCH Configuration - 180 kt

A Matrix =

$$\begin{bmatrix}
-0.1194 & 0.0033 & -0.0614 & -0.0989 & 1.7148 & -0.0096 & -0.0003 & -9.8135 & -0.0000 \\
0.0031 & -0.2666 & -0.0350 & -1.7045 & 0.0417 & -92.2670 & 9.8134 & 0.0000 & -0.0000 \\
-0.0957 & -0.0152 & -1.4374 & -0.9099 & 92.3500 & -0.0095 & -0.0210 & 0.1321 & 0.0000 \\
-0.0612 & -0.1787 & 0.0925 & -17.7810 & -0.0200 & 0.5225 & -0.0016 & -0.0042 & -0.0000 \\
0.0238 & 0.0012 & 0.1151 & -0.1091 & -3.2367 & 0.0029 & 0.0014 & -0.0003 & -0.0000 \\
-0.0303 & 0.0148 & -0.0429 & -2.9732 & 0.3583 & -1.2730 & -0.0005 & -0.0009 & -0.0000 \\
0.0000 & 0.0000 & 0.0000 & 1.0000 & -0.0000 & -0.0135 & 0.0000 & 0.0000 & 0.0000 \\
0.0000 & 0.0000 & 0.0000 & 0.0000 & 1.0000 & -0.0021 & 0.0000 & 0.0000 & 0.0000 \\
0.0000 & 0.0000 & 0.0000 & 0.0000 & 0.0021 & 1.0001 & 0.0000 & 0.0000 & 0.0000
\end{bmatrix}$$

B Matrix =

$$\begin{bmatrix}
-2.7618 & -5.2892 & 2.7365 & 13.6080 & 0.0912 \\
-6.8105 & -5.2118 & -6.5929 & -0.0219 & 0.0252 \\
-109.7700 & -58.4560 & 14.9460 & 0.0195 & 0.0022 \\
2.9838 & -31.6850 & -136.3600 & 11.1800 & -15.1700 \\
39.2030 & 38.3490 & -13.2320 & 0.9851 & -0.4834 \\
-1.1218 & -11.4080 & -20.0190 & 1.7755 & -21.7120 \\
0.0000 & 0.0000 & 0.0000 & 0.0000 & 0.0000 \\
0.0000 & 0.0000 & 0.0000 & 0.0000 & 0.0000 \\
0.0000 & 0.0000 & 0.0000 & 0.0000 & 0.0000
\end{bmatrix}$$

HCH Configuration - 200 kt

A Matrix =

$$\begin{bmatrix}
-0.1228 & 0.0028 & -0.0616 & -0.0877 & 1.7450 & 0.0117 & -0.0001 & -9.8133 & -0.0000 \\
0.0053 & -0.2908 & -0.0408 & -1.8120 & 0.0931 & -102.5200 & 9.8126 & -0.0018 & -0.0000 \\
-0.1474 & -0.0189 & -1.6753 & -1.0425 & 102.4100 & -0.0126 & 0.1092 & 0.1492 & 0.0000 \\
-0.0440 & -0.1425 & 0.0515 & -20.6340 & 1.0263 & 1.0616 & 0.0005 & -0.0014 & -0.0000 \\
0.0155 & 0.0010 & 0.1518 & -0.4003 & -3.4681 & 0.0267 & 0.0015 & -0.0001 & 0.0000 \\
-0.0246 & 0.0257 & -0.0056 & -3.3753 & 0.2929 & -1.2993 & -0.0000 & -0.0004 & 0.0000 \\
0.0000 & 0.0000 & 0.0000 & 1.0000 & 0.0002 & -0.0152 & 0.0000 & 0.0000 & 0.0000 \\
0.0000 & 0.0000 & 0.0000 & 0.0000 & 0.9999 & 0.0111 & 0.0000 & 0.0000 & 0.0000 \\
0.0000 & 0.0000 & 0.0000 & 0.0000 & -0.0111 & 1.0001 & 0.0000 & 0.0000 & 0.0000
\end{bmatrix}$$

B Matrix =

$$\begin{bmatrix}
1.2012 & -0.4128 & 1.1239 & 14.2510 & -0.0000 \\
-7.4325 & -5.3048 & -3.3685 & -0.0329 & 0.0375 \\
-95.6910 & -57.0400 & 12.3500 & 0.0354 & -0.0080 \\
-10.8840 & -36.6400 & -120.2900 & 12.8300 & -15.5690 \\
46.2850 & 41.5850 & -15.0670 & 1.1447 & -0.5964 \\
-1.2075 & -8.4804 & -18.8450 & 2.1248 & -22.6760 \\
0.0000 & 0.0000 & 0.0000 & 0.0000 & 0.0000 \\
0.0000 & 0.0000 & 0.0000 & 0.0000 & 0.0000 \\
0.0000 & 0.0000 & 0.0000 & 0.0000 & 0.0000
\end{bmatrix}$$

D.3 CCH Configuration Matrices

The structure of the CCH configuration's control matrix and vector are as follows

$$\mathbf{B} = \begin{bmatrix}
X_{\bar{\theta}_0} & X_{\theta_{diff}} & X_{\theta_{1s}} & X_{\theta_{1c}} & X_{\theta_{prop}} & X_{\theta_{1c\ diff}} \\
Y_{\bar{\theta}_0} & Y_{\theta_{diff}} & Y_{\theta_{1s}} & Y_{\theta_{1c}} & Y_{\theta_{prop}} & Y_{\theta_{1c\ diff}} \\
Z_{\bar{\theta}_0} & Z_{\theta_{diff}} & Z_{\theta_{1s}} & Z_{\theta_{1c}} & Z_{\theta_{prop}} & Z_{\theta_{1c\ diff}} \\
L_{\bar{\theta}_0} & L_{\theta_{diff}} & L_{\theta_{1s}} & L_{\theta_{1c}} & L_{\theta_{prop}} & L_{\theta_{1c\ diff}} \\
M_{\bar{\theta}_0} & M_{\theta_{diff}} & M_{\theta_{1s}} & M_{\theta_{1c}} & M_{\theta_{prop}} & M_{\theta_{1c\ diff}} \\
N_{\bar{\theta}_0} & N_{\theta_{diff}} & N_{\theta_{1s}} & N_{\theta_{1c}} & N_{\theta_{prop}} & N_{\theta_{1c\ diff}} \\
0 & 0 & 0 & 0 & 0 & 0 \\
0 & 0 & 0 & 0 & 0 & 0 \\
0 & 0 & 0 & 0 & 0 & 0
\end{bmatrix} \quad \text{and} \quad \mathbf{u} = \begin{bmatrix} \bar{\theta}_0 \\ \theta_{diff} \\ \theta_{1s} \\ \theta_{1c} \\ \theta_{prop} \\ \theta_{1c_{diff}} \end{bmatrix} \tag{D.2}$$

CCH Configuration - Hover

A Matrix =

$$\begin{bmatrix}
-0.0279 & -0.0121 & 0.0152 & 0.0722 & 0.3080 & 0.0083 & -0.0002 & -9.7842 & 0.0000 \\
-0.0012 & -0.0263 & -0.0001 & -0.3227 & 0.0560 & -0.1511 & 9.7842 & -0.0002 & 0.0000 \\
0.0137 & -0.0007 & -0.2300 & 0.0048 & 0.1656 & 0.0002 & -0.0007 & -0.7698 & 0.0000 \\
0.0013 & -0.4002 & -0.0013 & -17.6460 & 0.0640 & -1.2420 & -0.0067 & -0.0021 & -0.0000 \\
0.1106 & 0.0874 & 0.0099 & 0.0816 & -3.3653 & 0.0082 & 0.0004 & -0.0012 & -0.0000 \\
0.0005 & -0.0732 & -0.0047 & -3.2005 & 0.0135 & -0.2227 & -0.0011 & -0.0004 & 0.0000 \\
0.0000 & 0.0000 & 0.0000 & 1.0000 & 0.0000 & 0.0787 & 0.0000 & 0.0000 & 0.0000 \\
0.0000 & 0.0000 & 0.0000 & 0.0000 & 1.0000 & -0.0001 & 0.0000 & 0.0000 & 0.0000 \\
0.0000 & 0.0000 & 0.0000 & 0.0000 & 0.0001 & 1.0031 & 0.0000 & 0.0000 & 0.0000
\end{bmatrix}$$

B Matrix =

$$\begin{bmatrix}
5.0417 & -1.4543 & -10.3930 & 1.4076 & 2.7574 & 1.4016 \\
-0.0101 & 0.0055 & -1.0392 & -10.6440 & 0.0003 & -0.9084 \\
-69.9200 & 19.9170 & -0.8193 & 0.0984 & -0.0000 & 0.0980 \\
-0.1712 & 8.3586 & -2.7222 & -192.8900 & 0.1532 & -3.9127 \\
0.6136 & -0.3758 & 36.1900 & -0.7052 & 0.0005 & -15.3360 \\
-0.3505 & 21.0950 & -0.5015 & -34.9450 & 0.0240 & -0.6899 \\
0.0000 & 0.0000 & 0.0000 & 0.0000 & 0.0000 & 0.0000 \\
0.0000 & 0.0000 & 0.0000 & 0.0000 & 0.0000 & 0.0000 \\
0.0000 & 0.0000 & 0.0000 & 0.0000 & 0.0000 & 0.0000
\end{bmatrix}$$

CCH Configuration - 20 kt

A Matrix =

$$\begin{bmatrix}
-0.0305 & -0.0111 & 0.0155 & 0.0721 & -0.4058 & 0.0165 & -0.0002 & -9.7867 & 0.0000 \\
-0.0023 & -0.0518 & -0.0002 & 0.3890 & 0.0566 & -10.2500 & 9.7867 & -0.0015 & -0.0000 \\
-0.1477 & 0.0005 & -0.3093 & 0.0228 & 10.4900 & -0.0006 & -0.0171 & -0.7376 & 0.0000 \\
-0.0340 & -0.3771 & 0.0166 & -17.7810 & 0.1397 & -1.2924 & -0.0067 & -0.0022 & -0.0000 \\
0.0994 & 0.0780 & 0.0353 & 0.0668 & -3.4918 & 0.0067 & 0.0004 & -0.0012 & -0.0000 \\
-0.0119 & -0.0616 & -0.0049 & -3.3889 & 0.0584 & -0.3574 & -0.0012 & -0.0004 & 0.0000 \\
0.0000 & 0.0000 & 0.0000 & 1.0000 & 0.0001 & 0.0754 & 0.0000 & 0.0000 & 0.0000 \\
0.0000 & 0.0000 & 0.0000 & 0.0000 & 1.0000 & -0.0017 & 0.0000 & 0.0000 & 0.0000 \\
0.0000 & 0.0000 & 0.0000 & 0.0000 & 0.0017 & 1.0028 & 0.0000 & 0.0000 & 0.0000
\end{bmatrix}$$

B Matrix =

$$\begin{bmatrix}
4.0095 & -1.7643 & -9.8193 & 1.4266 & 3.2469 & 1.6814 \\
-0.1865 & -1.5935 & -1.0598 & -10.3160 & 0.0003 & -0.9882 \\
-67.4300 & 22.8840 & -5.8696 & 0.0985 & -0.0008 & 0.1179 \\
-0.2555 & 0.1509 & -2.8508 & -191.4400 & 0.3066 & -4.0278 \\
4.8717 & -0.6608 & 36.2300 & -0.7275 & 0.0026 & -15.5430 \\
-0.2929 & 17.7580 & -0.6147 & -33.7910 & 0.0532 & -0.6209 \\
0.0000 & 0.0000 & 0.0000 & 0.0000 & 0.0000 & 0.0000 \\
0.0000 & 0.0000 & 0.0000 & 0.0000 & 0.0000 & 0.0000 \\
0.0000 & 0.0000 & 0.0000 & 0.0000 & 0.0000 & 0.0000
\end{bmatrix}$$

CCH Configuration - 40 kt

A Matrix =

$$\begin{bmatrix}
-0.0391 & -0.0090 & 0.0181 & 0.0673 & -0.8972 & 0.0341 & -0.0002 & -9.7919 & 0.0000 \\
-0.0022 & -0.0771 & -0.0019 & 0.9028 & 0.0506 & -20.4910 & 9.7918 & -0.0022 & 0.0000 \\
-0.1583 & 0.0049 & -0.4527 & 0.0584 & 20.7640 & -0.0001 & -0.0289 & -0.6641 & 0.0000 \\
-0.0431 & -0.3349 & -0.0217 & -17.9190 & 0.1926 & -1.3414 & -0.0066 & -0.0025 & -0.0000 \\
0.0744 & 0.0536 & 0.0562 & 0.0320 & -3.6328 & 0.0029 & 0.0005 & -0.0012 & -0.0000 \\
-0.0135 & -0.0484 & -0.0182 & -3.5146 & 0.0920 & -0.4877 & -0.0013 & -0.0005 & 0.0000 \\
0.0000 & 0.0000 & 0.0000 & 1.0000 & 0.0002 & 0.0678 & 0.0000 & 0.0000 & 0.0000 \\
0.0000 & 0.0000 & 0.0000 & 0.0000 & 1.0000 & -0.0029 & 0.0000 & 0.0000 & 0.0000 \\
0.0000 & 0.0000 & 0.0000 & 0.0000 & 0.0030 & 1.0023 & 0.0000 & 0.0000 & 0.0000
\end{bmatrix}$$

B Matrix =

$$\begin{bmatrix}
2.9740 & -2.3000 & -9.0447 & 1.4249 & 4.2452 & 2.2569 \\
-0.3192 & -3.2328 & -1.0676 & -9.6369 & -0.0002 & -1.1553 \\
-67.7470 & 26.2490 & -10.9320 & 0.0958 & -0.0024 & 0.1587 \\
-0.9236 & -4.4730 & -3.0674 & -188.9500 & 0.7312 & -4.3177 \\
10.3310 & -0.5135 & 36.5510 & -0.7542 & 0.0067 & -15.9830 \\
-0.4093 & 12.8290 & -0.7208 & -32.6180 & 0.1276 & -0.6119 \\
0.0000 & 0.0000 & 0.0000 & 0.0000 & 0.0000 & 0.0000 \\
0.0000 & 0.0000 & 0.0000 & 0.0000 & 0.0000 & 0.0000 \\
0.0000 & 0.0000 & 0.0000 & 0.0000 & 0.0000 & 0.0000
\end{bmatrix}$$

CCH Configuration - 60 kt

A Matrix =

$$\begin{bmatrix}
-0.0501 & -0.0081 & 0.0196 & 0.0594 & -1.0117 & 0.0531 & -0.0002 & -9.8012 & 0.0000 \\
-0.0015 & -0.1039 & -0.0036 & 1.0331 & 0.0436 & -30.7550 & 9.8011 & -0.0026 & 0.0000 \\
-0.0923 & 0.0091 & -0.5741 & 0.0858 & 30.9410 & 0.0010 & -0.0458 & -0.5072 & 0.0000 \\
-0.0218 & -0.3152 & -0.0556 & -17.9350 & 0.1873 & -1.3819 & -0.0063 & -0.0028 & -0.0000 \\
0.0593 & 0.0317 & 0.0683 & 0.0031 & -3.7705 & -0.0004 & 0.0005 & -0.0012 & -0.0000 \\
-0.0073 & -0.0404 & -0.0286 & -3.5725 & 0.1188 & -0.6139 & -0.0013 & -0.0005 & 0.0000 \\
0.0000 & 0.0000 & 0.0000 & 1.0000 & 0.0002 & 0.0518 & 0.0000 & 0.0000 & 0.0000 \\
0.0000 & 0.0000 & 0.0000 & 0.0000 & 1.0000 & -0.0047 & 0.0000 & 0.0000 & 0.0000 \\
0.0000 & 0.0000 & 0.0000 & 0.0000 & 0.0047 & 1.0013 & 0.0000 & 0.0000 & 0.0000
\end{bmatrix}$$

B Matrix =

$$\begin{bmatrix} 2.3365 & -2.6615 & -8.3497 & 1.3871 & 4.8298 & 2.6248 \\ -0.5202 & -5.2533 & -1.0728 & -9.1512 & -0.0015 & -1.2606 \\ -75.8230 & 25.2820 & -17.5400 & 0.0903 & -0.0041 & 0.1851 \\ -4.3932 & -13.6420 & -3.8874 & -187.2100 & 1.2032 & -4.4692 \\ 16.1250 & -0.3336 & 37.4400 & -0.7514 & 0.0113 & -16.3170 \\ -1.2774 & 7.7493 & -1.0479 & -31.8100 & 0.2062 & -0.5614 \\ 0.0000 & 0.0000 & 0.0000 & 0.0000 & 0.0000 & 0.0000 \\ 0.0000 & 0.0000 & 0.0000 & 0.0000 & 0.0000 & 0.0000 \\ 0.0000 & 0.0000 & 0.0000 & 0.0000 & 0.0000 & 0.0000 \end{bmatrix}$$

CCH Configuration - 80 kt

A Matrix =

$$\begin{bmatrix} -0.0594 & -0.0089 & 0.0203 & 0.0512 & -0.6849 & 0.0704 & -0.0002 & -9.8095 & 0.0000 \\ -0.0012 & -0.1330 & -0.0051 & 0.7022 & 0.0413 & -41.0300 & 9.8092 & -0.0023 & 0.0000 \\ -0.0436 & 0.0131 & -0.6597 & 0.1044 & 41.1540 & 0.0052 & -0.0685 & -0.3080 & 0.0000 \\ -0.0139 & -0.3165 & -0.0690 & -17.8450 & 0.1980 & -1.4117 & -0.0055 & -0.0028 & -0.0000 \\ 0.0544 & 0.0187 & 0.0779 & -0.0130 & -3.8978 & -0.0026 & 0.0005 & -0.0011 & -0.0000 \\ -0.0046 & -0.0362 & -0.0330 & -3.6399 & 0.1503 & -0.7401 & -0.0012 & -0.0005 & 0.0000 \\ 0.0000 & 0.0000 & 0.0000 & 1.0000 & 0.0002 & 0.0314 & 0.0000 & 0.0000 & 0.0000 \\ 0.0000 & 0.0000 & 0.0000 & 0.0000 & 1.0000 & -0.0070 & 0.0000 & 0.0000 & 0.0000 \\ 0.0000 & 0.0000 & 0.0000 & 0.0000 & 0.0070 & 1.0005 & 0.0000 & 0.0000 & 0.0000 \end{bmatrix}$$

B Matrix =

$$\begin{bmatrix} 1.8703 & -2.9057 & -7.7530 & 1.3275 & 5.2499 & 2.6841 \\ -0.7366 & -7.9604 & -1.0909 & -8.9070 & -0.0033 & -1.2527 \\ -85.2550 & 23.0940 & -25.3800 & 0.0847 & -0.0047 & 0.1893 \\ -6.9739 & -26.7590 & -4.8206 & -186.3400 & 1.7217 & -4.3729 \\ 21.5920 & -0.3847 & 38.7750 & -0.7185 & 0.0132 & -16.4770 \\ -2.0535 & 3.5413 & -1.4564 & -31.2720 & 0.2873 & -0.4551 \\ 0.0000 & 0.0000 & 0.0000 & 0.0000 & 0.0000 & 0.0000 \\ 0.0000 & 0.0000 & 0.0000 & 0.0000 & 0.0000 & 0.0000 \\ 0.0000 & 0.0000 & 0.0000 & 0.0000 & 0.0000 & 0.0000 \end{bmatrix}$$

CCH Configuration - 100 kt

A Matrix =

$$\begin{bmatrix}
-0.0667 & -0.0107 & 0.0215 & 0.0418 & -0.1675 & 0.0845 & -0.0002 & -9.8133 & 0.0000 \\
-0.0010 & -0.1641 & -0.0066 & 0.1615 & 0.0407 & -51.2960 & 9.8127 & -0.0015 & 0.0000 \\
-0.0153 & 0.0173 & -0.7246 & 0.1208 & 51.3840 & 0.0095 & -0.0931 & -0.1440 & 0.0000 \\
-0.0119 & -0.3288 & -0.0755 & -17.6960 & 0.2135 & -1.4353 & -0.0044 & -0.0027 & -0.0000 \\
0.0527 & 0.0114 & 0.0881 & -0.0213 & -4.0152 & -0.0045 & 0.0004 & -0.0009 & -0.0000 \\
-0.0036 & -0.0341 & -0.0349 & -3.7484 & 0.1763 & -0.8673 & -0.0010 & -0.0005 & 0.0000 \\
0.0000 & 0.0000 & 0.0000 & 1.0000 & 0.0001 & 0.0147 & 0.0000 & 0.0000 & 0.0000 \\
0.0000 & 0.0000 & 0.0000 & 0.0000 & 1.0000 & -0.0095 & 0.0000 & 0.0000 & 0.0000 \\
0.0000 & 0.0000 & 0.0000 & 0.0000 & 0.0095 & 1.0001 & 0.0000 & 0.0000 & 0.0000
\end{bmatrix}$$

B Matrix =

$$\begin{bmatrix}
1.5100 & -3.0761 & -7.1384 & 1.2448 & 5.6148 & 2.5332 \\
-0.9707 & -11.5140 & -1.1226 & -8.7341 & -0.0057 & -1.1628 \\
-94.0170 & 21.0570 & -33.7680 & 0.0806 & -0.0038 & 0.1783 \\
-8.7581 & -41.7720 & -5.6703 & -185.7800 & 2.3283 & -4.0956 \\
27.0070 & -0.5681 & 40.4930 & -0.6602 & 0.0113 & -16.5320 \\
-2.6968 & -0.0121 & -1.8505 & -30.8760 & 0.3797 & -0.3264 \\
0.0000 & 0.0000 & 0.0000 & 0.0000 & 0.0000 & 0.0000 \\
0.0000 & 0.0000 & 0.0000 & 0.0000 & 0.0000 & 0.0000 \\
0.0000 & 0.0000 & 0.0000 & 0.0000 & 0.0000 & 0.0000
\end{bmatrix}$$

CCH Configuration - 120 kt

A Matrix =

$$\begin{bmatrix}
-0.0724 & -0.0131 & 0.0245 & 0.0311 & 0.3466 & 0.0956 & -0.0002 & -9.8143 & 0.0000 \\
-0.0008 & -0.1975 & -0.0081 & -0.3957 & 0.0400 & -61.5510 & 9.8133 & -0.0005 & 0.0000 \\
-0.0005 & 0.0214 & -0.7773 & 0.1367 & 61.6180 & 0.0100 & -0.1178 & -0.0305 & 0.0000 \\
-0.0115 & -0.3477 & -0.0805 & -17.5100 & 0.2264 & -1.4600 & -0.0026 & -0.0025 & -0.0000 \\
0.0518 & 0.0071 & 0.0997 & -0.0258 & -4.1249 & -0.0063 & 0.0003 & -0.0008 & -0.0000 \\
-0.0032 & -0.0333 & -0.0356 & -3.9052 & 0.1928 & -0.9960 & -0.0008 & -0.0005 & 0.0000 \\
0.0000 & 0.0000 & 0.0000 & 1.0000 & 0.0000 & 0.0031 & 0.0000 & 0.0000 & 0.0000 \\
0.0000 & 0.0000 & 0.0000 & 0.0000 & 0.9999 & -0.0120 & 0.0000 & 0.0000 & 0.0000 \\
0.0000 & 0.0000 & 0.0000 & 0.0000 & 0.0120 & 0.9999 & 0.0000 & 0.0000 & 0.0000
\end{bmatrix}$$

B Matrix =

$$\begin{bmatrix}
1.3390 & -3.1837 & -6.3835 & 1.1443 & 5.9481 & 2.2305 \\
-1.2342 & -16.0630 & -1.1785 & -8.5030 & -0.0093 & -1.0300 \\
-102.2500 & 19.4370 & -42.4310 & 0.0779 & -0.0015 & 0.1563 \\
-10.3460 & -58.6060 & -6.5280 & -185.1700 & 3.0141 & -3.7206 \\
32.5570 & -0.8340 & 42.5880 & -0.5830 & 0.0062 & -16.5240 \\
-3.2780 & -3.3541 & -2.2248 & -30.5780 & 0.4842 & -0.1978 \\
0.0000 & 0.0000 & 0.0000 & 0.0000 & 0.0000 & 0.0000 \\
0.0000 & 0.0000 & 0.0000 & 0.0000 & 0.0000 & 0.0000 \\
0.0000 & 0.0000 & 0.0000 & 0.0000 & 0.0000 & 0.0000
\end{bmatrix}$$

CCH Configuration - 140 kt

A Matrix =

$$\begin{bmatrix}
-0.0769 & -0.0156 & 0.0297 & 0.0200 & 0.7223 & 0.1048 & -0.0002 & -9.8143 & 0.0000 \\
-0.0007 & -0.2338 & -0.0099 & -0.8352 & 0.0389 & -71.7980 & 9.8127 & 0.0004 & 0.0000 \\
0.0056 & 0.0249 & -0.8209 & 0.1505 & 71.8540 & 0.0099 & -0.1439 & 0.0346 & 0.0000 \\
-0.0107 & -0.3726 & -0.0864 & -17.3030 & 0.2375 & -1.4841 & -0.0004 & -0.0023 & -0.0000 \\
0.0508 & 0.0044 & 0.1133 & -0.0295 & -4.2337 & -0.0083 & 0.0003 & -0.0007 & -0.0000 \\
-0.0027 & -0.0338 & -0.0358 & -4.1085 & 0.2012 & -1.1244 & -0.0004 & -0.0005 & 0.0000 \\
0.0000 & 0.0000 & 0.0000 & 1.0000 & -0.0001 & -0.0035 & 0.0000 & 0.0000 & 0.0000 \\
0.0000 & 0.0000 & 0.0000 & 0.0000 & 0.9999 & -0.0147 & 0.0000 & 0.0000 & 0.0000 \\
0.0000 & 0.0000 & 0.0000 & 0.0000 & 0.0147 & 0.9999 & 0.0000 & 0.0000 & 0.0000
\end{bmatrix}$$

B Matrix =

$$\begin{bmatrix}
1.4340 & -3.2371 & -5.3690 & 1.0381 & 6.2671 & 1.8104 \\
-1.5527 & -21.7270 & -1.2824 & -8.0894 & -0.0150 & -0.8812 \\
-109.8100 & 18.0730 & -51.1440 & 0.0759 & 0.0013 & 0.1261 \\
-12.0660 & -78.1090 & -7.5286 & -183.5900 & 3.7683 & -3.2936 \\
38.3880 & -1.1604 & 45.0440 & -0.4945 & -0.0001 & -16.5430 \\
-3.8329 & -6.9111 & -2.5973 & -30.2350 & 0.6010 & -0.0750 \\
0.0000 & 0.0000 & 0.0000 & 0.0000 & 0.0000 & 0.0000 \\
0.0000 & 0.0000 & 0.0000 & 0.0000 & 0.0000 & 0.0000 \\
0.0000 & 0.0000 & 0.0000 & 0.0000 & 0.0000 & 0.0000
\end{bmatrix}$$

CCH Configuration - 160 kt

A Matrix =

$$\begin{bmatrix}
-0.0807 & -0.0181 & 0.0372 & 0.0119 & 0.9546 & 0.1130 & -0.0002 & -9.8141 & 0.0000 \\
-0.0007 & -0.2740 & -0.0122 & -1.1516 & 0.0415 & -82.0410 & 9.8117 & 0.0011 & 0.0000 \\
0.0037 & 0.0270 & -0.8470 & 0.1598 & 82.0950 & 0.0091 & -0.1763 & 0.0685 & 0.0000 \\
-0.0099 & -0.4138 & -0.0944 & -17.0620 & 0.2631 & -1.5025 & 0.0019 & -0.0022 & -0.0000 \\
0.0506 & 0.0024 & 0.1342 & -0.0355 & -4.3738 & -0.0108 & 0.0002 & -0.0006 & -0.0000 \\
-0.0024 & -0.0372 & -0.0368 & -4.3313 & 0.2135 & -1.2492 & -0.0001 & -0.0005 & -0.0000 \\
0.0000 & 0.0000 & 0.0000 & 1.0000 & -0.0001 & -0.0070 & 0.0000 & 0.0000 & 0.0000 \\
0.0000 & 0.0000 & 0.0000 & 0.0000 & 0.9998 & -0.0180 & 0.0000 & 0.0000 & 0.0000 \\
0.0000 & 0.0000 & 0.0000 & 0.0000 & 0.0180 & 0.9999 & 0.0000 & 0.0000 & 0.0000
\end{bmatrix}$$

B Matrix =

$$\begin{bmatrix}
1.6360 & -3.2686 & -4.0065 & 0.9608 & 6.5819 & 1.3065 \\
-1.9684 & -28.2640 & -1.4896 & -7.2760 & -0.0250 & -0.7260 \\
-113.9900 & 16.1790 & -58.9490 & 0.0762 & 0.0039 & 0.0902 \\
-14.0800 & -103.5200 & -8.8946 & -176.9800 & 4.5513 & -2.7790 \\
45.0090 & -1.4909 & 47.8220 & -0.4088 & -0.0063 & -17.0230 \\
-4.4569 & -11.5530 & -3.0601 & -29.0460 & 0.7234 & 0.0831 \\
0.0000 & 0.0000 & 0.0000 & 0.0000 & 0.0000 & 0.0000 \\
0.0000 & 0.0000 & 0.0000 & 0.0000 & 0.0000 & 0.0000 \\
0.0000 & 0.0000 & 0.0000 & 0.0000 & 0.0000 & 0.0000
\end{bmatrix}$$

CCH Configuration - 180 kt

A Matrix =

$$\begin{bmatrix}
-0.0836 & -0.0204 & 0.0494 & 0.0034 & 1.0622 & 0.1206 & -0.0002 & -9.8140 & 0.0000 \\
-0.0008 & -0.3189 & -0.0147 & -1.3648 & 0.0430 & -92.2780 & 9.8105 & 0.0017 & 0.0000 \\
-0.0073 & 0.0266 & -0.8535 & 0.1617 & 92.3430 & 0.0072 & -0.2022 & 0.0850 & 0.0000 \\
-0.0081 & -0.4731 & -0.1029 & -16.6260 & 0.2811 & -1.4998 & 0.0039 & -0.0020 & -0.0000 \\
0.0508 & 0.0008 & 0.1665 & -0.0438 & -4.5423 & -0.0135 & 0.0001 & -0.0007 & -0.0000 \\
-0.0019 & -0.0432 & -0.0364 & -4.5363 & 0.2077 & -1.3671 & 0.0003 & -0.0005 & -0.0000 \\
0.0000 & 0.0000 & 0.0000 & 1.0000 & -0.0002 & -0.0087 & 0.0000 & 0.0000 & 0.0000 \\
0.0000 & 0.0000 & 0.0000 & 0.0000 & 0.9998 & -0.0206 & 0.0000 & 0.0000 & 0.0000 \\
0.0000 & 0.0000 & 0.0000 & 0.0000 & 0.0206 & 0.9998 & 0.0000 & 0.0000 & 0.0000
\end{bmatrix}$$

B Matrix =

$$\begin{bmatrix} 2.1866 & -3.0636 & -2.1298 & 0.8279 & 6.9008 & 0.6143 \\ -2.4323 & -35.3630 & -1.7420 & -5.8775 & -0.0423 & -0.5034 \\ -114.3500 & 13.8470 & -65.0660 & 0.0717 & 0.0064 & 0.0414 \\ -16.1180 & -136.6100 & -10.3790 & -163.3800 & 5.3268 & -2.0336 \\ 52.7630 & -1.9274 & 51.2760 & -0.2943 & -0.0122 & -18.1250 \\ -4.9069 & -17.4330 & -3.4217 & -26.8230 & 0.8465 & 0.2535 \\ 0.0000 & 0.0000 & 0.0000 & 0.0000 & 0.0000 & 0.0000 \\ 0.0000 & 0.0000 & 0.0000 & 0.0000 & 0.0000 & 0.0000 \\ 0.0000 & 0.0000 & 0.0000 & 0.0000 & 0.0000 & 0.0000 \end{bmatrix}$$

CCH Configuration - 200 kt

A Matrix =

$$\begin{bmatrix} -0.0852 & -0.0219 & 0.0711 & -0.0134 & 1.0568 & 0.1295 & -0.0001 & -9.8139 & 0.0000 \\ -0.0006 & -0.3685 & -0.0160 & -1.4772 & 0.0286 & -102.5000 & 9.8096 & 0.0018 & 0.0000 \\ -0.0302 & 0.0223 & -0.8394 & 0.1507 & 102.6000 & 0.0039 & -0.1951 & 0.0924 & 0.0000 \\ -0.0034 & -0.5466 & -0.1047 & -15.6550 & 0.2327 & -1.4375 & 0.0045 & -0.0012 & -0.0000 \\ 0.0504 & 0.0002 & 0.2153 & -0.0535 & -4.7153 & -0.0163 & 0.0000 & -0.0008 & -0.0000 \\ -0.0008 & -0.0497 & -0.0270 & -4.6790 & 0.1268 & -1.4750 & 0.0007 & -0.0004 & 0.0000 \\ 0.0000 & 0.0000 & 0.0000 & 1.0000 & -0.0002 & -0.0094 & 0.0000 & 0.0000 & 0.0000 \\ 0.0000 & 0.0000 & 0.0000 & 0.0000 & 0.9998 & -0.0199 & 0.0000 & 0.0000 & 0.0000 \\ 0.0000 & 0.0000 & 0.0000 & 0.0000 & 0.0199 & 0.9999 & 0.0000 & 0.0000 & 0.0000 \end{bmatrix}$$

B Matrix =

$$\begin{bmatrix} 3.5917 & -2.2041 & 0.5620 & 0.4869 & 7.2324 & -0.4510 \\ -2.7253 & -42.5920 & -1.8539 & -3.6329 & -0.0707 & -0.2007 \\ -111.2500 & 11.3320 & -68.7400 & 0.0489 & 0.0088 & -0.0329 \\ -17.1840 & -178.9600 & -11.1840 & -140.1600 & 6.0457 & -1.0939 \\ 61.8990 & -2.5941 & 55.9520 & -0.1218 & -0.0176 & -20.0280 \\ -4.2298 & -24.0420 & -2.9671 & -23.6120 & 0.9680 & 0.2402 \\ 0.0000 & 0.0000 & 0.0000 & 0.0000 & 0.0000 & 0.0000 \\ 0.0000 & 0.0000 & 0.0000 & 0.0000 & 0.0000 & 0.0000 \\ 0.0000 & 0.0000 & 0.0000 & 0.0000 & 0.0000 & 0.0000 \end{bmatrix}$$

References

[1] Leishman, J., *Principals of Helicopter Aerodynamics*, Cambridge University Press, second edition, 2006.

[2] Johnson, W., *Helicopter Theory*, Dover Publications, Inc., second edition, 1994.

[3] Newman, S., *The Foundations of Helicopter Flight*, Edward Arnold, London, 1994.

[4] Newman, S., "The compound helicopter configuration and the helicopter speed trap," *Aircraft Engineering and Aerospace Technology*, Vol. 69, (5), 1997, pp. 408.

[5] Filippone, A., *Flight Performance of Fixed and Rotary Wing Aircraft*, Elsevier Ltd., first edition, 2006.

[6] Sekula, M. and Gandhi, F., "Effects of Auxiliary Lift and Propulsion on Helicopter Vibration Reduction and Trim," *AIAA Journal of Aircraft*, Vol. 41, (3), 2004, pp. 645–656.
doi: 10.2514/1.496

[7] Prouty, R., *Helicopter Performance, Stability, and Control*, Robert E. Krieger Publishing Company, Inc., reprint edition, 1990.

[8] Orchard, M. and Newman, S., "Some design issues for the optimisation of the compound helicopter configuration," American Helicopter Society 56th Annual Forum, 2000.

[9] M.Buhler and Newman, S., "The Aerodynamics of the Compound Helicopter Configuration," *The Aeronautical Journal*, Vol. 100, (994), 1996, pp. 111–120.

[10] Orchard, M. and Newman, S., "The compound helicopter - why have we not succeeded before?" *The Aeronautical Journal*, Vol. 103, (1028), 1999, pp. 489–495.

[11] Blackburn, W., "Methods for Improving Handling Qualities of Compound Aircraft," American Helicopter Society 23rd Annual Forum, 1967.

[12] Wyrick, D., "Extension of the High-Speed Flight Envelope of the XH-51A Compound Helicopter," USAAVLABS TR 65-71, 1965.

[13] Dumond, R. and Simon, D., "Flight Investigation of Design Features of the S-67 Winged Helicopter," *Journal of the American Helicopter Society*, Vol. 18, (3), 1973, pp. 2–9.
doi: 10.4050/JAHS.18.2

[14] Segel, R., Jenney, D., and Gerdes, W., "Final Report NH-3A (Sikorsky S-61F) Flight Test Program," Sikorsky Aircraft Report SER-611344, 1969.

[15] Meyers, D., Tompkins, L., and Goldberg, J., "16H-1A flight test research program," USAAVLABS TR-67-58, 1968.

[16] Prouty, R., "The Lockheed Helicopter Experience," American Helicopter Society 65th Forum, 2009.

[17] Arcidiacono, P., DeSimone, G., and Occhiato, J., "Preliminary Evaluation of RSRA Data Comparing Pure Helicopter, Auxiliary Propulsion and Compound Helicopter Flight Characteristics," American Helicopter Society 36th Annual Forum, 1980.

[18] Ruddell, A., "Advancing Blade Concept (ABC) Development," American Helicopter Society 32nd Annual Forum, 1976.

[19] Lentine, F., Groth, W., and Oglesby, T., "Research in Maneuverability of the XH-51A Compound Helicopter," USAAVLABS Technical Report 68-23, 1968.

[20] Balmford, D. and Benger, B., "The Compound Helicopter - A Concept Revisited," 17th European Rotorcraft Forum, 1991.

[21] Jordan, T., Humpherson, D., and Benger, B., "The compound helicopter - The rotorcraft for the 21st Century?" American Helicopter Society 49th Annual Forum, 1993.

[22] Maisel, M., Guilianetti, D., and Dugan, D., "The History of the XV-15 Tilt Rotor Research Aircraft: From Concept to Flight," Monograph 17 NASA SP-2000-4517, 2000.

[23] Ormiston, R., "Low-Disk Loading Compound Rotorcraft for High-Speed and Aerodynamic Efficiency," International Powered Lift Conference 2010, 2010.

[24] Felker, F., Maisel, M., and Betzina, M., "Full-Scale Tilt-Rotor Hover Performance," *Journal of the American Helicopter Society*, Vol. 31, (2), 1986, pp. 10–18.
doi: 10.4050/JAHS.31.10

[25] Houston, S., "The Gyrodyne - A Forgotten High Performer?" *Journal of the American Helicopter Society*, Vol. 52, (4), 2007, pp. 382 – 391.
doi: http://dx.doi.org/10.4050/JAHS.52.382

[26] Orchard, M. and Newman, S., "The fundamental configuration and design of the compound helcopter," *Proceedings of the Institution of Mechanical Engineers, Part G: Journal of Aerospace Engineering*, Vol. 217, (6), 2003, pp. 297–315.
doi: 10.1243/095441003772538570

[27] Moodie, A. and Yeo, H., "Design of a Cruise-Efficient Compound Helicopter," *Journal of the American Helicopter Society*, Vol. 57, (3), 2012.
doi: 10.4050/JAHS.57.032004

[28] Yeo, H. and Johnson, W., "Optimum Design of a Compound Helicopter," *AIAA Journal of Aircraft*, Vol. 46, (4), 2009.
doi: 10.2514/1.40101

[29] Russell, C. and Johnson, W., "Exploration of Configuration Options for a Large Civil Compound Helicopter," American Helicopter Society 69th Annual Forum, 2013.

[30] Tannabe, Y., Aoyama, T., Kobiki, N., Sugiura, M., Miyashita, R., Sunada, S., Kawachi, K., and Nagao, M., "A Conceptual Study of High Speed Rotorcraft," 40th European Rotorcraft Forum, 2014.

[31] Polmar, N. and Kennedy, F., *Military Helicopters of the World*, Arms and Armour Press, London, 1981.

[32] Burgess, R., "The ABC Rotor - A Historical Perspective," American Helicopter Society 60th Annual Forum, 2004.

[33] Bagai, A., "Aerodynamic Design of the X2 Technology Demonstrator Main Rotor Blade," American Helicopter Society 64th Annual Forum, 2008.

[34] Blackwell, R. and Millott, T., "Dynamics Design Characteristics of the Sikorsky X2 Technology Demonstrator Aircraft," American Helicopter Society 64th Annual Forum, 2008.

[35] Walsh, D., Weiner, S., Bagai, A., Lawerence, T., and Blackwell, R., "Development Testing of the Sikorsky X2 Technology Demonstrator," American Helicopter Society 65th Annual Forum, 2009.

[36] Padfield, G., *Helicopter Flight Dynamics: the Theory and Application of Flying Qualities and Simulation Modelling*, Blackwell Publishing, second edition, 2007.

[37] Bramwell, A., *Helicopter Dynamics*, Edward Arnold, first edition, 1976, p. 212.

[38] Johnson, W., *Rotorcraft Aeromechanics*, Cambridge University Press, Cambridge, U.K., 2013.

[39] Thomson, D., "Development of a Generic Helicopter Mathematical Model for Application to Inverse Simulation," Internal Report No. 9216, Department of Aerospace Engineering, University of Glasgow, UK, 1992.

[40] Padfield, G. and Charlton, M., "Aspects of RAE flight research into helicopter agility and pilot control strategy," Helicopter Handling Qualities Specialists Meeting, 1986.

[41] Thomson, D. and Bradley, R., "The principles and practical application of helicopter inverse simulation," *Simulation Practice and Theory*, Vol. 6, (1), 1998, pp. 47–70.
doi: 10.1016/S0928-4869(97)00012-8

[42] Bradley, R., Padfield, G., Murray-Smith, D., and Thomson, D., "Validation of helicopter mathematical models," *Transactions of the Institute of Measurement and Control*, Vol. 12, (186), 1990.
doi: 10.1177/014233129001200405

[43] Rutherford, S. and Thomson, D., "Helicopter inverse simulation incorporating an individual blade rotor model," *AIAA Journal of Aircraft*, Vol. 34, (5), 1997, pp. 627–634.
doi: 10.2514/2.2239

[44] Houston, S., "Rotorcraft Aeromechanics Simulation for Control Analysis - Mathematical Model Definition," Internal Report No. 9123, Department of Aerospace Engineering, University of Glasgow, UK, 1991.

[45] Mansur, M., "Development and Validation of a Blade Element Mathematical Model for the AH-64A Apache Helicopter," NASA-TM-108863, 1995.

[46] Pitt, D. and Peters, D., "Rotor Dynamic Inflow Derivatives and Time Constants from Various Inflow Models," 9th European Rotorcraft Forum, 1983.

[47] Nowak, M., Prasad, J., and Peters, D., "Development of a Finitie State Model for a Coaxial Rotor in Forward Flight," American Helicopter Society 70th Annual Forum, 2014.

[48] Zhao, J. and He, C., "Real-Time Simulation of a Coaxial Rotor Configurations with Combined Finite State Dynamic Wake and VPM," American Helicopter Society 70th Annual Forum, 2014.

[49] Chen, R., "A Survey of Nonuniform Inflow Models for Rotorcraft Flight Dynamics and Control Applications," NASA TM 102219, 1989.

[50] Leishman, J. and Syal, M., "Figure of Merit Definition for Coaxial Rotors," *Journal of the American Helicopter Society*, Vol. 53, (3), 2008, pp. 290–300.
doi: 10.4050/JAHS.53.290

[51] Leishman, J. and Ananthan, S., "An Optimum Coaxial Rotor System for Axial Flight," *Journal of the American Helicopter Society*, Vol. 53, (4), 2008, pp. 366–381.
doi: 10.4050/JAHS.53.366

[52] Kim, H. and Brown, R., "A Rational Approach to Comparing the Performance of Coaxial and Conventional Rotors," *Journal of the American Helicopter Society*, Vol. 55, (1), 2010, pp. 012003.
doi: 10.4050/JAHS/55.012003

[53] Kim, H. and Brown, R., "A Comparison of Coaxial and Conventional Rotor Performance," *Journal of the American Helicopter Society*, Vol. 55, (1), 2010, pp. 012004.
doi: 10.4050/JAHS.55.01.2004

[54] Paglino, V., "Forward Flight Performance of a Coaxial Rigid Rotor," American Helicopter Society 27th Annual Forum, 1971.

[55] Harrington, R., "Full-Scale-Tunnel Investigation of the Static-Thrust Performance of a Coaxial Helicopter Rotor," NACA TN-2318, 1951.

[56] Dingeldein, R., "Wind-Tunnel Studies of the Performance of Multirotor Configurations," NACA TN 3236, 1954.

[57] Bagai, A. and Leishman, J., "Free-Wake Analysis of Tandem, Tilt-Rotor and Coaxial Rotor Configurations," *Journal of the American Helicopter Society*, Vol. 41, (3), 1995, pp. 196–207.
doi: 10.4050/JAHS.41.196

[58] Von Mises, R., *Theory of Flight*, Dover Publications, 1959.

[59] Hartman, E. and Biermann, D., "The Aerodynamic Characteristics of Full-Scale Propellers Having 2, 3 and 4 Blades of Clark Y and R.A.F. Airfoil Sections," NACA-TR-640, 1938.

[60] Sequeira, C. J., Willis, D. J., and Peraire, J., "Comparing Aerodynamic Models for Numerical Simulation of Dynamics and Control of Aircraft," 44th AIAA Aerospace Sciences Meeting, 2006.

[61] Dreier, M., *Introduction to Helicopter and Tiltrotor Flight Simulation*, American Institute of Aeronautics & Astronautics, Washington D.C., first edition, 2007.

[62] Wright, J. and Cooper, J., *Introduction to Aircraft Aeroelasticity and Loads*, John Wiley and Sons Ltd, Chichester, West Sussex, U.K., second edition, 2015.

[63] Wood, T. and Peryea, M., "Reduction of Tiltrotor Download," *Journal of the American Helicopter Society*, Vol. 40, (3), 1995, pp. 42–51.
doi: 10.4050/JAHS.40.42

[64] Lynn, R., "Wing- Rotor Interactions," *Journal of Sound and Vibration*, Vol. 4, (3), 1966, pp. 388–402.

[65] Felker, F. and Light, J., "Aerodynamics Interactions Between a Rotor and Wing in Hover," American Helicopter Society 42th Annual Forum, 1986.

[66] McVeigh, M., Grauer, W., and Paisley, D., "Rotor/Airframe Interactions on Tiltrotor Aircraft," *Journal of the American Helicopter Society1*, Vol. 35, (3), 1990, pp. 43–51.
doi: 10.4050/JAHS.35.43

[67] Frandenburgh, E. and Chuga, G., "Flight Program on the NH-3A Research Helicopter," Technical report, 1968.

[68] Sheldahi, R. and Klimas, P., "Aerodynamic Characterisitics of Seven Symmetrical Airfoil Sections through 180-Degree of Angle of Attack for Use in Aerodynamic Analysis of Vertical Axis Wind Turbines," Sandia National Laboratories Energy Report, 1981.

[69] Anderson, J., *Fundamentals of Aerodynamics*, McGraw-Hill Book Company, fourth edition, 2007.

[70] Harris, F., "Rotor Performance at High Advance Ratio; Theory versus Test," NASA/CR2008215370, 2008.

[71] Hodara, J. and Smith, M., "Improvements of Crossflow Aerodynamic Predictions for Forward Flight," 40th European Rotorcraft Forum, 2014.

[72] Johnson, W., "Rotorcraft Aeromechanics Applications of a Comprehensive Analysis," HeliJapan 1998: AHS International Meeting on Rotorcraft Technology and Disaster Relief, 1998.

[73] Ballin, M., "Valiation of a real-time engineering simulation of the UH-60A helicopter," NASA TM-88360, 1987.

[74] Keys, C., "Performance Prediction of Helicopters," *Rotor-Wing Aerodynamics*, edited by W. Stepniewski, Dover Publications, Inc., 1981.

[75] Cooke, A. and Fitzpatrick, E., *Helicopter Test and Evaluation*, Blackwell Science, Oxford, U.K., 2002.

[76] Yeo, H., "Investigation of UH-60A Rotor Performance and Loads at High Advance Ratios," *Journal of Aircraft*, Vol. 50, (2), 2013, pp. 576–589.
doi: 10.2514/1.C031958

[77] Abbe, T., Blackwell, R. H. J., and Jenney, D., "Advancing Blade Concept (ABC) Dynamics," American Helicopter Society 33rd Annual Forum, 1977.

[78] Jenney, D., "ABC Aircraft Development Status," Sixth European Rotorcraft and Powered Lift Form, 1980.

[79] Arents, D., "An Assessment of the Hover Performance of the XH-59A Advancing Blade Concept Demonstration Helicopter," USAAMRDL-TN-25, 1977.

[80] Yeo, H. and Johnson, W., "Investigation of Maximum Blade Loading Capability of Lift-Offset Rotors," *Journal of the American Helicopter Society*, Vol. 59, (1), 2014, pp. 1–12.
doi: 10.4050/JAHS.59.012005

[81] Torres, M., "A Wing on the SA.341 Gazelle Helicopter and its Effects," *Vertica*, Vol. 1, (1), 1976, pp. 67–73.

[82] Walsh, D., Weiner, S., Arifian, K., Lawerence, T., Wilson, M., Millott, T., and Blackwell, R., "High Airspeed Testing of the Sikorsky X2 Technology Demonstrator," American Helicopter Society 67th Annual Forum, 2011.

[83] Zimmer, H., "The Aerodynamic Calculation of Counter Rotating Coaxial Rotors," 11th European Rotorcraft Forum, 1985.

[84] Lim, J., McAlister, K., and Johnson, W., "Hover Performance Correlation for Full-Scale and Model-Scale Coaxial Rotors," *Journal of the American Helicopter Society*, Vol. 54, (3), 2009, pp. 32005.
doi: 10.4050/JAHS.54.032005

[85] Johnson, W., "Influence of Lift Offset on Rotorcraft Performance," AHS Specialist's Conference on Aeromechanics, 2008.

[86] Allan, B. and Schaeffler, N., "Numerical Investigation of Rotorcraft Fuselage Drag Reduction using Active Flow Control," American Helicopter Society 67th Annual Forum, 2011.

[87] Ferguson, K. and Thomson, D., "Flight dynamics investigation of compound helicopter configurations," *AIAA Journal of Aircraft*, Vol. 52, (1), 2014.
doi: 10.2514/1.C032657

[88] Williams, R. and Montana, P., "A Comprehensive Plan for Helicopter Drag Reduction," American Helicopter Society Symposium on Helicopter Aerodynamic Efficiency, 1975.

[89] Anon., *Jane's All the World's Aircraft*, Jane's Information Group, 85th edition, 1994.

[90] Keys, C., "Performance Prediction of Helicopters," *Rotary-wing Aerodynamics*, edited by W. Stepniewski, Chap. Volume II, 1979.

[91] Sanderson, A., "Projected Power and Specific Fuel Consumption Development of the Rolls Royce Gem Engine," American Helicopter Society 37th Annual Forum, 1981.

[92] Tischler, M. and Remple, R., *Aircraft and Rotorcraft System Identification*, American Institute of Aeronautics & Astronautics, Reston, VA, second edition, 2012.

[93] Houston, S., "Validation of a non-linear individual blade rotorcraft flight dynamics model using a perturbation method," *The Aeronautical Journal*, Vol. 98, (977), 1994, pp. 260–266.

[94] Stevens, B. and Lewis, F., *Aircraft Control and Simulation*, John Wiley and Sons, second edition, 2003.

[95] Blake, B. and Alansky, I., "Stability and Control of the YUH-61A," *Journal of the American Helicopter Society*, Vol. 22, (1), 1977, pp. 2–10.
doi: 10.4050/JAHS.22.2

[96] Cook, M., *Flight Dynamics Principles*, Elsevier Ltd., third edition, 2013.

[97] Ruddell, A., "Advancing Blade Concept (ABC) Technology Demonstrator," USAAVRADCOM-TR-81-D-5, 1981.

[98] AGARD, "Rotorcraft System Identification," Final Report of WG18, AGARD AR 280, 1991.

[99] AGARD, "Rotorcraft System Identification," AGARD LS 178, 1991.

[100] Houston, S., "Rotorcraft Simulation for Design Applications," European Simulation Multiconference, 1992.

[101] Padfield, G., "SA330 Puma Identificaton Results," AGARD Lecture Series 178, 1991.

[102] Thomson, D. and Bradley, R., "Inverse simulation as a tool for flight dynamics research - Principles and applications," *Progress in Aerospace Sciences*, Vol. 42, (3), May 2006, pp. 174–210.
doi: 10.1016/j.paerosci.2006.07.002

[103] Thomson, D. and Bradley, R., "An analytical method of quantifying helicopter agility," Proceedings of the 12th European Rotorcraft Forum, 1986.

[104] Thomson, D. and Bradley, R., "An investigation of pilot strategy in helicopter nap-of-the-earth manoeuvres by comparison of flight data and inverse simulation," Royal Aeronautcal Society: helicopter handling qualities and control, 1988.

[105] Thomson, D. and Bradley, R., "The use of inverse simulation for conceptual design," 16th European Rotorcraft Forum, 1990.

[106] Thomson, D. and Bradley, R., "The use of inverse simulation for preliminary assessment of helicopter handling qualities," *The Aeronautical Journal*, Vol. 101, (1007), 1997, pp. 287 – 294.

[107] Cameron, N., Thomson, D., and Murray-Smith, D., "Pilot modelling and inverse simulation for initial handling qualities assessment," *The Aeronautical Journal*, Vol. 107, (1074), 2003, pp. 511– 520.

[108] Hess, R., Gao, C., and Wang, S., "Generalized technique for inverse simulation applied to aircraft maneuvers," *AIAA Journal of Guidance, Control and Dynamics*, Vol. 14, (5), 1991, pp. 920–926.
doi: 10.2514/3.20732

[109] Hess, R. and Gao, C., "A Generalized Algorithm for Inverse Simulation Applied to Helicopter Maneuvering Flight," *Journal of the American Helicopter Society*, Vol. 38, (4), 1993, pp. 3 – 15.
doi: 10.4050/JAHS.38.3

[110] Avanzini, G., de Matteis, G., and de Socio, L., "Two-Timescale-Integration Method for Inverse Simulation," *Journal of Guidance, Control and Dynamics*, Vol. 22, (3), 1999, pp. 395–401.
doi: 10.2514/2.4410

[111] Avanzini, G. and de Matteis, G., "Two-timescale inverse simulation of a helicopter model," *Journal of Guidance, Control and Dynamics*, Vol. 24, (2), 2001, pp. 330–339.
doi: 10.2514/2.4716

[112] Celi, R., "Optimization-Based Inverse Simulation of a Helicopter Slalom Maneuver," *Journal of Guidance, Control and Dynamics*, Vol. 23, (2), 2000, pp. 289–297.
doi: 10.2514/2.4521

[113] de Matteis, G., de Socio, L., and Leonessa, A., "Solution of Aircraft Inverse Problems by Local Optimization," *AIAA Journal of Guidance, Control and Dynamics*, Vol. 18, (3), 1995, pp. 567–571.
doi: 10.2514/3.21424

[114] Horn, J., Calise, A., and Prasad, J., "Flight Envelope Cueing on a Tilt-Rotor Aircraft Using Neural Network Limit Prediction," *Journal of the American Helicopter Society*, Vol. 46, (1), 2001, pp. 23–31.
doi: 10.4050/JAHS.46.23

[115] Horn, J., Calise, A., and Prasad, J., "Flight Envelope Limit Detection and Avoidance for Rotorcraft," *Journal of the American Helicopter Society*, Vol. 46, (1), 2001, pp. 253–262.
doi: 10.4050/JAHS.46.23

[116] Sahani, N. and Horn, J., "Adaptive Model Inversion Control of a Helicopter with Structural Load Limiting," *Journal of Guidance, Control and Dynamics*, Vol. 29, (2), 2006, pp. 411–420.
doi: 10.2514/1.13391

[117] Rysdyk, R. and Calise, A., "Adaptive Model Inversion Flight Control for Tiltrotor Aircraft," American Helicopter Society 54th Annual Forum, 1998.

[118] Kim, B. and Calise, A., "Nonlinear Flight Control Using Neural Networks," Proceedings of the AIAA Guidance, Navigation and Control Conference, 1994.

[119] Leitner, J., Calise, A., and Prasad, J., "Analysis of Adaptive Neural Network for Helicopter Flight Control," Proceedings of the AIAA Guidance, Navigation and Control Conference1, 1995.

[120] Slotine, J. and Li, W., *Applied Nonlinear Control*, Prentice-Hall, New Jersey, 1991.

[121] Calise, A. and Rysdyk, R., "Nonlinear adaptive flight control using neural networks," *Control Systems, IEEE*, Vol. 18, (6), 1998.
doi: 10.1109/37.736008

[122] Olson, J. and Scott, M., "Helicopter Design Optimization for Maneuverability and Agility," American Helicopter Society 45th Annual Forum, 1989.

[123] Johnson, K., *Prediction of Operational Envelope Maneuverability Effects of Rotorcraft Design*, Ph.D, Georgia Institute of Technology, 2013.

[124] Levine, L., Warburton, F., and Curtiss Jr, H., “Assessment of Rotorcraft Agility and Maneuverability with Pilot-in-the-loop Simulation,” American Helicopter Society 41st Annual Forum, 1985.

[125] Whalley, M., “Development and Evaluation of an Inverse Solution Technique for Studying Helicopter Maneuverability and Agility,” USAAVSCOM TR 90-A-008, 1991.

[126] Rutherford, S., *Simulation Techniques for the Study of the Manoeuvring of Advanced Rotorcraft Configurations*, Ph.D thesis, University of Glasgow, 1997.

[127] Thomson, D. and Bradley, R., “Mathematical Definition of Helicopter Maneuvers,” *Journal of the American Helicopter Society*, Vol. 4, (1), 1997, pp. 307 – 309.
doi: 10.4050/JAHS.42.307

[128] Lu, L., Murray-Smith, D. J., and Thomson, D., “Issues of numerical accuracy and stability in inverse simulation,” *Simulation Modelling Practice and Theory*, Vol. 16, (9), October 2008, pp. 1350–1364.
doi: 10.1016/j.simpat.2008.07.003

[129] Padfield, G., “Capturing requirements for tiltrotor handling qualities - case studies in virtual engineering,” *The Aeronautical Journal*, Vol. 112, (1134), 2008, pp. 433 – 449.

[130] Anon., “Handling qualities requirements for military rotorcraft,” Aeronautical design standard ADS-33E-PRF, United States Army Aviation and Troop Command, 2000.

[131] Celi, R., “Analytical Simulation of ADS-33 Mission Task Elements,” American Helicopter Society 63rd Annual Forum, 2007.

[132] Thomson, D., *Evaluation of helicopter agility through inverse solution of the equations of motion*, Ph.D thesis, University of Glasgow, 1987.

[133] Lappos, N. and Padfield, G., “Design of Helicopters for Agility,” AGARD AR-314 Operational Agility, 1994.

[134] Ferguson, K. and Thomson, D., “Performance comparison between a conventional helicopter and compound helicotper configurations,” *Proceedings of the Institution of Mechanical Engineers, Part G: Journal of Aerospace Engineering*, 2015.
doi: 10.1177/0954410015577997

[135] Ruddell, A., "XH-59A ABC Technology Demonstrator Altitude Expansion and Operational Tests," USAAVRADCOM TR 81-D-35, 1981.

[136] McHugh, F. and Clark, R., "Wind Tunnel Investigation of Rotor Lift and Propulsive Force at High Speed Data Analysis," NASA CR 145217-1, 1977.

[137] McHugh, F. and Clark, R., "Wind Tunnel Investigation of Rotor Lift and Propulsive Force at High Speed Data Analysis," NASA CR 145217-2, 1977.

[138] McHugh, F., "What Are the Lift and Propulsive Force Limits at High Speed for the Conventional Rotor?" American Helicopter Society 34th Annual Forum, 1978.

[139] Padfield, G., "Rotorcraft Handling Qualities Engineering: Managing the Tension between Safety and Performance," *Journal of the American Helicopter Society*, Vol. 58, (1), 2013, pp. 1–27.
doi: 10.4050/JAHS.58.011001

[140] Charlton, M., Howell, S., Padfield, G., Jones, J., Bradley, R., MacDonald, R., Thomson, D., and Leacock, G., "A Methodology for the Prediction of Pilot Workload and the Influence of Effectiveness in Rotorcraft Mission Tasks," 24th European Rotorcraft Forum, 1998.

[141] Cooper, G. and Harper, R., "The Use of Pilot Ratings in the Evaluation of Aircraft Handling Qualities," NASA TM D-51333, 1969.

[142] Key, D., "A New Handling Qualities Specification for US Military Rotorcraft," Proceedings of International Conference, Helicopter Handling Qualities and Flight Control, RAeSoc, 1988.

[143] Leacock, G., *Helicopter inverse simulation for workload and handling qualities estimation*, Ph.D thesis, University of Glasgow, 2000.

[144] Anon., "Military Specification: Helicopter Flying and Ground Handling Qualities, General Requirements for MIL-H-8501A," , 1961.

[145] Mitchell, D., Doman, D., Key, D., Klyde, D., Legget, D., Moorhouse, D., Mason, D., Raney, D., and Schmidt, D., "Evolution, Revolution, and Challenges of Handling Qualities," *Journal of Guidance, Control and Dynamics*, Vol. 27, (1), 2004, pp. 12–28.

[146] Ashkenas, I. and Walton, R., "Analytical Review of Military Helicopter Flying Qualities," Systems Technology Inc. TR 143-1, 1967.

[147] Tischler, M., Iver, C., Mansur, M., Cheung, K., Berger, T., and Berrios, M., "Handling-Qualities Optimization and Trade-offs in Rotorcraft Flight Control Design," RAeS Rotorcraft Handling-Qualities Conference, 2008.

[148] Irwin, J., Spano, M., Bender, J., and Schwerke, M., "MH-47G Digital AFCS Evolution," American Helicopter Society 67th Annual Forum, 2011.

[149] Hoefinger, M. and Blanken, C., "Flight Testing the ADS-33E Cargo Helicopter Handling Qualities Requirements Using a CH-53G," *Journal of the American Helicopter Society*, Vol. 58, (1), 2013, pp. 1–11.
doi: JAHS.58.012002

[150] Padfield, G., "The Making of Helicopter Flying Qualities: A Requirements Perspective," *The Aeronautical Journal*, Vol. 102, (1011), 1998, pp. 409 – 437.

[151] M. Tischler, editor, *Advances in Aircraft Flight Control*, Taylor and Francis Ltd, London, U.K., 1996.

[152] Key, D., Blanken, C., and Hoh, R., "Some Lessons Learned in Three Years with ADS-33C," AHS/NASA Conference on Piloting Vertical Flight Aircraft, 1993.

[153] Ham, J., Metzger, M., and Hoh, R., "Handling Qualities Testing Using the Mission Oriented Requirements of ADS-33C," American Helicopter Society 48th Annual Forum, 1992.

[154] Morgan, J. and Baillie, S., "ADS-33C Related Handling Qualities Research Performed Using the NRC Bell 205 Airbone Simulator," AHS/NASA Conference on Piloting Vertical Flight Aircraft, 1993.

[155] Blanken, C., Hoh, R., Mitchell, D., and Key, D., "Test Guide for ADS-33E-PRF," Special Report AMR-AF-08-07, 2008.

[156] Kothmann, B. and Armbrust, J., "RAH-66 Commanche Core AFCS Control Law Development," American Helicopter Society 58th Annual Forum, 2002.

[157] Sahasrabudhe, V., Faynberg, A., Pozdin, M., Cheng, R., Tischler, M., Stumm, A., and Lavin, M., "Balancing CH-53K Handling Qualities and Stability Margin Requirements in the Presence of Heavy External Loads," American Helicopter Society 63rd Annual Forum, 2007.

[158] Meyer, M. and Padfield, G., "First Steps in the Development of Handling Qualities Criteria for a Civil Tilt Rotor," *Journal of the American Helicopter Society*, Vol. 50, (1), 2005, pp. 33 – 45.
doi: 10.4050/1.3092841

[159] Padfield, G., Brookes, D., and Meyer, M., "Progress in Civil Tilt-Rotor Handling Qualities," *Journal of the American Helicopter Society*, Vol. 51, (1), 2006, pp. 80 – 91.
doi: 10.4050/1.3092880

[160] Press, W., Teukolsky, S., Vetterling, W., and Flannery, B., *Numerical Recipes in FORTRAN: the art of scientific computing*, Cambridge University Press, Cambridge, U.K., second edition, 1993.
doi: 0521437164